

# Measurements of Beyond Standard Model Interactions with the UCNA and nEDM@SNS Experiments

Thesis by  
Xuan Sun

In Partial Fulfillment of the Requirements for the  
Degree of  
Doctorate of Philosophy

The Caltech logo, consisting of the word "Caltech" in a bold, orange, sans-serif font.

CALIFORNIA INSTITUTE OF TECHNOLOGY  
Pasadena, California

2022  
Defended November 29, 2021

© 2022

Xuan Sun  
ORCID: 0000-0001-8817-4643

All rights reserved

## DEDICATION

For my Mother and Father.

## ACKNOWLEDGEMENTS

First off, I'd like to acknowledge my advisor, Dr. Brad Filippone. He has been a sound role model, wise mentor, and supportive friend throughout my time at Caltech. I leave this PhD program a better person and this is largely thanks to such excellent mentorship. I'd also like to extend my appreciation to my collaborators at Caltech and those I met at Los Alamos National Lab. Everyone's story and journey through this academic field has served and continues to serve as a source of guidance and inspiration.

I want to thank my mother, Huiyun Shi, and my father, Yufei Sun. I am infinitely appreciative of their sacrifices to give me this opportunity. Words are simply not enough.

I want to thank my wonderful girlfriend, Lauren McAlpine, for all her support throughout the difficult times in this program. She was there to pick me up when I was down, steady the ship when I was rocked, and share my laughter at the brightest moments. Without her, this journey would have far less shine.

I'd like to thank all my friends I met at Caltech. I greatly appreciate meeting all of you and having all our adventures together. I only wish I could list everyone by name.

I'd like to thank the Crossleys and Raymers (and now the Sentners) for being a supportive network even while I've been away. I will continue to come back with new overly science topics to discuss and hope you will continue to want to listen.

In rapid succession, I'd like to thank Brad Plaster's research group at University of Kentucky for warmly hosting me in 2016; the pick-up group at Caltech volleyball for giving me a non-physics outlet every week; Ernie for keeping me well fed (a little too well); the wonderful people at Come On Out - Japan for giving me the most enriching experience of my lifetime (twice!); and the McAlpines and the Okomotos for welcoming me into their homes.

I've been blessed to cross paths with so many truly amazing people. Bittersweet, this too shall pass. I, for one, have savored every minute. And the next steps along the path of life can only hope to be so full and vibrant as those I have traced so far.

## ABSTRACT

Ultracold neutrons (UCNs) are neutrons that have been cooled such that their kinetic energy is on the order of their gravitational potential energy. Experimentally, ultracold neutrons are valuable because at these energies they are trappable and provide experimenters with long observation times. In fact, their observation times are on the order of the free neutron decay lifetime — allowing direct observation of neutron  $\beta$ -decay. Many contemporary experiments measuring high-precision processes involving neutrons use UCNs. Two such experiments are UCNA and nEDM@SNS, both of which form the basis of this work.

UCNA is an experiment that took place at Los Alamos National Laboratory. In this work, we analyze the 2010-2013 UCNA datasets on neutron  $\beta$ -decay using UCNs. These datasets were originally designed to measure the asymmetry parameter,  $A$ , in neutron  $\beta$ -decay. However, there was also sensitivity to another physical parameter in the neutron  $\beta$ -decay rate: the Fierz interference term,  $b$ . The Fierz interference term in neutron  $\beta$ -decay acts as a probe of beyond Standard Model (SM) physics interactions, specifically scalar and tensor couplings in the weak interaction. Due to the vector - axial-vector nature of the weak interaction in the SM, any non-zero measurements of  $b$  would be indicative of new, beyond SM couplings. In this work, we present the extraction of the Fierz interference term as measured by neutron  $\beta$ -decay for the 2010, 2011-2012, and 2012-2013 UCNA datasets. We present these measurements using two methods: a direct extraction by measuring shape distortions in the  $\beta$ -decay electron spectrum, and an energy dependence in the asymmetry,  $A_0$ . These two methods across the three datasets yield six new measurements of  $b$  from neutron  $\beta$ -decay data. Our final result is the weighted average of the three asymmetry-extracted  $b$  results.

The UCNA datasets were also sensitive to another type of beyond SM interaction: neutron decaying to dark matter with an accompanying positron-electron pair (first proposed in [FG18a]). This decay channel was originally proposed in order to resolve the discrepancy between two measurement methods of the neutron lifetime: bottle experiments which measure neutron population as a function of time, and beam experiments which measure the decay protons from conventional neutron  $\beta$ -decay. Due to the experimental setup of the UCNA apparatus, the UCNA dataset was sensitive to such a decay channel. Using the 2012-2013 UCNA dataset which had functioning timing data, we effectively rule out this decay channel as the sole

explanation for the neutron lifetime discrepancy for  $\approx 84\%$  of the available decay phase space. Furthermore, we set branching ratio limits on this decay channel as compared to the conventional weak interaction mediated decay.

The last project in this work is the construction of a large scale magnet for the nEDM@SNS experiment. The nEDM@SNS experiment is an experiment designed to measure the neutron electric dipole moment (nEDM) and will take place at the Spallation Neutron Source (SNS) in Oak Ridge National Laboratory (ORNL). This experiment will take place in 2027 and make a leading precision measurement on the nEDM. Part of the experiment is the magnetic system and, within that system, the  $B_0$  magnet which will provide a DC holding field to UCNs within the experiment's measurement volume. The assembly procedure for constructing the  $B_0$  magnet is detailed and intermediate quality checks as well as a post-construction room temperature magnetic field map are presented. The preliminary results indicate that the completed  $B_0$  magnet satisfies the specifications and will be useable in the nEDM@SNS experiment.

## PUBLISHED CONTENT AND CONTRIBUTIONS

- [Sun+20] X. Sun et al. “Improved limits on Fierz interference using asymmetry measurements from the Ultracold Neutron Asymmetry (UCNA) experiment”. In: *Phys. Rev. C* 101 (3 Mar. 2020), p. 035503. doi: [10.1103/PhysRevC.101.035503](https://doi.org/10.1103/PhysRevC.101.035503). URL: <https://link.aps.org/doi/10.1103/PhysRevC.101.035503>.  
X. Sun performed data analysis and systematic studies that entail the final extracted measurement of the Fierz interference parameter in the free neutron beta decay from UCNA 2011-2013 datasets, wrote the associated manuscript.
- [Sun+19] X. Sun et al. “Search for neutron dark decay:  $n \rightarrow \chi + e^+e^-$ ”. In: *EPJ Web Conf.* 219 (2019). Ed. by T. Jenke et al., p. 05008. doi: [10.1051/epjconf/201921905008](https://doi.org/10.1051/epjconf/201921905008).  
X. Sun wrote this more technical manuscript for the EPJ Web of Conferences, PPNS 2018 conference.
- [Sun+18] X. Sun et al. “Search for dark matter decay of the free neutron from the UCNA experiment:  $n \rightarrow \chi + e^+e^-$ ”. In: *Phys. Rev. C* 97 (5 May 2018), p. 052501. doi: [10.1103/PhysRevC.97.052501](https://doi.org/10.1103/PhysRevC.97.052501). URL: <https://link.aps.org/doi/10.1103/PhysRevC.97.052501>.  
X. Sun performed data analysis and studies on re-calibrated UCNA 2012-2013 data in order to analyze novel dark matter decay channel. Extracted limits from data and wrote manuscript.
- [Hic+17] K. P. Hickerson et al. “First direct constraints on Fierz interference in free neutron  $\beta$  decay”. In: *Phys. Rev. C* 96.4 (2017). [Addendum: *Phys. Rev. C* 96,no.5,059901(2017)], p. 042501. doi: [10.1103/PhysRevC.96.042501](https://doi.org/10.1103/PhysRevC.96.042501), [10.1103/PhysRevC.96.059901](https://doi.org/10.1103/PhysRevC.96.059901). arXiv: [1707.00776](https://arxiv.org/abs/1707.00776) [nucl-ex].  
X. Sun contributed to the systematic studies of the extraction of the Fierz interference parameter from the UCNA 2010 dataset. Programmed and used a GEANT4 simulation in conjunction with existing data calibration pipeline to study systematic effects. Wrote portion of manuscript.

## TABLE OF CONTENTS

Dedication . . . . .	iii
Acknowledgements . . . . .	iv
Abstract . . . . .	v
Published Content and Contributions . . . . .	vii
Table of Contents . . . . .	vii
List of Illustrations . . . . .	xiii
List of Tables . . . . .	xxvii
Chapter I: Introduction . . . . .	1
1.1 The Neutron . . . . .	1
1.2 Ultracold Neutrons . . . . .	2
1.2.1 Definition . . . . .	2
1.2.2 Properties . . . . .	3
1.2.3 Production . . . . .	5
1.3 Neutron Beta Decay . . . . .	6
1.3.1 The Weak Interaction in the Neutron . . . . .	7
1.3.2 Neutron Beta Decay and Correlation Coefficients . . . . .	9
1.3.2.1 The Asymmetry Term, $A$ . . . . .	10
1.3.2.2 The Fierz Interference Term, $b$ . . . . .	11
1.3.2.3 The Neutron Lifetime, $\tau$ . . . . .	12
1.4 Neutron Electric Dipole Moments . . . . .	13
1.4.1 nEDM Experiments: Past, Present, Projected . . . . .	14
1.4.2 Beyond Standard Model Searches . . . . .	16
1.4.2.1 CP Violation . . . . .	16
1.4.2.2 Baryon Asymmetry . . . . .	17
Chapter II: The UCNA experiment . . . . .	20
2.1 Overview of Experiment . . . . .	20
2.2 UCN Polarization and Transport: From Source to Experiment . . . . .	21
2.2.1 UCN Production at LANL . . . . .	22
2.2.2 Exiting the UCN Source Volume . . . . .	24
2.2.3 Gate Valve and Pre-Polarizing Magnet . . . . .	24
2.2.4 Switcher for UCN Measurements . . . . .	25
2.2.5 7 T Polarizing Magnet (AFP) . . . . .	25
2.2.6 Neutron Polarization . . . . .	26
2.3 The UCNA Spectrometer . . . . .	26
2.3.1 Decay Trap . . . . .	27
2.3.2 Multi-Wire Proportional Chamber (MWPC) . . . . .	28
2.3.3 Plastic Scintillator . . . . .	29
2.3.4 Magnetic Field . . . . .	29
2.3.5 Calibration Sources . . . . .	30

2.3.6	Xenon Mapping . . . . .	31
2.3.7	Supplemental Components . . . . .	32
2.4	Data-Taking Runs . . . . .	32
2.4.1	2010 Dataset . . . . .	32
2.4.2	2011-2012 Dataset . . . . .	32
2.4.3	2012-2013 Dataset . . . . .	33
2.4.4	Event Types . . . . .	33
2.4.5	Octet Structure . . . . .	34
Chapter III: UCNA Simulations . . . . .		36
3.1	GEANT4: A Particle Tracking Software Package . . . . .	37
3.2	ROOT: A Data Analysis Software Package . . . . .	37
3.3	The UCNA Apparatus in Simulation . . . . .	38
3.3.1	Detector Construction Class . . . . .	38
3.3.1.1	Decay Trap . . . . .	39
3.3.1.2	Wirechamber (MWPC) . . . . .	41
3.3.1.3	Plastic Scintillators . . . . .	41
3.3.1.4	Detector Package Frame . . . . .	42
3.3.1.5	E&M Fields . . . . .	42
3.3.2	Physics List Class . . . . .	43
3.3.3	Primary Generator Action Class . . . . .	43
3.3.3.1	Initial Kinematics Generation . . . . .	43
3.3.4	Particle Tracking Classes . . . . .	45
3.3.4.1	Run Action . . . . .	47
3.3.4.2	Event Action . . . . .	48
3.3.4.3	Tracker . . . . .	50
3.4	Post-Processing: Applying the Detector Response Model . . . . .	51
3.4.1	Position Map Corrections . . . . .	53
3.4.2	Finite PMT Resolution . . . . .	53
3.4.3	Energy Calibration Distortions . . . . .	54
3.4.4	Trigger Function . . . . .	54
3.4.5	Creating a Reconstructed Energy . . . . .	55
3.5	Motivation for Using Simulation . . . . .	55
3.5.1	Event Types Identification . . . . .	55
3.5.2	Energy and Timing Spectra Reconstruction . . . . .	56
Chapter IV: UCNA: Fierz Interference Analysis . . . . .		59
4.1	The Fierz Interference Term . . . . .	59
4.1.1	UCNA Sensitivity to Fierz . . . . .	60
4.2	The Spectral Extraction Method . . . . .	60
4.2.1	The Super-Sum Spectrum . . . . .	61
4.2.1.1	Motivation and Definition . . . . .	61
4.2.1.2	Fitting the Energy Spectra . . . . .	62
4.2.1.3	Blinding the Spectral Extraction . . . . .	64
4.2.2	Dominant Systematic Uncertainty: Energy Calibration . . . . .	67
4.2.2.1	Calibration Variation Selection Procedure . . . . .	70
4.2.2.2	2010 Dataset Study Results . . . . .	71

4.2.2.3	2011-2012 Dataset Study Results . . . . .	73
4.2.2.4	2012-2013 Dataset Study Results . . . . .	79
4.2.3	Other Systematic Effects . . . . .	81
4.2.3.1	Background Subtraction . . . . .	82
4.2.3.2	Energy Resolution . . . . .	83
4.2.3.3	Backscattering . . . . .	83
4.2.3.4	Detector Inefficiency . . . . .	83
4.2.4	Other Spectral Systematic Studies . . . . .	84
4.2.4.1	End Point Correction Studies . . . . .	84
4.2.4.2	LED Studies . . . . .	85
4.2.5	Summary of Spectral Extraction Method . . . . .	85
4.3	The Asymmetry Extraction Method . . . . .	86
4.3.1	The Asymmetry Definition . . . . .	87
4.3.1.1	Constructing an Asymmetry . . . . .	87
4.3.1.2	Asymmetry with Fierz Interference . . . . .	88
4.3.1.3	Blinding the Asymmetry Extraction . . . . .	89
4.3.2	The Fierz Interference from Asymmetry Extraction . . . . .	89
4.3.2.1	Statistical Uncertainty . . . . .	89
4.3.3	Systematic Studies . . . . .	90
4.3.3.1	Energy Response Systematic Uncertainty . . . . .	90
4.3.3.2	Electron Backscattering . . . . .	92
4.3.3.3	$\cos\theta$ . . . . .	93
4.3.3.4	Background Subtraction . . . . .	94
4.3.3.5	Detector Trigger Efficiency . . . . .	96
4.3.3.6	Energy Resolution . . . . .	96
4.3.3.7	Inner Bremsstrahlung . . . . .	97
4.3.4	Summary of Asymmetry Extraction Method . . . . .	98
4.4	Combining the Extraction Methods . . . . .	99
4.4.1	Energy Fit Window Study . . . . .	100
4.4.2	Position Fit Window Study . . . . .	103
4.4.3	Discussion on Unblinding Criteria . . . . .	104
4.4.4	Weighted Averages . . . . .	106
4.5	Results and Discussion . . . . .	107
Chapter V: UCNA: Dark Matter Decay Analysis	. . . . .	109
5.1	The Neutron Lifetime Anomaly . . . . .	109
5.1.1	The Neutron Lifetime . . . . .	109
5.1.2	Experimental Methods: Bottle Experiments . . . . .	110
5.1.3	Experimental Methods: Beam Experiments . . . . .	112
5.1.4	The Anomaly . . . . .	114
5.2	A Dark Matter Decay Channel . . . . .	116
5.3	UCNA Analysis of Dark Matter Decay . . . . .	118
5.3.1	Overview of UCNA Sensitivity to Decay . . . . .	118
5.3.2	Event Classification . . . . .	120
5.3.3	Coincidence Time Calibration . . . . .	121
5.3.3.1	The TDC Data . . . . .	121

5.3.3.2	Simulations of the Timing Spectrum . . . . .	125
5.3.3.3	Discussion on Background Subtraction . . . . .	127
5.3.4	Detection Efficiency Estimates . . . . .	128
5.3.4.1	Kinematic Acceptance . . . . .	128
5.3.4.2	Timing Window Acceptance . . . . .	129
5.3.4.3	Trigger Function Efficiency . . . . .	134
5.3.4.4	Electron-Positron Detector Response . . . . .	136
5.3.4.5	Final Total Acceptance . . . . .	137
5.4	UCNA Extracted Limits . . . . .	137
5.4.1	Bin Aliasing Study . . . . .	138
5.4.2	Look-Elsewhere Effect Correction . . . . .	138
5.4.3	Final Exclusion Limits . . . . .	139
5.4.4	Discussion . . . . .	139
Chapter VI: nEDM@SNS: $B_0$ Magnet	. . . . .	142
6.1	The Neutron Electric Dipole Moment . . . . .	142
6.1.1	Overview of nEDM@SNS Experiment . . . . .	142
6.1.1.1	Introduction . . . . .	142
6.1.1.2	Experimental Highlights . . . . .	143
6.1.1.3	Two Complementary Measurements . . . . .	145
6.2	The $B_0$ Magnet . . . . .	147
6.2.1	Constructing the $B_0$ Magnet . . . . .	148
6.2.1.1	UVT: A Vacuum Lamination Table . . . . .	150
6.2.1.2	Inner Core Hoops . . . . .	151
6.2.1.3	Lead End Caps (LECs) . . . . .	153
6.2.1.4	Superior Lead End Caps (SLECs) . . . . .	154
6.2.1.5	Boss Rings . . . . .	157
6.2.1.6	Story Sticks . . . . .	157
6.2.1.7	Stiffening Gussets . . . . .	159
6.2.1.8	Wire Tensioners . . . . .	159
6.2.1.9	Final Assembly of $B_0$ Magnet . . . . .	162
6.2.2	Covid-19 Considerations . . . . .	162
6.2.3	Testing the Assembly Components . . . . .	166
6.2.3.1	The ROMER Arm . . . . .	166
6.2.3.2	Calibrating the ROMER Arm . . . . .	167
6.2.3.3	UVT Surface Measurements . . . . .	167
6.2.3.4	Gauge Plates Inner Circumference Measurements .	169
6.2.3.5	Wire Slot Position Measurements . . . . .	170
6.2.3.6	Liquid Nitrogen Cold Tests . . . . .	172
6.2.4	Testing the $B_0$ Magnet Performance . . . . .	175
6.2.4.1	Room Temperature Field Measurements . . . . .	175
6.2.4.2	Results and Comparison to Free Space Model . .	177
6.3	nEDM@SNS Experiment Outlook . . . . .	179
6.3.1	The Polarization Transmission Measurement . . . .	181
6.3.2	The nEDM Measurement . . . . .	181
Chapter VII: Conclusion	. . . . .	182

7.1	Where Are We Now? . . . . .	182
7.1.1	Fierz Interference Measurements . . . . .	182
7.1.2	Dark Matter Decay Limits . . . . .	184
7.1.3	$B_0$ Benchmark Measurements . . . . .	185
7.2	What's Next? . . . . .	186
7.2.1	UCNA+ . . . . .	186
7.2.2	nEDM@SNS . . . . .	188
	Bibliography . . . . .	190

## LIST OF ILLUSTRATIONS

<i>Number</i>	<i>Page</i>
1.1 Different temperature regimes (expressed in $eV$ ) for neutrons. A thermal distribution is included for an ensemble of neutrons produced at room temperature and 30K. Figure taken from [Liu09]. . . . .	3
1.2 A Feynmann diagram of the neutron beta decay, mediated by the weak interaction, showing a conversion of a $d$ quark to a $u$ quark and associated output particles that form the decay interaction in equation 1.4. . . . .	7
1.3 Measurements of the neutron electric dipole moment throughout history. Notably, the most stringent completed experiment is at $d_n \approx 10^{-26} e \cdot cm$ , whereas the projected sensitivity of nEDM@SNS is $d_n \approx 10^{-28} e \cdot cm$ (indicated by the red star). In addition, the point in time when the most sensitive experiments switched over from beam methods to UCN methods is indicated. Finally, as a historical note, the discovery of CP violation in the Standard Model (via $K_0$ decays) is indicated as well. That is, CP violation that is intrinsic in the SM due to a complex phase in the CKM matrix. Figure, with minor modifications, taken from [Pen12]. . . . .	15
2.1 A simplistic diagram of the spectrometer components of the UCNA apparatus. The cylinder in the center is the decay trap and the polarized neutrons (represented as spheres) are nominally contained within the cylinder (here they are shown outside to simplify the visuals). The imposed magnetic field is along the axis of the decay trap, and the detectors are a pair of wirechambers and plastic scintillators (with other infrastructure that is not shown). . . . .	21
2.2 A schematic diagram of the UCN source. An incoming pulsed proton beam produces spallation neutrons which are moderated to cold temperatures through various moderators. Ultra-cold neutrons (UCNs) are produced after final interactions with Solid Deuterium ( $SD_2$ ). These UCNs travel 1 $m$ upwards to further cool and are then sent downstream to UCN experiments. See text for additional details. . . . .	22

2.3 An overhead schematic diagram of Area B showing the UCN source, UCN infrastructure, and the UCNA experiment. In this schematic, the UCNs start in the bottom right at the “UCN $SD_2$ Source” and travel to the upper left into the “1 T Spectrometer”. Key elements along the path of the UCNs are labelled and each are described further in dedicated subsections in the text. . . . .	23
2.4 A top view cross-sectional schematic view of the UCNA experiment apparatus. In this schematic as shown, UCNs travel from the bottom of the diagram into the central $\beta$ decay volume. Their decay products, specifically the electrons, are shaped outwards towards the East Detector and West Detector. . . . .	27
2.5 Simple schematic of an electron’s trajectory in an expanding magnetic field [Men14], describing the path of the UCN $\beta$ -decay electrons in UCNA as they traverse from a 1 $T$ field region to the 0.6 $T$ field region at the detectors. . . . .	30
2.6 Simple schematic of the scintillator calibration [Bro18]. A paddle which holds the calibration sources is inserted into the decay trap while under vacuum. The paddle is translated in the shown horizontal direction across the region of the scintillators. At fixed locations, the paddle is held still and a calibration run is taken. . . . .	31
2.7 A schematic diagram of various $\beta$ -decay electron events in the UCNA apparatus [Pla+12]. Several combinations of events are used in the subsequent analyses. Internally, the “no backscattering” events were often termed “Type 0”. . . . .	34
3.1 An off-axis screen shot of the generated GEANT4 simulation of the UCNA apparatus. Visualization is implemented via QT visualization drivers. The standard detector construction geometry is shown with one electron simulated. There is an imposed magnetic field across the entire detector and electric fields within the wirechambers (section 3.3.1.5). See text for details on each simulation element. A Cartesian coordinate axis is included at the simulation volume origin. . . . .	39

3.2 (a) Comparison between new kinematics generation of UCNA $\beta$ -decay events (red) and the original $\beta$ -decay event kinematics used in the 2010 asymmetry analysis (blue). (b) The fractional residuals of the comparison of Monte Carlo generated kinematics spectra in (a). The error bars are statistical and propagated them forward with standard error propagation [HH10]. A constant line is fitted to the residuals (black) from 200 keV to 650 keV, consistent with the energy range used in the final Fierz extraction. . . . .	46
3.3 Simulated initial momentum direction distribution of $\beta$ -decay electron events along the z-axis shown in raw counts (a total of $10^8$ events were sampled). This causes a modification to the initial decay kinematics generated in figure 3.2, with a PDG value of $A_0 = -0.1184$ (as of 2015). . . . .	47
3.4 Two different initial $\beta$ -decay electron energy spectra. The one corresponding to $b = 0$ represents the Standard Model kinematics and is shown as a standalone in figure 3.2. The remaining maximal $b$ is shown after running our initial kinematics generation and introducing a $b$ coefficient of the form in equation 3.2. Normalization is implicitly done by setting a fixed number of events generated (here we used $10^8$ total events). . . . .	48
3.5 Example $E_{recon}$ spectra from combined PMT response for simulation (red) and data (blue) for all conversion electron source data ( $^{137}Ce$ , $^{113}Sn$ , $^{207}Bi$ ) after application of the calibration. This is for a random run that included all three sources within the fiducial volume at the same time. Figure from [Bro18] and the individual PMT comparisons between simulation and data prior to being combined into $E_{recon}$ are also given there. . . . .	52
3.6 An energy spectrum of the energy deposited in the MWPC for Type 2 (red) and Type 3 (blue) events and all Type2 + Type 3 events (green). We note that in the electronics these events are indistinguishable since they both produce a trigger on the same side detector. However, in the GEANT4 simulation we are able to access “true” event typing. The low energies plotted are related to the energies deposited in the MWPC. In the data analysis pipeline, the thresholds identified from these plots can be used to set a cut on MWPC energy deposition and improve Type 2/3 identification fidelity. . . . .	57

4.1	The error envelope chosen for the UCNA 2010 asymmetry analysis [Men14]. A histogram of calibration source data is generated for each energy speak and shown with a rotation. The mean and RMS of the reconstructed energy error histograms is used to set the data points. The error envelope is a piece-wise linear interpolation of the calibration source data, chosen in the original asymmetry analysis to conservatively over-constrain the energy uncertainty since it was a subdominant uncertainty. The reconstructed energy error is reconstructed data minus GEANT4 Monte Carlo simulations. . . . .	68
4.2	A diagram illustrating the different steps in the simulation processor to turn initial $\beta$ -decay electron kinematics into processed, “detector-like” events. We note that step 1, generating a $b = 0$ Standard Model spectrum is not shown but it is the input into $E_{prim}$ in the diagram. In addition, step 5 is not shown but it is the fitting that occurs on the final $E'_{recon}$ spectrum generated at the conclusion of the event processing. . . . .	69
4.3	A sample distribution of energy calibration variation polynomials for visual interpretation. Polynomials are chosen via brute-force grid search with an accept-reject procedure (see text). Polynomials up to $2\sigma$ in our error envelope are kept. We show the 2010 error envelope here. These polynomial distributions are used to generate new pseudo energy calibrations. . . . .	71
4.4	A distribution of different neutron $\beta$ -decay electron kinetic energy spectra, after passing through the detector response model. In particular, all the varied spectra assume the same shape at low energies due to the presence of the trigger function. The shown spectra use energy variation polynomials that are significantly larger than those shown in figure 4.3 — this is chosen for visual illustration purposes. The range of polynomials shown here is $\pm 5 \text{ keV}$ for the offset term, $\pm 2\%$ for the linear term, and $\pm 0.01\%$ for the quadratic term. A $b \rightarrow \infty$ spectrum is given for comparison (black). . . . .	72
4.5	The shape factor of the neutron $\beta$ -decay spectrum as a function of reconstructed energy. Error bars are propagated using standard error propagation. The shape factor is defined as $\frac{r_{data} - r_{MC}}{r_{MC}}$ and is fitted with a line to extract a $b$ value. This represents one methodology for $b$ extraction from energy spectra and was used in the final results in [Hic+17]. . . . .	73

4.6 Energy error envelopes that have been symmetrized for 2011-2012, 2012-2013 calibration source data. These are the final error envelopes used in the asymmetry analysis [Bro+18]. The calibration residual is defined as $\frac{E_{MC} - E_{Data}}{E_{Data}}$ . . . . .	75
4.7 The error envelope generated from the 2011-2012 calibration source data, applying the new methodology for constructing error envelopes (see text). $1\sigma$ and $2\sigma$ bands are shown. The error envelope is not symmetrized; this leads to an asymmetric systematic uncertainty but significantly reduces the overall spread of accepted energy calibration variations. . . . .	76
4.8 Energy calibration variations, similar to figure 4.3, shown for the 2011-2012 asymmetry error envelope. Polynomials up to $3\sigma$ are shown. Distributions of the energy variations are shown at five “slices” — each of the four calibration source energy peaks and the $\beta$ -decay energy spectrum end point (included as an additional reference but not used in final decision making). The distribution fitted with a Gaussian approximately matches the error envelope $\sigma$ at the calibration source energy peaks. This ensures that our variation distribution is an accurate statistical representation of the error envelope. . . . .	77
4.9 The $\chi^2$ distribution of each energy calibration variation (blue) (a) before and (b) after re-sampling against a theoretical $\chi^2$ distribution (red). The resulting energy calibration variations can now be approximated as “statistical” and are used in the systematic studies (see text). . . . .	78
4.10 The error envelope generated from the 2012-2013 calibration source data, same as figure 4.7. . . . .	79

4.11 Calibration source energy reconstructions, shown as a function of calibration period. There are two distinct calibration sets corresponding to the 2011-2012 and 2012-2013 data-taking run. The gap in the middle is due to a portion of the 2012-2013 calibration being faulty. The horizontal bars are the errors (and central value) from the error envelope for each data-taking year. Some data points have 0 error bar which simply means that data point had no calibration data. We highlight that the calibration source energy peaks approximately agree at the $^{137}Ce$ peak and both $^{207}Bi$ peaks. There is a non-trivial disagreement between the $^{113}Sn$ peaks year-to-year. This is explored as a systematic study (see text). . . . .	80
4.12 Distribution of extracted values of $b_n$ from applying energy calibration variations to $b = 0$ simulated asymmetry data. We highlight the bias and spread as estimators of the error associated with the energy calibration variations on the asymmetry extraction of Fierz interference. The peak at $b = 0$ for the 2010 dataset is likely due to the symmetric error envelope used allowing a larger phase space of energy calibration variations that produce a $b = 0$ . . . . .	91
4.13 Summary of the percentage corrections applied to the final asymmetry as a function of energy for the electron backscattering systematic effect for both years (see [Bro18] for further details). We used the uncertainties at the end point energies of the fit window to estimate the effect on $b$ (see text). . . . .	94
4.14 Same as figure 4.13 except correcting for the $\cos\theta$ systematic effect. .	95
4.15 Distribution of the quenched energy deposited into the West detectors (minimum energy deposited $> 0 \text{ keV}$ ) when generating $10^5$ photons with $400 \text{ keV}$ initial kinetic energy, pointed directly at the West detector. This gives an effective trigger probability for photons due to inner Bremsstrahlung at the midpoint of our neutron $\beta$ -decay energy range. . . . .	98

4.16	A 2D histogram showing the resulting weighted error using a four-point weighted average, in the color bar, of $b$ where the statistical error is the error used for the super-ratio extraction and the systematic error is the used for the super-sum extraction. The high energy cut off was originally fixed at $\approx 740 \text{ keV}$ . In terms of minimizing the weighted average error on $b$ , there is a large acceptable region for the low-energy cut off. The error is varied due to changing the low-energy cut offs for the 2011-2012 dataset against the 2012-2013 dataset. . . . .	102
4.17	Different low energy fit window's $p$ values. A high energy cut off at $645 \text{ keV}$ is fixed. A dashed line is included at $10^{-2}$ to represent the 1% probability that this fit was a statistical anomaly. We use $10^{-2}$ as an approximate cut off before deciding a fit was dominated by uncertainties that were non-statistical (hence systematic). In general, we see the same behavior as discussed in section 4.2.2.4 with regards to the tin stitching: the 2012-2013 uncertainties are systematically shifted compared to the 2011-2012 uncertainties. . . . .	103
4.18	$b$ extractions for different octets from GEANT4 simulations (red) and real data (blue). The simulation is created using initial kinematics generated from Monte Carlo, run through the GEANT4 simulation, and processed with our detector response model (unique to each octet) in order to generate "data-like" datasets from which the $b$ value can be extracted. The data is created by using the same detector response model as the simulation uses. . . . .	105
5.1	Simple schematic illustrating the concept of neutron lifetime bottle experiments [Fri22]. At minimum, two different holding times are used to measure remaining neutron populations and the differences in number and time can be used to deduce a neutron lifetime. . . . .	111
5.2	A schematic diagram of a typical neutron beam lifetime experiment. The slow neutron beam can be characterized before the decay volume as well as being counted after the decay volume. Figure taken from [Wie14]. . . . .	113

- 5.3 Historical trend of neutron lifetime experimental measurements. Orange points are beam experiments and blue points are bottle experiments. The shaded regions are weighted averages  $\pm 1$  standard deviation of uncertainty for beam vs bottle methods. Figure is taken and modified from [Cas21]. Details of each experiment are in [Wie18] and [Gon+21]. . . . . 115
- 5.4 A diagram showing the travel paths of a proposed dark matter decay producing a  $e^+e^-$  pair, compared to a Type 1 backscatter event [Swa18]. Both would register the same electronic signature, but there exists a lower limit on the Type 1 backscatter travel time, which is set by the maximum velocity and the crossing distance between detectors ( $4.4\text{ m}$ ). The  $e^+e^-$  pair has no such limitations. This timing signature is critical in the event separation that allows our analysis to proceed (see text). . . . . 120
- 5.5 Timing spectra taken from East (red) and West (blue) TDCs in raw channel count, operated in a “common stop” mode, for Type 1 backscatter events. Self-timing peaks are seen centered around channel 3150 (red) and 3250 (blue). Significantly more electronic jitter is seen in the West TDC. A flat 150 channel offset has been applied in order to align the Type 1 backscatter peak at channel 2600. A conversion of  $44\text{ ps}/ch$  was applied. Figure first published in [Sun+19]. . . . . 123
- 5.6 A simple diagram of wire connections between the TDCs and the UCNA detector [Fil18]. This was used as a guide to estimate the time delays due to potentially mismatched cable lengths (see text). . . 124
- 5.7 Shows the background-subtracted, relative time differences between events that first trigger the East detector (blue) and events that first trigger the West detector (black). An overlaid GEANT4 simulation (red) with a  $2\text{ ns}$  timing resolution shows the expected timing spectrum for conventional  $\beta$ -decay Type 1 backscatter events. Dotted lines illustrate the chosen time window used in this analysis to identify candidate dark matter decays. Bin width of 50 ps. The channels are converted to time using the setting from the electronics. This figure was first published in [Sun+18; Sun+19]. . . . . 126

- 5.8 A simulated timing spectrum of a Type 1 decay event (red) vs a  $e^+e^-$  dark matter decay event (black), assuming a 1% branching ratio for the dark matter decay. The timing spectrum is generated by sampling a simple three-body phase space for the  $\chi, e^+, e^-$  and assuming the maximum available summed kinetic energy, 644 keV, for the  $e^+e^-$  pair. The dotted line represents the chosen timing window for this analysis. Bin width of 50 ps. Figure first published in [Sun+19]. . . . . 127

5.9 Simulated timing spectra for Type 1 backscatter events taken from GEANT4 simulation with different timing resolutions applied in post-processing (0 ns in purple, 2 ns in green). Background-subtracted data for East (red) and West (blue) TDCs also shown. From inspection, 2 ns makes the Type 1 backscatter timing peak match. Studies were performed with 1 ns time steps but not shown in order to simplify the overall presentation. . . . . 128

5.10 A simple diagram of the kinematic efficiency. The  $\chi$  particle is the dark matter particle and lost in the UCNA detector. The positron-electron pair must travel in opposite directions (a) to be detected or else their signal is washed out by the conventional Type 0 decays (b). In this diagram, the East and West detectors would be on the left and right respectively. . . . . 129

5.11 Monte Carlo simulation of arrival times in the detectors for a three-body decay where  $m_\chi$  is a minimum and hence there is maximum available kinetic energy to the  $e^+e^-$  of 644 keV. Timing spectra are overlaid for events generated in the center of the UCNA decay trap (green) and uniformly populated throughout the decay trap (black). The large bin at 100 ns represents an “over-fill” bin — a bin where all the events beyond are contained as well. In reality, there would be an arbitrarily long tail to the spectrum that extends  $> 100$  ns. . . . . 130

5.12 Energy spectrum of (a) background and (b) foreground runs, for three separate time-windows. We note that there is factor  $\approx 5$  difference between live times for the foreground and background runs, hence the differences in total count numbers. Clear structure of a neutron  $\beta$ -decay backscattering peak at 300 keV is visible for time-windows  $> 12$  ns in the foreground runs. Dashed lines at 0 keV, 800 keV indicate the energy region of interest used for the present analysis. Figure first published in [Sun+18]. . . . . 132

- 5.13 Number of background-subtracted events accepted within our chosen timing window as a function of the high time cut off. Three different low time cut offs are used:  $-2\text{ ns}$  (black),  $0\text{ ns}$  (red),  $2\text{ ns}$  (green). We note that the  $-2\text{ ns}$  is unphysical unless there was systematic electronic jitter in the TDCs. Vertical error bars are set by  $\sqrt{N}$  of the total number of counts and horizontal error bars are set to  $1\text{ ns}$  arbitrarily. The final chosen timing window for the West TDC was  $[2\text{ ns}, 12\text{ ns}]$  in order to cut out the additional dead-time from wire length differences (see text). For the East TDC, we used  $[0, 12\text{ ns}]$ . Efficiencies were adjusted for these East/West time window discrepancies. . . . . 133
- 5.14 Background-subtracted  $e^+e^-$  pair kinetic energy spectra for events in the chosen analysis time-window. For comparison, simulated positive dark matter decay signals at summed  $e^+e^-$  kinetic energies of  $322\text{ keV}$ ,  $644\text{ keV}$  are overlaid, assuming 1% branching ratio. Bin widths of  $25\text{ keV}$ . Figure first published in [Sun+18; Sun+19]. . . . . 134
- 5.15 A diagram of the impact of the detector response model on simulated Monte Carlo spectra. The initial spectra is also presented for comparison. These simulated events have been processed with the 2012-2013 UCNA dataset calibration. The low energy effects ( $< 200\text{ keV}$ ) are primarily due to the trigger function. . . . . 135
- 5.16 A comparison of the energy deposition spectra for electrons vs positrons in the UCNA GEANT4 simulation. Simulated by pointing  $10^5$  positron events with initial kinetic energy  $322\text{ keV}$  from the center of the decay trap towards the East detector. The number of positrons detected in the  $322\text{ keV}$  bin is 85% that of the electrons. All other events events are assumed to be “lost” from the efficiency calculation perspective. These positrons are converted into annihilation  $\gamma$ s that deposit energy in our detector over a range from  $0 - 1\text{ MeV}$  which is broad when compared to the peak width. . . . . 137
- 5.17 Total  $e^+e^-$  pair acceptance as a function of summed kinetic energy. We multiply three different efficiencies in this final acceptance: the kinematic efficiency, the timing window efficiency, and the trigger efficiency. Furthermore, we correct for the positron-electron differences in detector response via GEANT4 simulation calculated efficiencies. Figure first published in [Sun+18; Sun+19]. . . . . 138

5.18 Confidence limits on the branching ratio of the neutron dark decay channel, as a function of the kinetic energy of the produced $e^+e^-$ pair. This is directly related to the proposed $\chi$ mass by $m_\chi = m_n - 2m_e - E_{e^+e^-}$ , which has a range of $937.900 \text{ MeV} < m_\chi < 938.543 \text{ MeV}$ in [FG18a]. A branching ratio of $10^{-2}$ , which would be required to explain the neutron lifetime anomaly if $n \rightarrow \chi + e^+e^-$ were the only allowed dark matter final state, is shown by the dashed line. Data taken from figure 5.14 is used to generate final confidence limits. We checked for bin aliasing and look-elsewhere effect (see text). Figure first published in [Sun+18; Sun+19]. . . . .	140
6.1 Engineer's diagram showing the $B_0$ magnet structure, constructed from G10 material [Ale21]. The wire windings are also shown. Several components in the structure are highlighted: the wire tensioners (purple), boss rings (yellow), inner hoops (red), story sticks (blue), and stiffening gussets (green). All components are described in the text. . . . .	149
6.2 Photograph of author with the UVT in the synchrotron lab area at Caltech. Photo taken after UVT was delivered and surfaces were cleaned. Both sets of gauge plates were cleaned and laid out on the table for initial quality checks. . . . .	151
6.3 Photograph of completed dry fit assembly of an inner hoop. In this picture, the dry fit was completed and then disassembled to prepare for the gluing operation. The top layer segments are laid in position and then flipped over so that the glue side is upright. At this point in time, Saran wrap had not been prepared on the UVT — we added that into the procedure soon afterwards. . . . .	152
6.4 Photograph of completed inner hoop gluing and curing. Vacuum was removed and plastic sheet removed. In this picture, we can see the wooden feather blocks, Saran wrap around the hoop, and tell-tale discolorations that indicate where glue has been spread on the outer surfaces of the hoop. . . . .	154

- 6.5 A schematic of the different elements within the magnet package. The center axis of the cryostat is given on the left-hand side and the different elements are placed according to their radial position in the experiment apparatus. The work in this section describes the Pb End Cap and the  $B_0$  Coil. In section 6.2.4.1 we briefly discuss the Metglas Flux Return and Pb Side Shield. . . . . 155
- 6.6 Photographs showing (a) completed LEC glued to a sheet of lead and (b) the same LEC zoomed in on several features cut out. The lead will give additional magnetic shielding once the magnet is in a cryogenic environment (the lead goes superconducting). The cutting is done with piano wire and filing tools. . . . . 156
- 6.7 Photograph of first gluing operation. (a) Gluers applied glue directly to the surface of the SLEC and spread by hand. Some components were moved off the UVT on to separate work stations to have more working space. At this stage, there was little order to the operation and the total working time was 2-3 hours. (b) After gluing and assembly was completed, vacuum was applied and the whole assembly cured on the UVT. The SLEC had significantly looser tolerances so a set of small G10 gauge plates were used instead of the typical robust Aluminum gauge plates. Towels were laid over the sharper edges in order to protect the plastic sheet. A seam in the plastic was bunched up and channeled down to the green-taped lead brick — this technique yields a better vacuum and less overall leakage. . . . . 158
- 6.8 Photograph of first completed boss ring, removed from rest in the gauge plates, prior to position measurements with the ROMER arm. We highlight the challenge with this gluing operation by noting the large number of feature cut outs compared to previous magnet components (figures 6.6a and 6.4). . . . . 159
- 6.9 Photograph of inventory of gussets and story sticks after procurement, stored in the synchrotron lab at Caltech. . . . . 160
- 6.10 Photograph of a test set-up for the wire tensioners. Two tensioners are attached to a test segment of the boss ring (foreground) with a similar set-up in the background at the end of the two poles. Copper wire of 24-gauge is wound to mimic the final magnet winding. In the completed magnet, 72 of these wire tensioners are on each boss ring. 161

- 6.11 Photograph of completed  $B_0$  magnet structure with partial winding. The winding pattern is such that we wound half the coil at a time. In this picture, we can identify the elements of figure 6.1. Wire tensioners are “loaded” using toothpicks, pictured in each wire tensioner. In the final magnet deployment, toothpicks will be removed to give spring tension to the wire winding. . . . . 163
- 6.12 Simplistic floor plan diagram of gluing operation. The layout and worker placement was designed in order to comply with Covid-19 safety protocols (see text). Upon receiving approval, we were able to continue gluing  $B_0$  magnet components throughout the lockdown. . . . 164
- 6.13 Photograph of the ROMER arm mounted to the UVT. Power and connection wires extend from the ROMER to the Dell workstation used to operate the ROMER arm. . . . . 168
- 6.14 Measurements of the height of the ROMER arm against two orthogonal axes X (a) and Y (b). The coordinate axes are defined relative to the position of the ROMER arm base which is mounted to the UVT. The height includes a fixed offset for the height of the base. . . . . 169
- 6.15 Distribution of ROMER arm captured points along the interior radius of the Aluminum gauge plates, taken when mounted on the UVT. An offset in X-Y has been applied to center the data taken from the ROMER arm by using the calibration holes on the UVT (see text). Falls within our positional tolerances of  $\pm 0.010$  inches. . . . . 170
- 6.16 Photograph of author on the UVT ready to take wire slot measurements with the ROMER arm. On the right is a zoom in photograph of the custom-made wire slot measurement tool, designed to reliably position the ROMER arm to capture the wire slot. . . . . 171
- 6.17 An example of the typically distribution of wire slot position measurements for a completed hoop. Dashed red lines are at  $\pm 0.030^\circ$  indicate our tolerances of  $\pm 0.5$  cm at cryogenic temperatures. This distribution is typical of our better hoops. For the first hoop glued, we were around  $\pm 0.030^\circ$  and we steadily improved the RMS with each subsequent gluing. Cold cycling with liquid nitrogen also improved the RMS of the wire slot distributions. . . . . 172

- 6.18 Photograph comparison of boss rings before and after cold cycling. In each of these pictures, the top segment is the bottom boss ring and the bottom segment is the top boss ring. They have been flipped from their standard order so we could test the narrow edges of the wire slots together. In the upper figure, the bottom boss ring had not been cold cycled. In the lower figure, the bottom boss ring had been cold cycled once. There is clear visual evidence of relaxation and improved wire slot positioning after cold cycling. This is corroborated with gauge pin measurements, described in more detail in the text. . . . . 174
- 6.19 Photograph of completed mapper arm set-up, installed in the central volume of the  $B_0$  magnet. The original mapper arm structure (table, vertical shape, mapper arm) is lengthened by placing a 6 ft. tall 80-20 structure underneath. The entire structure is bolted to the floor to ensure stability and alignment of the mapper arm to the  $B_0$  magnet is done via laser level. This view is along the X direction of the  $B_0$  magnet and one of the cardinal directions in the magnet coordinate axes. . . . . 176
- 6.20 Diagram of LabVIEW program used to automate mapping procedure. Individual modules correspond to instruments used by the Caltech research group. Adapted from DAQ program used by graduate student Umit Coskun working on the cryo-probe array. . . . . 178
- 6.21 Magnetic field mapping data. The mapper arm was translated to several different heights relative to the center of the magnet. The values are background subtracted. Discontinuities or jumps in the field values likely correspond to disturbances in the field (for example, a car driving by outside the lab). The magnetic field  $B_0$  direction is along the X axis in the chosen coordinate system. The  $B_0$  values when translated along the z axis (b) have a 1.5 cm offset applied due to the position of the axes probes in the probe arm. . . . . 179
- 6.22 Same data as figure 6.21 except overlaid with prediction from Comsol model of the  $B_0$  magnet. A flat 2.5 mG offset is applied which aligns the field strengths at the center of the magnet. The same offset in the z translation as described in figure 6.21 is applied. . . . . 180

## LIST OF TABLES

<i>Number</i>	<i>Page</i>
1.1 Fermi potentials of common materials used in UCNA and nEDM@SNS experiments. Values taken from [GRL91] and [Chu+19] and references therein. . . . .	4
1.2 Classification of bilinear covariants. . . . .	9
1.3 Summary of next generation nEDM experiments located at major UCN source laboratories. Most experiments are expected to reach these sensitivities by 2030. Projected sensitivities taken from [Fil21]. . . . .	16
2.1 Results for average polarization fractions for the datasets presented in this dissertation work. For the 2010 result, see [Men14]. For the 2011-2012, 2012-2013 results, see [Dee19; Bro18]. In the later years, we present polarization for spin-flipper off (-) and spin-flipper on (+) states. . . . .	26
2.2 Final event type fractions for detectable event types in the UCNA detector. Taken from the final 2011-2012, 2012-2013 datasets used in the asymmetry analysis. There are similar fractions for event types in the 2010 dataset. Event types that are not categorized as Type 0, 1, 2, 3 are not detected. . . . .	34
2.3 Run structure for the octet data-taking sequence, consisting of A and B type quartets. Table taken from [Pla+12]. $\pm$ refers to spin state: + is spin flipper on and – is spin flipper off. $\beta$ is regular $\beta$ -decay runs, $B$ is background runs, and $D$ is depolarization runs. . . . .	35
3.1 List of user-defined materials used in the UCNA apparatus simulation in GEANT4. Molar densities and volume densities are not provided for every material because they are not necessarily needed to define the material in GEANT4. Aluminum and Copper are defined twice because the top section is elements and the remaining three sections are materials — GEANT4 treats them differently. The gases use the nominal fill pressures and the plastic scintillator is given by the Eljen EJ-204 datasheet (see section 2.3.3 for more details). . . . .	40

4.1	Summary of $1\sigma$ systematic uncertainties on the 2010 UCNA dataset extraction of Fierz interference [Hic+17]. These uncertainties are generally extracted from simplistic Monte Carlo studies except for the “Energy Response”, which is studied using the full GEANT4 simulation. . . . .	82
4.2	Summary of systematic uncertainties on $b_n$ greater than $10^{-4}$ . The energy calibration variation uncertainty is computed for different error envelopes; however, the values are ultimately the same for all three datasets. Similarly, other effects were computed separately for each dataset but we conservatively took the larger uncertainty (see text) when there was not an appreciable difference. Table first published in [Sun+20]. . . . .	99
4.3	Summary of $1\sigma$ fit results for 5 independent measurements of $b_n$ . The number of events is given after all cuts are applied. The spectral extractions use the energy calibration uncertainty combined in quadrature with other systematic uncertainties estimated with the techniques in [Hic+17]. Only the asymmetry results (bold values) are used in the weighted average. Table first published in [Sun+20]. We note the large $\frac{\chi^2}{\text{ndf}}$ from the spectral extraction methods indicates the dominance of systematic uncertainty in the spectral analysis compared to the asymmetry-extracted analysis. . . . .	108
5.1	Value of trigger function for Type 0 events on 2012-2013 reconstructed energy spectrum for different energy bins spanning the low energy range ( $< 100 \text{ keV}$ ) of UCNA apparatus. The quoted energy value is the midpoint of the bin (for example, the $35 \pm 5 \text{ keV}$ bin has trigger probability 0.05%). . . . .	135

## Chapter 1

### INTRODUCTION

In this dissertation, we focus on three key measurements of physical parameters of the neutron, specifically using Ultracold Neutrons (UCNs). These measurements compose Chapters 4, 5, and 6. In order to place these results in context, specifically the work in Chapters 4 and 5, we start by presenting an overview of the UCNA experiment in Chapter 2. In Chapter 3, we discuss the implementation of the same UCNA apparatus in a GEANT4 simulation for systematic studies in the later analysis in this dissertation.

In Chapter 4, we discuss the extraction of the Fierz interference term from the UCNA datasets. In Chapter 5, we present the analysis and associated limits on a hypothesized neutron to dark matter decay channel with an accompanying electron-positron pair. In Chapter 6, we switch experimental contexts and present an overview of the nEDM@SNS experiment and discuss the construction and assembly of one key apparatus component: the  $B_0$  magnet.

In Chapter 7, we conclude with the highlights of the work discussed in this dissertation and provide an outlook to the near future for experiments such as UCNA+ and nEDM@SNS.

In this Introduction, we present an overview of the physical processes that are investigated in the rest of this dissertation. In particular, we pay special attention to physical processes involving UCNs in order to provide context for the results extracted in later chapters in this work. The organization is as follows: we describe the neutron and then a subclass of neutrons called Ultracold Neutrons (UCNs) which have convenient experimental properties. We then discuss the weak interaction and neutron  $\beta$ -decay, the decay probed by the correlation coefficients  $A$  and  $b$ . We also present an overview of the neutron lifetime,  $\tau$ , as a result of this  $\beta$ -decay. Finally, we close with a discussion of the neutron electric dipole moment (nEDM) in order to provide an introduction for the nEDM@SNS experiment.

#### **1.1 The Neutron**

The neutron is a simple composite particle made of three quarks. It is charge neutral (zero charge) and composed of two down ( $d$ ) quarks and one up ( $u$ ) quark. The

$d$  quarks carry  $-\frac{1}{3}e$  charge, where  $e$  is the fundamental electron charge. The  $u$  quark carries  $+\frac{2}{3}e$  charge. Their masses are  $m_u \approx 3 \text{ MeV}/c^2$  and  $m_d \approx 7 \text{ MeV}/c^2$  [Gri08]. The quarks are bound together by the strong force in order to comprise the neutron. The neutron has a mass of  $939.5653 \text{ MeV}/c^2$ , a magnetic moment, and spin- $\frac{1}{2}$  [Ber07].

We highlight the contrast between the neutron and the proton, both of which are called “nucleons”. The proton is comprised of two  $u$  quarks and one  $d$  quark. Its mass is  $938.2719 \text{ MeV}/c^2$  [Ber07] and it is also spin- $\frac{1}{2}$ . It has a charge of  $+e$ . The proton has a lower mass than the neutron. In fact, the proton is the lightest baryon which implies that the free proton is a stable particle (assuming Baryon number conservation). In contrast, the free neutron, with its higher mass, can decay into a proton. This is discussed further in section 1.3.

## 1.2 Ultracold Neutrons

Ultracold neutrons (UCNs) are essentially neutrons that have kinetic energy  $\lesssim 350 \text{ neV}$ . UCNs exhibit useful physical properties from an experimental perspective. Both the experiments in this dissertation and a growing field of fundamental measurement experiments are using UCNs due to these advantageous properties.

### 1.2.1 Definition

Ultracold Neutrons (UCNs) were originally hypothesized in the 1950-1960s by Zel'dovitch [Zel59] as neutrons that have been cooled to extremely low temperatures. At these velocities, their own gravitational potential energy is on the order of their kinetic energy and hence gravitational effects on the UCNs become relevant.

UCNs can be functionally defined as neutrons that have the following equivalent kinematic properties:

- Their individual velocities are  $< 8 \text{ m/s}$ .
- Their kinetic energies are  $< 300 \text{ neV}$ .
- Their speeds correspond to  $mK$  (if the gas of UCNs was in thermal equilibrium with a bath held at  $mK$  temperatures).
- Their de Broglie wavelengths are  $> 10\text{s}$  of  $nm$ .

Furthermore, UCNs have gravitational potential energy  $102 \text{ neV/m}$ . Figure 1.1 shows different regimes of neutrons based on their kinetic energies.

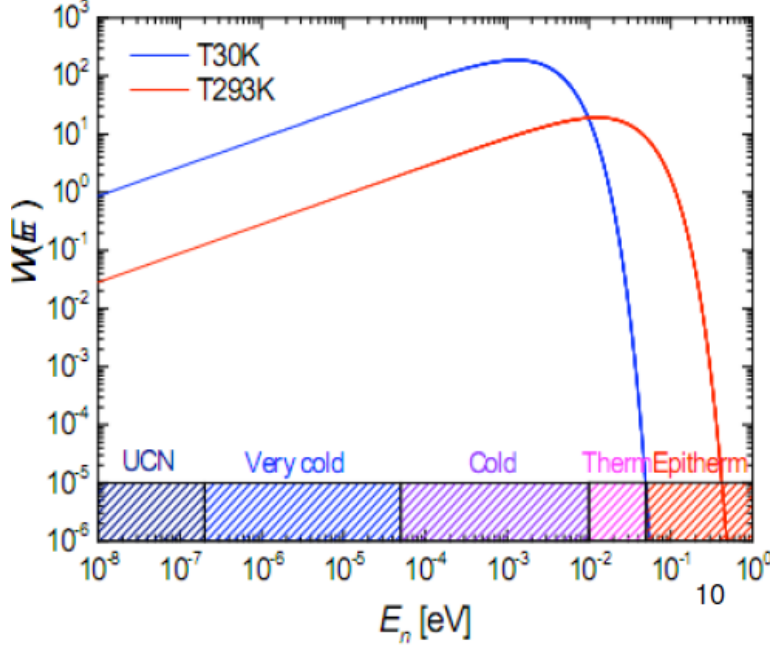


Figure 1.1: Different temperature regimes (expressed in  $eV$ ) for neutrons. A thermal distribution is included for an ensemble of neutrons produced at room temperature and  $30K$ . Figure taken from [Liu09].

### 1.2.2 Properties

UCNs, at their typical kinetic energies, exhibit several convenient properties for experimentalists. We focus on two: the ability of UCNs to fully reflect off the surfaces of certain materials, and the ability to contain UCNs due to their gravitational potential.

Due to the long wavelengths of UCNs, when they impinge upon a surface made of several atoms in a regular lattice structure, they see an effective solid surface. This is because the long wavelength of the UCNs cannot resolve the interatomic spacing of the material. At a simplistic level, the potential due to this regularly spaced atomic surface can be modeled by

$$V = \frac{2\pi\hbar^2}{m} Na \quad (1.1)$$

where  $m$  is the neutron mass,  $N$  is the number density of the material, and  $a$  is defined as the scattering length<sup>1</sup>. This potential is derived from taking a “forest”

---

<sup>1</sup>We note that this derivation implicitly assumes the material to have a positive scattering length ( $a > 0$ ) and hence serve as a material wall. There are instances of a negative scattering length which imply that the neutron would accelerate forward upon impinging on the material surface. These materials are not generally considered to be suitable for trapping UCNs.

of delta-function potentials located at each atomic center and assuming a uniform number density (the full treatment is found in [GRL91]). For different materials, this effective potential is called the “Fermi potential” and this quantity allows for direct comparisons of materials based on UCN reflectivity.

We can model UCNs as a quantum particle interacting with a surface that is represented by a potential  $V$ . This reduces down to the standard, well-known problem of solving for the reflection,  $R$ , and transmission,  $T$ , coefficients of a particle impinging upon a square potential of height  $V$ . One can follow the traditional calculation for a one-dimensional square potential and derive  $R$ ,  $T$ , and a penetration length,  $\lambda$  (again, the full treatment is found in [GRL91]). This is the distance within the material where the transmission coefficient of a wave falls to  $\frac{1}{e}$  of the original transmission probability, since within the classically forbidden potential the penetrating wave decays as an exponential. Aside from loss mechanisms which can typically be safely guarded against, good neutron reflectors act as perfectly reflective walls for UCNs (they provide a high Fermi potential for many penetration lengths into the material) and enable them to be trapped and bottled. This allows for effective, efficient UCN storage — one of the major experimental upsides of using UCNs to study neutron physics effects. The Fermi potentials of several common materials is given in table 1.1.

Material	$V$ [neV]
Nickel ( $^{58}\text{Ni}$ )	335
Iron (Fe)	210
Beryllium (Be)	252
Copper (Cu)	168
Stainless Steel	190

Table 1.1: Fermi potentials of common materials used in UCNA and nEDM@SNS experiments. Values taken from [GRL91] and [Chu+19] and references therein.

The second convenient property of UCNs is their low kinetic energies and the subsequent influence of their gravitational potential energy. As mentioned before, UCNs can be treated as a ballistic particle with simple kinematics. They are under the influence of their gravitational potential which can classically be given by

$$V_g = mgh \quad (1.2)$$

where  $m$  is the neutron mass,  $g$  is the gravitational constant, and  $h$  is the height given some reference height. For UCNs, their gravitational potential is  $102 \text{ neV}/m$ .

Hence, a UCN which has kinetic energy  $300 \text{ neV}$  can rise  $\approx 2.94 \text{ m}$  in height before converting all of its kinetic energy into potential energy and turning over. This is an advantage because it means that for UCNs stored in a bottle of height  $\frac{E_{UCN}}{102 \text{ nev/m}}$  can typically be trapped from above by gravity. We note that at typical UCN densities, the UCN-UCN collisions negligibly affect the trapping time. Thus one can construct a trap on all sides with fully UCN reflective material but leave the top open as long as the container is high enough. This allows access into the UCN volume for control, diagnostics, and measurements. One example of such an experiment is UCN $\tau$ , further described in [Fri22] and discussed briefly in Chapter 5.

### 1.2.3 Production

Since the free neutron is not a stable particle, all free neutrons which eventually become UCNs must be extracted from nuclei which contains bound neutrons. This extraction process and the subsequent cooling stages to reach UCN temperatures is referred to as UCN production. We note that there are several different neutron sources and moderation techniques available to produce UCNs. Here, we describe only the general concept of moderation into the UCN regime that is relevant for UCNA and nEDM@SNS.

For these experiments, neutrons are produced by spallation which is the process of colliding a beam of light nuclei on a heavy nuclei target. The absorption of the light nuclei leads to a heavier, excited state nucleus. The resulting decay of the excited nucleus produces fast neutrons which can be thermalized to room temperatures by a highly reflective chamber (for example, Los Alamos National Laboratory, LANL for short, uses Beryllium and Graphite walls) that contains the neutrons and brings them into thermal equilibrium at room temperature. From there, they travel towards a series of layers of cold ( $\approx 20 \text{ K} - 100 \text{ K}$ ) polyethylene beads (or other moderator) where elastic collisions within the beads further reduce the thermal kinetic energies of the neutrons into the cold regime.

We now briefly discuss the techniques used to produce UCNs from cold neutrons in the UCNA and nEDM@SNS experiments. These are not the only moderation techniques available and [GRL91] provides a survey of several different experiments using different UCN moderation procedures.

At LANL, these cold neutrons then interact with a solid deuterium ( $SD_2$ ) source. These cold neutrons can interact with the lattice structure of the  $SD_2$  and excite

a phonon which is carried away into the bulk material. This phonon excitation decreases the energy of the cold neutron, lowering it into the UCN regime. We note that when the UCNs leave the source, they gain a 109  $neV$  kinetic energy boost from the Fermi potential of the  $SD_2$ . Section 2.2.1 discusses the details of UCN production at LANL.

At nEDM@SNS, there is a similar method for UCN production planned except the cold-to-UCN moderator is superfluid  $^4He$  and these UCNs are produced in-situ (in the measurement volume region). This is called superthermal production - when UCNs are produced out of thermal equilibrium with the production material and is the same conceptually as the method at LANL. It has been shown that liquid  $^4He$  can perform this moderation [GP77]. Within superfluid  $^4He$  - that is, liquid  $^4He$  that has been cooled to  $\lesssim 2 K$  temperatures and reached a Bose-Einstein condensate state - cold neutrons can be further cooled by transferring their energy into the  $^4He$  by generating phonons. By generating a single-phonon excitation in liquid  $^4He$ , a cold neutron can lose nearly all its remaining kinetic energy and reach the ultracold regime. This process of phonon excitation works for neutrons with kinetic energy corresponding to  $\approx 12 K$  or, equivalently, a wavelength of 8.9 Å. This is typically called “down-scattering”. The inverse process, called “up-scattering”, can be shown via the principle of detailed balance (again, [GRL91]) to be

$$r_{up} = r_{down} e^{-\frac{\Delta}{k_B T}} \quad (1.3)$$

where  $r_{up}$  is the rate of up-scattering by an amount of energy  $\Delta$ ,  $r_{down}$  is the rate of down-scattering by the same energy, and  $T$  is the temperature of the moderator. For low temperatures such as superfluid liquid  $^4He$  in the nEDM@SNS experiment, the up-scattering rate is greatly suppressed by the multiplicative Boltzmann factor. Thus, this procedure produces a significant excess of cold neutrons downscattering compared to UCNs upscattering. Current theoretical estimates and experimentally measured sources verify this technique in order to produce leading UCN concentrations in a measurement volume.

### 1.3 Neutron Beta Decay

The free neutron, which is a neutron that is not bound within a nuclei, is capable of decaying via the following interaction:



where  $n$  is the neutron,  $p$  a proton,  $e^-$  an electron, and  $\bar{\nu}_e$  an anti-neutrino of the electron type. The rest energy difference, namely  $(m_n - m_p - m_e)c^2 = 782 keV$ ,

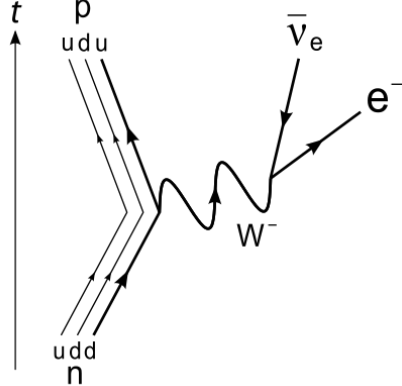


Figure 1.2: A Feynmann diagram of the neutron beta decay, mediated by the weak interaction, showing a conversion of a  $d$  quark to a  $u$  quark and associated output particles that form the decay interaction in equation 1.4.

is transferred as kinetic energy to the three-body decay of the final state particles in order to conserve energy.

This decay can be shown as a Feynmann diagram in figure 1.2. In this diagram, one internal  $d$  quark from the neutron is transformed into an  $u$  quark via emission of a  $W^-$  boson which subsequently decays into an electron and electron anti-neutrino. The  $u$  quark together with the unchanged  $d$  and  $u$  quark form a proton. The presence of a mediating  $W^-$  is characteristic of the weak interaction.

### 1.3.1 The Weak Interaction in the Neutron

The weak interaction is one of four fundamental forces, along with the gravitational force, the electromagnetic force, and the strong force. The electromagnetic force is mediated by exchange of a photon and the strong force is mediated by exchange of gluons at the quark distance-scale and pions at the nucleus distance-scale.

The (charged) weak interaction, namely one that exchanges an intermediary charged boson  $W^\pm$ , is responsible for transforming a quark into another type of quark. The weak interaction affects all quarks and leptons. The mediators of the weak interaction ( $W^\pm$  and  $Z$ ) are massive and with masses given by [Gri08]

$$M_{W^\pm} = 80.40 \pm 0.03 \text{ GeV}/c^2 \quad (1.5)$$

$$M_Z = 91.188 \pm 0.002 \text{ GeV}/c^2 \quad (1.6)$$

The weak interaction Hamiltonian is given by the form

$$H = G_F(\bar{\psi}_n \gamma_\mu (1 - \gamma^5) \psi_p)(\bar{\psi}_{\bar{\mu}} \gamma^\mu (1 - \gamma^5) \psi_e) \quad (1.7)$$

where  $G_F$  is the Fermi coupling constant of the weak interaction. We note that the weak interaction is a vector - axial-vector (V-A) form. This leads to a vertex factor<sup>2</sup> for neutron  $\beta$ -decay given qualitatively by

$$\frac{-ig_w}{2\sqrt{2}}\gamma^\mu(1-\gamma^5) \quad (1.8)$$

where  $g_w = \sqrt{4\pi\alpha_w}$  is called the “weak coupling constant” and has the same role as the standard coupling constants in quantum electrodynamics or quantum chromodynamics.

In the decay described by figure 1.2, the vertex factor in equation 1.8 would hold for the “bare” interaction, for example at the electron - anti-neutrino vertex. This is because particles at this vertex are fundamental particles in a vacuum. At the  $u, d$  vertex, we must make an additional modification to the interaction Hamiltonian and associated interaction vertex. This is due to the quark interactions (QCD) within the neutron happening in the presence of two “spectator” quarks — that is, the remaining  $u, d$  quarks that do not participate in the decay but modify the couplings. The Hamiltonian and interaction vertex then become

$$H = G_F(V_{ud}\bar{\psi}_n\gamma_\mu(1-\lambda\gamma^5)\psi_p)(\bar{\psi}_{\bar{\mu}}\gamma^\mu(1-\gamma^5)\psi_e) \quad (1.9)$$

$$\frac{-ig_w}{2\sqrt{2}}V_{ud}\gamma^\mu(1-\lambda\gamma^5) \quad (1.10)$$

where now we introduce  $V_{ud}$  which is the first element of the Cabibbo-Kobayashi-Maskawa (CKM) mixing matrix. The CKM matrix describes the coupling of different generations of quarks to each other when they undergo the flavor-changing weak decay (in neutron decay, we are coupling a  $d$  quark to a  $u$  quark and hence we take  $V_{ud}$ ). Furthermore, we introduce a  $\lambda$  term which is defined as

$$\lambda = \frac{C_A}{C_V} = \frac{g_A}{g_V} \quad (1.11)$$

and represents the relative coupling strengths of the vector and the axial-vector interactions in the neutron decay.

The V-A nature of the weak interaction arises from the  $\gamma^\mu(1-\gamma^5)$  form in equations 1.7 and 1.8. By definition, the different interactions have different behaviors under parity transformations and are summarized in table 1.2. Namely, in the weak interaction, both the vector  $\gamma^\mu$  and axial-vector  $\gamma^\mu\gamma^5$  interaction terms are present.

---

<sup>2</sup>The factor associated with each vertex in a standard Feynmann diagram representation of a decay or interaction. See [Gri08] or standard text for additional details.

Covariant	Classification
$\bar{\psi}\psi$	scalar
$\bar{\psi}\gamma^5\psi$	pseudoscalar
$\bar{\psi}\gamma^\mu\psi$	vector
$\bar{\psi}\gamma^\mu\gamma^5\psi$	axial vector
$\bar{\psi}\sigma^{\mu\nu}\psi$	tensor

Table 1.2: Classification of bilinear covariants.

Following the definition of the weak interaction vertex in equation 1.8 (or, equivalently, the Hamiltonian interaction form in equation 1.7), we can define two types of  $\beta$ -decay transitions when we note that the true weak interaction leads to a mixture of vector and axial-vector transitions. The Fermi transition is defined as a decay that proceeds purely through vector (or scalar) couplings and produces  $\Delta J = 0$ , where  $J$  is the orbital angular momentum, and no parity change. The Gamow-Teller transition is defined as a decay that proceeds purely through axial-vector (or tensor) couplings and produces  $\Delta J = 0, \pm 1$  with no parity change. These two classes of transitions are important because their relative strengths represent the admixture of different decay channels available to a weak nuclei decay. In particular, the neutron decays via an admixture of the Fermi and Gamow-Teller transitions and the limits in Chapter 4 contribute to overall measurements of the strength of these couplings.

### 1.3.2 Neutron Beta Decay and Correlation Coefficients

Taking the fully generalized Hamiltonian of the weak interaction [LY56], we can express the fully generalized differential decay rate of the (polarized) neutron as a function of the emitted electron's energy, momentum and spin, the neutrino's momentum, and the spin of the decay proton (see [JTW57a; JTW57b] for a complete description). The full description of the differential decay rate simplifies greatly when we note that, in UCNA, we have polarized neutrons (initial state), and we integrate over all other kinematic and polarization parameters except the decay electron's momentum (notably, we are insensitive to the decay proton and neutrino). Under these conditions, we obtain a final simplified differential decay rate given by

$$\frac{d\Gamma}{dE_e d\Omega_e} = \frac{1}{2} \frac{F(\pm Z, E_e)}{(2\pi)^4} p_e E_e (E_0 - E_e)^2 \xi \left[ 1 + b \frac{m_e}{E_e} + A \frac{\langle \vec{J} \rangle}{J} \cdot \frac{\vec{p}_e}{E_e} \right] \quad (1.12)$$

where  $E_e$  is the total decay electron energy,  $m_e$  is the rest mass of the electron,  $p_e$  is the momentum of the electron,  $\vec{J}$  here represents the spin state of the initial decay neutron, and the quantity on the left hand side is the full differential decay

rate of the free (polarized) neutron. In addition,  $F(\pm Z, E_e)$  is the Fermi function which is a shape correction to the decay electron spectrum that arises from Coulomb interactions [Wil82].

The individual constants,  $b$  and  $A$  in this case, are the correlation coefficients that, at this stage, must be experimentally determined and provide insights into the underlying physics in the neutron  $\beta$ -decay. We note there are several other decay correlation coefficients in the fully general decay rate such as  $a, c, B, D, J, I, K', M, N, Q, R, S, T, U, W, V$ , and more, which are not shown in equation 1.12.

### 1.3.2.1 The Asymmetry Term, $A$

In the decay rate in equation 1.12, the  $A$  coefficient is called the “asymmetry” term and it represents the fractional decay rate of electrons whose momentum is aligned vs anti-aligned with the neutron polarization (initial spin direction). The asymmetry analysis is the topic of [Men14; Bro18] and indeed the work in the later chapters of this dissertation build upon the analysis procedures, studies, and insights derived in those works.

In equation 1.12, the asymmetry term  $A$  does not account for energy dependent corrections and is traditionally distinguished from the experimentally measured asymmetry by redefining it as  $A_0$ . The experimentally measured asymmetry which is energy dependent is redefined as  $A$ . The connection between the two is given by

$$A(E_e) = P_n A_0 \beta \langle \cos \theta \rangle \quad (1.13)$$

where  $P_n$  is the neutron polarization,  $\beta = \frac{v}{c}$  where  $v$  is the electron velocity, and  $c$  is the speed of light.  $\langle \cos \theta \rangle \approx \frac{1}{2}$  in the UCNA apparatus.

The asymmetry can be expressed in terms of the coupling constants of the vector and axial-vector weak interaction components

$$A_0 = -2 \frac{\lambda(\lambda + 1)}{1 + 3\lambda^2} \quad (1.14)$$

where  $\lambda$  is defined in equation 1.11 and for the neutron this result is derived by taking  $M_F = 1$  (Fermi matrix element) and  $M_{GT} = \sqrt{3}$  (Gamow-Teller matrix element). These simple coefficients arise from the simple structure of the neutron and point towards one of the advantages of using neutrons for studies: the lack of complicated nuclear  $\beta$ -decay theory corrections.

Given the relation in equation 1.14, high-precision measurements of  $A$  then become a powerful probe of the value of  $\lambda$  and hence the relative coupling strengths of the

vector vs axial-vector components of the weak interaction. In fact,  $A$  measurements currently provide the most precise measurements of  $\lambda$  with  $\lambda = \frac{g_A}{g_V} = -1.2783(22)$  [Bro+18]. These measurements can be combined with the neutron lifetime,  $\tau_n$ , which is also sensitive to  $\lambda$  in order to test the electroweak Standard Model [Gon+21].

### 1.3.2.2 The Fierz Interference Term, $b$

The  $b$  coefficient in equation 1.12 is called the Fierz interference term and manifests itself in the decay rate as an energy shift in the electron energy spectrum. The description of  $b$  and analysis associated with extracting a value for  $b$  from the various UCNA datasets comprise the work in Chapter 4. The topic of Fierz interference in the UCNA experiment is covered in [Hic13] and the work in this dissertation builds upon it and presents an alternative extraction methodology.

The Fierz interference term,  $b$ , with its multiplicative factor,  $\xi$ , can be expressed as [JTW57a]

$$b\xi = \pm 2\gamma \text{Re} \left[ |M_F|^2 \lambda_{J'J} (C_S C_V^* - C'_S C_V'^*) + |M_{GT}|^2 (C_T C_V^* - C'_T C_A'^*) \right] \quad (1.15)$$

where the + (-) sign indicates  $\beta^-$  ( $\beta^+$ ) decay,  $\gamma = \sqrt{1 - \alpha^2 Z^2}$ ,  $\alpha$  is the fine structure constant,  $Z$  is the atomic number, and  $\lambda_{J'J}$  is given by

$$\lambda_{J'J} = \begin{cases} 1 & J \rightarrow J' = J - 1 \\ \frac{1}{J+1} & J \rightarrow J' = J \\ \frac{-J}{J+1} & J \rightarrow J' = J + 1 \end{cases} \quad (1.16)$$

where  $J, J'$  are the angular momenta of the original and final nuclei respectively, and  $\xi$  is given by

$$\xi = |M_F|^2 (|C_S|^2 + |C_V|^2 + |C'_S|^2 + |C_V'|^2) + |M_{GT}|^2 (|C_T|^2 + |C_A|^2 + |C'_T|^2 + |C'_A|^2) \quad (1.17)$$

where  $|M_F|^2$  and  $|M_{GT}|^2$  are the conventional Fermi and Gamow-Teller nuclear matrix elements, the subscripts  $S, T, V, A$  refer to scalar, tensor, vector, and axial-vector (see table 1.2), the  $C_i, C'_i$  denote coupling constants (see [LY56] for further details on the couplings, [JTW57a] for details on  $b$ ).

Assuming a V-A nature of the weak interaction, we can see from equation 1.15 that the  $b$  term is identically 0. Hence, searches for Fierz interference represent probes of beyond Standard Model physics and, in particular for neutron  $\beta$ -decay,

would represent probes of scalar and tensor couplings in the weak interaction. Measurements of Fierz interference can be related to beyond Standard Model scalar and tensor couplings by using effective field theories as described most recently in [GNS19] and the references therein describe other physically motivated theories for non-zero Fierz interference in neutron decay.

For the neutron, the Fierz interference term simplifies to become

$$b = \frac{b_F + 3\lambda^2 b_{GT}}{1 + 3\lambda^2} \quad (1.18)$$

where  $b$  here specifically refers to the Fierz interference for the neutron,  $b_F$  represents the Fermi component of the Fierz interference which is sensitive to scalar interactions, and  $b_{GT}$  represents the Gamow-Teller component of the Fierz interference which is sensitive to tensor interactions. This simplification arises due to the simple nature of the neutron and the lack of complicated nuclear structure to consider.

### 1.3.2.3 The Neutron Lifetime, $\tau$

As described previously, the free neutron will decay into a proton via equation 1.4 due to the favorable energy differences in initial and final state. The lifetime of this decay is also partially covered in Chapter 5 when we explore the potential for a neutron to decay via an unknown dark matter decay channel. Thus, in this introduction, we provide a short overview of the neutron mean lifetime.

The neutron lifetime measurement is the topic of [Fri22] and additional details are provided there. The neutron lifetime can be roughly calculated using the Feynmann diagram in figure 1.2 and the vertices given in equations 1.8 and 1.10.

In the low-momentum limit ( $Q \ll m_W$ ), the propagator term of the decay can be approximated as  $\frac{ig_{\mu\nu}}{m_W^2}$  which yields the following matrix element for the decay:

$$\begin{aligned} M &= i\bar{\psi}_n K_\mu \psi_p \frac{ig_{\mu\nu}}{m_W^2} \bar{\psi}_e J^\nu \psi_{\nu_e} \\ &= \frac{g_W^2 V_{ud}}{8m_W^2} \bar{\psi}_n \gamma_\mu (1 - \lambda \gamma^5) \psi_p \bar{\psi}_e \gamma^\mu (1 - \gamma^5) \psi_{\nu_e} \end{aligned} \quad (1.19)$$

where  $\psi_{n,p,e,\nu_e}$  are the spin wave functions of the neutron, proton, electron and electron anti-neutrino, and we have inserted equation 1.8 for  $J^\nu$  and equation 1.10 for  $K_\mu$ . We can use the matrix element of the decay to directly compute the decay

rate (and hence the lifetime) via Fermi's Golden Rule

$$\frac{1}{\tau_{i \rightarrow f}} = \frac{2\pi}{\hbar} |M|^2 \rho(E_f) \quad (1.20)$$

where  $i$  represents the initial state,  $f$  represents the final state, and  $\rho$  is a density of states. Using equation 1.19, this yields

$$\tau = \frac{64\pi^3 \hbar m_W^4}{m_e^5 c^2 g_w^4 |V_{ud}|^2 (1 + 3\lambda^2) f} \quad (1.21)$$

where  $f$  is a statistical factor to account for the integral over the energy phase space of the decay.

This simple derivation illustrates the theoretical calculation of the neutron lifetime. In practice, this computation is difficult due to non-trivial higher-order corrections to the neutron  $\beta$ -decay. However, modern calculations can achieve a theoretical prediction on  $\tau_n$  within the uncertainty of current  $\tau_n$  measurements. We note that calculations are limited by theory uncertainties whereas experimental measurements are reaching new precision benchmarks from improvements in measurement techniques.

In Chapter 5, we further examine the neutron lifetime and, in particular, analyze the UCNA dataset under the paradigm of an exotic, beyond Standard Model decay mode involving a dark matter decay channel. This would be a supplementary (ideally present at the 1% branching ratio) decay channel to the conventional neutron  $\beta$ -decay described in equation 1.4.

#### 1.4 Neutron Electric Dipole Moments

Recall from the discussion in the beginning of this chapter that the neutron is a bound state of three quarks: two  $d$  quarks with  $-\frac{1}{3} e$  charge each and one  $u$  quark with  $+\frac{2}{3} e$  charge. If the center of charge for each of these quarks had some spatial distribution, there would, in principle, be an induced electric dipole moment due to the definition of the dipole moment  $\vec{d} := q\vec{x}$ , where  $q$  is the magnitude of the charge and  $\vec{x}$  is the vector of characteristic displacement between the charges. Furthermore, since the neutron is a spin- $\frac{1}{2}$  particle with a magnetic moment, the interaction Hamiltonian of the neutron in the presence of electric and magnetic fields is given by

$$H = - \left( \vec{d} \cdot \vec{E} + \vec{\mu} \cdot \vec{B} \right) \quad (1.22)$$

where  $\vec{d}$  is the electric dipole moment and  $\vec{\mu}$  is the magnetic dipole moment. This then reduces for the neutron to

$$H = -\frac{2ex}{\hbar} (\vec{s} \cdot \vec{E}) - \gamma (\vec{s} \cdot \vec{B}) \quad (1.23)$$

where  $e$  is the fundamental electric charge,  $x$  is the characteristic distance between charges,  $\vec{s}$  is the spin vector of the neutron,  $\gamma$  is the gyromagnetic ratio, and  $\vec{E}, \vec{B}$  are the applied electric and magnetic fields respectively. We note that in this expression we have redefined the electric dipole moment as  $d = ex$ .

We can examine the effects of the Hamiltonian in equation 1.22 under the effect of different symmetry transformations. The symmetries of parity (P), charge (C), and time (T) are defined as

- P: the inversion of all spatial coordinates through the origin.  $\hat{P} |\psi(x, y, z)\rangle \rightarrow |\psi(-x, -y, -z)\rangle$ .
- T: the inversion of the time coordinate.  $\hat{T} |\psi(t)\rangle \rightarrow |\psi(-t)\rangle$ .
- C: the transformation of all particles into their antiparticles.  $\hat{C} |\psi\rangle \rightarrow |\bar{\psi}\rangle$ .

We note the product transformation of  $CPT$  of any system is an invariant quantity, which is a theorem of Quantum Field Theory. When we examine equation 1.22, we can identify that the  $\vec{d} \cdot \vec{E}$  term is  $C$  even,  $P$  odd, and  $T$  odd. Thus, if the magnitude  $d \neq 0$ , the neutron EDM indicates a Hamiltonian that violates  $T$  and  $CP$  symmetries. We note that the magnetic term,  $\vec{\mu} \cdot \vec{B}$ , is even in  $C$ ,  $P$ , and  $T$ .

#### 1.4.1 nEDM Experiments: Past, Present, Projected

Searches for the nEDM have been of primary importance as an avenue to probe new CP violating beyond Standard Model (SM) physics. The importance of discovering new CP violation is discussed in section 1.4.2. The progress in sensitivity of nEDM measurements is shown graphically in figure 1.3. We highlight that this figure also includes the projected sensitivity of the nEDM@SNS experiment, one of the two experiments that form the bulk of the work in this dissertation.

Today, the field of nEDM searches has grown as nEDMs continue to prove their value in probing exotic theories of physics. Typically, beyond SM theories or extensions to the SM manifest as larger nEDM (and other EDM) values. Thus, throughout history, the neutron EDM search has ruled out a significant portion of SM extension theories, as evidenced by the projected nEDM values of popular theories listed in

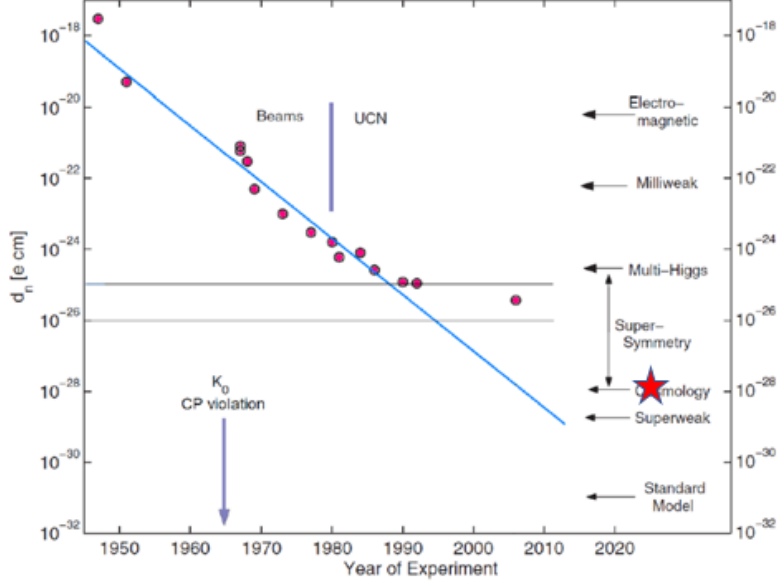


Figure 1.3: Measurements of the neutron electric dipole moment throughout history. Notably, the most stringent completed experiment is at  $d_n \approx 10^{-26} e \cdot cm$ , whereas the projected sensitivity of nEDM@SNS is  $d_n \approx 10^{-28} e \cdot cm$  (indicated by the red star). In addition, the point in time when the most sensitive experiments switched over from beam methods to UCN methods is indicated. Finally, as a historical note, the discovery of CP violation in the Standard Model (via  $K_0$  decays) is indicated as well. That is, CP violation that is intrinsic in the SM due to a complex phase in the CKM matrix. Figure, with minor modifications, taken from [Pen12].

figure 1.3. However, there is still a large discovery potential between the current best published limits on the nEDM ( $\approx 10^{-26} e \cdot cm$ ) compared to the SM “floor” ( $\approx 10^{-31} e \cdot cm$ ). In these five orders of magnitude, there are many compelling beyond SM physics concepts to probe (see [Chu+19] and references therein for a comprehensive review)<sup>3</sup>.

The next-generation of nEDM searches is underway with experiments currently underway. For example, the most recent published value was by PSI and is  $d_n = 0.0 \pm 1.1_{\text{stat}} \pm 0.2_{\text{syst}} \times 10^{-26} e \cdot cm$  [Abe+20]. The goal for next-generation nEDM experiments is to improve the precision by a factor  $\approx 10 - 100$  (see table 1.3 for a summary of planned experiments). The nEDM@SNS is among the most ambitious in design sensitivity, aiming for a final sensitivity of  $\approx 10^{-28} e \cdot cm$ .

---

<sup>3</sup>In addition, much of the discussion in this chapter on CP violation and their relation to nEDMs can be found in greater detail in [Chu+19]

Experiment Name	Projected Sensitivity at 90% Confidence [ $10^{-28} e \cdot cm$ ]
Current Limits	180
ILL-PNPI	< 100 (phase 1); < 10 (phase 2)
ILL Crystal	< 100
PSI EDM	< 20
PanEDM	< 40
Munich/ILL	< 10
TUCAN/TRIUMF	< 20
nEDM@SNS	< 3
ESS	< 50
LANL	< 30

Table 1.3: Summary of next generation nEDM experiments located at major UCN source laboratories. Most experiments are expected to reach these sensitivities by 2030. Projected sensitivities taken from [Fil21].

### 1.4.2 Beyond Standard Model Searches

The remaining question to answer is the significance of finding a (or setting more precise limits on) a neutron EDM. Due to the current five orders of magnitude of “discovery space” for beyond SM non-zero nEDMs, the search for a non-zero nEDM acts as a search to probe beyond SM physics models that contain new sources of CP-violation. In the following sections, we discuss the necessity of new CP-violating interactions and provide one motivation for the search for such interactions: explaining the prevalence of matter over anti-matter in the universe.

#### 1.4.2.1 CP Violation

Currently, in the SM, there are two natural sources of CP violation: a complex phase in the CKM matrix and a CP-violating phase in Quantum Chromodynamics (QCD).

Within the SM, there is intrinsic CP-violation in the form of an empirical phase, called  $\delta$ , in the CKM matrix. This phase, measured in experiment as  $\approx 10^{-3}$ , allows for the current CP violation seen in the decay of the Kaon system and, more recently discovered, in the decay of the neutral  $B$  meson systems [Gri08]. In fact, this value is consistent with the CP-violating branching ratios found in these Kaon and  $B$  meson decays and corroborated by theoretical understanding of the general decay parameters.

Additionally, there has been a proposed phase in the strong interaction, parametrized by  $\bar{\theta}$ , that would contain a CP violating term. This parameter would enter in the interactions of the internal quark structure and contribute to the neutron EDM,

producing an nEDM value given by [Hoo21]

$$d_n \approx 10^{-16} \bar{\theta} e \cdot cm. \quad (1.24)$$

Where first proposed, the phase  $\bar{\theta}$  did not relate to any fundamental symmetry and hence the value was naively expected to be order  $\approx 1$ . Contemporary published limits on  $d_n < 10^{-26} e \cdot cm$  implies constraints of  $|\bar{\theta}| < 10^{-10}$ . This astonishingly small value seems to be indicative of a fundamental constraint. Neutron EDM results continue to exacerbate the strong CP problem, namely the diminishing value of  $|\bar{\theta}|$ . Proposals such as axions have emerged to explain this phenomenon and [Hoo21] provides a review on such proposals.

However, both of these sources of CP violation are insufficient to explain a critical phenomenon in our universe — that of the baryon asymmetry. Sufficient CP violation can give rise to a preference for matter over anti-matter (see next subsection). This is a preference that is reflected in our current universe which is matter dominated and not one with equal amounts of matter and anti-matter. In the following section, we briefly explore the implication of this reality on new sources of CP-violation.

#### 1.4.2.2 Baryon Asymmetry

One of the major open questions that the search for new sources of CP violation (in this case, through neutron EDMs) aims to answer is that of the matter - anti-matter asymmetry in the universe, otherwise known as the baryon asymmetry. In the early universe, one source for the net preference of matter over anti-matter is called baryogenesis and refers to the creation of more baryons compared to anti-baryons.

In order to achieve this, three conditions must be met:

1. Violation of baryon number  $B$ .
2. Departure from thermodynamic equilibrium.
3. Both C- and CP-violating processes.

These three conditions are called the Sakharov conditions [Sak67]. There are a multitude of theories that have been proposed that satisfy these conditions in order to explain the level of matter - anti-matter asymmetry we see in the current universe. Here, we give an intuitive explanation of these conditions and direct the interested

reader to [Chu+19] and references therein for more technical details of the different theories.

(1) In order for there to be a net amount of matter, the baryon number in the universe must have increased from an initial  $B = 0$  (equal matter and anti-matter), and hence the baryon number must not be a fundamental symmetry. (2) Whatever interactions that lead to a preference for matter must not reach thermodynamic equilibrium or else those same interactions, in the conditions of the early universe, would proceed backwards and lead to the preferential deletion of matter. (3) The third condition refers essentially to those processes which preferentially select matter over anti-matter naturally come with intrinsic C or CP-violation.

In our previous discussions of the SM, there are all the ingredients to satisfy the Sakharov conditions. Notably, the phase  $\delta$  in the CKM matrix plays the role of CP-violation. However, current experimental measurements of related observables indicate that the value of the CP-violation in the SM is far too weak to explain the matter - radiation ratios observed in the current universe (one measure of how much anti-matter annihilated with matter in the early universe). Thus, new sources of CP violation at the levels needed to explain the current matter - anti-matter asymmetry could exist in order to properly satisfy the Sahkarov conditions and explain the current matter abundance in our universe (see [CDS12] and references therein for an in-depth review of the baryon asymmetry problem). Those sources of CP-violation are what nEDMs hope to discover in the next-generation of experiments.

CP-violation contributes to the explanation of the baryon asymmetry by acting as a necessary ingredient in modern models of baryogenesis - that is, the preferential creation of baryons over anti-baryons in the early universe and thus leading to the current baryon asymmetry in the universe. One such theory for baryogenesis is called electroweak baryogenesis (reviewed, for instance, in [MR12]). It can be described as the breaking of the electro-weak symmetry as a result of the cooling of the universe. The hot plasma of the universe forms “bubbles” of electro-weak broken phases that introduce a baryon asymmetry. These bubbles move and grow until the universe has cooled to the point where only the electro-weak broken phase remains. With the right parameters, this results in the baryon asymmetry observed in our current universe.

Another popular theory that seeks to explain the baryon asymmetry is called “leptogenesis”. It was originally proposed in [FY86], reviewed in detail in [CDS12] (see also [BPY05; Dom+21] and references therein), and we present a brief description

here. Leptogenesis seeks to explain the baryon asymmetry by introducing an earlier lepton asymmetry that then propagates into a baryon asymmetry via the KRS mechanism [KRS85]<sup>4</sup>. Leptogenesis adds three families of massive, right-handed neutrinos as an extension to the Standard Model<sup>5</sup>. Together, this new extended neutrino model can introduce a lepton mixing matrix analogous to the quark mixing CKM matrix. Furthermore, these right-handed neutrinos also seek to explain the small observed masses of the Standard Model left-handed neutrinos via the seesaw mechanism (see, for example, [Dom+21]). Lastly, certain leptogenesis models are congruent with axion-like particles as dark matter candidates. Thus, leptogenesis has become quite a popular theory for creating a lepton asymmetry that propagates into a baryon asymmetry while simultaneously proposing to explain the observed small (non-zero) masses of neutrinos and act as a potential dark matter candidate.

---

<sup>4</sup>The KRS mechanism proposes that at the high temperatures of the early Universe, transitions between gauge vacua can occur unsuppressed via thermal fluctuations, compared to the suppressed transitions from tunneling. These transitions can lead to anomalous non-conservation of baryon number.

<sup>5</sup>Recall the three families of neutrinos,  $\nu_e$ ,  $\nu_\mu$ ,  $\nu_\tau$ , in the Standard Model are all left-handed.

## *Chapter 2*

# THE UCNA EXPERIMENT

In this chapter, we present a broad-level overview of the Ultracold Neutron Asymmetry (UCNA) experiment. This experiment has been detailed extensively in theses [Men14; Bro18; Hic13] as well as being the experimental foundation for published results in [Men+13; Bro+18], and the references therein. We restrict ourselves to providing a high level overview in order to provide context for the analysis work in the remainder of this dissertation which focuses on novel measurements from the completed 2010-2013 UCNA datasets.

We start this chapter with a brief description of Area B at Los Alamos National Laboratory (LANL), where UCNA is located. We discuss briefly the production of ultra-cold neutrons (UCNs) at the UCN facility at LANL and their transport through various experiment components and laboratory infrastructure to the UCNA experiment (and other UCN experiments housed in the same location). We afford special attention to describing the different components of the UCNA experiment apparatus and in particular the main spectrometer. These components are discussed again at length in Chapter 3 when they are simulated in software. Finally, we close this section with a description of the intricacies of the data-taking structure with UCNA.

### 2.1 Overview of Experiment

The Ultracold Neutron Asymmetry experiment, or UCNA for short, was an experiment designed to measure the asymmetry parameter in the free neutron  $\beta$ -decay using ultra-cold neutrons (UCNs) (see section 1.3.2.1). The UCNA experiment located in Area B at LANL was a part of the Los Alamos Neutron Science Center (LANSCE). The work in this dissertation focuses on the UCNA experimental runs in 2010, 2011-2012, and 2012-2013 (the same datasets as in [Men14; Hic13; Bro18]). The main differences between each running year are the apparatus geometries and running conditions. They are described in more detail later in this chapter and as they become relevant in later analysis work.

At a summary level, the UCNA apparatus itself is effectively a spectrometer designed to measure the energy (primarily), position, and timing (secondarily) of neutron

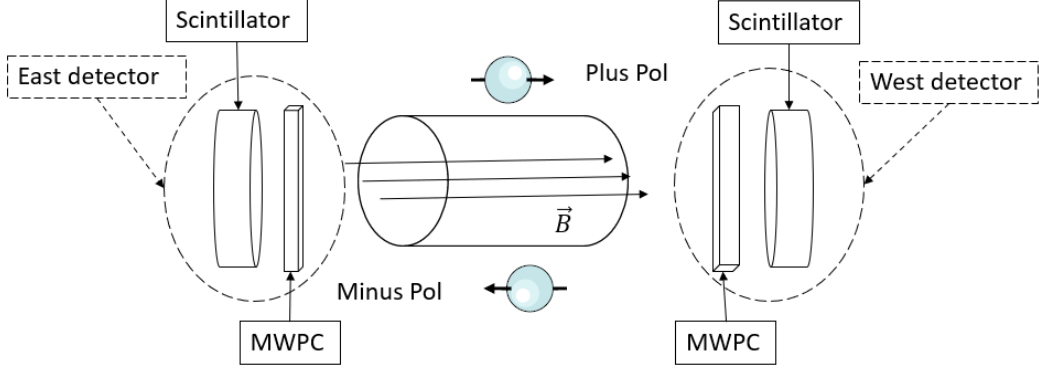


Figure 2.1: A simplistic diagram of the spectrometer components of the UCNA apparatus. The cylinder in the center is the decay trap and the polarized neutrons (represented as spheres) are nominally contained within the cylinder (here they are shown outside to simplify the visuals). The imposed magnetic field is along the axis of the decay trap, and the detectors are a pair of wirechambers and plastic scintillators (with other infrastructure that is not shown).

$\beta$ -decay electrons. Polarized UCNs are trapped in a central cylinder and held until they undergo  $\beta$ -decay. An imposed 1 T magnetic field directs the  $\beta$ -decay electrons outwards to detectors on either side, interchangeably called “East and West detectors” or “detectors 1 and 2”. Along the way to the detectors, the  $\beta$ -decay electrons pass through various experiment components which are described later in section 2.3. A simplistic diagram is shown in figure 2.1. In addition to the main spectrometer, we also discuss briefly the production of UCNs at LANL and their travel to the UCNA apparatus.

At the conclusion of the 2013 data-taking run, the UCNA experiment completed its final run. The most recent asymmetry data was analyzed and published in [Bro+18]. Afterwards, the apparatus was left untouched in Area B at LANL. There are proposals underway to restart the UCNA experiment after a hardware improvement which would be called UCNA+ [Sau18].

## 2.2 UCN Polarization and Transport: From Source to Experiment

The following sections briefly describe the UCN production at LANL and their transport to the UCNA apparatus. Schematics of the source and LANL infrastructure to UCNA can be found in figures 2.2 and 2.3 respectively.

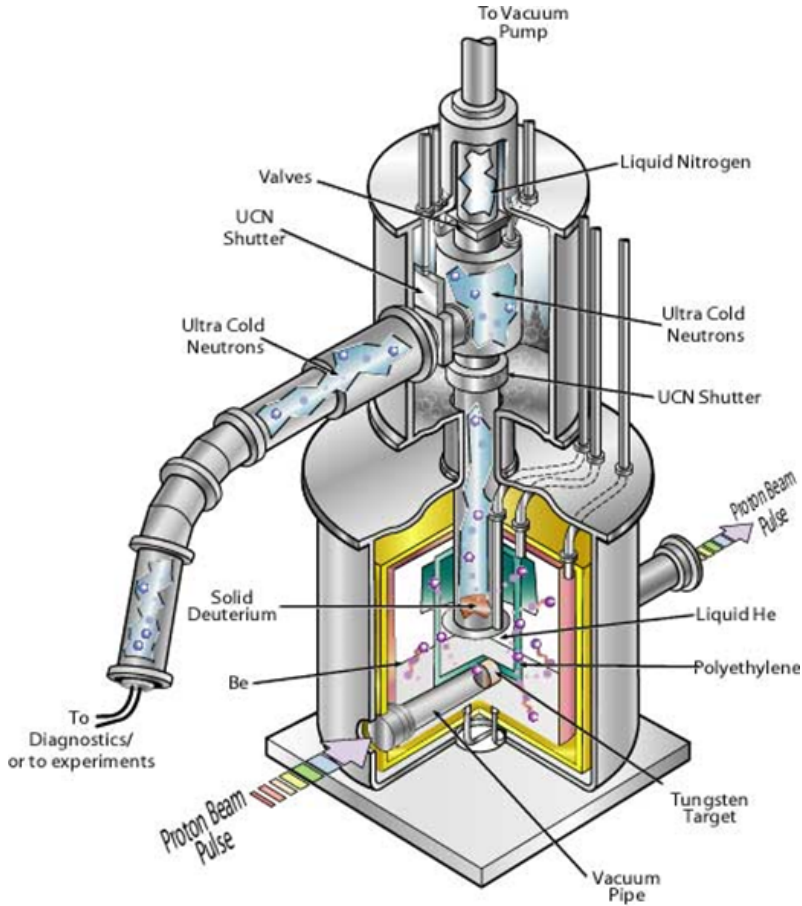


Figure 2.2: A schematic diagram of the UCN source. An incoming pulsed proton beam produces spallation neutrons which are moderated to cold temperatures through various moderators. Ultra-cold neutrons (UCNs) are produced after final interactions with Solid Deuterium ( $SD_2$ ). These UCNs travel 1 m upwards to further cool and are then sent downstream to UCN experiments. See text for additional details.

### 2.2.1 UCN Production at LANL

The UCN source at LANL is a Solid Deuterium ( $SD_2$ ) source. The basic foundational principles can be found in [Liu02], and the performance is characterized in [Sau+04; Sau+13]. In particular, [Ito+18] describes an upgraded version of the UCN source at LANL. Some of the relevant components of the source in this dissertation are discussed as well as a contemporary description of the upgraded source performance. We note that the contents of [Ito+18] do not reflect the source performance in this dissertation's work but rather add additional contemporary context for the LANL UCN source for future experimental work.

UCNs are produced by the LANL  $SD_2$  source via spallation (see section 1.2.3 for

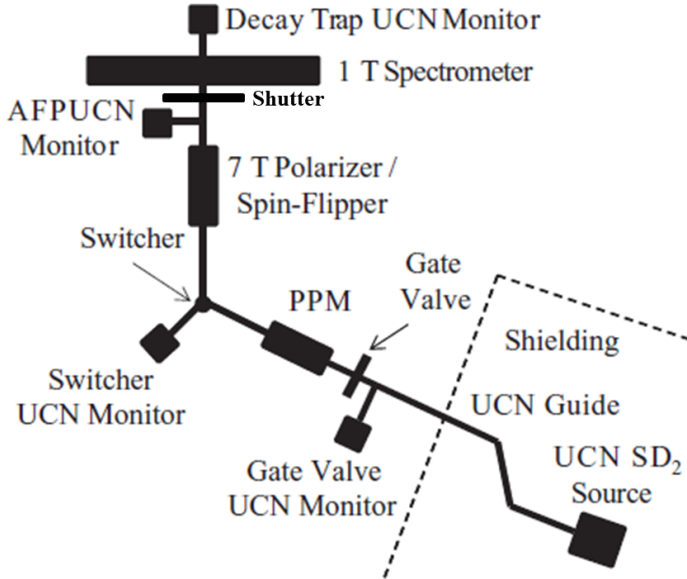


Figure 2.3: An overhead schematic diagram of Area B showing the UCN source, UCN infrastructure, and the UCNA experiment. In this schematic, the UCNs start in the bottom right at the “UCN  $SD_2$  Source” and travel to the upper left into the “1 T Spectrometer”. Key elements along the path of the UCNs are labelled and each are described further in dedicated subsections in the text.

general description). To achieve this, an 800  $MeV$  pulsed proton beam impinges upon a tungsten spallation target. Neutrons with energies  $\approx 20\ MeV$  are produced, moderated to room temperature, and directed towards the  $SD_2$  source. Beryllium reflector material (which redirects neutrons) surrounds the target in order to achieve a larger flux of neutrons directed towards the  $SD_2$  source. As the spallation neutrons travel towards the  $SD_2$ , a layer of polyethylene beads held at  $\approx 20\ K - 100\ K$  (via recycled gas from the  $SD_2$  cooling) will cool the neutrons to cold neutron (CNs) temperatures. The resulting CNs enter into a Nickel-58 coated UCN-reflecting volume (recall from table 1.1 that Nickel-58 has sufficient Fermi potential to reflect UCNs) that contains a few  $cm$  thick block of  $SD_2$  held at  $\approx 5.5\ K - 8\ K$ . As discussed in section 1.2.3, the  $SD_2$  moderates the CNs to UCNs with a temperature equivalent of  $\approx mK$ . Upon reaching a UCN state, optimized UCN rates are achieved by separating the UCNs from the  $SD_2$  source - in UCNA this is done via a Nickel-58 coated “trap door” that rests directly above the  $SD_2$  source (called the “flapper” internally). After the flapper, the UCN volume extends  $\approx 1\ m$  vertically in order to convert the kinetic energy gained by exiting the  $SD_2$  into gravitational potential energy. At the top of this  $\approx 1\ m$  pipe, the UCN guide pipes are fed outwards and begin their travel towards the UCN experiments housed away from the source.

These various components in the UCN source are shown in figure 2.2.

For the experimental runs discussed in this dissertation, the UCN yields were measured at the UCN guide exit just outside the shielding stack. A neutron capture on vanadium foil technique was used and benchmarked our UCN production densities at  $44 \pm 5 \text{ UCN}/\text{cm}^3$  [Sau+13]. In addition, as discussed above in section 2.2.1, [Ito+18] provides a more contemporary measurement of UCN source performance at LANL.

### 2.2.2 Exiting the UCN Source Volume

A short summary of the UCN transport is given below. Each component the UCNs interact with in the travel to the UCNA apparatus is discussed as well.

The initial vertical 1 *m* transport guides are stainless steel coated with Nickel-58 (Fermi potential of 342 *neV*). These guides are then connected to standard stainless steel (Fermi potential of 189 *neV*) horizontal neutron guides for transport through the biological shielding that surrounds the source towards the UCN experiment area. Within the UCN guide system, there are two 45° bends that remove neutrons in the interim energies between the higher energy Nickel-58 coating Fermi potential and the lower energy stainless steel Fermi potential [Pla+12]. These higher energy neutrons are deposited in the shielding. Upon exiting the biological shielding, the UCNs continue forward along the UCN guides to a gate valve. The geometry described above is shown in figure 2.3. The figure also shows all the remaining components that will be discussed in the subsequent sections.

### 2.2.3 Gate Valve and Pre-Polarizing Magnet

Beyond the biological shielding, the UCNs continue to travel along the stainless steel guides, passing through a gate valve. The purpose of the gate valve is to separate the UCNA apparatus volume from the source volume while the proton beam is on (and hence UCNs are being produced). This allows the experiment to take full background data with all nominal operations except with no UCNs transported into the UCNA volume. In a nominal data-taking run, the gate valve is left open and UCNs pass through with no interaction.

Beyond the gate valve is a 6 *T* pre-polarizing magnet (PPM). The PPM imposes a longitudinal field for the UCNs to polarize along and minimizes UCN losses when transporting through a Zirconium foil, located in the center of the magnet, which is in place to separate the vacuum of the UCN source from the vacuum of the rest

of the apparatus. The full details of the PPM can be found in [Hol12; Hol+12]. The separation of these volumes significantly reduces the amount of radioactive contaminants that can be transported into the UCNA experiment. Beyond the PPM, we have mostly polarized UCNs and must maintain this polarization for proper spin manipulation downstream (see section 2.2.5). As such, the UCN guides switch to non-magnetic materials such as electropolished copper.

Throughout the lifetime of the experiment, sections were replaced until the guides were primarily Diamond-like carbon (DLC) coated copper, which has a Fermi potential of 249 *neV* [Atc+07]. The production of DLC UCN guides and their resulting UCN transport is covered in [Mak05]. Further development of UCN guide coating, including the DLC copper UCN guides used in the 2010-2013 UCNA apparatus, is covered in [Mam10]. During the operation of the experiment in the 2010-2013 data-taking runs (this dissertation’s work), the guides were made of pure copper but the decay trap had been replaced with DLC-coated copper.

#### **2.2.4 Switcher for UCN Measurements**

After the PPM, the longitudinally-polarized UCNs move along the DLC-coated copper guides (again, chosen to maintain polarization). They then reach a “switcher” valve — a component that switches the passage of the UCNs. In nominal data-taking runs, the UCNs are directed by the switcher towards the UCNA apparatus. When the switcher is activated, the decay trap volume of the apparatus (section 2.3.1) is connected to a  ${}^3He$  UCN detector [Mor+09] for part of the polarimetry measurements.

#### **2.2.5 7 T Polarizing Magnet (AFP)**

After the switcher, the UCNs continue past a 7 *T* primary polarizing magnet, called the Adiabatic Fast Passage (AFP) spin flipper. The goal of this magnet is to produce a highly polarized population of UCNs for loading into the UCNA detector as well as performing spin flipping. The details of the AFP spin flipper can be found in [Hol12; Hol+12]. A summary of its performance is presented in [Men14; Bro18] as it pertains to the 2010, 2011-2012, 2012-2013 UCNA data-taking runs. After the AFP, the UCNs are guided into the main detector apparatus decay trap volume (section 2.3.1 and onwards). There, they are held until they undergo neutron  $\beta$ -decay, the discussion of which forms the remainder of this chapter. The total transit time until the first UCNs arrive when using the characteristic speeds in our experiment is several seconds.

We note that from 2011 onwards a shutter was installed between the decay trap and the guides that empty into the decay trap. This was to allow any residual neutrons in the coupling guides to empty into the decay trap before depolarization measurements [Dee19].

### 2.2.6 Neutron Polarization

Recall that the goal of UCNA is to measure the asymmetry of the neutron  $\beta$ -decay. This asymmetry exists along the magnetic moment of the neutron and the resulting direction of the  $\beta$ -decay electron. In order to have directionality, the incoming neutrons must be polarized. In the UCNA experiment, maintaining a high polarization fraction and properly characterizing depolarization is one of the topics in [Dee19] for the 2011-2012 and 2012-2013 datasets. For the previous data-taking runs, polarization is covered in [Hol12]. The relevant polarization details for the 2010, 2011-2012, 2012-2013 UCNA asymmetry analyses is presented in publications [Men+13; Bro+18].

In terms of performance, the UCNA experiment was able to achieve final polarization fractions given in table 2.1.

Year	Spin State	Value
2010	$< P >$	$\approx 0.995 \pm 0.005$
2011-2012	$P^-$	$0.9970 \pm 0.0030$
2011-2012	$P^+$	$0.9939 \pm 0.0025$
2012-2013	$P^-$	$0.9979 \pm 0.0015$
2012-2013	$P^+$	$0.9952 \pm 0.0020$

Table 2.1: Results for average polarization fractions for the datasets presented in this dissertation work. For the 2010 result, see [Men14]. For the 2011-2012, 2012-2013 results, see [Dee19; Bro18]. In the later years, we present polarization for spin-flipper off (-) and spin-flipper on (+) states.

## 2.3 The UCNA Spectrometer

The main UCNA spectrometer is where the bulk of the details of this chapter are focused. It is the topic of several in-depth discussions in [Pla+08; Pla+12; Pla+19] as well as theses that this dissertation is built upon such as [Men14; Bro18]. Some details of the different components of the UCNA spectrometer are necessary to understand the simulations (Chapter 3) and analyses (Chapters 4 and 5) covered in this dissertation. As such, each element is summarized in detail individually. A schematic of the UCNA spectrometer is given in figure 2.4.

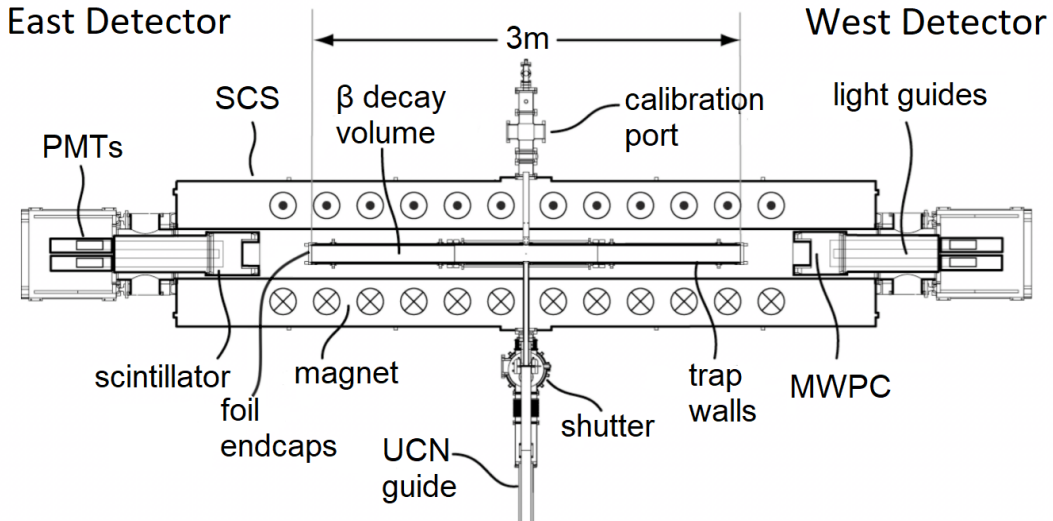


Figure 2.4: A top view cross-sectional schematic view of the UCNA experiment apparatus. In this schematic as shown, UCNs travel from the bottom of the diagram into the central  $\beta$  decay volume. Their decay products, specifically the electrons, are shaped outwards towards the East Detector and West Detector.

### 2.3.1 Decay Trap

In figure 2.4, the UCNs enter the central decay trap. Within the decay trap, the UCNs are held until they undergo free neutron  $\beta$ -decay. The details of the trap are presented in this section.

The decay trap is 3  $m$  in length, 12.4  $cm$  in diameter, and constructed out of electropolished copper (originally) and later DLC-coated copper (2010 onwards [Mam10]) which acts as a UCN reflector. The vacuum maintained in the decay trap was  $10^{-5}$  Torr during data-taking operation. The UCN density in the decay trap was measured via a  $^3He$  UCN detector located below a  $0.64\text{ cm}^2$  hole in the decay trap.

On the East and West sides of the decay trap are thin foils designed to contain the neutrons within the central volume (while allowing  $\beta$ -decay electrons to pass). The goal was to increase the UCN density and decay rate. These decay trap end caps (interchangeably called the decay trap windows) were different for the three data-taking runs 2010, 2011-2012, 2012-2013 and are discussed later in section 2.4. We note these year-to-year changes in the decay trap windows were one of the main drivers for choosing to separate the final analyses into three distinct dataset analyses.

Until now, we have focused on the UCNs from production, through transport, and ultimately into the decay trap for holding and decay. For the remainder of this

section, we shift our focus instead to the UCN  $\beta$ -decay products given in equation 1.4, specifically the electron, as they travel through the spectrometer. We note the proton is not tracked due to its very low kinetic energy, and the electron anti-neutrino is not tracked due to the negligible probability of identifying neutrinos in our apparatus.

### 2.3.2 Multi-Wire Proportional Chamber (MWPC)

When the neutron  $\beta$ -decay electrons are produced, they are directed outwards towards either the East or West detectors via the 1 T imposed magnetic field (described in section 2.3.4). After passing through the decay trap windows, the first major component the  $\beta$ -decay electron interacts with is the multi-wire proportional chamber (MWPC), occasionally termed the “wirechamber” in this work. The main details of the MWPCs are discussed in [Ito+07] and again in [Pla+12]. A basic summary of the geometry, technical settings, and advantages are given below in order to give the reader context for the MWPC utility in future chapters. Details relevant for the 2010-2013 data-taking runs are in [Men14; Bro18].

The wirechambers consist of two cathode “planes” (a plane of 64 parallel wires) arranged perpendicular to each other. The wires were gold-plated aluminum and were  $50 \mu m$  thick in the 2010 data-taking run and  $78.2 \mu m$  thick in the 2011-2013 data-taking runs. They are separated by  $2.54 mm$  from each other and cover a fiducial volume in the central decay trap of  $12.6 \times 12.6 cm^2$ . The two cathode planes are separated by  $1 cm$ . Within the center of the cathodes is an anode plane (wires oriented vertically) with  $10 \mu m$  diameter gold-plated tungsten wires. The entire wirechamber was nominally filled with 100 Torr neopentane gas ( $C_5H_{12}$ ), which provides high detection efficiency for the passage of charged particles. For some data-taking runs in 2012-2013, the neopentane gas ran out and isobutane ( $C_5H_{10}$ ) was used instead. The gas and wires are separated from the vacuum of the spectrometer apparatus by  $6 \mu m$  aluminized Mylar windows. The front window is reinforced with Kevlar strings located at  $5 mm$  intervals.

During operation, the MWPC provides additional signal measurements in UCNA. Charged particles passing through the MWPC ionize the gas within. A 2700 V potential difference is applied to the anode (cathodes held at ground) and the charged particles will drift under this potential difference towards either the cathode or anode plane. The integrated wire signals are read out and these signals provide a measure of energy deposited within the MWPC. Furthermore, charge deposition on the

wires provide position reconstruction for the passage of charged particles and allow the analyzers to make fiducial radial cuts on the decay trap. The perpendicular arrangements of the cathode planes yields horizontal-vertical positioning (X-Y in the UCNA coordinate system).

In addition to the fiducial position cut, the MWPC assists with other analysis decisions. Recall that the PMTs are located outside of the detector package and must use sets of 12 light guides to collect the scintillation light (discussed in section 2.3.3). The position reconstruction of the MWPC allows for corrections due to PMT/light-guide interactions. As well, the additional lower threshold energy deposition on the MWPC allows for more stringent event type classification (see section 2.4.4). Finally, the MWPC itself is highly insensitive to gamma rays - in the analysis, gamma ray suppression is greatly improved by using a coincidence trigger cut between the MWPC and plastic scintillator. This gamma ray suppression is utilized in section 4.3.3.7. Together with the plastic scintillator, the MWPC adds significant hardware and analysis advantages in our signal reconstruction, as we will see in further analyses in Chapters 4 and 5, as well as the original asymmetry analyses in [Men+13; Bro+18].

### 2.3.3 Plastic Scintillator

Just beyond the MWPC is the plastic scintillator which nominally converts all the kinetic energy of the  $\beta$ -decay electron into a detectable light signal [Pla+08; Pla+12]. In UCNA, a 15 cm diameter, 3.5 mm thick disk was used. The disk was “EJ-204”, made by Eljen Technology. The thickness was chosen to fully stop  $\beta$ -decay electrons up to the endpoint energy (782 keV). The diameter was chosen to cover the fiducial volume of the decay trap. The plastic scintillators on the East and West sides are each surrounded by 12 light guides which feed out  $\approx 1\text{ m}$  to four photo-multiplier tubes (PMTs) located outside the 0.6 T field (see section 2.3.4 for a discussion on field expansion). This was necessary since PMTs are not able to operate in fields as large as those in UCNA. Prior to 2010, UCNA used Burle 8850 PMTs. Afterwards, they were upgraded with Hamamatsu R7725 PMTs and custom-designed bases [Hic13]. A Bismuth-207 pulser gain monitoring system was added to each PMT and they are briefly discussed again in section 4.2.2.4.

### 2.3.4 Magnetic Field

In this section, we discuss the imposed magnetic fields in the UCNA apparatus. Within the decay trap, the UCNs that enter are polarized and thus aligned (or anti-

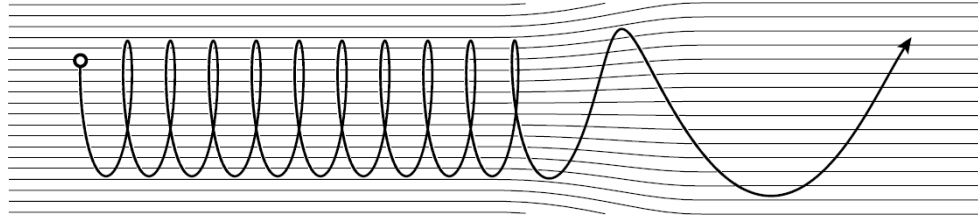


Figure 2.5: Simple schematic of an electron’s trajectory in an expanding magnetic field [Men14], describing the path of the UCN  $\beta$ -decay electrons in UCNA as they traverse from a 1  $T$  field region to the 0.6  $T$  field region at the detectors.

aligned) with the imposed magnetic field. This magnetic field was 1  $T$  in magnitude and oriented along the axis of the decay trap. This field profile was designed to direct the  $\beta$ -decay electrons from the UCN decay towards detectors on either East or West side, giving  $\approx 4\pi$  angular acceptance of  $\beta$ -decay electrons. The magnetic field was a uniform 1  $T$  within the decay trap, and smoothly changed to 0.6  $T$  outside of the decay trap windows prior to the MWPCs. This reduction in field strength increases the Larmor radius of the spiralling  $\beta$ -decay electrons and allows the electron to impinge upon the wire chamber and plastic scintillator at more normal angles, reducing the probability of backscattering (discussed in section 3.5.1).

In reality, there were small magnetic field distortions away from the described smooth transition. The measurements and characterization of such field distortions in the apparatus can be found in [Men14; Bro18]. When simulating these fields in Chapter 3, the field with no distortions was used. Previous theses studied the effects of these small field distortions in simulation.

### 2.3.5 Calibration Sources

Throughout the course of the data-taking runs, regular calibration runs were taken. The calibration runs consisted of using conversion electron sources<sup>1</sup>. In this dissertation, we worked with Cerium-137 ( $^{137}Ce$ ), Tin-113 ( $^{113}Sn$ ), and Bismuth-201 ( $^{207}Bi$ ). These corresponded to conversion electron peaks at energies 130 keV ( $^{137}Ce$ ), 368 keV ( $^{113}Sn$ ), 496 keV ( $^{201}Bi$ ), and 994 keV ( $^{201}Bi$ ). Additional calibration runs were taken with  $^{109}Cd$ ,  $^{114m}In$ , and  $^{137}Cs$  but ultimately not used in the final analysis. The calibration sources were chosen to utilize fixed energy electrons that spanned the kinetic energy range of the neutron  $\beta$ -decay electrons.

---

<sup>1</sup>A conversion electron is an emission electron that occurs when an excited nucleus de-excites. The excited nucleus interacts electromagnetically with an orbital electron. That electron is emitted from the bound nuclear system.

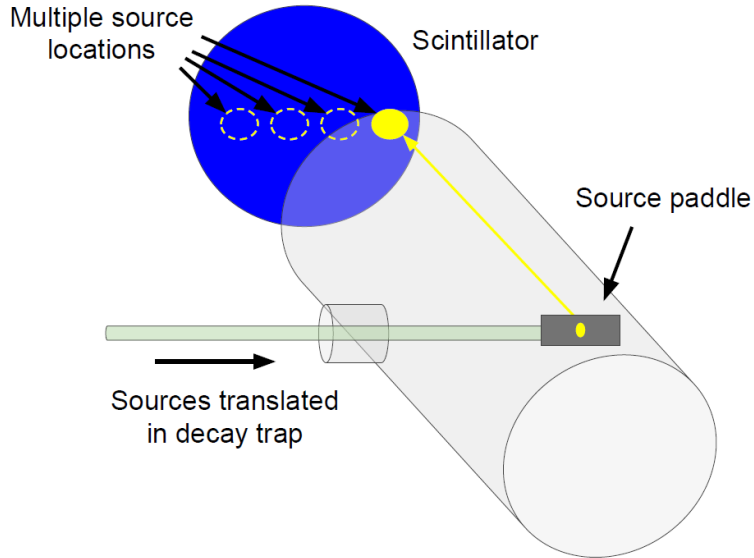


Figure 2.6: Simple schematic of the scintillator calibration [Bro18]. A paddle which holds the calibration sources is inserted into the decay trap while under vacuum. The paddle is translated in the shown horizontal direction across the region of the scintillators. At fixed locations, the paddle is held still and a calibration run is taken.

Calibration runs were taken by inserting a paddle into the decay trap with the calibration source placed in the paddle. This set-up is shown in figure 2.6. The calibration runs were taken periodically throughout the calendar year. Due to the manual nature of the source calibrations, it was up to the on-shift experimenter’s ability to perform high-quality, repeatable calibrations. In the data-taking sequence, the octets (defined in section 2.4.5) are calibrated according to the calibration period that preceded them chronologically.

### 2.3.6 Xenon Mapping

Starting in the 2010 data-taking run (and hence relevant for the work in this dissertation), an additional calibration method was used which utilized neutron-activated Xenon. This gaseous Xenon would fill the volume of the UCNA decay trap and provide position-dependent energy responses for the entire detector fiducial volume. These activated Xenon runs were used to extract position-dependent energy responses that are later folded into the detector response model in downstream analyses. Additional details for the position maps in these datasets can be found in [Men14; Bro18].

### 2.3.7 Supplemental Components

There are additional components surrounding the detector package. Some of these are present in the simulations described in Chapter 3 as additional material in order to account for multi-scattering effects. Surrounding the apparatus are a collection of detectors that register cosmic muons. One of these is an argon/ethane sealed drift tube system, originally described in [Rio+11], attached to the spectrometer around the sides. A second set of “backing vetos” sit behind the plastic scintillators. Since the plastic scintillator nominally fully stops  $\beta$ -decay electrons, coincidence signals in the muon vetos allow for discrimination against events that travel through the entire detector package on axis. These additional flags help discriminate electron-like events which did not originate from neutron  $\beta$ -decay and are used in later analyses, most notably in Chapter 5.

## 2.4 Data-Taking Runs

The data-taking runs for UCNA can be roughly grouped by the years during which the data was taken. This corresponds to different beam on cycles at LANL. Throughout this dissertation, each dataset is distinguished by their year: 2010, 2011-2012, 2012-2013. The principle differences are the decay trap geometries and are explicitly discussed below.

### 2.4.1 2010 Dataset

The 2010 data-taking run was the original operating configuration of UCNA in production mode for the work in this dissertation. The principle measurement was the neutron  $\beta$ -decay asymmetry, described in publication [Men+13] and forms the thesis work of [Men14]. Internally, this dataset was called the “thick window” dataset, referencing the thicker decay trap windows compared with later 2011-2012, 2012-2013 data-taking runs. The 2010 data-taking run had 700 nm Mylar windows with a 300 nm Beryllium coating. These thicker windows lead to larger backscattering corrections and the 2011-2012 operating goal was to improve these corrections (and associated uncertainties) by lowering the backscattering ratio.

### 2.4.2 2011-2012 Dataset

The 2011-2012 data-taking run included upgrades in the apparatus with notably the thinner decay trap windows: 500 nm Mylar on both East and West ends, with 150 nm coating of Beryllium. We note that the 2011-2012 dataset asymmetry analysis (and subsequent 2012-2013 analysis) are covered in publication [Bro+18] and the topic

of thesis [Bro18].

### 2.4.3 2012-2013 Dataset

The 2012-2013 data-taking run had 130 nm (East) and 180 nm (West) windows made of 6F6F material [Hoe03], coated with 150 nm of Beryllium. The asymmetric windows were designed to allow different fractions of  $\beta$ -decay electrons to pass through and hence allow for studies of various systematic effects for different window thicknesses. In addition, during the 2012-2013 run, one of the Bismuth-207 gain monitors on the West detector PMTs was non-operational. This led to a reduced quality in the gain monitoring and hence the energy reconstruction. This is discussed again in section 4.2.2.4.

### 2.4.4 Event Types

Within the UCNA apparatus there are various materials that the  $\beta$ -decay electrons can interact with from their point of origin (within the decay trap) to their destination (fully stopped in the plastic scintillator). Each material boundary gives a non-zero probability of interaction and, in particular, changing the momentum direction of the  $\beta$ -decay electron. This is a systematic effect that must be carefully studied since misidentification of event types can change the measured asymmetry decay rates [Men+13; Bro+18], distort the energy spectrum (Fierz interference, Chapter 4), or introduce unphysical triggers (dark matter decay, Chapter 5).

Figure 2.7 shows a diagram of the various event types present in the UCNA detector. As described in [Pla+19] (and others), the event types used in the asymmetry analyses and propagated into the work in this dissertation are type 0 (single trigger, no backscatter), type 1 (double trigger), types 2 and 3 (single trigger with a MWPC scatter). The different geometries in the different data-taking runs yield different event type fractions. The population fractions of each event type is given in table 2.2 [Bro18].

We highlight this section on event types because their individual classifications are quite relevant for the analyses in this dissertation. In the asymmetry analysis, the different backscattering ratios are a significant contribution to the systematic error [Men+13; Bro+18]. In Chapter 4, Fierz interference, we discuss the necessity of a robust energy calibration: proper event classification yields different energy calibrations for each event type and must be properly accounted for. In Chapter 5, dark matter decay, we require a robust Type 1 classification for the potential dark matter decay identification. All of this is to emphasize the value of proper event

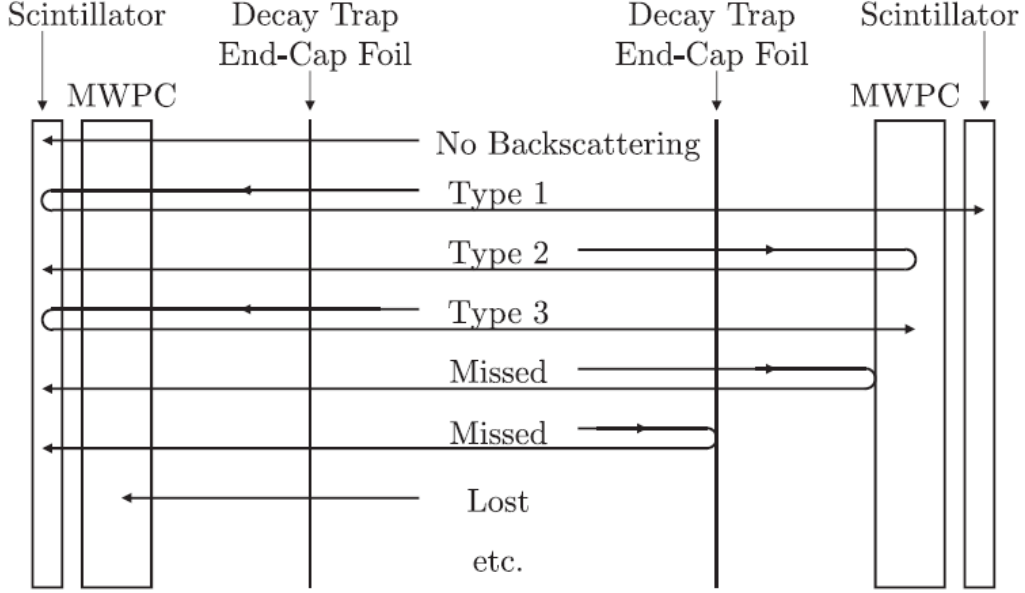


Figure 2.7: A schematic diagram of various  $\beta$ -decay electron events in the UCNA apparatus [Pla+12]. Several combinations of events are used in the subsequent analyses. Internally, the “no backscattering” events were often termed “Type 0”.

Event Type	Fraction of Detected
No Backscatter (Type 0)	94.4%
Type 1	3.3%
Type 2	1.1%
Type 3	1.2%

Table 2.2: Final event type fractions for detectable event types in the UCNA detector. Taken from the final 2011-2012, 2012-2013 datasets used in the asymmetry analysis. There are similar fractions for event types in the 2010 dataset. Event types that are not categorized as Type 0, 1, 2, 3 are not detected.

identification carried through the subsequent work on UCNA data, even several years after the fact in the novel dark matter decay analysis.

#### 2.4.5 Octet Structure

In this section, we discuss the data-taking sequence in the operation of the UCNA experiment. In particular, we detail the choices in the run sequences in the context of minimizing potential errors in the calibrations. The sequence of events is given in table 2.3. This particular run sequence cancels all linear drifts in background rates [Pla+12] and hence provide additional robustness against systematic effects.

The three main types of runs are:  $\beta$  - beta decay runs,  $B$  - background runs,  $D$  -

depolarization run. The beta decay runs are the conventional runs where UCNs are loaded into the decay trap and the  $\beta$ -decay electrons are detected and recorded by the spectrometer. The background runs are when the gate valve (section 2.2.3) is closed but otherwise all operations are normal. The background runs are  $\frac{1}{5}^{th}$  the run time of the foreground runs in order to optimize the signal-to-noise ratio for the asymmetry extraction. The depolarization runs are used to measure the polarization fraction of the UCNs loaded into the decay trap and are performed at regular intervals since they are directly part of the formula for the asymmetry extraction (shown in equation 1.13).

A1	A2	A3	A4	A5	A6	A7	A8	A9	A10	A11	A12
$B^-$	$\beta^-$	$D^-$	$B^+$	$\beta^+$	$D^+$	$\beta^+$	$D^+$	$B^+$	$\beta^-$	$D^-$	$B^-$
B1	B2	B3	B4	B5	B6	B7	B8	B9	B10	B11	B12
$B^+$	$\beta^+$	$D^+$	$B^-$	$\beta^-$	$D^-$	$\beta^-$	$D^-$	$B^-$	$\beta^+$	$D^+$	$B^+$

Table 2.3: Run structure for the octet data-taking sequence, consisting of A and B type quartets. Table taken from [Pla+12].  $\pm$  refers to spin state: + is spin flipper on and – is spin flipper off.  $\beta$  is regular  $\beta$ -decay runs, B is background runs, and D is depolarization runs.

The chosen octet structure provides additional safeguards against linear order systematic drifts. These pose a challenge in Chapter 4, Fierz interference, and warrant further discussion (see section 4.3.1.1). In particular, analyses on the UCNA datasets can be integrated (full year’s dataset together) or split octet-by-octet. Throughout this dissertation and the course of the actual analysis, both were often used to illustrate and characterize systematic effects in the data.

### *Chapter 3*

## UCNA SIMULATIONS

In this chapter, we discuss the re-implementation of the UCNA spectrometer apparatus into the GEANT4 simulation software package. This work primarily builds upon the simulations used in [Men14] but with some key changes for the updated UCNA geometries and subsequent data analyses. The 2011-2013 geometries are discussed previously and a complete summary of changes is given in [Bro18]. In particular, for the analysis work in this dissertation, additional parameters of interest were generated, simulated, and recorded (described in later sections in this chapter). This led to a recreated simulation with similar simulated geometry (with minor changes to track the real detector upgrades), updated input kinematics, updated input physics, and a new programming architecture.

We note that a GEANT4 simulation existed of the UCNA apparatus which was developed for the previous asymmetry analysis in [Men14]. However, the particular simulation implementation was greatly entangled with the rest of the analysis pipeline and hence primarily targeted towards assisting an asymmetry extraction. In order to perform the analyses in this dissertation, a conscientious decision was made to recreate the simulation in order to have a stand-alone UCNA detector simulation that could be interrogated at different stages relevant for our work. The previous UCNA simulation developed in [Men14] was used as a guide and relevant output parameters were benchmarked with previous simulation outputs along the way.

The main reason for using such a detailed GEANT4 simulation are for comprehensive systematic uncertainty studies. In the original UCNA experiment, the experiment was designed so that the extraction of the asymmetry (the original quantity of interest) would be limited by statistical error<sup>1</sup>. However, the analyses in this dissertation, namely Fierz interference (Chapter 4) and dark matter decay (Chapter 5), were not the original design goal of UCNA. Instead, they are supplementary analyses using the same UCNA datasets and, as such, were oftentimes limited by systematic errors. Thus, the GEANT4 simulation became the major tool available to study the systematic uncertainties, primarily in the spectral extraction of the

---

<sup>1</sup>In any good experiment design, the goal is to be limited by statistical errors. The experimenter always wants to control the systematic errors so that they are subdominant.

Fierz interference (section 4.2), the first analysis, chronologically, presented in this dissertation.

### 3.1 GEANT4: A Particle Tracking Software Package

For this work, a simulation of the UCNA detector programmed in GEANT4 was used. GEANT4 stands for “GEometry ANd Tracking (*4<sup>th</sup>* version)” and is a software library for the simulations of particles traveling through and interacting with fields and materials. It is provided in C++ and maintained by the GEANT4 collaboration [Ago+03].

At a high-level, GEANT4 uses Monte Carlo methods to track various physical effects on a particle as that particle travels through a simulated environment of materials and fields. At each step throughout the geometry, a list of physics processes are sampled given the particle’s species and kinematics. The relevant properties of the particle are changed based on which physics processes occur, secondary particles are created and tracked, and the primary particle moves to the next step in the simulated volume. In this work, the primary application of the GEANT4 simulation was to recreate an accurate representation of the UCNA apparatus and to track  $\beta$ -decay electrons within the apparatus. In particular, we were interested in extracting physical quantities such as energy deposited, position, and timing of  $\beta$ -decay electrons stopping in a scintillator volume. All of these parameters can be cross-checked in simulation against their input kinematics and a “true” efficiency can be extracted. This is a key functionality of the simulation used in the analyses described in Chapters 4 and 5.

We note that in the previous asymmetry analysis [Men14], a separate PENELOPE simulation was used. PENELOPE stands for ‘Penetration and ENergy LOss of Positrons and Electrons’ [Age19]. The results of the GEANT4 simulation and PENELOPE simulation were benchmarked against each other and consistent. At Caltech, the main effort (and expertise) was on the GEANT4 simulation and hence the GEANT4 simulation was retained and utilized in this work.

### 3.2 ROOT: A Data Analysis Software Package

ROOT is a data analysis software package. The details, manuals, and code can be found in [Teaa] and we provide a short summary description here to preface the ROOT-generated figures and fitting performed in later Chapters.

ROOT is a series of C++ libraries that are commonly used by high-energy physicists for data processing and statistical analysis. Its main utility in this dissertation is pro-

viding standard and customizable statistical analysis on data which was formatted for ROOT libraries, as well as data visualizations (generally in the form of histograms). ROOT provides functionality in the form of C++ Object Oriented Programming (OOP) for data pre-processing [Men14], fitting (section 4.2.1.2), and visualization (Chapters 4 and 5). ROOT is ubiquitous in the high-energy physics community and its characteristic ROOT-generated figures appear throughout the remainder of this dissertation.

### 3.3 The UCNA Apparatus in Simulation

In any GEANT4 simulation, there are three minimum essential components: a detector construction class, a physics list, and a primary generator action. These three components (or “objects”, in the language of C++ OOP) describe a minimum functioning simulation where a simulated volume is created with some components, a particle is created with some species information and initial kinematics, and a series of physics processes that the particle may undergo is defined. With these definitions, any GEANT4 simulation can execute. However, with only these definitions, there is no sensible way to read out the simulation output. In the subsequent sections, we will detail the implementation of these three classes and additional classes used to extract information from the simulation (what we occasionally call “interrogation”).

#### 3.3.1 Detector Construction Class

The detector construction is the first of three essential classes required for any GEANT4 simulation. Within the detector construction class, all the geometry elements and electromagnetic fields must be placed. This consists of shapes, sizes, locations, materials, and field strengths. For example, in the UCNA simulation, key elements described in the preceding section 2.3 such as the decay trap, MWPCs, plastic scintillators, etc. must be defined and placed in a simulated volume here. With all the components placed, the final simulated geometry can be seen in figure 3.1.

Within the detector construction class, a global volume<sup>2</sup> is defined and the geometry elements are placed. There are additional commands implemented to tune simulation parameters such as pre-set detector geometries, vacuum pressure, running with the calibration source holder, using calibration sources, and so on. These commands

---

<sup>2</sup>All GEANT4 simulations must execute in a volume called the “world” volume. This is the outer boundaries of the physics simulation space. For our simulation, the boundaries of the simulation are set at  $\pm 1$  m in x,y and  $\pm 4$  m in z.

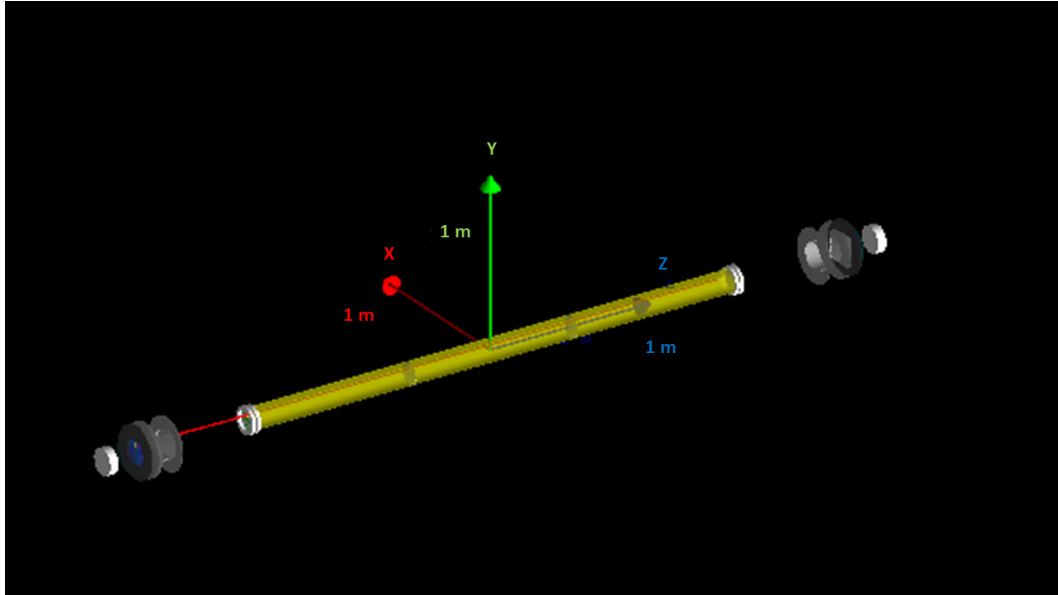


Figure 3.1: An off-axis screen shot of the generated GEANT4 simulation of the UCNA apparatus. Visualization is implemented via QT visualization drivers. The standard detector construction geometry is shown with one electron simulated. There is an imposed magnetic field across the entire detector and electric fields within the wirechambers (section 3.3.1.5). See text for details on each simulation element. A Cartesian coordinate axis is included at the simulation volume origin.

helped with automation of previous systematic studies in the  $A$  analysis but were not necessary and generally omitted in the targeted studies described in this work.

Within the detector construction classes, we define several materials. These materials are created here and accessed in other classes to construct user-defined materials for the different apparatus elements. The materials and their programmed property summaries can be seen in table 3.1.

### 3.3.1.1 Decay Trap

The decay trap in UCNA is described in section 2.3.1. Here we provide a brief overview of the implementation in simulation. In figure 3.1, the decay trap is represented by the yellow tube that spans the origin along the z-axis. In the simulation, the decay trap is a 3 m long, 2.45 inch in radius, tube of copper with 300 nm Beryllium-coated 700 nm Mylar windows on either side. These window thicknesses are changed for each datasets corresponding geometry which was discussed in section 2.4. Polyethylene collimators are implemented and the entire decay trap is positioned at (0, 0, 0), aligned along the z-axis in the simulation coordinate system.

Material	Composition	Density [g/mol]	Density [g/cm <sup>3</sup> ]
Hydrogen	Z=1	1.0079	
Carbon	Z=6	12.0107	
Nitrogen	Z=7	14.0067	
Oxygen	Z=8	15.9994	
Fluorine	Z=9	18.9984	
Aluminum	Z=13	26.9815	
Chromium	Z=24	51.9961	
Iron	Z=26	55.845	
Nickel	Z=28	58.6934	
Copper	Z=29	63.55	
Zinc	Z=30	65.39	
Beryllium	Z=4	9.01	1.848
Aluminum	Z=13	26.98	2.7
Silicon	Z=14	28.09	2.33
Copper	Z=29	63.55	8.96
Tungsten	Z=74	183.84	19.3
Gold	Z=79	196.97	19.3
Brass	0.7Cu + 0.3Zn		8.5
Stainless Steel 304	0.7Fe + 0.2Cr + 0.1Ni		8.03
Kevlar	$N_2C_{14}H_{10}O_2$		1.44
Mylar	$C_5H_4O_2$		1.4
Polyethylene	$C_2H_4$		0.95
6F6F	$N_2C_{34}H_{14}O_4F_{12}$		1.48
Pentane Gas	$C_5H_{12}$		Pressure = 100 Torr
Nitrogen Gas	$N_2$		Pressure = 95 Torr
Scintillator	$C_{4.68}H_{5.15}$		1.032

Table 3.1: List of user-defined materials used in the UCNA apparatus simulation in GEANT4. Molar densities and volume densities are not provided for every material because they are not necessarily needed to define the material in GEANT4. Aluminum and Copper are defined twice because the top section is elements and the remaining three sections are materials — GEANT4 treats them differently. The gases use the nominal fill pressures and the plastic scintillator is given by the Eljen EJ-204 datasheet (see section 2.3.3 for more details).

The perceptive reader will notice two off-yellow disks located within the decay trap at  $\pm 0.5$  m along the z-axis. These are called “trap monitors” and they are volumes of vacuum (consistent with the rest of the decay trap) where we designate GEANT4 to read out the kinematic variables. These have no physical correspondence to the real experiment. They are purely a simulation artefact used for in-trap monitoring and, crucially, backscattering identification and studies. This is the first of several advantages we note in utilizing a full GEANT4 simulation of the UCNA apparatus.

### 3.3.1.2 Wirechamber (MWPC)

The multi-wire proportional chamber (MWPC) used in the UCNA experiment was discussed in section 2.3.2. In the simulation, the MWPCs were constructed separately and placed separately for the East and West detectors. The MWPCs use Mylar windows with 32 Kevlar strings (spaced 5  $mm$  apart) to contain the Neopentane fill gas at 100 Torr pressure and 298  $K$  temperature. The cathode planes are made with Aluminum wires and separated by 1  $cm$ . An anode plane is made with Tungsten wires, placed in between the cathode planes, and a 2700  $V$  potential difference is applied. The MWPC can be seen in figure 3.1 as a grey rectangular box at  $\approx +2\ m$ .

### 3.3.1.3 Plastic Scintillators

The plastic scintillators used in UCNA were discussed in section 2.3.3. In the simulation, the plastic scintillators were constructed and placed separately for the East and West detectors, as with the MWPCs. They were disks of radius 7.5  $cm$ , thickness 3.5  $mm$ . Again, these dimensions were chosen to cover the fiducial volume of the decay trap and fully stop any neutron  $\beta$ -decay electron within the material. The plastic scintillators can be seen in figure 3.1 as the blue circular disk at  $\approx -2\ m$  along the z-axis. A dead layer of 3  $\mu m$  was implemented, where energy deposited in the dead layer is “lost” and not recorded as the energy deposited in the scintillator. The dead layer was studied and chosen to match energy loss studies, as discussed in [Men14].

A few other geometry components are also simulated. A backing veto (10  $cm$  radius, 1 inch thickness) is placed behind the plastic scintillator. The backing veto is designed to discriminate external particles. However, in the context of the simulation where only one primary particle is created and tracked at a time, the backing veto exists to more faithfully reproduce the UCNA detector geometry, specifically in case of multiple scatterings off materials that eventually reach the plastic scintillator (and hence the read-out). In addition, 12 light guides are placed outside the plastic scintillator volume to mimic the real detector.

Eljen Technologies was commissioned to create the plastic scintillator material used in the experiment. The datasheet can be found under EJ-204. The details of the material are reproduced in the GEANT4 material simulation (see table 3.1).

### 3.3.1.4 Detector Package Frame

The detector package frame consists of the housing, additional shielding, and mechanical infrastructure that holds the plastic scintillator (section 3.3.1.3) and MWPC (section 3.3.1.2) in space. They are simulated due to their potential for interactions with  $\beta$ -decay electrons on the way to the plastic scintillators. There are some collimators (Aluminum), an exit window (Aluminum again), a nitrogen ( $N_2$ ) gas box, and additional material behind the detectors (Stainless Steel 304). All of these materials were summarized in table 3.1.

### 3.3.1.5 E&M Fields

Within the simulation, there are two main fields that are implemented: the global magnetic field and the electric fields within the MWPC active regions.

The global magnetic field is 1  $T$  within the central decay trap region and 0.6  $T$  by the time it reaches the MWPC, with a smooth interpolation in between. This magnetic field profile was designed in order to minimize the backscattering effects at the MWPC and plastic scintillator faces by changing the  $\beta$ -decay electron momentum so that they impinge along a more normal angle. The effect of such a field on the  $\beta$ -decay electron trajectory is shown in figure 2.5. Within the code, the overall field is implemented via the class GlobalField. The  $z$ -axis location defines the position, and the field strength is given by:  $z = \pm 1.5 \text{ m}$ ,  $B = 1.0 \text{ T}$ ;  $z = \pm 2.2 \text{ m}$ ,  $B = 0.6 \text{ T}$ ;  $z = \pm 3 \text{ m}$ , the field is 0.6  $T$ . The GEANT4 library smoothly interpolates the field in between the user-defined points. We note that additional work was done on magnetic field profile variations in the  $A$  analysis, the details of which can be found in [Men14]. However, the minor variations in the field as given by field map data did not produce an appreciable difference in the measured energy spectra and detection efficiencies. Hence, the more rudimentary field profile was taken in this re-implemented version of the GEANT4 simulation.

The MWPC active region fields were implemented via a separate class called MWPCField. This defines an electric field generated from a 2700 V potential difference set between the anode and cathode planes in the MWPC. We note within the MWPCField region, the same global magnetic field is applied to ensure continuity in the simulated volume. The electric fields are placed in the detector construction class within the MWPC region.

### 3.3.2 Physics List Class

The physics list class is the second of three necessary classes in order to run a minimal GEANT4 simulation. This class defines the physics processes that a particle may experience as they are transported through our simulated geometry. In the original GEANT4 simulation, PENELOPE and standard GEANT4 physics lists were used for comparison. However, in the studies in this dissertation, only the standard Livermore electromagnetism (EM) physics list was used. The package used was called G4EMLivermorePhysics. In addition, pre-defined particles such as gamma rays (called G4Gamma), electrons (G4Electron), and positrons (G4Positrons) were used. The details of the physics list can be found in [Men14] and references within.

### 3.3.3 Primary Generator Action Class

The primary generator action is the third, and last, of three necessary classes in order to run a GEANT4 simulation. In the original implementation of the GEANT4 simulation, the primary generator action defined the weak interaction  $\beta$ -decay kinematics, sampled the functional form, and selected energies and momenta all within the GEANT4 implementation class while performing random sampling, function generation with ROOT. Since the program executed them together, this was difficult to disentangle and make modifications. Hence, in a re-implementation of the simulation, all particles that will be simulated in GEANT4 have their initial kinematics read in from an external file. The kinematics in that file are generated separately in ROOT with probabilistic sampling and the various form factors that are characteristic of neutron  $\beta$ -decay. The initial kinematics and final read out components of the GEANT4 simulation are all printed to the same file for post-processing analysis. These simplified implementations allowed us to perform significantly more informative studies, which we illustrate in this section and later in Chapter 4.

Furthermore, we note that a separate implementation was written to simulate the different gamma rays and conversion electron decays for the calibration sources described in section 2.3.5. The calibration was generated separately in the asymmetry analysis [Bro18] and ultimately this component of the simulation was not used.

#### 3.3.3.1 Initial Kinematics Generation

A valuable development in the simulation and data analysis pipeline was gaining access to and modifying the input  $\beta$ -decay electron kinematics. During the re-implementation process, we identified a method to separate out the input kinematics

generation and hence make systematic studies on modified input kinematics when propagated throughout the overall GEANT4 simulation.

This was done by utilizing C++ code from the original simulation that created the different physical form factors and performed an accept-reject Monte Carlo sampling procedure to recreate the initial energy spectrum of the  $\beta$ -decay electrons. This code was separated from the GEANT4 simulation and instead written as stand-alone C++ code that outputted the event kinematics. The events were subsequently loaded into the GEANT simulation and simulated on an event-by-event basis. Critically, with this separation, we were able to implement a non-zero asymmetry term and a non-zero Fierz term in our simulations and hence perform systematic studies.

There are several physical corrections to the leading-order weak interaction neutron  $\beta$ -decay form factor. The physics of these corrections is covered in [Men14]. Here, we list the different form factors used in the initial  $\beta$ -decay electron kinematics generation and the associated references. These functions were taken from the previous implementation of the UCNA GEANT4 simulation.

1. The Coulomb Fermi function. Termed Wilkinson's  $F_0$  in [Wil82; Wil89; Wil90; Wil93].
2. Non-zero charge radius correction. Parametrized as  $L_0$  in [Wil90].
3. Electron-nucleon non-zero size wavefunction convolution. Called VC and AC in [Wil90].
4. Coulomb effect on recoil corrections. Termed  $Q$  in [Wil82].
5. Outer radiative corrections. Termed  $g\alpha/2\pi$  in [Wil95].
6. Recoil corrections and weak magnetism for the free neutron [Bil+59].

Upon successfully porting over these functions, we are able to make modifications to our initial kinetic energy spectrum for  $\beta$ -decay electrons. In this dissertation, we introduce a non-zero asymmetry term and non-zero Fierz term as follows:

$$P(E_K, \theta) = \Gamma_{b=0}(E_K) + \langle P \rangle A_0 \Gamma_{b=0}(E_K) + b \Gamma_{b \rightarrow \text{inf}}(E_K) \quad (3.1)$$

where  $P$  on the left-hand side is the probability density function,  $E_K$  is kinetic energy of the  $\beta$ -decay electron,  $\Gamma$  is the Standard Model form factor with  $b$  terms included,

$\langle P \rangle$  is the spin state (a proxy for the polarization and chosen to be  $\pm 1$ ), and  $A_0$  is the Particle Data Group (PDG) value of the asymmetry term (-0.1184, as of the year 2015). There is an implicit normalization in the right-hand side of equation 3.1 since we sample a fixed number of events. In the original implementation of the simulation, only the first term on the right-hand side was accessible.

In the Fierz-only studies described in later chapters, the introduction of a non-zero  $b$  term and averaging over the two different spin states reduces equation 3.1 to (with an appropriate normalization since the event generation is for a fixed number of events)

$$\Gamma_b(E_e) = \left(1 + b \frac{m_e}{E_e}\right) \Gamma_{SM} \quad (3.2)$$

In the new implementation of these initial  $\beta$ -decay electron kinematics, comparison spectra with the previous kinematics were generated and shown in 3.2. The residuals are also plotted and show consistency between this new methodology and the event generation in the previous asymmetry analysis in [Men14]. This consistency check allowed for confident modifications to the spectra that provided additional utility in the simulations that followed. The main modifications are the introduction of an asymmetry term (figure 3.3) and a Fierz interference term (figure 3.4). In particular, the introduction of the Fierz interference term was invaluable in the extraction of a Fierz interference measurement via the spectral method, section 4.2.

### 3.3.4 Particle Tracking Classes

The remainder of this section on the GEANT4 simulation discusses the non-essential tracker classes. These classes allow the user different access points into the simulation in order to interrogate various physical parameters from the simulation. We use the initial kinematics set in section 3.3.3, propagate it through the detector geometry set in section 3.3.1, and subject it to physics processes set in section 3.3.2. In the subsequent sections, we start with the broadest level of particle tracking and move towards finer grain tracking towards the end. We note that in these various classes, there are potential redundancies where multiple classes may interrogate the simulation for the same physical quantity — we illustrate where our particular simulation chooses to output stored quantities.

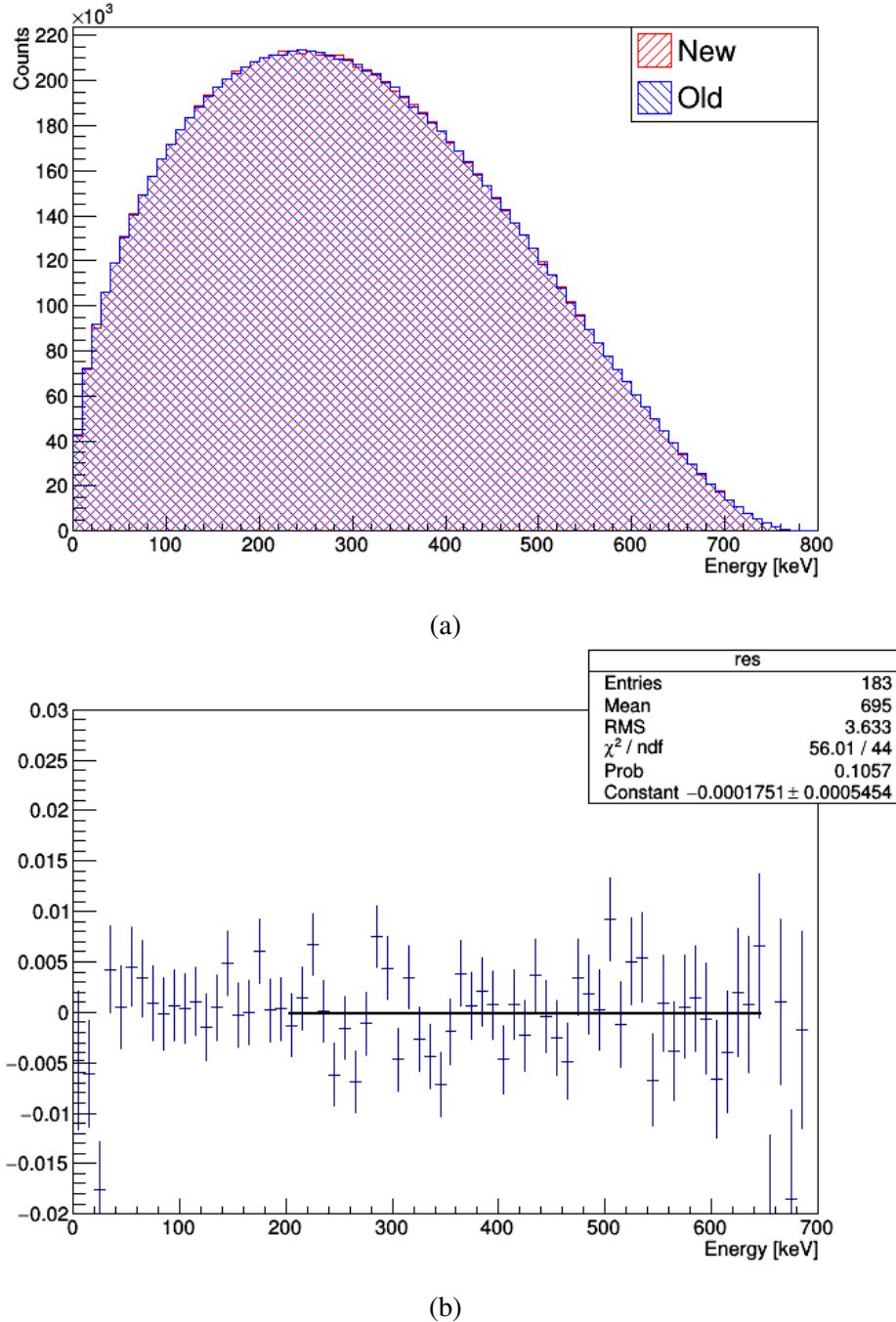


Figure 3.2: (a) Comparison between new kinematics generation of UCNA  $\beta$ -decay events (red) and the original  $\beta$ -decay event kinematics used in the 2010 asymmetry analysis (blue). (b) The fractional residuals of the comparison of Monte Carlo generated kinematics spectra in (a). The error bars are statistical and propagated them forward with standard error propagation [HH10]. A constant line is fitted to the residuals (black) from 200 keV to 650 keV, consistent with the energy range used in the final Fierz extraction.

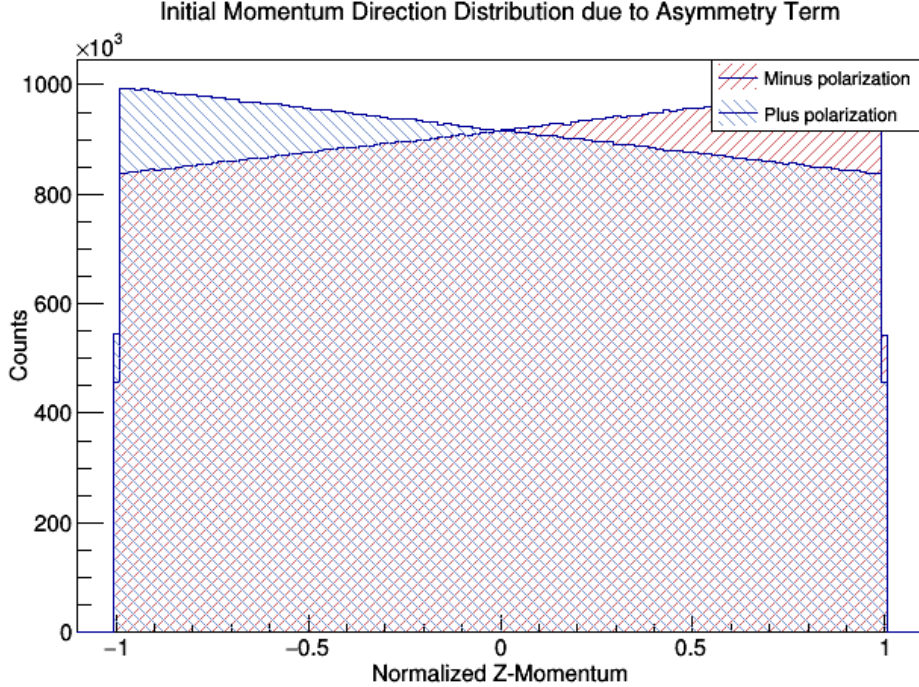


Figure 3.3: Simulated initial momentum direction distribution of  $\beta$ -decay electron events along the z-axis shown in raw counts (a total of  $10^8$  events were sampled). This causes a modification to the initial decay kinematics generated in figure 3.2, with a PDG value of  $A_0 = -0.1184$  (as of 2015).

### 3.3.4.1 Run Action

At the coarsest level, the run action is a class that executes at the beginning and end of each simulation, after a fixed number of primary particles have been simulated. In our GEANT4 implementation, we only use the run action for standard print-out and diagnostics, as well as tracking the number of events aborted. Some events need to be aborted in the simulation due to long transit times. For example, if the particle's initial momentum is nearly perpendicular to the magnetic field, there would be an extremely long transit time that is not recorded in the actual electronics of the data-taking runs. Fewer than 1 in  $10^5$  events were aborted either due to this phenomenon or any other effect that caused particles to be “trapped”.

In principle, the run action class is what controls parallelization in GEANT4. With some additional programming work, GEANT4 simulations can be parallelized and the run action oversees the distribution of batch programs to other computer cores. Within the simulation software, run action would track the progress of each sub-program and aggregate the results afterwards. There was an attempt to utilize this

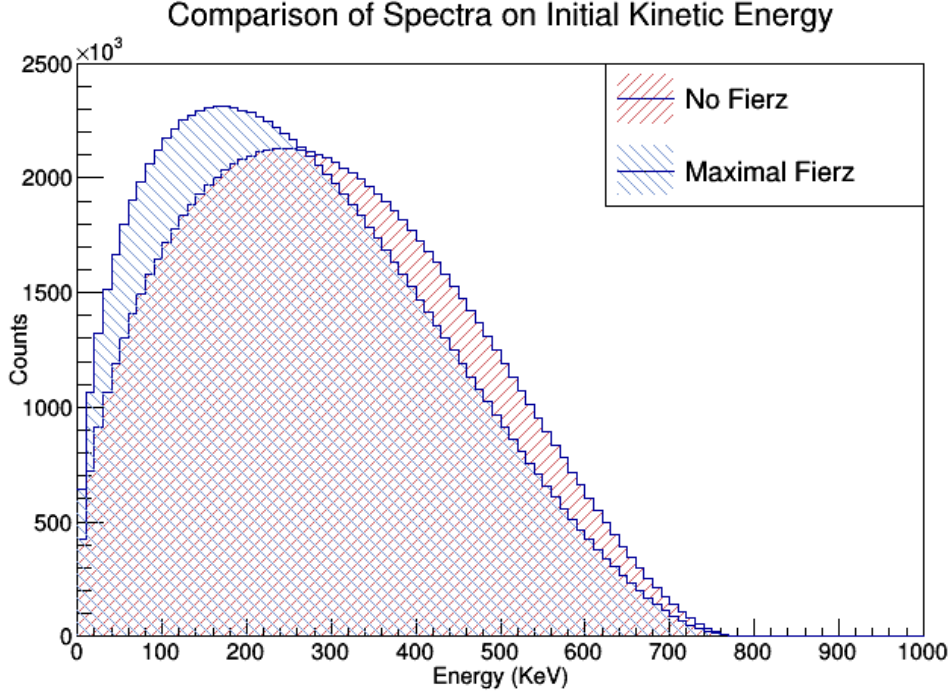


Figure 3.4: Two different initial  $\beta$ -decay electron energy spectra. The one corresponding to  $b = 0$  represents the Standard Model kinematics and is shown as a standalone in figure 3.2. The remaining maximal  $b$  is shown after running our initial kinematics generation and introducing a  $b$  coefficient of the form in equation 3.2. Normalization is implicitly done by setting a fixed number of events generated (here we used  $10^8$  total events).

automatic parallelization procedure in GEANT4. However, due to complications with file input/output, this path towards parallelization was ultimately abandoned. Instead, we note that GEANT4 is easily batched by nature; since the simulation runs a set number of events one at a time, we could instead start multiple instances of simulations with a subset of events. In practice, we achieved a “manual parallelization” by running bash scripts that started  $N$  instances of simulations with  $\frac{1}{N}$  total events each, where  $N$  was the number of cores we wished to run on.

### 3.3.4.2 Event Action

The next-level of particle tracking is called the event action which executes at the beginning of each event. An event for our typical purposes was defined as an electron generated within the decay trap, traveling until it is stopped by materials in the UCNA apparatus (typically the plastic scintillator) or some maximum time has elapsed and the event is deemed “trapped” and hence aborted. Within the

event action, we are able to track many kinematic parameters that are useful on a per-event basis. In particular, in event action the initial kinematics of the particle can be stored and compared with the final deposited energies within the GEANT4 simulated geometry for a single event.

It is important to discuss that in GEANT4 particles travel through volumes and interact with materials and fields. Nominally, these interactions are not stored and hence after the particle step is resolved, these interactions are lost. The user may define in the code a series of “sensitive detectors” (SDs). These are volumes (or objects in the OOP sense) in the GEANT4 simulation that will record the various kinematics that pass through them and can be extracted at the completion of the event (or total run, if desired). In our event action, we register four volumes as SDs: the East/West scintillators and East/West MWPCs. In event action, we define an output file that stores the initial event kinematics and final read out parameters of the GEANT4 simulation (described below). We also implement a clock to decide if an event is “trapped” and needs to be aborted.

At the end of an event, all the kinematic variables that are stored in the SDs are accessible and printed to an output file. In addition, some programming overhead are also printed to the file, as well as the initial event kinematics for comparison studies. Below is a list of the key parameters printed to file. When applicable, these are recorded for both the East and West scintillators and wirechambers.

1. Name of the SD volume
2. Energy [keV]
3. Quenched energy [keV]<sup>3</sup>
4. Time the particle entered the SD [ns]
5. Energy weighted by position in x, y, z [keV × cm]
6. Energy weighted by position squared in x, y, z [keV × cm<sup>2</sup>]
7. Angle the particle entered the SD from as measured by the surface normal [degrees]

---

<sup>3</sup>A discussion of the quenching factor is included in [Men14; Bro18]. Essentially, the light output of the plastic scintillator “quenches” at higher light yields and so a non-linear factor must be applied in order to properly account for the light yield as a function of energy deposited. In the GEANT4 simulation, this is done by adjusting the energy deposited with this additional quenching factor, described by “Birk’s law”. Both quantities are stored and outputted by the simulation.

8. Angle the particle exited the SD from as measured by the surface normal [degrees]
9. The incoming kinetic energy of the particle [keV]
10. The outgoing kinetic energy of the particle [keV]

### 3.3.4.3 Tracker

Within the GEANT4 simulation, the finest grain of resolution in the simulation comes from the TrackerHit class and the TrackerSD class. Within the simulation, each “track” is a fixed distance in the world volume that a particle travels. When a particle starts its track and ends it, the list of physical processes that can occur are sampled, in some order on the backend of the GEANT4 libraries, via Monte Carlo sampling. Then, when any physical processes that change the kinematics of the tracked particle occur, the kinematics are updated and the differences in energy and momenta are either lost or recorded in a sensitive detector located within the simulation. The TrackerHit class maintains a record of variables for each “track” the particle travels through. The TrackerSD class records the kinematics that the particle loses within a particular SD volume.

In essence, the TrackerHit class stores different variables as class parameters (in the OOP sense) that are accessible while the particle traverses the geometry. These variables are listed below - we restrict ourselves to only the ones with physical relevance and interpretation, as well as some standard programming bookkeeping for future reference.

1. TrackID - a unique ID for this track.
2. Incident kinetic energy when particle enters into this track.
3. Energy deposited in this region (by definition, a SD).
4. Quenched energy deposited in this region.
5. Hit time - the time of entry of the particle into the volume.
6. Hit position - where the particle entered the volume.
7. Energy deposition weighted by position and position squared. These are relevant for calculating an energy reconstruction based on scintillator position.

8. Incident momentum - the momentum the particle had when entering the volume.
9. Exit momentum - the momentum the particle had when exiting the volume.
10. Particle species ID - a flag that indicated  $\beta$ -decay electrons as opposed to photons or other particles.
11. Process name - the name of the physics process which created this track. In certain physical processes, a cascade of tracks can be created and GEANT4 records each one and resolves those secondary particles automatically.
12. Volume name - the name of the volume where the track is located.
13. Creator volume name - the name of the volume where the track was created.

Within TrackerSD, a collection of tracker hits is created and stored for each SD. In the original asymmetry simulation, there were  $\approx 12$  SDs for use in calibration and analysis. For the Fierz analysis, only four SDs were used: the East and West plastic scintillators and the East and West MWPCs. This was due to the simplified analysis requirements of the Fierz interference extraction and studying the UCNA detector response after one analysis had already been completed (publication [Men+13]).

After the hits collection is created, each tracker hit associated with a SD is stored within the hits collection. Then, once a particle is completed within a SD volume, a final function is called that accumulates all the kinematics from all the tracker hits within the SD. This, for example, sets the track ID, gets the particle ID, adds up all the energy deposited within the SD of this name, applies a quenching factor, and so on. The integrated kinematic parameters stored in the SDs are then accessible and printed out at the end of an event in the Event Action (discussed above in section 3.3.4.2).

### 3.4 Post-Processing: Applying the Detector Response Model

After the simulation of the neutron  $\beta$ -decay electrons is completed, the final output of the simulation are energy deposited and quenched energy deposited in the plastic scintillators (among other kinematic quantities). Critically, this does not yet resemble an output that matches the data, which is a reconstructed energy. In order to convert the pure simulated energy deposition, we must apply the detector response model which modifies the deposited energy by the noise of the real detector to create

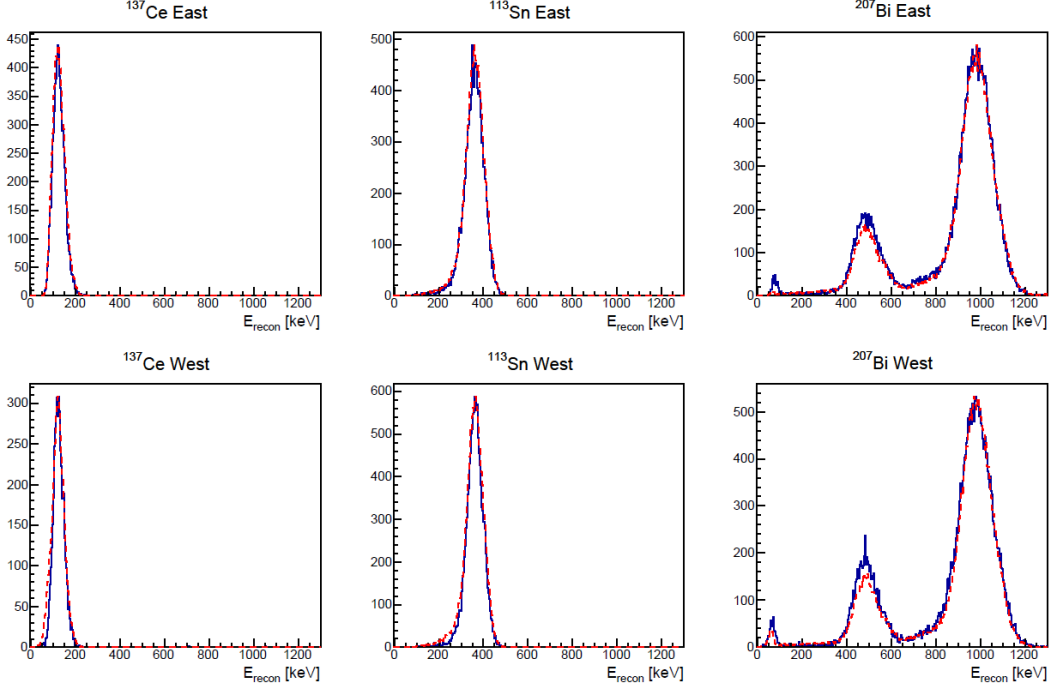


Figure 3.5: Example  $E_{\text{recon}}$  spectra from combined PMT response for simulation (red) and data (blue) for all conversion electron source data ( $^{137}\text{Ce}$ ,  $^{113}\text{Sn}$ ,  $^{207}\text{Bi}$ ) after application of the calibration. This is for a random run that included all three sources within the fiducial volume at the same time. Figure from [Bro18] and the individual PMT comparisons between simulation and data prior to being combined into  $E_{\text{recon}}$  are also given there.

a simulation output that is data-like, and then combines those quantities into a final reconstructed energy.

The real detector response model used in the work in this dissertation is taken from the 2011-2013 asymmetry analysis and is described in detail in Chapter 4.2 of [Bro18]. Here, we provide a brief overview of the various effects accounted for in the detector response model. Figure 3.5 gives a comparison of this detector model applied to calibration data and calibration simulations. We note that these comparisons were generated with the old GEANT4 simulations however the comparison is valid for our recreated simulation described in this chapter. The subsequent sections describe briefly the different analysis procedures in the detector response model that go into generating the comparison in figure 3.5. These effects are applied to simulated initial  $\beta$ -decay electron kinematic spectra (as shown in figure 3.2) in order to illustrate what must be accounted for when converting pure Monte Carlo simulated spectra into “data-like” simulated spectra.

After settling on an analysis procedure for the Fierz interference, we then went back and applied our procedure to the integrated 2010 dataset. As a result, we used octet-by-octet or calibration period-by-calibration period measured detector responses for the 2011-2012, 2012-2013 datasets while for the 2010 dataset we used the entire year’s integrated data and calibration together. The following effects are described to provide additional context for how the simulation output is modified. We will see later in Chapters 4 and 5 how these different detector effects also become relevant in the UCNA dataset analyses.

### 3.4.1 Position Map Corrections

The first effect that the detector response model applies to the simulation output is the position map corrections. The analyzer (interchangeably called the “Simulation Processor” or simply the “processor”) takes as input the geometry that the GEANT4 simulation was executed with. It then loads the corresponding position maps as determined in [Men14; Bro18]. Throughout the analysis, there was a flag to process the simulations like the individual octets: we would either process simulation events on an event-by-event basis until we reached the same number of events as the desired octet, or we would process  $16\times$  the number of events (in order to create a “high statistics” Monte Carlo so the statistical error would be dominated by the real data in any comparison). The octets had different position maps associated with their activated Xenon position mapping run. Further details of the activated Xenon position map extraction on the 2011-2013 UCNA datasets can be found in [Bro18].

The position of the particle can be extracted from the tracked information in the GEANT4 geometry. Specifically, at the end of the event, the variable “Hit Position” is used to determine where the particle was located on the face of the plastic scintillator. This position is then compared with the proper position map to extract a correction factor for this event’s light yield.

### 3.4.2 Finite PMT Resolution

The second effect that the detector response model applies to the simulation output is the smearing of the energy resolution due to the finite PMT resolution in the hardware. For each geometry, there is a calibration on each of the four East PMTs and the four West PMTs energy resolutions. This is reported in the form of nPE/keV, otherwise known as the “number of photo-electrons” per keV deposited and is unique to each geometry and PMT. For each scintillators quenched energy,  $E_Q$ , a Gaussian with mean  $E_Q$  and standard deviation of  $\alpha_i\eta(x, y)$  where  $\eta$  is the position map factor

discussed above (section 3.4.1), and  $\alpha_i$  is a resolution factor for PMT  $i$ <sup>4</sup>. This creates eight quenched energies, one for each PMT in the UCNA apparatus, smeared with the PMT resolution and position map effects.

After the four smeared quenched energies for each detector are calculated, they are combined using their sampled photo-electron statistics as weights. This results in a weighted average of quenched energy deposited in the East and West detectors respectively.

### 3.4.3 Energy Calibration Distortions

In principle, the next processor effect to be applied is a modification for energy non-linearities. Energy calibration variation polynomials up to cubic order in averaged quenched energies<sup>5</sup> are used to modify the energy response of the East and West detectors. This is discussed extensively in the Fierz interference spectral extraction, section 4.2. However, in a nominal simulation processor run, there are no energy calibration variations applied and this step is skipped.

### 3.4.4 Trigger Function

The fourth simulation processor effect applied is the trigger function. The trigger function is loaded depending on the calibration period used since there is a trigger function of the East and West detectors for each calibration period. Additional details on the trigger logic and extraction methodology is given in [Bro18].

The trigger threshold is then sampled to determine if there was a trigger in either the East or West detectors. Trigger flags are set based on this probabilistic sampling. Afterwards, the event type classification is assigned based on the triggers in the East, West detectors and MWPCs and the simulation’s time flag for which SD triggered first.

We highlight the presence of this trigger function because it is a hardware-based effect. In the GEANT4 simulation, any amount of energy can be lost by our simulated particle in the scintillator SD and hence when we interrogate that SD we can extract any amount of energy deposited. The real experiment does not work the same way.

---

<sup>4</sup>The actual calculations of  $\alpha_i$  is non-trivial and detailed extensively in [Bro18]. The results of those  $\alpha_i$  extractions are loaded directly into the Simulation Processor and applied to the simulation data.

<sup>5</sup>From this point onwards, this weighted average of smeared quenched energies per detector side is called the visible energy,  $E_{vis}$ . We take care not to confuse with the actual data  $E_{vis}$  which is the final weighted signals in East and West plastic scintillators. However, since the simulation processor is intended to make simulations look “data-like”, this is similar to a data  $E_{vis}$ .

There is a minimum required energy for the  $\beta$ -decay electron to produce enough light in the scintillator such that it can be transported out towards the PMTs and generate a detectable signal. This is characterized extensively in [Bro18] and forms an important component of the UCNA detector response at low energies (where the trigger function dominates).

### 3.4.5 Creating a Reconstructed Energy

The final process applied by the simulation processor is to convert the “data-like” quenched energies in the East and West detectors into a reconstructed energy. The details of this conversion formula for the 2011-2013 UCNA datasets is given in [Bro18]. After this final processor stage, the simulation output quenched energy deposition has been converted into a reconstructed energy that mimics the hardware effects of the detector.

## 3.5 Motivation for Using Simulation

Up until this point, we have been discussing in detail the coding implementation of various elements of the UCNA apparatus in simulation. It warrants a discussion, then, why we might want to use such a detailed simulation. Recall from the beginning of this chapter that the goal of the simulation was to perform systematic studies for the analysis method.

### 3.5.1 Event Types Identification

One of the primary utilities of the GEANT4 simulation was extracting “true” event type identification. By using the decay trap monitors (section 3.3.1.1) and other SDs in the asymmetry analysis [Men14], and the initial particle kinematics in the follow-up asymmetry analysis [Bro18], we are able to identify true event types and compare them to data signals. A comprehensive description of Monte Carlo and data comparison for event type identification is given in the previous references as well.

As we highlight in the 2010 UCNA asymmetry analysis, one of the leading sources of systematic error was the correction (and associated error) in the “backscattering” and “ $\cos\theta$ ” effects (described later in Chapter 4 and again in Chapter 5). These are effects that are related to multi-scattering in the UCNA apparatus and hence directly tied in with proper event identification and energy reconstruction. In that asymmetry analysis, these two systematic effects were modeled separately and their errors assumed to be uncorrelated and thus added together in quadrature. Separately,

the two formed the 2<sup>nd</sup> ( $\pm 0.34\%$ ) and 4<sup>th</sup> ( $\pm 0.30\%$ ) largest systematic errors (polarization was the largest at  $\pm 0.56\%$  and targeted for improvement for the 2011-2013 data-taking runs). The full list of systematic corrections and associated uncertainties can be found in [Men+13].

However, upon completing the re-implementation of the GEANT4 simulation, we had access to the loss in energy/detection efficiency for various decays. As a result, we were able to create refined models for event discrimination and ultimately fold in more reliable event classification in the final asymmetry analysis (which used all event types to reach maximal statistical precision). This allowed us to model the systematic effects associated with backscattering and  $\cos\theta$  together as one effect, leading to a significant improvement in systematic uncertainty. See figure 3.6 for an example of a GEANT4 generated type 2-3 energy spectra (see figure 2.7 for a description of event type definitions). We note that in the real-world data stream, there would be no way to access this spectral shape because the electronic triggers of the two events are the same. Hence, the value of being able to better characterize our data event types using the GEANT4 simulation becomes apparent.

### 3.5.2 Energy and Timing Spectra Reconstruction

With a proper standalone GEANT4 simulation, we could access key kinematic parameters. In particular, we could produce an energy spectrum of  $\beta$ -decay electrons processed through our detector geometry. Previously, such an energy spectrum (in particular, adjusted for 2011-2012, 2012-2013 geometries) was not available due to the entanglement between the asymmetry analysis pipeline and simulation framework. Since the re-implementation of the GEANT4 simulation was such a large task, we carefully benchmarked our figures of merit throughout the programming of the new simulation. As significant elements were added in code, the output  $\beta$ -decay electron spectrum in Edep (energy deposited) and QEdep (quenched energy deposited) were read out by the plastic scintillators and vetted against in-house simulated spectra using the old GEANT4 simulation. The spectra were consistent (or checked until they were) throughout the development of the new GEANT4 simulation. We note that we specify Edep and QEdep because the proper unit of reconstructed energy comes after applying a post-simulation processor (internally called the “analyzer”) to the simulated data. The analyzer accounts for the various detector response effects discussed above in section 3.4.

With a high-fidelity GEANT4 simulation, we could reproduce the effects that were

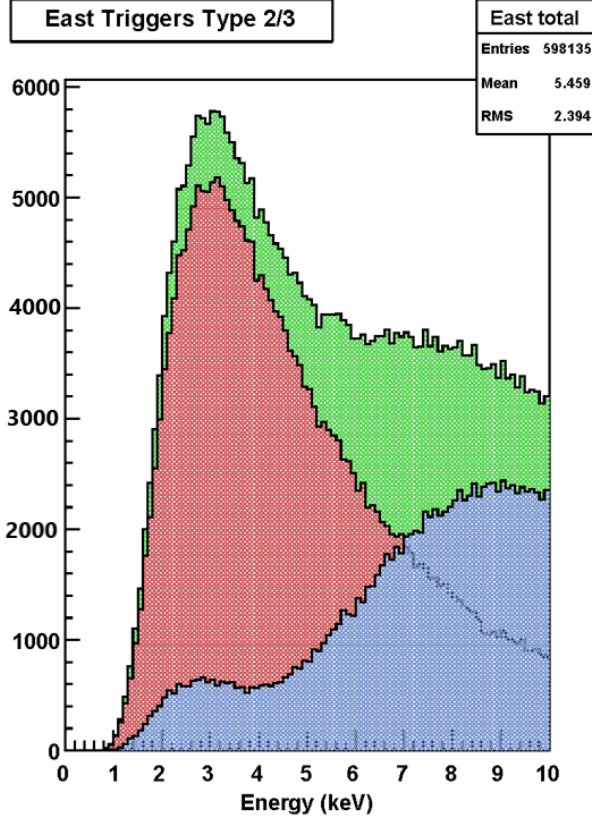


Figure 3.6: An energy spectrum of the energy deposited in the MWPC for Type 2 (red) and Type 3 (blue) events and all Type2 + Type 3 events (green). We note that in the electronics these events are indistinguishable since they both produce a trigger on the same side detector. However, in the GEANT4 simulation we are able to access “true” event typing. The low energies plotted are related to the energies deposited in the MWPC. In the data analysis pipeline, the thresholds identified from these plots can be used to set a cut on MWPC energy deposition and improve Type 2/3 identification fidelity.

studied in the asymmetry analysis. In addition, by modifying the input kinematics, we could study the systematic effects of including both the asymmetry term and the Fierz interference term together or separately. This allows for individual systematic studies and also for any correlation effects. In particular, this was valuable when we discuss our first attempt at characterizing the Fierz interference extraction: setting limits on the energy calibration uncertainty (see section 4.2).

We also note here that the timing spectrum was available in the GEANT4 simulation. As discussed in the tracker section (section 3.3.4.3) the time each track was made in a SD was recorded in units of nanoseconds. This timing spectrum could be extracted and used to better understand our detector geometries, e.g., by giving further insights

into travel paths for different event types. This particular use becomes extremely relevant in Chapter 5 where we discuss the 2012-2013 UCNA dataset, which had working Time-to-Digital (TDC) converters attached to the PMTs on either detector so we were able to vet our timing data against the GEANT4 simulation, thereby providing significant advantages to the analysis in Chapter 5.

## C h a p t e r ~ 4

### UCNA: FIERZ INTERFERENCE ANALYSIS

In this chapter, we describe the Fierz interference extractions. Chronologically, this analysis was the first project worked on and the last analysis completed since the nature of the later UCNA datasets allowed for more detailed analyses. In particular, the unblinded, completed asymmetry data analysis from the UCNA 2010 dataset left us with little potential for modifications. However, the 2011-2012 and 2012-2013 blinded datasets were more accessible and allowed for more involved studies prior to unblinding.

This chapter illustrated our efforts to extract the Fierz Interference term via two measurement techniques: the spectral extraction and the asymmetry extraction (occasionally termed “fit” in this dissertation). We discuss blinding the data analysis in the 2011-2012, 2012-2013 datasets. We present additional studies to characterize the two extraction methods. Finally we combine the measurements and present our final limits on the Fierz Interference term.

#### **4.1 The Fierz Interference Term**

The Fierz interference term,  $b$ , was previously described in section 1.3.2 (see also [LY56; JTW57a] for an early introduction to  $b$ , [Fie37] for the original publication). As a reminder, it manifests as an energy distortion term in the overall  $\beta$ -decay electron spectrum in equation 1.12. Since it is only an energy distortion, it is present even in quantities that integrate over the decay angle and spin.

The Fierz interference is of interest for several reasons. First, in the Standard Model neutron  $\beta$ -decay,  $b = 0$ . Therefore, limits on Fierz provide insights into beyond Standard Model physics. Namely, Fierz interference is particularly sensitive to scalar and tensor couplings (see, for example, [GNS19] for a review) which are not present in the Standard Model weak decay, a purely vector - axial-vector decay. Secondly, many calculations and limits set on modern decay coefficients (for example,  $A$  as in [Men+13; Bro+18]) assume  $b = 0$ . The presence of a non-zero  $b$  would distort the current measurements on several of these kinematic decay coefficients. Hence, setting more stringent limits on  $b$  contributes to more robust measurements on other neutron  $\beta$ -decay coefficients by further reducing potential uncertainty contributions

from beyond Standard Model physics contained in a non-zero  $b$ .

The UCNA experiment was discussed in great detail in Chapter 2. Due to the nature of the asymmetry measurement, UCNA recorded several key kinematic observables that allow for a direct extraction of a Fierz interference term — in particular, a robust energy measurement of the neutron  $\beta$ -decay electron spectrum that is directly related to  $b$  in equation 1.12. As well, we will see later that the asymmetry, termed  $A_0$ , also provides sensitivity to a non-zero  $b$  value. Hence, it was a natural extension to the UCNA 2010-2013 datasets to extract a  $b$  measurement. This would provide the added advantage of being the first direct measurement of  $b$  using data from UCNs.

This chapter builds upon two publications, one of which I was co-author and another where I was the main author. The focus of section 4.2 describes the work in [Hic+17]. The focus of sections 4.2, 4.3, and 4.4 describe the work in [Sun+20].

#### 4.1.1 UCNA Sensitivity to Fierz

As an overview, the spectral extraction involves fitting an energy spectrum to identify a small energy distortion of the shape  $\frac{m_e}{E_e}$ , while the asymmetry extraction involves fitting the  $A_0(E_e)$  with the Standard Model term ( $A_{0,b \neq 0}$ ) and a non-zero  $b$  term which manifests as  $\frac{1}{1+b\frac{m_e}{E_e}}$ . Both of these methods have advantages and disadvantages, which are detailed in the remainder of this chapter. However, we note that both are accessible by the UCNA dataset. The spectral fit is feasible because each octet of  $\beta$ -decay data has an energy reconstruction with associated systematic errors (and subdominant statistical errors). The asymmetry fit is feasible because an overall asymmetry coefficient,  $A_0$ , is fit across our energy window in the asymmetry analysis and it is a simple matter to introduce an energy dependence of the form for non-zero  $b$  to the fit.

In summary and at a high-level, for the spectral fit, the analyzer only needs a reconstruction of the  $\beta$ -decay rate as a function of energy and the uncertainty in that energy reconstruction. For the asymmetry fit, the analyzer only needs the final, unblinded  $A_0$  coefficient with uncertainties (primarily statistical, as we will see in section 4.3) as a function of energy, which was provided by the asymmetry analysis.

## 4.2 The Spectral Extraction Method

In order to perform a spectral fit to a non-zero Fierz interference value, we first illustrate the form of a neutron  $\beta$ -decay spectrum with a Fierz term (see figure 3.4). In this spectrum, the modified initial event kinematics generation described in

section 3.3.3.1 was used to generate these spectra. Additionally, due to the nature of the sampling code, there was an implicit normalization applied since a set number of events are selected to sample and accept.

Conceptually, the task of extracting Fierz interference from the neutron  $\beta$ -decay dataset reduces to analyzing the shape of said  $\beta$ -decay spectrum and seeing what fractional components of the Standard Model ( $b = 0$ ) spectrum and the maximal Fierz spectrum ( $b \rightarrow \infty$ ) is the closest to our data spectrum. This can be done on a per-octet basis (see section 2.4.5 for a description of octets) to minimize run-to-run systematics or integrated over the entire run. In the upcoming sections we illustrate the methods and challenges in implementing this analysis procedure.

### 4.2.1 The Super-Sum Spectrum

#### 4.2.1.1 Motivation and Definition

In the UCNA detectors we measure four detector rates for production data on a per-octet basis. These rates can be written as a function of decay electron total energy,  $E_e$ , and angle,  $\theta$ , between the neutron spin and electron momentum by using equation 1.12 and integrating over the neutrino momentum:

$$\begin{aligned} r_1^\uparrow(E_e) &= \frac{1}{2}\eta_1(E_e)N^\uparrow(1 + b_n m_e/E_e + A y(E_e))\Gamma(E_e) \\ r_2^\uparrow(E_e) &= \frac{1}{2}\eta_2(E_e)N^\uparrow(1 + b_n m_e/E_e - A y(E_e))\Gamma(E_e) \\ r_1^\downarrow(E_e) &= \frac{1}{2}\eta_1(E_e)N^\downarrow(1 + b_n m_e/E_e - A y(E_e))\Gamma(E_e) \\ r_2^\downarrow(E_e) &= \frac{1}{2}\eta_2(E_e)N^\downarrow(1 + b_n m_e/E_e + A y(E_e))\Gamma(E_e) \end{aligned} \quad (4.1)$$

where, for example,  $r_2^\uparrow$  corresponds to the rate in detector 2 for spin  $\uparrow$  (neutron polarization aligned with the imposed magnetic field),  $y(E_e) \equiv \langle P \rangle \beta \langle \cos\theta \rangle$ , with  $\langle P \rangle$  the average polarization, and  $\beta = v/c$  with  $v$  the  $\beta$ -decay electron velocity,  $c$  the speed of light, and  $\Gamma(E_e)$  is the Standard Model unpolarized decay rate. These four rates are expressed in terms of the detector efficiencies,  $\eta_{1,2}(E_e)$ , and the number of stored UCN for the spin states,  $N^{\uparrow,\downarrow}$ .

In order to perform the spectral fit on our data, we take advantage of a convenient quantity called the “super-sum”. The super-sum is defined as follows:

$$\Sigma(E_e) = \frac{1}{2}\sqrt{r_{East}^\uparrow r_{West}^\downarrow} + \frac{1}{2}\sqrt{r_{East}^\downarrow r_{West}^\uparrow} \quad (4.2)$$

where, for example,  $r_{East}^\uparrow$  corresponds to the rate in the East detector for spin up runs.

Using the relationships for each detector rate in equation 4.1, we find the super-sum  $\Sigma(E)$  reduces to the following form:

$$\Sigma(E_e) = \sqrt{\eta_{East}\eta_{West}N^\uparrow N^\downarrow}(1 + b\frac{m_e}{E_e})\Gamma(E_e) \quad (4.3)$$

where here,  $E_e$  represents the  $\beta$ -decay electron energy,  $\eta_{East/West}(E_e)$  represents each detector's (energy-dependent) efficiency, and  $N^{\uparrow/\downarrow}$  are each UCN state's loading number.

With the definition of the super-sum spectrum in equation 4.3, we see the clear advantages of this quantity: the detector efficiencies and loading discrepancies are absorbed as an overall multiplicative factor. In other words, the effects that affect the asymmetry such as East vs West detection efficiencies or spin state discrepancies are pulled out of the spectral shape of the super-sum spectrum and hence any fit to the spectrum shape will account for these effects via a normalization constant. As we will see later, this effectively disentangles the spectral fit from any contributions that affect the asymmetry fit. Additional details of the super-sum can be found in [Hic13].

#### 4.2.1.2 Fitting the Energy Spectra

The energy spectrum can be fit with a variable  $b$  value via several methods. One method is via shape factors which we discuss later in this chapter. The principle method used for fitting in this analysis work was by generating two baseline Monte Carlo simulations, processed with all detector effects to look “data-like”. These baseline Monte Carlo simulations are the terms in equation 3.1. Namely, we generate a processed Monte Carlo histogram with  $b = 0$  (the 1<sup>st</sup> term on the right-hand side) and  $b \rightarrow \infty$  (the 3<sup>rd</sup> term on the right-hand side). We note the second term on the right-hand side is 0 when we take the data over the full octet (or the full year). These terms are the Standard Model decay rate ( $b = 0$ ) and the same decay rate with a multiplicative factor of  $m_e/E_e$  ( $b \rightarrow \infty$ ), as shown in equation 3.2 and given again here

$$\Gamma_b(E_e) = \left(1 + b\frac{m_e}{E_e}\right)\Gamma_{SM} \quad (4.4)$$

Due to the event generation procedure described in section 3.3.3.1 yielding a fixed number of events, we do not actually generate the decay rates for  $\Gamma_b(E_e)$ ,  $\Gamma_{SM}(E_e)$ , and  $\Gamma_{b \rightarrow \infty}(E_e)$ . Instead, we generate a probability distribution for each and get

$P_b(E_e)$ ,  $P_{SM}(E_e)$ , and  $P_{b \rightarrow \infty}$ . Following the prescription in equation 3.11 of [Hic13], we get

$$P_b(E_e) = \frac{1 + b\left(\frac{m_e}{E_e}\right)}{1 + b\left\langle\frac{m_e}{E_e}\right\rangle} P_{SM}(E_e) \quad (4.5)$$

where  $\left\langle\frac{m_e}{E_e}\right\rangle$  represents the expected value of  $\frac{m_e}{E_e}$  over the energy range of interest of  $P_{SM}(E_e)$ . By noting  $\Gamma_{b \rightarrow \infty}(E_e) = \frac{m_e}{E_e} \Gamma_{SM}(E_e)$ , and  $P_{SM} = \frac{\Gamma_{SM}}{\int \Gamma_{SM} dE'}$ , we can derive

$$\begin{aligned} P_{b \rightarrow \infty} &= \frac{\frac{m_e}{E_e} \Gamma_{SM}}{\int \frac{m_e}{E'} \Gamma_{SM} dE'} \\ &= \frac{\frac{m_e}{E_e} P_{SM} \int \Gamma_{SM} dE'}{\int \frac{m_e}{E'} \Gamma_{SM} dE'} \\ &= P_{SM} \frac{m_e}{E_e} \left[ \frac{\int \frac{m_e}{E'} \Gamma_{SM} dE'}{\int \Gamma_{SM} dE'} \right]^{-1} \\ &= P_{SM} \frac{m_e}{E_e} \left\langle \frac{m_e}{E_e} \right\rangle^{-1} \\ \implies \left\langle \frac{m_e}{E_e} \right\rangle P_{b \rightarrow \infty}(E_e) &= \frac{m_e}{E_e} P_{SM}(E_e) \end{aligned} \quad (4.6)$$

where we have suppressed the energy label for each decay rate and probability distribution.

Furthermore, we note that the data histograms are converted into a probability distribution by normalizing each bin by the total number of events in the energy range. Thus, they can be represented by  $f_{data}(E_e) := P_b(E_e)$ . Plugging the result from equation 4.6 into equation 4.5, we get

$$f_{data}(E_e) = P_b(E_e) = \frac{P_{SM}(E_e) + b\left\langle \frac{m_e}{E_e} \right\rangle P_{b \rightarrow \infty}(E_e)}{1 + b\left\langle \frac{m_e}{E_e} \right\rangle} \quad (4.7)$$

where, again,  $E_e$  represents the total energy of the electron,  $m_e$  is the electron mass, the expectation value is done over the energy fit region (tabulated numerically) of the Standard Model probability distribution, and  $b$  is a free parameter that represents the Fierz interference.

The histogram fitting in equation 4.7 was accomplished using two methods with ROOT libraries. First, in our initial analysis procedure, we used the ROOT object

called `TFractionFitter` [Teab]. This class takes as input several Monte Carlo histograms and one data histogram and performs a fit to extract the fractions of the Monte Carlo histograms present in the data histogram. It uses statistical uncertainties in all input histograms and fits with a likelihood fit using Poisson statistics. By its definition, this class seemed optimized for our purposes. However, quality checks using various input  $b$  values in “data-like” Monte Carlo (what is called our “data histogram”) did not show consistency. Ultimately, these inconsistent results led us to choose a different fitting procedure than the built-in ROOT class, one that would provide consistent results with test cases.

The second fitting procedure chosen and the one that was ultimately used was a self-programmed fitting using a  $\chi^2$  minimization with the ROOT object called `TMinuit` [Jam]. This worked by taking the bin contents of the different Monte Carlo histograms, combined with a functional form with free parameters (notably  $b$  and  $A$ ), and fitting the data histogram to these combined Monte Carlo histograms and minimizing the  $\chi^2$  function over the bins in the energy fit region. The minimization routine chosen in `TMinuit` was `MIGRAD`. The results of this fitter reproduced test cases and provided sensible values and uncertainties in the fitted parameters.

#### 4.2.1.3 Blinding the Spectral Extraction

After the publication of the UCNA 2010 dataset Fierz interference direct spectral extraction (summarized later in section 4.2.5), there was a move towards blinding the data for the subsequent UCNA 2011-2012 and 2012-2013 datasets to ensure a more robust analysis. For an in-depth discussion on blinding data analyses in experimental physics, see [KR05]. In summary, there are several case studies of physics experiments throughout history that show unconscious bias ultimately leading to convergences in experimental measurements. These convergences are non-statistical in nature and their prevalence can be explained by unconscious bias. Blinding thus was introduced as a method of combating this human factor and has lead to a successful reinterpretation of experimental measurements, producing a distribution that fluctuates within experimental uncertainties. The community as a whole has generally concluded blinding to be a crucial step in validating the integrity of experimental analysis results. With this in mind, we decided to blind the 2011-2012 and 2012-2013 Fierz interference extractions. Below, we describe the blinding methodology for the direct spectral analysis.

Recall from the previous section, section 4.2.1.2, that we use two baseline Monte

Carlo histograms, processed through the GEANT4 simulation and with the detector response model to become “data-like”. We then use these data-like histograms to fit the real data histogram and extract a fractional presence of the  $b = 0$  histogram and the  $b = \infty$  histogram. These fractional percentages directly relate to a  $b$  value.

In order to perform the blinding, there would be no way to reliably modify the data since we only have one true dataset and a priori we do not know what  $b$  value that dataset would extract. Instead, what we do is modify the baseline Monte Carlo histograms. By “mixing in” a percentage of events from the  $b \rightarrow \infty$  histogram, we distort the  $b = 0$  histogram and transform it into a  $b \neq 0$ . In particular, when we mix in  $b \rightarrow \infty$  events into the  $b = 0$  histogram, the baseline  $b = 0$  histogram shifts to  $b > 0$  (the energy peak shifts to lower energy, which physically is what a  $b > 0$  distortion induces) and hence when we fit a standard  $b = 0$  histogram with these two “blinded” baseline histograms, we would produce a  $b < 0$  value. We note this is the first “case”: creating a blinded  $b < 0$  value.

To show this explicitly, we start by taking the results of equation 4.5,  $P_b(E_e) = \frac{1+b\langle\frac{m_e}{E_e}\rangle}{1+b\langle\frac{m_e}{E_e}\rangle} P_{SM}(E_e)$ , and that in equation 4.6,  $P_{b \rightarrow \infty} = P_{SM} \frac{m_e}{E_e} \left\langle \frac{m_e}{E_e} \right\rangle^{-1}$ . Also, the fitting is defined in equation 4.7 as  $f_{data}(E_e) = \frac{P_{SM}(E_e) + b\langle\frac{m_e}{E_e}\rangle P_{b \rightarrow \infty}(E_e)}{1+b\langle\frac{m_e}{E_e}\rangle}$ .

We now introduce a mixing percentage,  $r$ , to our  $b = 0$  distribution. That is, each event in the  $b = 0$  histogram is sampled and with probability  $r$  that event is replaced by the corresponding numbered event from the  $b \rightarrow \infty$  histogram. We note both generated histograms have the same number of events. This results in the following transformation on our baseline SM distribution:

$$P_{SM} \mapsto (1 - r)P_{SM} + rP_{b \rightarrow \infty} \quad (4.8)$$

where  $P_{SM}$  and  $P_{b \rightarrow \infty}$  have implicit energy dependence that we suppress for the sake of notation here. Replacing  $P_{SM}$  in equation 4.7 with the result from equation 4.8, we get

$$\begin{aligned} f_{data}(E_e) &= \frac{P'_{SM}(E_e) + b\langle\frac{m_e}{E_e}\rangle P_{b \rightarrow \infty}(E_e)}{1 + b\langle\frac{m_e}{E_e}\rangle} \\ &= \frac{(1 - r)P_{SM}(E_e) + rP_{b \rightarrow \infty}(E_e) + b\langle\frac{m_e}{E_e}\rangle P_{b \rightarrow \infty}(E_e)}{1 + b\langle\frac{m_e}{E_e}\rangle} \\ &= \frac{(1 - r)P_{SM}(E_e) + [r + b\langle\frac{m_e}{E_e}\rangle]P_{b \rightarrow \infty}(E_e)}{1 + b\langle\frac{m_e}{E_e}\rangle} \end{aligned} \quad (4.9)$$

The goal here is to introduce a false  $b$  value that then becomes our blinded  $b$  value. In order to determine the  $b$  value introduced by a mixing percentage  $r$ , we replace the  $f_{data}(E_e)$  distribution with a  $b = 0$  Monte Carlo distribution. This gives us

$$P_{SM}(E_e) = \frac{(1-r)P_{SM}(E_e) + [r + b\langle\frac{m_e}{E_e}\rangle]P_{b \rightarrow \infty}(E_e)}{1 + b\langle\frac{m_e}{E_e}\rangle} \quad (4.10)$$

For equation 4.10 to be true, we can set the coefficient in front of  $P_{SM}$  to 1 and the coefficient in front of  $P_{b \rightarrow \infty}(E_e)$  to 0. Solving both of these gives the same answer since this problem is over-constrained.

$$\therefore b = \frac{-r}{\langle\frac{m_e}{E_e}\rangle} \quad (4.11)$$

$b$  is the Fierz interference value we are trying to introduce as a blinding and  $r$  is a percentage of events we are mixing between a SM distribution and a  $b \rightarrow \infty$  distribution.

The second case is producing a blinded  $b > 0$  value. We can repeat the same procedure except we mix  $b = 0$  and  $b = -1$  events together. Due to the form of  $b$  in equation 3.1,  $b = -1$  is the lowest possible value (any more negative values would induce a negative decay rate in the equation). Hence  $b = -1$  conceptually represents the opposite of  $b \rightarrow \infty$ , an effective  $b \rightarrow -\infty$ . By mixing in  $b = -1$  events, the baseline Monte Carlo histogram transform from  $b = 0$  to  $b < 0$  (the energy peak shifts to a high energy) and hence when we fit a standard  $b = 0$  histogram, we produce a  $b > 0$  value.

To show this explicitly, we again use a mixing percentage,  $r$ , of  $b = -1$  events in our  $b = 0$  distribution. This results in the following transformation on our baseline SM distribution:

$$P_{SM} \mapsto (1-r)P_{SM} + rP_{b=-1} \quad (4.12)$$

where  $P_{SM}$  and  $P_{b=-1}$  (and  $P_{b \rightarrow \infty}$  below) have implicit energy dependence that we again suppress for the sake of notation. When we use equations 4.5 and 4.6, we also get

$$\begin{aligned} P_{b=-1} &= \frac{1 - \frac{m_e}{E_e}}{1 - \langle\frac{m_e}{E_e}\rangle} P_{SM} \\ &= \frac{P_{SM}}{1 - \langle\frac{m_e}{E_e}\rangle} - \frac{\frac{m_e}{E_e} P_{SM}}{1 - \langle\frac{m_e}{E_e}\rangle} \\ &= \frac{1}{1 - \langle\frac{m_e}{E_e}\rangle} \left[ P_{SM} - \langle\frac{m_e}{E_e}\rangle P_{b \rightarrow \infty} \right] \end{aligned} \quad (4.13)$$

Plugging this result into equation 4.12, the new baseline distribution we are fitting with becomes  $P_{b \rightarrow \infty}$  and

$$P_{SM} \mapsto (1 - r)P_{SM} + \frac{r}{1 - \langle \frac{m_e}{E_e} \rangle} \left[ P_{SM} - \langle \frac{m_e}{E_e} \rangle P_{b \rightarrow \infty} \right] \quad (4.14)$$

Now we collect the terms in front of  $P_{SM}$  and  $P_{b \rightarrow \infty}$  and equate this to a  $b = 0$  Standard Model histogram, giving

$$P_{SM} = \frac{\left[ (1 - r) + \frac{r}{1 - \langle \frac{m}{E} \rangle} \right]}{1 + \langle \frac{m}{E} \rangle} P_{SM} + \frac{\left[ b \langle \frac{m}{E} \rangle + \frac{r \langle \frac{m}{E} \rangle}{1 - \langle \frac{m}{E} \rangle} \right]}{1 + \langle \frac{m}{E} \rangle} P_{b \rightarrow \infty} \quad (4.15)$$

In order for equation 4.15 to hold, the coefficient in front of  $P_{SM}$  must be 1 and the coefficient in front of  $P_{b \rightarrow \infty}$  must be 0. Again, solving both of these gives the same answer since this problem is over-constrained.

$$\therefore b = \frac{r}{1 - \langle \frac{m}{E} \rangle} \quad (4.16)$$

where, again,  $b$  is the Fierz interference term we are trying to introduce and  $r$  is a percentage of events we are mixing between a  $b = 0$  (SM) spectrum and a  $b = -1$  (maximal Fierz in positive energy shift for the spectrum peak) spectrum.

Equations 4.11 and 4.16 represent the blinded value of  $b$  chosen by sampling a percentage of events from a  $b \rightarrow \infty$  distribution and a  $b = -1$  distribution and using them to replace the same number of events from a  $b = 0$  distribution. Afterwards, we tested equations 4.11 and 4.16 by fitting a known input  $b$  value with equation 4.7 and confirmed that they produced a blinded  $b$  value when fitting a  $b = 0$  spectrum. We then randomly sampled which formula to use, corresponding to whether we blinded with  $b < 0$  or  $b > 0$ , and then chose an unknown value of  $r$  corresponding to a blinding value  $b \in [-0.075, 0.075]$ .

#### 4.2.2 Dominant Systematic Uncertainty: Energy Calibration

From prior studies on the UCNA experiment and Fierz Interference extractions, the dominant source of uncertainty was well-known: the energy calibration [Hic13]. In particular, prior to our published results in [Hic+17; Sun+20], current limits on Fierz at the time implied that the energy calibration would have to be correct at the  $\approx 0.1\% - 1\%$  level for a new, competitive limit on the Fierz Interference.

During the pre-Fierz asymmetry analysis, one of the subdominant uncertainties (for the asymmetry extraction) carried through was the energy reconstruction error.

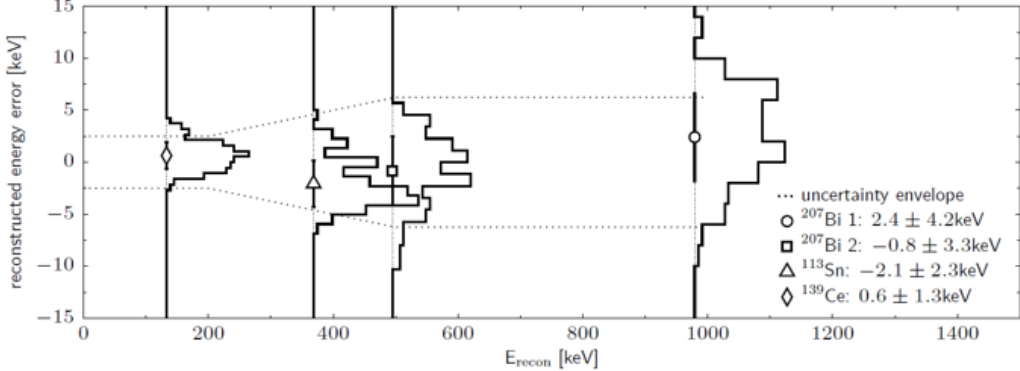


Figure 4.1: The error envelope chosen for the UCNA 2010 asymmetry analysis [Men14]. A histogram of calibration source data is generated for each energy speak and shown with a rotation. The mean and RMS of the reconstructed energy error histograms is used to set the data points. The error envelope is a piece-wise linear interpolation of the calibration source data, chosen in the original asymmetry analysis to conservatively over-constrain the energy uncertainty since it was a subdominant uncertainty. The reconstructed energy error is reconstructed data minus GEANT4 Monte Carlo simulations.

These energy reconstruction errors can generally be differentiated by the corresponding data-taking year. Calibration sources, described in section 2.3.5, give the energy reconstruction uncertainty at four fixed energies - the conversion electron energy of  $^{137}Ce$ ,  $^{113}Sn$ , and  $^{207}Bi$  (two peaks). In the 2010 dataset analysis, a linear interpolation was taken in order to interpolate the energy reconstruction uncertainty and the result is shown in figure 4.1. This “error envelope” is created by taking the reconstructed energy of the conversion electron events and subtracting the Monte Carlo simulation prediction for such calibration sources. The residuals are histogrammed across all the calibration source runs for a given year’s dataset and the resulting mean and standard deviation are shown in the same figure. Additional details on the 2010 error envelope can be found in [Men14].

Once we have this energy reconstruction uncertainty, we use it to set quantitative limits on the dominant systematic uncertainty in a  $b$  extraction. We performed these studies using the procedure described below. Figure 4.2 shows the intermediate steps that are applied to the simulated  $\beta$ -decay electron event as it passes through the various processor steps.

1. Generate a  $b = 0$  Standard Model neutron  $\beta$ -decay electron spectrum.
2. Simulate the electrons, event-by-event, in our GEANT4 simulation. We ex-

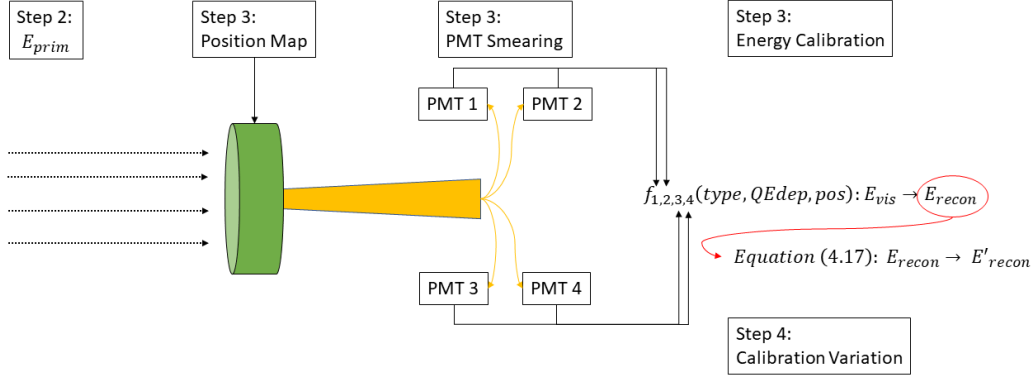


Figure 4.2: A diagram illustrating the different steps in the simulation processor to turn initial  $\beta$ -decay electron kinematics into processed, “detector-like” events. We note that step 1, generating a  $b = 0$  Standard Model spectrum is not shown but it is the input into  $E_{prim}$  in the diagram. In addition, step 5 is not shown but it is the fitting that occurs on the final  $E'_{recon}$  spectrum generated at the conclusion of the event processing.

tract a final deposited energy and quenched<sup>1</sup> energy in the sensitive detectors in our simulation (see section 3.3.4 for a description of our Sensitive Detectors).

3. Take each event’s quenched energy, position, and event type classification, and apply the post-processor detector response model. See section 3.4 for a detailed description of the effects applied.
4. We note that within the detector response model in the previous step, energy calibration variations are applied. This is done to extract a distribution of systematic  $b$  responses due to a potential energy calibration uncertainty or distortion. The details of these energy variations are described below.
5. At the conclusion, we have an energy calibration varied energy spectrum for the neutron  $\beta$ -decay electrons from simulation with an initial input  $b = 0$  (Standard Model) and all the detector effects applied. We then fit with two basis spectra,  $b = 0$  and  $b \rightarrow \infty$  (maximal Fierz), to extract the fractional presence of the  $b \rightarrow \infty$  spectrum and convert that to a numerical value for  $b$ . We note the two basis spectra are processed through the GEANT4 simulation and have the detector response model applied but have no energy calibration variation applied.

---

<sup>1</sup>The quenched energy represents an energy deposition modification given by Birk’s Law. The treatment for quenching in UCNA from 2010-2013 is detailed in [Men14; Bro18].

This procedure was implemented for different distributions of input energy calibration corresponding to different sampling methodology and different error envelopes for the three year’s datasets (2010 described above, 2011-2013 described below). As well, as a final study, we changed the input  $b$  values to study the systematic effects that would be present due to a true non-zero  $b$  value. Having a robust Monte Carlo simulation, described in Chapter 3, allowed us to fold-in several different systematic effects for a more accurate reconstruction of the  $b$ -modified neutron  $\beta$ -decay electron spectrum.

#### 4.2.2.1 Calibration Variation Selection Procedure

In the procedure in the previous section, we discussed applying energy calibration variations to the processed event energy in order to study the effects of the energy calibration uncertainty (interchangeably called the error envelope). The energy calibration variations are carried out by modifying the reconstructed energy with a polynomial variation in the reconstructed energy. Polynomials of up to order  $E_{recon}^3$  were chosen. The extracted Fierz interference was mostly affected by terms up to  $E_{recon}^2$  so in order to speed up computation, after a systematic study on polynomial orders confirmed that 3<sup>rd</sup> polynomials did not contribute significantly more than 2<sup>nd</sup> order, we only took polynomials up to second order for further analysis. Polynomial variations were chosen due to the polynomial nature of the energy non-linearity in the PMTs used in the experiment (Hamamatsu R7725 PMTs with custom-designed bases, more details in [Hic13]). The variations are thus of the form

$$E'_{recon} = A + (1 + B)E_{recon} + CE_{recon}^2 + DE_{recon}^3 \quad (4.17)$$

where the coefficients  $A, B, C, D$  are chosen via a brute force grid search (more details below). We note that the  $(0, 0, 0, 0)$  set of coefficients corresponds to the original analyzer calibration.

The selection procedure is detailed in later sections for each error envelope. As an overview, the polynomials are sampled up to a  $2\sigma$  error envelope (the uncertainty shown in figure 4.1 for example multiplied by 2). They are accepted with fractional Gaussian probabilities based on which error band ( $1\sigma$  or  $2\sigma$ ) they populate where each band is normalized for total number of energy calibration variations. The distribution of polynomials is checked against the measured mean and RMS of the calibration sources and the end point energies (only in 2011-2013 analysis) to ensure consistency at different energy “slices”. Finally, the  $\chi^2/n$  for each energy

### Non-linearity Polynomial Variations

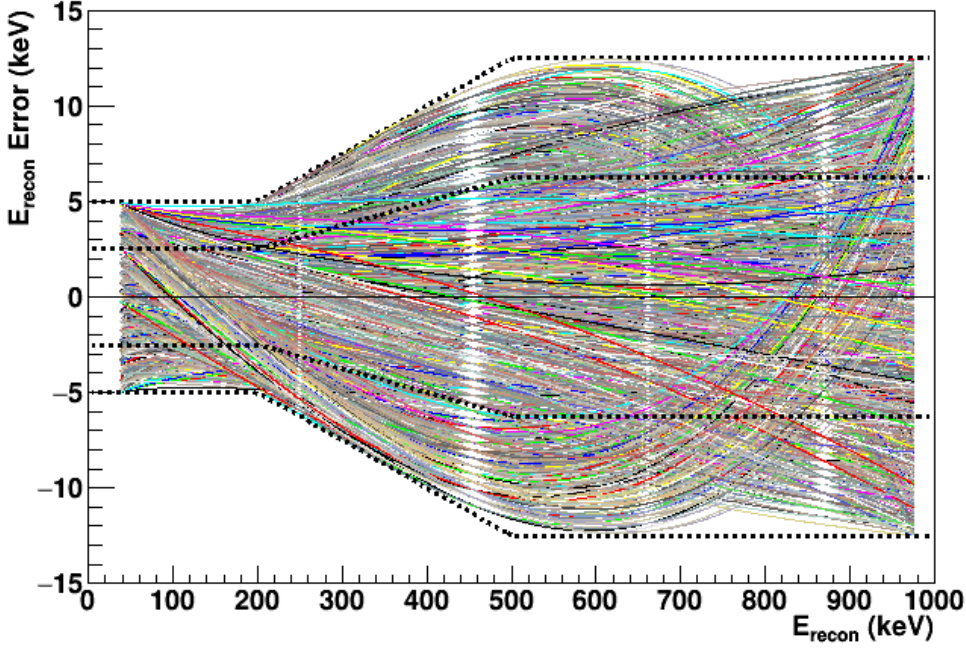


Figure 4.3: A sample distribution of energy calibration variation polynomials for visual interpretation. Polynomials are chosen via brute-force grid search with an accept-reject procedure (see text). Polynomials up to  $2\sigma$  in our error envelope are kept. We show the 2010 error envelope here. These polynomial distributions are used to generate new pseudo energy calibrations.

calibration polynomial is sampled against a theoretical  $\chi^2/n$  distribution (only in 2011-2013) to extract a “statistical” distribution of variation polynomials. After this distribution is extracted, they are applied to a  $b = 0$  Monte Carlo, detector response model processed  $\beta$ -decay spectrum. An initial polynomial sampling can be seen in figure 4.3. A sample of spectral variations can be seen in figure 4.4.

After applying these energy calibration variations, we get a distribution of  $1\sigma$  and  $2\sigma$  probability energy spectra which can be used to extract a “false  $b$  signal” — namely, a non-zero  $b$  which is purely induced by the energy calibration variation. This is the estimation of the systematic uncertainty in  $b$  due to the energy calibration uncertainty and it is the dominant source of uncertainty in the spectral extraction method as we will see in later sections.

#### 4.2.2.2 2010 Dataset Study Results

One can characterize the Fierz interference term in the form of a shape factor, which is defined as the fractional difference between a Monte Carlo simulation  $b = 0$  and

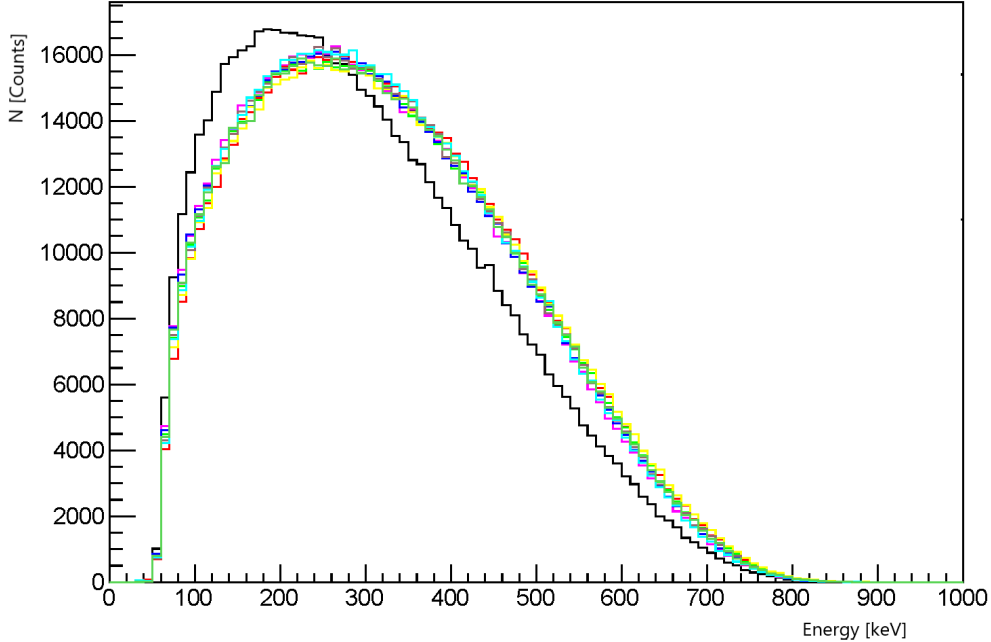


Figure 4.4: A distribution of different neutron  $\beta$ -decay electron kinetic energy spectra, after passing through the detector response model. In particular, all the varied spectra assume the same shape at low energies due to the presence of the trigger function. The shown spectra use energy variation polynomials that are significantly larger than those shown in figure 4.3 — this is chosen for visual illustration purposes. The range of polynomials shown here is  $\pm 5 \text{ keV}$  for the offset term,  $\pm 2\%$  for the linear term, and  $\pm 0.01\%$  for the quadratic term. A  $b \rightarrow \infty$  spectrum is given for comparison (black).

the data. The shape factor for the 2010 dataset can be seen in figure 4.5. The shape factor in the figure uses all the integrated 2010 data and a line is fit to the slope to extract the  $b$  value. We note this is not the only fit methodology available but provides the same extracted  $b$  values as using basis Monte Carlo (the methodology used in this dissertation work).

The shape factor analysis was repeated in the 2011-2012, 2012-2013 dataset analysis but split across octets since the overall data structure was more accessible. The shape factors provided an interesting qualitative study for octet-to-octet variations but ultimately it was not used for the final  $b$  extraction due to incompatibility with a combined fit using the asymmetry data (extensively described in section 4.3).

As an aside, the analysis presented in [Hic+17] was completed concurrently with this analysis. The results of the two systematic studies on the energy calibration uncertainty were consistent. The final extracted result was performed on the same

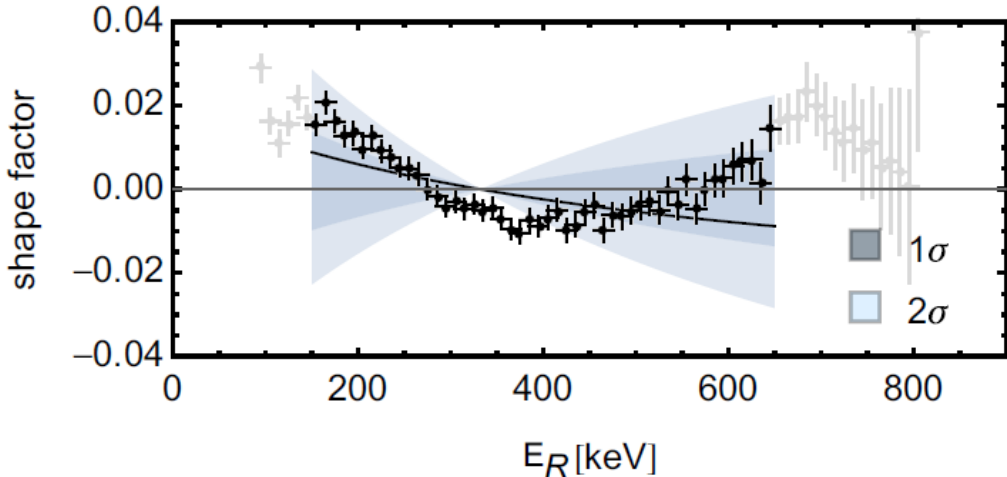


Figure 4.5: The shape factor of the neutron  $\beta$ -decay spectrum as a function of reconstructed energy. Error bars are propagated using standard error propagation. The shape factor is defined as  $\frac{r_{data} - r_{MC}}{r_{MC}}$  and is fitted with a line to extract a  $b$  value. This represents one methodology for  $b$  extraction from energy spectra and was used in the final results in [Hic+17].

2010 dataset and calibration parameters but were otherwise completed independently with only some conceptual coordination. Thus, the work in this dissertation acts as a separate check on the quality of the results obtained in our joint publication.

#### 4.2.2.3 2011-2012 Dataset Study Results

After the 2010 UCNA dataset Fierz Interference analysis, we published the first direct extraction of Fierz interference from neutron  $\beta$ -decay data. This was valuable to the community as a first measurement and an initial commentary on difficulties associated with extracting Fierz from neutron  $\beta$ -decay data. In particular, the currently planned Nab experiment aimed to measure  $b$  with a precision of 0.001 [Fry+19] but subsequently needed to invest more effort in lowering projected energy reconstruction systematic uncertainties after our published results. The extracted value itself was valuable but not the key feature of this analysis since we aimed to improve the precision using the remaining UCNA data. Throughout the work on the 2010 UCNA analysis, we developed a pipeline for analysis using the spectral fit and wanted to extend this to the 2011-2012, 2012-2013 datasets which were being worked on concurrently (see [Bro18] for a comprehensive description) and hence we intended to have more direct control over the data for systematic studies and analysis procedures with a focus on Fierz interference.

The principal difference in the spectral extraction method when we switched to the 2011-2012 (and 2012-2013) dataset was differences in the energy calibration error envelope. During the 2010 dataset analysis, a more sophisticated method for the error envelope definition than the linear interpolation between calibration source error points was developed. The method was as follows: calibration polynomials up to second order were chosen and accepted-rejected with probability based on the four calibration source points in experimental run. The resulting “envelope” of these accepted calibration curves formed a new, asymmetric error envelope.

We note this new method for developing an error envelope was being done concurrently in time with the asymmetry analysis. When the new error envelopes were finalized, the asymmetric nature of the error envelope would have necessitated non-trivial changes in the analysis pipeline to accommodate asymmetric energy calibration error. However, since the energy calibration uncertainty was subdominant (and indeed largely suppressed) in the asymmetry analysis, a conservative symmetric error envelope was taken where the largest  $\pm$  deviation from 0 reconstructed error was used as the  $\pm$  error in both directions. This is shown in figure 4.6. This modification enabled smooth integration of a new error envelope constructed with a more sophisticated sampling methodology into the asymmetry analysis pipeline.

In contrast, the energy calibration uncertainty is the dominant source of uncertainty in the Fierz extraction. Hence, utilizing this symmetric error envelope would introduce a much larger spread in associated  $b$  uncertainty. So for the spectral extraction method, we take the original asymmetric error envelopes where the final ensemble of calibration polynomials define the full error envelope. We show  $1\sigma$  and  $2\sigma$  bands in figure 4.7.

As with the 2010 spectral fit, once we have the error envelope we can define 1-, 2-, and  $3\sigma$  error bands (note that in figure 4.7 we show up to  $2\sigma$ ). We set the standard Gaussian distributed probabilities for each energy calibration variation to lie in any particular error bands:  $1\sigma \approx 68\%$ ,  $2\sigma \approx 95\%$ ,  $3\sigma \approx 99.7\%$  ([HH10] or standard statistics text). Then, a brute-force grid search on calibration polynomial coefficients  $A, B, C, D$ , equation 4.17, is performed. Then, in an improvement from the 2010 dataset analysis, we take and examine the distribution of calibration residuals at each of the four calibration source energy peaks. The resulting mean and standard deviation of such residuals distribution is compared with the mean and standard deviation of the energy error envelope. In some instances, the distribution was narrower than the value of the error envelope at the calibration source peak

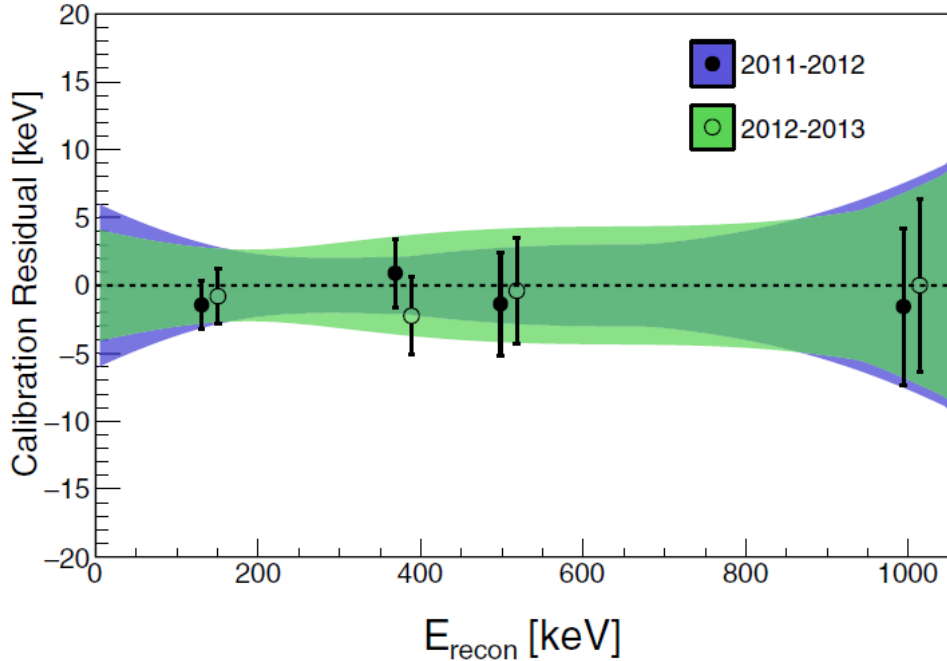


Figure 4.6: Energy error envelopes that have been symmetrized for 2011-2012, 2012-2013 calibration source data. These are the final error envelopes used in the asymmetry analysis [Bro+18]. The calibration residual is defined as  $\frac{E_{MC} - E_{Data}}{E_{Data}}$ .

energies. In those cases, the width of the error envelope was artificially expanded to accommodate more calibration variations until their distribution matched the original error envelope. This was a conservative decision to ensure we were not underestimating our variation distribution. The calibration variation distribution and the associated energy cross-sections are shown in figure 4.8. We note that we conservatively allow the standard deviation at each calibration source energy to match that of the real calibration source data. In practice, when one limits the calibration variations to polynomials up to second order, no single polynomial would satisfy every calibration source maximal standard deviation. Hence, this is a conservative sampling of non-linear energy calibration polynomials that corresponds to a conservative limit on the associated Fierz interference distribution. This was done in order to not restrict the full range of energy calibration polynomials and thus systematically bias our error extraction. The value of the spectral extraction was highly dependent on obtaining an accurate measure of the energy calibration uncertainty and hence we opted to aim for a conservative distribution over biasing the dominant error term in our systematic studies.

We now discuss one more process-improvement in the 2011-2012, 2012-2013

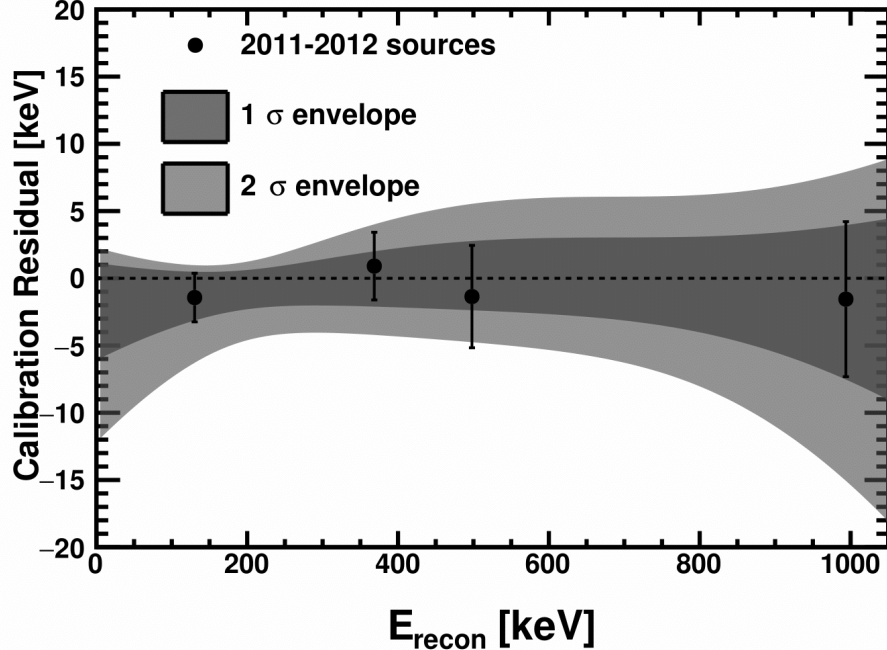


Figure 4.7: The error envelope generated from the 2011-2012 calibration source data, applying the new methodology for constructing error envelopes (see text).  $1\sigma$  and  $2\sigma$  bands are shown. The error envelope is not symmetrized; this leads to an asymmetric systematic uncertainty but significantly reduces the overall spread of accepted energy calibration variations.

spectral extractions compared to the simpler 2010 dataset spectral extraction: resampling our polynomial distribution against a theoretical  $\chi^2$  distribution. Recall our previous discussion of taking a conservative acceptance of polynomial variations. The resulting distribution is uncharacteristic of Gaussian statistics. In order to address this, we take the number of degrees of freedom of the polynomial variation<sup>2</sup> and produce a theoretical  $\chi^2$  distribution (shown in figure 4.9a).

We then convert this theoretical distribution into a probability by

$$P(\text{accept}) = \frac{N_{\chi^2}}{\max(N_{\chi^2})} \quad (4.18)$$

and sample each calibration variation polynomial's true  $\chi^2$  value against it. The resulting distribution is shown in figure 4.9b. This accept-reject sampling transforms the distribution of energy calibration variations into one that can be approximated as statistically distributed. This then represents the systematic error in extracted  $b$

---

<sup>2</sup>The number of degrees of freedom was 1. We have three parameters in the second order polynomial and four calibration source peaks to fit.

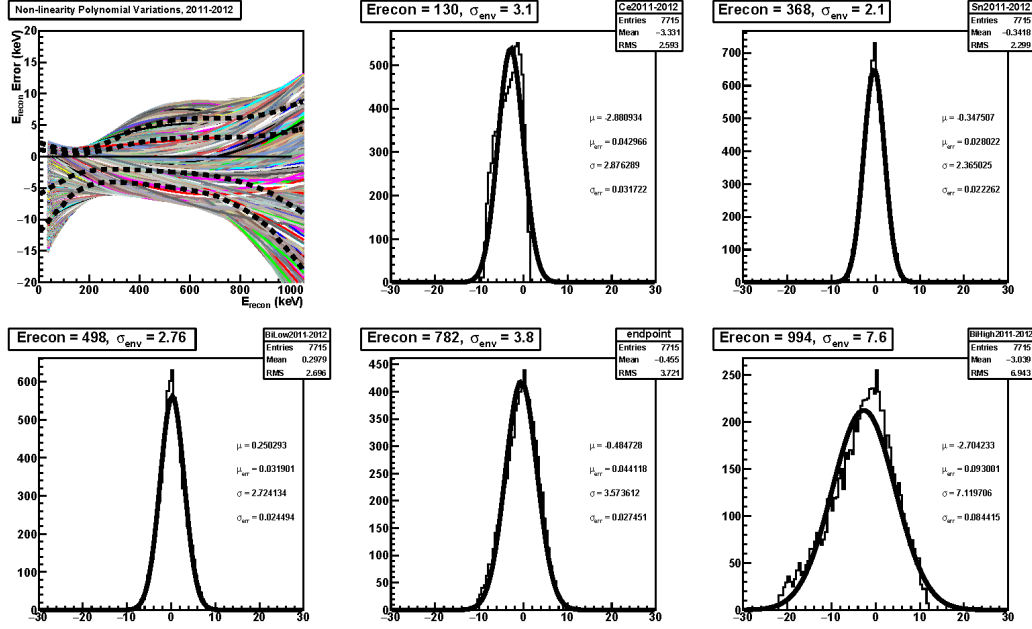


Figure 4.8: Energy calibration variations, similar to figure 4.3, shown for the 2011-2012 asymmetry error envelope. Polynomials up to  $3\sigma$  are shown. Distributions of the energy variations are shown at five “slices” — each of the four calibration source energy peaks and the  $\beta$ -decay energy spectrum end point (included as an additional reference but not used in final decision making). The distribution fitted with a Gaussian approximately matches the error envelope  $\sigma$  at the calibration source energy peaks. This ensures that our variation distribution is an accurate statistical representation of the error envelope.

values due to statistical fluctuations in energy calibration variations across the entire year’s dataset.

The results of this systematic study on the energy calibration uncertainty resulted in error bars of  $[-0.098, +0.105]$  for 2011-2012, and  $[-0.115, +0.173]$  for 2012-2013 (discussed and derived in the next section). This does not compare favorably with the 2010 UCNA dataset analysis  $[-0.058, +0.087]$ . One major reason is because the quality of the energy calibration was slightly worse as compared across the error envelopes, and the resulting larger uncertainties in energy calibration directly corresponded to larger uncertainties in extracted Fierz interference values. The goal of this analysis on the subsequent datasets was to improve the spectral fit error bar with the combined statistical precision and systematic analysis from the 2011-2012 and 2012-2013 datasets. Thus, we move on to the 2012-2013 spectral extraction and examine whether the combination could provide an improvement on a Fierz extraction compared to the 2010 UCNA dataset.

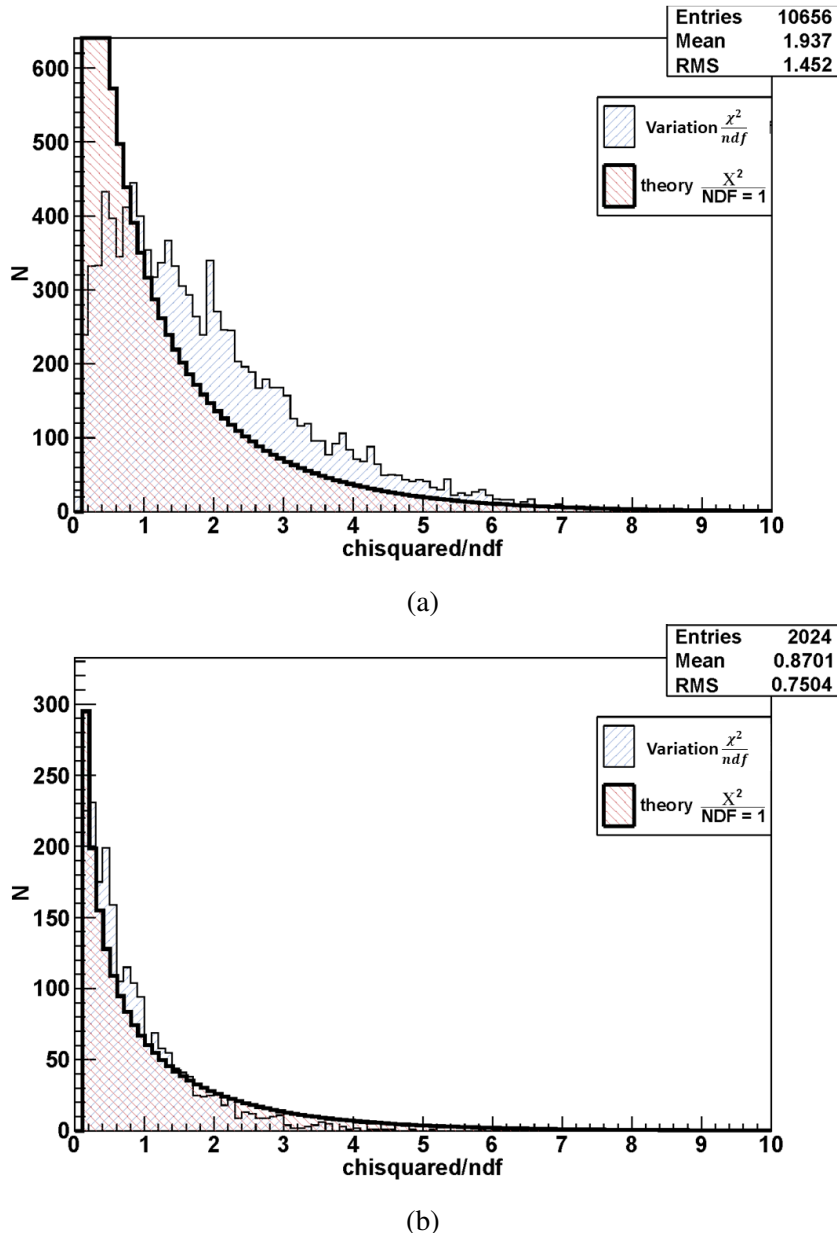


Figure 4.9: The  $\chi^2$  distribution of each energy calibration variation (blue) (a) before and (b) after re-sampling against a theoretical  $\chi^2$  distribution (red). The resulting energy calibration variations can now be approximated as “statistical” and are used in the systematic studies (see text).

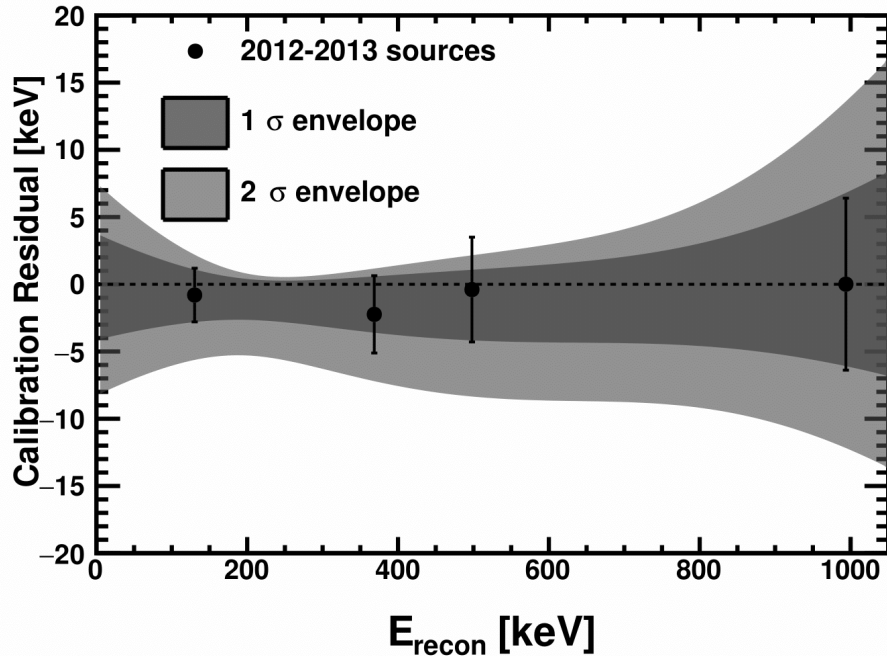


Figure 4.10: The error envelope generated from the 2012-2013 calibration source data, same as figure 4.7.

#### 4.2.2.4 2012-2013 Dataset Study Results

The discussion on the 2012-2013 spectral extraction proceeds very similarly to the 2011-2012 spectral extraction section which directly precedes this. This is due to the similarities in the analysis procedures between the two year's datasets, ultimately differing mostly by the extracted detector response quantities. The major difference between the two datasets was the error envelope, shown in figure 4.10.

The energy calibration in the region of interest ( $\approx 200 \text{ keV}$  to  $\approx 700 \text{ keV}$ ) appears to be worse in 2012-2013. This could be due to a multitude of factors. First, and most notably, during the actual data-taking runs in 2012-2013 there were fewer runs with calibration data taken. Hence, systematic drifts in the energy calibration could have propagated farther before being corrected in the 2012-2013 analysis since there were fewer reliable benchmarks for energy reconstruction. Second, in the 2012-2013 run, it was determined after the data-taking was completed that one of the four  $^{207}\text{Bi}$  pulser gain monitors coupled to the West side detector was not working and hence the reconstructed light yield from the West detector was slightly less reliable. These effects together produced a less reliable energy calibration in 2012-2013 compared to 2011-2012.

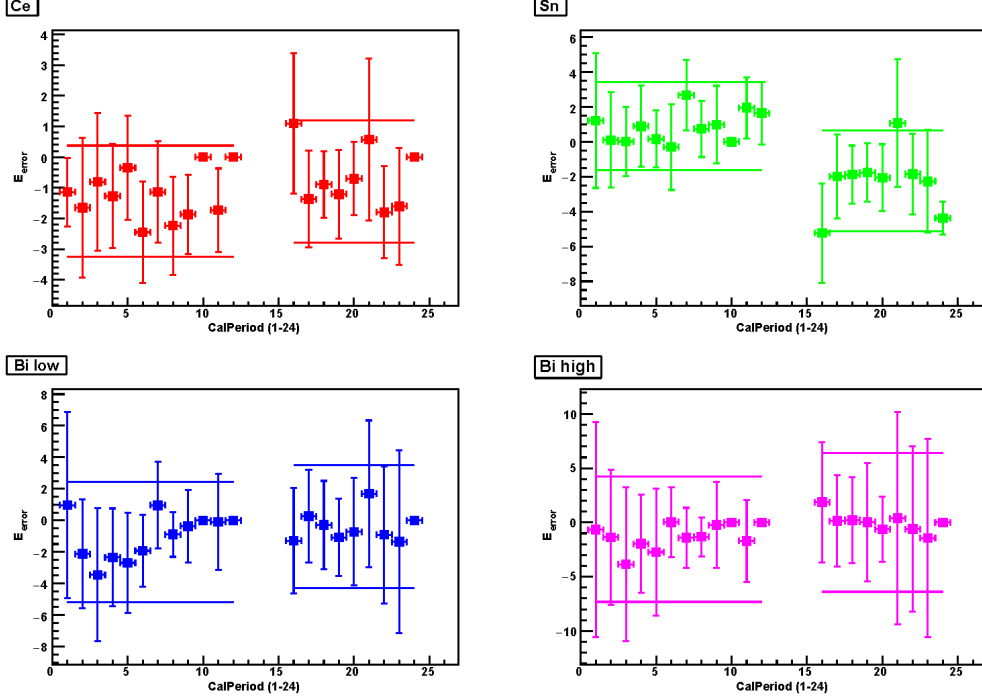


Figure 4.11: Calibration source energy reconstructions, shown as a function of calibration period. There are two distinct calibration sets corresponding to the 2011-2012 and 2012-2013 data-taking run. The gap in the middle is due to a portion of the 2012-2013 calibration being faulty. The horizontal bars are the errors (and central value) from the error envelope for each data-taking year. Some data points have 0 error bar which simply means that data point had no calibration data. We highlight that the calibration source energy peaks approximately agree at the  $^{137}\text{Ce}$  peak and both  $^{207}\text{Bi}$  peaks. There is a non-trivial disagreement between the  $^{113}\text{Sn}$  peaks year-to-year. This is explored as a systematic study (see text).

We studied the effect on  $b$  due to this energy calibration discrepancy. In particular, when we looked at the discrepancy in calibration runs, the source calibration as a function of calibration period for both year's datasets, we get the distribution shown in figure 4.11. From figure 4.11 we can immediately identify that three of the four calibration source peaks show comparable differences in their year-to-year spread. However,  $^{113}\text{Sn}$ , which has an energy peak (368.5 keV) that is close to the largest sensitivity region of Fierz interference (between  $\approx 200 \text{ keV}$  to  $\approx 300 \text{ keV}$ ), shows a discrepancy between the two year's of  $\approx 4.5 \text{ keV}$  in reconstructed energy. In order to understand the effect of this calibration source reconstruction discrepancy, we performed a piece-wise linear interpolation that corrected both the end point energy and the zero-point energy for each spectrum (2011-2012 reconstruction vs 2012-2013 reconstruction). This was performed on  $b = 0$  GEANT4 simulations to

act as a Monte Carlo study on this effect. Internally, this was called “tin stitching” and the prescription is described by

$$E_{stitch} = \begin{cases} \frac{364}{368.5} E_e & 0 < E_e < 368.5 \\ \left( \frac{782}{773.58} - 8.51 \right) E_e & 368.5 < E_e < 1000 \end{cases} \quad (4.19)$$

where the numbers are expressed in keV and chosen such that the end point energies match at 782 keV (see section 4.2.4.1 for more details) and that a correct  $^{113}\text{Sn}$  calibration energy peak at 368.5 keV is reconstructed to the 364 keV that the 2012-2013 calibration produced. We note that we chose to perform an “inverse” stitching by making the properly calibrated 2011-2012 spectrum resemble the incorrectly calibrated 2012-2013 spectrum. This was chosen to simplify the comparisons in code but ultimately does represent the magnitude of the  $b$  shift — the true shift would be the negative of the extracted value due to this stitching procedure. The value of  $b$  extracted after this procedure is applied on a sample 2011-2012 spectrum can be compared with the same spectrum without the energy modifications in equation 4.19 and the magnitude of the  $\Delta b$  can be found.

The Fierz interference extractions differed by about  $\approx 0.17$  when extracted from the  $b = 0$  Monte Carlo, detector-processed simulations using the 2011-2012 vs the 2012-2013 energy reconstruction. In particular, the 2011-2012 reconstruction produced an output  $b \approx 0$  which was consistent with the  $b$  input value. After applying the energy modification in equation 4.19, the extracted  $b$  value was  $\approx -0.17$ . This shows that the discrepancies introduced by the shift due to the  $^{113}\text{Sn}$  source energy reconstruction could be potentially substantial and cover a lot of the range of systematic shifts in the Fierz interference extraction. Unfortunately, at this stage, we did not have other energy benchmarks that could be used to reliably override the  $^{113}\text{Sn}$  calibration source peak. As a result, we accepted a larger uncertainty in the energy calibration (and potential offsets), particularly in the 2012-2013 energy calibration compared to the 2011-2012 calibration. Ultimately, this provided a qualitative justification for not relying principally on the spectral extraction method, particularly in 2012-2013, because we could not fully correct our energy calibration discrepancies.

### 4.2.3 Other Systematic Effects

In this section, we describe and examine quantitatively some other sources of potential systematic error in the spectral extraction of the Fierz interference term. We note that all other sources of systematic error in UCNA are negligible compared

to the energy calibration uncertainty when performing a spectral extraction on the Fierz interference term.

This analysis was initially completed via toy Monte Carlo studies in [Hic13]. Concurrently with the 2010 UCNA dataset extraction, the other systematic effects were quantified using the full UCNA 2010 geometry GEANT4 simulation (topic of Chapter 3) whenever possible as an independent check. A table of the systematic effects and their final quantitative contributions can be found in table 4.1. Each effect is described in more detail below. We note that this is only presenting the 2010 UCNA dataset systematics but that minor changes in detector geometry, negligible improvements in energy calibration, and the subdominant nature of these systematic effects imply that they are approximately adaptable to the 2011-2012 and 2012-2013 dataset spectral analyses. Indeed, for completeness these effects were calculated for the 2011-2012, 2012-2013 datasets and shown to be subdominant but ultimately not included explicitly in our final publication (see [Sun+20]) since they were not relevant to the overall spectral extracted Fierz interference values.

Contribution	$\sigma_b$
Background Subtraction	$\pm 0.005$
Energy Resolution	$\pm 0.01$
Electron Backscattering	$\pm 0.005$
Detector Inefficiency	$\pm 0.02$
Energy Response	$+0.087/-0.056$

Table 4.1: Summary of  $1\sigma$  systematic uncertainties on the 2010 UCNA dataset extraction of Fierz interference [Hic+17]. These uncertainties are generally extracted from simplistic Monte Carlo studies except for the “Energy Response”, which is studied using the full GEANT4 simulation.

#### 4.2.3.1 Background Subtraction

This effect refers to the error in the background model potentially propagating into the final energy reconstruction. In particular, underlying structures in the background model shape would influence the resulting shape of the  $\beta$ -decay electron spectrum. Monte Carlo studies on background rate fluctuations were compared against the overall high statistics of the UCNA electron detection and resulted in subdominant error due to this effect.

#### 4.2.3.2 Energy Resolution

Energy resolution refers to the finite resolution of the PMTs, expressed in units of the reconstructed energy. Since each energy bin “smears” to both higher and lower energies, the  $\beta$ -decay electron energy spectrum lowers the decay rate at the neutron  $\beta$ -decay energy spectrum peak and pushes the decay rates in each bin above the peak to higher energies. We note that low-energy events that get pushed to lower energies are removed due to the trigger acceptance characterized by a trigger function (see below). Ultimately, the shift in spectral shape due to energy resolution is again subdominant because this overall shift does not produce a polynomial signal that would be detectable as a non-zero  $b$ , as noted when studies were performed by introducing a secondary Gaussian energy resolution with characteristic width of several energy bins.

#### 4.2.3.3 Backscattering

Electron backscattering refers to an uncertainty associated with the events that are not classified as “Type 0” (see figure 2.7 for a reminder of event types). These additional event classifications have their own separate energy reconstruction that was less precise due to significantly fewer events. The spectral analyses avoid any complications with multi-scattering event types by simply excluding them. In contrast to the asymmetry analysis, we are able to do this because our uncertainty is not limited by statistics for the Fierz interference analysis. Thus, this systematic error in relation to  $b$  solely refers to the number of incorrectly identified Type 0 events compared to non Type 0 events. This is a quantity that was extracted from the GEANT4 simulation, as discussed in section 3.5. We set a limit on a Fierz interference systematic error by allocating the fractions of misidentified Type 0 events and performing a spectral extraction.

#### 4.2.3.4 Detector Inefficiency

The detector inefficiency refers to the trigger function — a function describing the number of events not detected due to their energy being insufficient to trigger the electronic hardware (see section 3.4.4 for more details). It is an energy dependent probability that, in principle, is calculated for both East and West detector. In order to estimate this effect, the detector inefficiency, which is the probability that the event does not trigger our apparatus, was varied by a large  $\pm 20\%$  factor in order to conservatively estimate this effect. The resulting spectra are fit and a  $b$  value is

extracted. We note due to the chosen low energy cut-off, the majority of effects due to the trigger function are excluded and hence why a large variation of 20% leads to subdominant systematic uncertainties.

#### 4.2.4 Other Spectral Systematic Studies

##### 4.2.4.1 End Point Correction Studies

An additional study in the energy reconstruction analysis was examining the effect of end point correcting the data. In order to do this, we fixed the end point energy of the neutron  $\beta$ -decay spectrum at identically 782 keV, the theoretical end point energy. The end point was extracted by using a Kurie plot which transforms the spectrum via a change of variables that can be fit with a line and the true end point energy can be extracted from said line. The advantage here is that fluctuations at the end of the spectrum do not define the end point — rather the high statistics bins in the middle of the energy range contribute the most to this line and hence dictate the end point energy (the chosen energy fit range of the line also ignores low statistics bins at either energy range). This was done on an octet-by-octet basis. Additional details on Kurie plots for the UCNA 2010, 2011-2012, and 2012-2013 datasets can be found in [Men14; Bro18]. As noted, this was done separately from the energy calibration variations because the linear variations and the linear end point correction would be entangled otherwise.

The results of this study indicated that the spread of fitted  $b$  values from octet-to-octet could be significantly reduced by fixing the end point energy. However, the spread of the  $b$  values was not the dominant source of uncertainty in the spectral extraction — the energy calibration uncertainty was the main source. Folding in an end point correction into the energy calibration variations would be similar to removing one degree of freedom for the variations (all purely linear variations). After studies on the end point correction were completed, it was ultimately decided that there was no additional reliable calibration data that would fix the end point since the energy calibration was performed on a PMT-by-PMT basis and did not constrain  $E_{recon}$  to produce a fixed end point energy. We did not want to change the original calibration used in the asymmetry analysis nor could we justifiably re-correct the energies to fix the end point energy. Thus, this remained an interesting study to see how much false  $b$  was contained in the end point variations.

#### 4.2.4.2 LED Studies

This section discusses qualitatively the implementation of an LED pulser in the 2011-2012, 2012-2013 UCNA data-taking runs. In these runs, an LED pulser was installed that pointed towards the plastic scintillators of the UCNA apparatus and pulsed with wavelengths corresponding to blue and red light. In principle, the different energy responses of the plastic scintillators and readout electronics could be reconstructed independently of the conversation electron calibration sources and instead be fully calibrated in-situ using these highly stable LED signals.

In practice, the LEDs were added into the apparatus without the necessary effort to integrate these data streams into the full analysis pipeline. It thus became difficult to calibrate them and extract physically relevant information. Furthermore, the data-taking procedure from previous run cycles was well-established amongst experimenters at LANL and hence these new LEDs were not always used for every data-taking run. This resulted in the presence of LED data that was inconsistent across the full dataset. Finally, the entangled nature of the analysis pipeline provided a barrier to implement incomplete (or piece-wise) LED data. In an ideal setting, the LEDs would have served as a separate energy calibration that would allow us to perform the end point corrections (section 4.2.4.1) and adjust the calibration source peaks (section 4.2.2.4). However, at their stage of development, they were ultimately not integrated in the final analysis pipeline.

#### 4.2.5 Summary of Spectral Extraction Method

The final spectral extractions of Fierz interference for the 2010, 2011-2012, and 2012-2013 datasets are summarized in the first three rows of table 4.3. The measurement values are  $b_{2010} = 0.067 \pm 0.005^{+0.090}_{-0.061}\text{sys}$ ,  $b_{2011-2012} = 0.072 \pm 0.004^{+0.108}_{-0.101}\text{sys}$ , and  $b_{2012-2013} = 0.044 \pm 0.008^{+0.174}_{-0.117}\text{sys}$ . At the time of publication, the  $b_{2010}$  measurement was the first direct extraction from neutron  $\beta$ -decay spectra. Our improved analysis pipeline ultimately did not improve the measurement in 2011-2012 and 2012-2013 but the subsequent measurements still added to the available set of  $b$  measurements.

We reiterate that the energy calibration error is the dominant source of error, that it was estimated using energy calibration variation polynomials consistent with the energy reconstruction uncertainty, and that the error did not improve year-to-year across the different UCNA datasets for reasons discussed in section 4.2.2.4. In reality, the spectral extraction was not a breakthrough measurement of the Fierz

interference since the measurement uncertainty was not a significant improvement on limits at the time of publication. However, the results were valuable as a test of neutron  $\beta$ -decay to extract values of the Fierz interference, and the measurements still contribute to the overall PDG average.

The spectral extraction proceeded to such level of detail because the original goal was to provide a supplementary result from the 2010, 2011-2012, and 2012-2013 UCNA datasets, namely a direct measurement on the Fierz interference. This was pursued for some time in an attempt to produce a competitive measurement by using the various methods described in the preceding sections to reduce the dominant systematic error. In the end, the efforts on constraining the energy calibration error were insufficient. Hence, at some point of diminishing returns, it was proposed to present both the direct spectral measurement and the asymmetry extraction of  $b$  (described extensively in the next section, 4.3). Previous estimates of the sensitivity of  $A$  to  $b$  internal to the collaboration showed that the asymmetry would yield a comparable precision measurement that would be limited by the statistical precision of  $A$ .

### 4.3 The Asymmetry Extraction Method

In this section, we describe the analysis to extract a value of the Fierz interference from the neutron  $\beta$ -decay asymmetry term,  $A$ , and specifically the energy-independent (within the Standard Model) representation,  $A_0$ . The asymmetry measurement and associated analysis was also completed by collaborators within the UCNA collaboration. Indeed, the reader will recall that UCNA was originally designed to measure  $A$  from UCNs. In fact, the detailed analysis of  $A$  that corresponds to the 2010 dataset and that which corresponds to the 2011-2012, 2012-2013 datasets can be found in [Men14; Bro18] respectively. Here, we build upon the work done in the asymmetry analysis, notably on calibration, detector response model, and systematic studies, to fit for a non-zero  $b$  term in the paradigm of non-zero  $b$ . This is termed the “asymmetry extraction”<sup>3</sup> method for Fierz interference since it uses the energy dependence of  $A_0$ , which is energy-independent in the Standard Model, to measure a value and uncertainty of  $b$ .

---

<sup>3</sup>This is not to be confused with the proper asymmetry extraction which is measuring the asymmetry value  $A$  and the energy independent asymmetry  $A_0$  from the UCNA datasets. In our context, “asymmetry extraction” refers to the measurement of the Fierz interference term if it were non-zero by fitting the  $A_0(E_e)$  with a Standard Model  $A_0$  constant and a non-zero  $b$  term.

### 4.3.1 The Asymmetry Definition

#### 4.3.1.1 Constructing an Asymmetry

A simple quantity to describe the asymmetry would be the conventional, occasionally termed “bonehead” asymmetry

$$A_{simple} = \frac{N_\uparrow - N_\downarrow}{N_\uparrow + N_\downarrow} \quad (4.20)$$

where, for example,  $N_\uparrow$  is the number of events detected with spin “up”<sup>4</sup>.

Here, we express the asymmetry term,  $A$ , from the conventional neutron  $\beta$ -decay, shown in equation 1.13, in terms of a relative number of decay electrons whose momenta are aligned with and anti-aligned with the neutron polarization. Let us consider why this is termed the bonehead asymmetry. In principle, this quantity would give the fractional discrepancy between decays aligned and anti-aligned with the neutron polarization and hence be a direct measurement of  $A$ . However, it is naive when faced with experimental discrepancies in the East and West detectors — variations in detector efficiencies would propagate directly into the final extracted  $A$  value using equation 4.20.

Instead of taking such a naive definition of the asymmetry as in equation 4.20, we make use of a quantity called the “super-ratio” that, similar to the earlier super sum in equation 4.2, has a particular combination of decay rates in our UCNA apparatus that yields convenient relationships for the experimenter. We define the super-ratio as

$$SR = \frac{r_1^\downarrow(E_e)r_2^\uparrow(E_e)}{r_1^\uparrow(E_e)r_2^\downarrow(E_e)} \quad (4.21)$$

where, for example,  $r_1^\downarrow$  is the decay rate in detector 1 (interchangeably called East), when the spin state is down (neutron polarization anti-aligned with the imposed magnetic field).

At a glance, we can see that this definition of the super-ratio allows the discrepancies in detector inefficiencies (assuming they are spin-independent), and discrepancies

---

<sup>4</sup>Spin “up” here and throughout this dissertation refers to the spin flipper on state. When the neutrons initially enter, their magnetic moments are aligned with the magnetic field and hence their spins are anti-aligned. When the spin flipper is on, the orientation is reversed and the spins are aligned with the magnetic field. In the “down” state, the spin flipper is off and the spins remain anti-aligned with the magnetic field. This assumes 100% polarization and in practice we use these runs to describe the dominant neutron spin state. See section 2.2.6 and [Dee19] for more discussion on the polarization.

in integrated counts between the spin states to cancel out. Furthermore, due to the presence of the decay rates in each detector on both numerator and denominator, energy-dependent non-linearities are suppressed to first order since the energy dependent effects are typically not spin-state dependent on an event-by-event basis. It is shown [Bro18] that this definition of the super-ratio in equation 4.21 can be used to express the asymmetry as

$$A(E_e) = \frac{1 - \sqrt{SR}}{1 + \sqrt{SR}} = P_n A_0 \beta < \cos\theta > \quad (4.22)$$

where  $P_n$  is the neutron polarization,  $\beta = \frac{v}{c}$  where  $v$  is the electron velocity and  $c$  is the speed of light.  $A_0$ , the asymmetry parameter of interest, can be extracted from this measured asymmetry in equation 4.22 once the polarizations and  $\beta$  are known. We further note that  $< \cos\theta > \approx \frac{1}{2}$  in our apparatus which integrates over the full hemisphere of neutron  $\beta$ -decay electrons that each detector will capture. However, there are subtle effects such as backscattering at large  $\theta$  angles ( $\approx \frac{\pi}{2}$ ) that lead to systematic corrections and uncertainties and hence this equality is only approximate.

Using the super ratio as defined in 4.21 gives a quantity that is physically relevant to the asymmetry that we want to extract and that is also robust against individual detector imperfections.

#### 4.3.1.2 Asymmetry with Fierz Interference

Now we consider how the asymmetry, specifically  $A_0$ , would be modified under the paradigm of non-zero  $b$ . In essence, the presence of a non-zero  $b$  term modifies all the decay coefficients and introduces an energy dependence to  $A_0$  of the form [GNS19]

$$A_{0,b}(E_e) = \frac{A_0}{1 + b \frac{m_e}{E_e}} \quad (4.23)$$

where  $A_0$  is the asymmetry term in the  $b = 0$  paradigm and is nominally energy-independent,  $m_e$  is the electron mass and  $E_e$  is the electron total energy.

Equation 4.23 gives a method for extracting  $b$  from  $A$  (specifically  $A_{0,b}(E_e)$ ): we can fit the measured asymmetry as a function of total energy  $E_e$  to find  $b$ . We note that this is possible because the asymmetry analysis allows us access to these terms; the final  $A_0$  is quoted as a single number (with associated uncertainty) but the extraction of that number was done by averaging over all the data as a function of energy with all Standard Model energy-dependent terms included. That analysis then fit the energy-dependent data to a constant value which yielded  $A_0$ .

During the Fierz interference spectral analysis, the asymmetry analysis of the 2011–2013 datasets occurred concurrently. As a result, we had access to blinded asymmetry data as a function of energy<sup>5</sup>. With the  $A_0$  expressed as a function of energy (even though all the energy-dependent terms had been accounted for), we were able to apply equation 4.23 to fit the asymmetry data and extract a  $b$  value. After we completed the spectral extraction and concluded that our spectral systematic errors (section 4.2.5) were too large to be competitive, we turned our attention to the super-ratio asymmetry extraction. In the following subsections, we discuss the various components of uncertainty in our super-ratio asymmetry extraction of the Fierz interference and show that the asymmetry extracted value, even when accounting for the different sources of uncertainty, becomes the leading precision measurement.

#### 4.3.1.3 Blinding the Asymmetry Extraction

The blinding on the asymmetry extracted Fierz interference is simple by comparison to the spectral extraction (section 4.2.1.3). We take the data (or data-like Monte Carlo) of the  $A_0$  values as a function of energy and apply the multiplicative factor in equation 4.23. Then, in order to blind the asymmetry data with an input value of  $b$ , we read in a pre-determined value of  $b$  between  $[-0.075, 0.075]$ . This is a reasonable range since our UCNA 2010 dataset results give a half-width of  $\sigma_b \approx 0.075$ .

We note that the method for blinding the asymmetry data chosen also modifies the extracted  $A_0$  parameter. Namely, when we multiply the asymmetry,  $A_0$ , by the denominator of equation 4.23 (i.e. by  $\frac{1}{1+b\frac{m_e}{E_e}}$ ), the newly extracted asymmetry,  $A_{0,b}$ , is not the same as the original  $A_0$ . This is because the multiplicative factor for the blinding is not chosen to be normalized to 1 over the fit region. There is no inherent disadvantage to this choice — we simply note that the extracted blinded asymmetry value,  $A_{0,b}$  is different from the unblinded asymmetry value,  $A_0$ .

#### 4.3.2 The Fierz Interference from Asymmetry Extraction

##### 4.3.2.1 Statistical Uncertainty

The asymmetry analysis was statistics-limited, namely that the statistical error was dominant and that all systematic errors were subdominant. Since the UCNA experiment was originally optimized to measure the  $A_0$  value, the design choices were made such that the resulting  $A_0$  measurement would be statistics limited. However,

---

<sup>5</sup>We note that the blinding described in the asymmetry analysis was applied on the asymmetry term,  $A_0$ , by modifying the detector rates in one of the detectors. The blinding of the Fierz interference terms described in sections 4.2.1.3 and 4.3.1.3 refer to dedicated efforts to blind the  $b$  term.

it is not immediately clear whether the  $b$  value extracted from the  $A_0$  results would also be statistics limited. We ultimately show in the following sections on systematic errors, 4.3.3, that this is the case: the super-ratio asymmetry suppresses the systematic effects at such a level that they are subdominant compared to the statistical error.

We fit each year’s UCNA dataset (2010, 2011-2012, 2012-2013) for  $b$  and extract statistical error bars of  $\pm 0.071$ ,  $\pm 0.063$ ,  $\pm 0.083$  respectively. The final results are given in table 4.3. In the following subsections we present the full Fierz interference error decomposition and the analysis choices that went into the final, unblinded super-ratio asymmetry extraction of Fierz interference.

### 4.3.3 Systematic Studies

In this section, we discuss the studies performed to quantify the various sources of potential systematic error in the asymmetry extraction of Fierz interference analysis. Our discussion starts with the energy calibration uncertainty since considerable effort was spent on this source of error in the spectral extraction. Once the foundation for such a study was laid, it was simple to adapt it to the asymmetry extraction and show, as expected, that the energy calibration uncertainties were suppressed to first order by using the super-ratio asymmetry.

#### 4.3.3.1 Energy Response Systematic Uncertainty

We start with a distribution of energy calibration variation polynomials for each datasets error envelope, described in detail in section 4.2.2.1 and apply them to a Monte Carlo  $b = 0$ ,  $A = A_{0,PDG}$  simulation with errors at each energy bin given by the statistical errors in the data. Thus, three Monte Carlo datasets are prepared, corresponding to the statistical errors for the 2010, 2011-2012, and 2012-2013 datasets. The Monte Carlo “data” is converted to  $A(E_e)$  by multiplying by energy-dependent terms such as  $\beta = \frac{v}{c}$  and the form factor corrections described in section 3.3.3.1. Next, for each year’s dataset, the Monte Carlo generated  $A(E_e)$  had each bin center shifted according to the energy calibration variations associated with that year’s energy envelope, resulting in a distribution of  $A(E'_e)$ . Finally, the varied  $A(E'_e)$  is divided by the aforementioned energy dependent effects with the new energy  $E'_e$  to recover an  $A'_0$ . When all the energy calibration variations are used, we get a distribution of  $A'_0$  values expressed as a function of energy (nominally a constant  $A'_0$  if the energy calibration had negligible impact). These  $A'_0(E_e)$  are

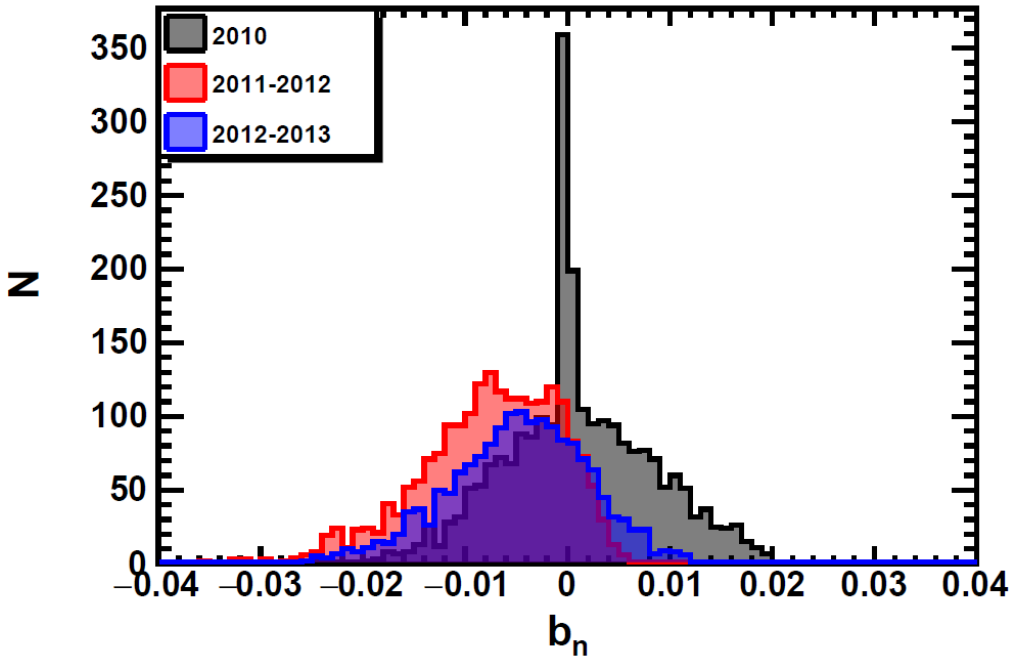


Figure 4.12: Distribution of extracted values of  $b_n$  from applying energy calibration variations to  $b = 0$  simulated asymmetry data. We highlight the bias and spread as estimators of the error associated with the energy calibration variations on the asymmetry extraction of Fierz interference. The peak at  $b = 0$  for the 2010 dataset is likely due to the symmetric error envelope used allowing a larger phase space of energy calibration variations that produce a  $b = 0$ .

fitted with equation 4.23 to extract a distribution of  $b$  as a result of energy calibration variations being applied to the asymmetry. The distributions can be seen in figure 4.12.

We note several highlights:

1. The asymmetric nature and bias of the 2011-2012 and 2012-2013 distributions is due to the asymmetric error envelopes selecting calibration variation polynomials with an overall bias.
2. The 2010 distribution has no such bias in fitted  $b$  value due to the symmetric error envelope. There is a large peak at  $b = 0$  due to the symmetric error envelope accepting a larger fraction of polynomials that do not significantly distort the  $b$  value.
3. There is an induced bias with the 2011-2012 and 2012-2013 distributions.

However, the RMS values from these variation distributions indicate that the systematic error is larger than the bias. We ultimately did apply a bias correction of 0.0050 for the 2011-2012 dataset and 0.0075 for the 2012-2013 dataset for the final extracted Fierz value due to this energy response asymmetric effect. These values are taken from the mean of the distributions shown in figure 4.12. Furthermore, we checked the spread of biases for an induced  $b$  effect. Namely, we reproduced the above procedure with a Monte Carlo input  $b$  of the data-fitted  $b \pm \sigma_{b,stat}$  and examine the range in central value offsets when applying the 2011-2012, 2012-2013 energy variations. The  $\pm \sigma_{b,stat}$  gives a spread in biases of  $\approx 0.0005$  for 2011-2012 and  $\approx 0.0006$  for 2012-2013. Both of these bias spreads are negligible by comparison to the overall energy response error bar. For completeness, we conservatively took the error as fully correlated with the energy calibration variation error (the RMS of the distributions in figure 4.12) and added them linearly in the final energy response uncertainty.

4. The final value for the energy response uncertainty was the same across all three datasets to within the last significant digit despite the different energy error envelopes. This again reinforces that the super-ratio asymmetry is largely insensitive to distortions in the energy response.
5. The final energy response error was 0.007. This is to be compared with the spectral extraction 4.2.5 where the final uncertainties associated with the spectral extraction range in magnitude from 0.058 to 0.173. The super-ratio asymmetry extraction method reduces the dominant source of error from the spectral extraction by a factor of  $\approx 10$ .

#### 4.3.3.2 Electron Backscattering

In this new extraction method for Fierz, we now concern ourselves with the dominant uncertainties in the asymmetry analysis which are those that result from  $\beta$ -decay electron scattering in the detectors. We discussed backscattering in UCNA in section 2.4.4 and provide a summary of different backscattering event types in figure 2.7. Here, our study of this systematic on Fierz interference is brief - the completed asymmetry analysis decomposed the sources of error from Monte Carlo studies in [Bro18].

We take the determined Monte Carlo correction to the asymmetry for backscattering,

shown in figure 4.13, and distort our Monte Carlo asymmetry by inducing a slope consistent with the uncertainty in the Monte Carlo correction (and error). We do this by taking the percentage  $1\sigma$  uncertainties at the low and high energies of our asymmetry Fierz interference extraction region and applying a  $\pm 1\sigma$  distortion to our Monte Carlo asymmetry at the low and high energies. This ultimately results in a  $\pm 0.31\%$  at the low energy and the same magnitude of  $\mp 0.31\%$  at the high energies. The distortion is then fit with a linear interpolation between the two points at either end of the fit region, resulting in two lines with opposite signs in slope<sup>6</sup>. We then fit the new distorted lines with equation 4.23 and extract a  $\pm \sigma_{b,backscattering}$ . A simple Monte Carlo study shows that taking a  $+(-)\sigma$  distortion at one end of a line and a  $-(+)\sigma$  distortion at the other end results in an error on the slope that is  $\sqrt{2}\sigma$ . Hence we divide by  $\sqrt{2}$  to get the final uncertainty due to backscattering. For the 2011-2012 and 2012-2013 datasets, these Monte Carlo corrections for backscattering and  $\cos\theta$  (discussed in the next section) resulted in a year-to-year difference on  $\Delta\sigma_b \approx 0.001$ , which is negligible compared to our overall uncertainty. To simplify the analysis and presentation, we conservatively took the larger uncertainty between 2011-2012 and 2012-2013 in Monte Carlo corrections and obtained a final systematic uncertainty due to backscattering of  $\sigma_b = 0.013$ .

#### 4.3.3.3 $\cos\theta$

The study for the  $\cos\theta$  systematic effect proceeds very similarly to the preceding section 4.3.3.2. This effect can be understood as the energy loss associated with angular acceptance of  $\beta$ -decay electrons. Because a minimum energy is needed to trigger the detectors in the UCNA apparatus, there is a preferential energy selection depending on the angle of incidence. In fact, recall this forms the motivation for the field profile chosen for the experiment, described in section 2.3.4. There is an energy dependence for the energy loss due to passing through the detectors and decay trap windows for different  $\beta$ -decay electrons depending on their initial decay angle and thus their trajectory as they spiral along the field lines (see figure 2.5 for a schematic). In the asymmetry analysis, this was termed the “ $\cos\theta$ ” effect.

A study of the  $\cos\theta$  effect on the asymmetry was also passed to us from the asymme-

---

<sup>6</sup>We chose a linear interpolation because it would be the most conservative estimate on uncertainty since a linear distortion would produce a maximal  $b$  compared to other polynomial functions. Why? We remind the reader of the form of the asymmetry due to a non-zero  $b$ , equation 4.23. For small values of  $b$ , one can Taylor expand the factor and reduce the equation to  $\approx 1 + b \frac{m_e}{E_e} + \dots$ , which is of the form of a linear distortion. Since we did not expect the systematic uncertainty to be dominant, we were satisfied taking a linear interpolation which would induce a maximal Fierz value.

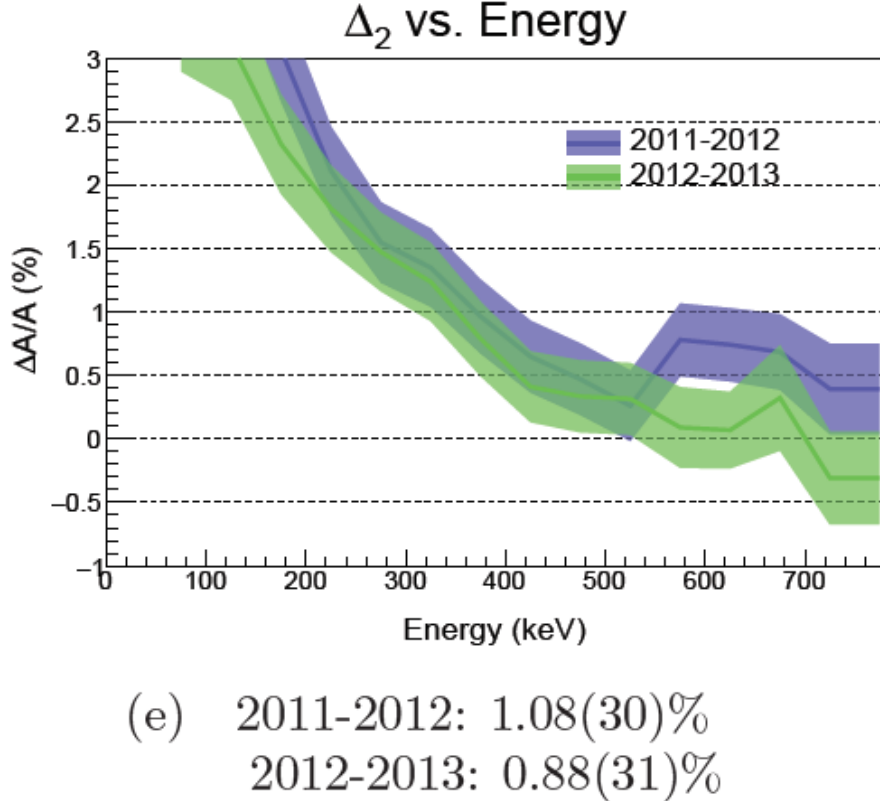
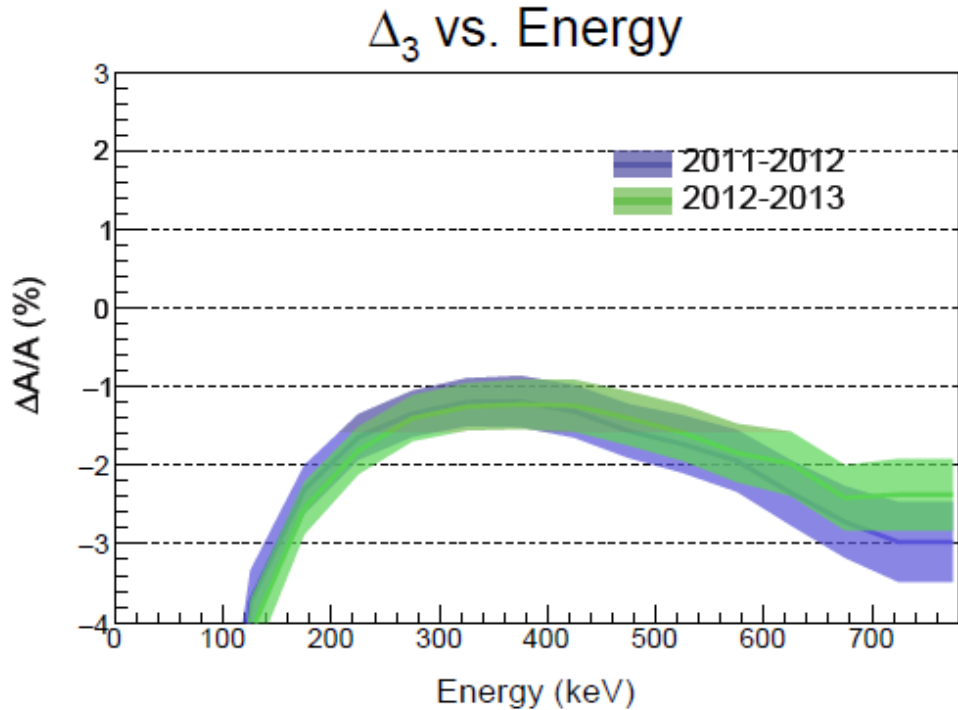


Figure 4.13: Summary of the percentage corrections applied to the final asymmetry as a function of energy for the electron backscattering systematic effect for both years (see [Bro18] for further details). We used the uncertainties at the end point energies of the fit window to estimate the effect on  $b$  (see text).

try analysis. The Monte Carlo corrections were completed and shown in figure 4.14. The  $\pm 1\sigma_{b,\cos\theta}$  uncertainties at the low and high energies of the Fierz interference extraction region are determined. They result in a  $\pm 0.31\%$  shift at low energies and a corresponding  $\mp 0.51\%$  shift at high energies. A linear distortion is applied to a Monte Carlo asymmetry between both shifts and the resulting distortions are fit for a  $b$  value. This results in  $\sigma_b = 0.017$  for both datasets. Again, there was a slight discrepancy between the two years 2011-2012, 2012-2013. The more conservative, larger error was taken but we note the difference was  $\Delta\sigma_b \approx 0.001$ .

#### 4.3.3.4 Background Subtraction

A simple Monte Carlo study on the impact of background subtraction was performed to quantify a limit on the  $1\sigma_b$  uncertainty due to the background. We used  $2 \times 10^7$  simulated neutron  $\beta$ -decay events (with spin up and spin down) and applied a  $1\sigma_N$



(e) 2011-2012:  $-1.53(33)\%$   
2012-2013:  $-1.51(33)\%$

Figure 4.14: Same as figure 4.13 except correcting for the  $\cos\theta$  systematic effect.

shift to the two detector rates based on the background model used in the asymmetry analysis. First, we converted the background model rates into background counts using the known ratios of live-time. Then, we increased or decreased the counts in every energy bin in both detectors, for both spin states, by  $1\sigma_N$  using Gaussian counting statistics, which was applicable at the statistics that the background model uses. We then fit with equation 4.23 to see what level of induced  $b$  this background distortion could create. We note this is much larger than an overall  $1\sigma$  effect because in this study every energy bin's event count was increased/decreased. As we have with other subdominant systematic effect, we stopped the study here to conservatively overestimate the  $1\sigma$  which yields  $\sigma_{b,background} < 0.009$ .

#### 4.3.3.5 Detector Trigger Efficiency

A study was done on the effect of the detector trigger efficiency (see section 3.4.4). Namely, we consider the effect of variations in the detection efficiency of low energy events in the UCNA apparatus. As with the 2010 UCNA spectral Fierz analysis, we estimate this effect by taking a variation of  $\pm 20\%$  in the detector inefficiency. That is, we vary the number of events not detected by 20% by adjusting the probability function for detection at each energy bin. This yields  $\sigma_{b,\text{efficiency}} = 0.002$ . This is subdominant compared to the overall asymmetry Fierz extraction.

We note that the detection trigger efficiency in the 2011-2012, 2012-2013 data analyses is  $> 98\%$  which is to be compared with that of the asymmetry and Fierz analyses in 2010 of  $> 90\%$ . This is due to the choice of low energy cut which is 40 keV higher in the 2011-2013 analyses. Ultimately, this contributes to lowering the influence of the trigger function as a source of potential error since the majority of the inefficiency is at low energies.

Furthermore, we emphasize at this stage that during the spectral analysis the detector trigger efficiency correction accounted for the backscattering effects and the  $\cos\theta$  energy loss, both of which are most probable at low energy. Thus, in the spectral extraction of the Fierz interference in section 4.2 we did not separately account for these energy-dependent effects. However, in the asymmetry analysis, these scattering effects are persistent to the final asymmetry and indeed compose a large fraction of the systematic error budget (see error decomposition in [Pla+19]). Hence separate studies were performed to analyze their impact on a potential asymmetry extraction of Fierz compared to the spectral extraction of Fierz.

#### 4.3.3.6 Energy Resolution

The energy resolution refers to the intrinsic inability for the photomultiplier tubes (PMTs) used in the experimental apparatus to fully reconstruct the energy deposited. In particular, there are counting statistics noise associated with the detection of number of photoelectrons that dictate how much light and therefore energy the PMTs read. The energy resolution uncertainty is the systematic effect on extracted  $b$  that a distortion in the energy resolution could produce. Conceptually, the energy resolution “smears” out a detected peak so effectively sharper peaks become broader. Due to the single-bump nature of the neutron  $\beta$ -decay electron spectrum, this detector effect broadens out the end point energies which ultimately distorts the shape and could influence a  $b$  extraction. However, in the super-ratio asymmetry, we will find

this effect cancels out to first order and is suppressed by a factor  $\approx 50$  compared with the spectral extraction energy resolution systematic error.

Typically, energy resolution of PMTs are given by a Gaussian peaked at the central value of the energy with a

$$\sigma_{E_e} = \frac{k}{\sqrt{E_e}} \quad (4.24)$$

where  $k$  is a constant representing the Full-Width Half-Maximum (FWHM) of a Gaussian peak at  $E_e$  and  $E_e$  is the true energy the PMT sees. The right-hand quantity  $\sigma_{E_e}$  is expressed in percent.

In the UCNA experiment, previous calibration using the  $^{207}\text{Bi}$  high energy peak placed the energy resolution at  $\approx 8\%$  per PMT at kinetic energy 1 MeV. We take a reasonable maximum variation of  $\pm 10\%$  on that 8% resolution. This gives a systematic error of  $\sigma_{b,resolution} = 0.0002$ . We compare this value with the  $\pm 0.01$  from the 2010 spectral extraction (see table 4.1). This is largely due to the energy-dependent systematics suppression intrinsic to the super-ratio.

#### 4.3.3.7 Inner Bremsstrahlung

Motivated by questions about our 2010 UCNA direct spectral extraction of Fierz interference at the APS’s annual DNP conference in October 2018, we investigated the potential systematic influences on the Fierz interference extraction due to inner Bremsstrahlung photons which would introduce an energy distortion if measured in coincidence with neutron  $\beta$ -decay electrons. The process can be understood semi-classically as the decay electron leaving the region of the decay proton. When the electron undergoes changing acceleration, the excess energy is released as a gamma and this process is called inner Bremsstrahlung. The main issue is if this gamma is detected in coincidence with a  $\beta$ -decay electron event because it would introduce additional energy in the detectors since the original energy loss for the electron due to radiative effects such as inner Bremsstrahlung are accounted for via the GEANT4 Physics List in our simulation.

In figure 4.15, we show the resulting spectrum from simulating a number of photons in our UCNA apparatus. The simulation takes  $10^6$  photon events at 400 keV and points them directly at our detector. We choose 400 keV because it is near the midpoint of the  $\beta$ -decay spectrum that we can trigger on. The total number of registered events when we apply an energy deposition cut on the scintillator and

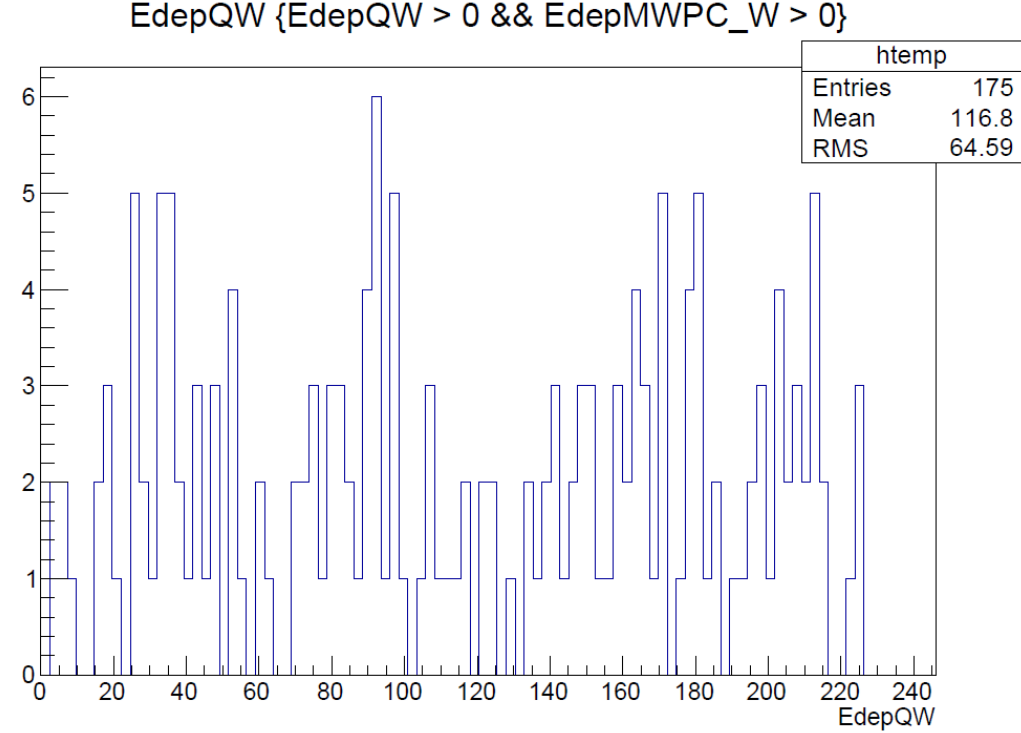


Figure 4.15: Distribution of the quenched energy deposited into the West detectors (minimum energy deposited  $> 0 \text{ keV}$ ) when generating  $10^5$  photons with  $400 \text{ keV}$  initial kinetic energy, pointed directly at the West detector. This gives an effective trigger probability for photons due to inner Bremsstrahlung at the midpoint of our neutron  $\beta$ -decay energy range.

MWPC (the same cuts used in the analysis) is 175. This amounts to a  $10^{-4}$  detection fraction of gammas. Furthermore, gammas in UCNA are not shaped in anyway and decay in a  $4\pi$  solid angle. Noting that the detectors are  $2.2 \text{ m}$  away from the center of the decay trap and that the plastic scintillator face is only  $15 \text{ cm}$  in diameter, we get an additional  $10^{-5}$  suppression factor from solid angle. Finally, we apply the branching ratio of detectable photons measured as  $\approx 3 \times 10^{-3}$  [Bal+16]. We conclude that for the  $\approx 5.3 \times 10^7$  decays in the UCNA integrated dataset, a negligible number would have produced a Bremsstrahlung  $\gamma + \beta$  coincidence in our detector.

#### 4.3.4 Summary of Asymmetry Extraction Method

In this analysis, we extracted the Fierz interference from the asymmetry constant term  $A_0$  which was determined in a concurrent analysis. During this extraction, we had access to the asymmetry data at different stages in its development. As a result, we were able to perform a Fierz interference extraction on the  $A_0$  data when plotted as a function of energy by using equation 4.23. The error in  $b$  is dominated by the

statistical error as is the original asymmetry dataset the result is derived from. The systematic errors are subdominant and, in particular, energy-dependent systematics that plague the spectral extraction of the Fierz interference are not present since the super-ratio (equation 4.21) suppresses them to first order. A summary of the statistic and systematic errors from the asymmetry extraction of the Fierz interference can be found in table 4.2.

Uncertainty Source	Systematic Uncertainty on $b_n$
Energy Response	$\sigma_b = 0.007$
Electron Backscattering	$\sigma_b = 0.013$
$\cos\theta$ Energy Loss	$\sigma_b = 0.017$
Background Subtraction	$\sigma_b < 0.009$
Detector Inefficiency	$\sigma_b = 0.002$
Energy Resolution	$\sigma_b = 0.0002$

Table 4.2: Summary of systematic uncertainties on  $b_n$  greater than  $10^{-4}$ . The energy calibration variation uncertainty is computed for different error envelopes; however, the values are ultimately the same for all three datasets. Similarly, other effects were computed separately for each dataset but we conservatively took the larger uncertainty (see text) when there was not an appreciable difference. Table first published in [Sun+20].

Here we note that in equation 4.23, there are two parameters to extract:  $b_n$  and  $A_0$ . When we introduce the paradigm that allows for non-zero  $b$ , we introduce a correlated error between  $b_n$  and  $A_0$ . Namely, when we fit each year's datasets with equation 4.23, we get new  $A_0$  values and new  $\sigma_{A_0}$  values which are  $\approx 10$  times larger than the PDG listed values of  $\sigma_{A_0}$ <sup>7</sup>. The new extracted values of  $A_0$  for the 2010, 2011-2012, and 2012-2013 UCNA datasets are  $A_{0,2010} = -0.1231 \pm 0.0048$ ,  $A_{0,2011-2012} = -0.1258 \pm 0.0044$ , and  $A_{0,2012-2013} = -0.1236 \pm 0.0059$ . We note that with the  $\approx 10\times$  increase in the error, the new extracted  $A_0$  from unblinded data are consistent with the PDG  $A_0$  values.

#### 4.4 Combining the Extraction Methods

Towards the conclusion of the supplementary Fierz interference analysis, we had essentially two additional spectral extractions, corresponding to datasets 2011-2012 and 2012-2013, and three new super-ratio asymmetry extractions, corresponding to datasets 2010, 2011-2012, and 2012-2013. The 2011-2012, 2012-2013 dataset

---

<sup>7</sup>PDG assumes  $b = 0$  since this is true within the Standard Model weak interaction which is a purely vector - axial-vector interaction and Fierz is sensitive to scalar and tensor interactions.

extracted  $b$  values were blinded. What remains was to unblind and combine these results into a final presented value of  $b$ .

#### 4.4.1 Energy Fit Window Study

As a study prior to combining our Fierz interference results, we were interested in the systematics vs statistics error trade-off when different energy windows are chosen. Conceptually, the trade off proceeds as follows. We have poorer quality energy calibration error envelopes at lower energies<sup>8</sup>. So we reduce in systematic uncertainty if we increase the low-energy fit window cut off. However, in order to perform a spectral fit, the  $\beta$ -decay spectrum must contain enough shape information and, in particular, the inflection point of a maximal Fierz spectrum, figure 3.4, which is around 250 keV must be retained for a high-quality fit. So from the spectrum perspective, we improve by raising the low-energy cut off region but not above the Fierz spectrum inflection point.

With the super-ratio asymmetry Fierz interference extraction method, we are limited by statistics. Due to the shape of the UCN  $\beta$ -decay electron spectrum, we gain more statistics by including low-energy bins, up until we start running in to the trigger function at which point there are no more included events because the trigger function diminishes very quickly below 100 – 150 keV. Then from the asymmetry perspective, the optimal Fierz extraction comes from lowering the low-energy cut but not below 150 keV.

Furthermore, this conceptual discussion does not consider the geometric, calibration, and statistics differences between the 2011-2012 and 2012-2013 datasets (recall that we are not considering the 2010 dataset for the time being since it was unblinded). Of course, in principle, we can take different energy fit regions for the two different extraction methods. We note however that ultimately the asymmetry Fierz extraction would likely have to be fixed at the same asymmetry fix region that was used in the  $A_0$  extraction. This is because we took the asymmetry data from that analysis and the resulting calibration, analysis, and interpretations are performed for a certain energy fit region. So then the only interpretation from these energy fit region studies is whether or not there is another clearly optimal choice for asymmetry — if not, then we should default to that which was used in the asymmetry analysis.

The studies used both blinded super-sum spectrum data and blinded super-ratio

---

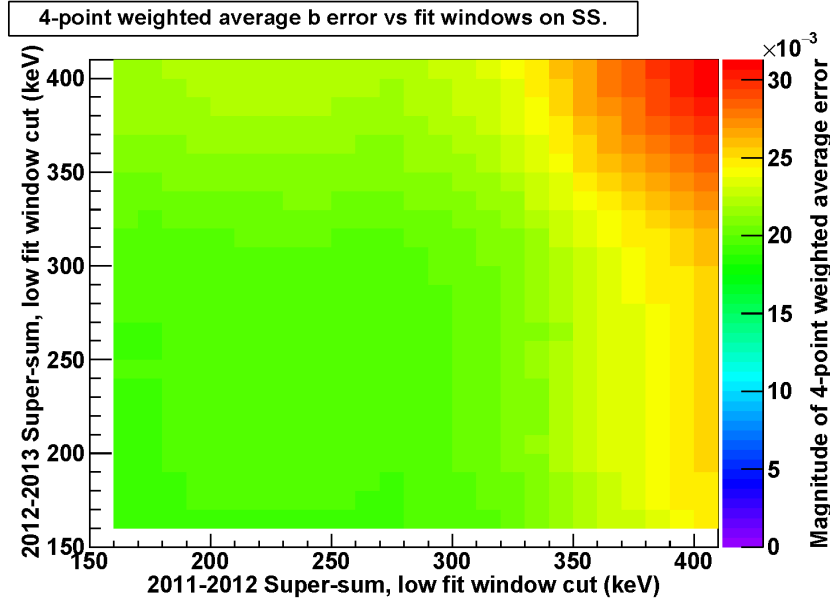
<sup>8</sup>We also have poorer energy calibration envelopes at high energies, but due to the decreased sensitivity to Fierz away from the  $\beta$ -decay spectrum peak this is less of a concern.

asymmetry data. We held either the super-sum or super-ratio fit windows fixed and varied first the low-energy threshold of the other dataset, for both 2011-2012 and 2012-2013 datasets. Once we settled on an “optimal” low-energy threshold, we would hold that fixed and check the super-ratio or super-sum fits by varying the high-energy cutoff, for both year’s datasets. This iterative optimization order was chosen because the low-energy window had a more direct impact on the extracted Fierz interference results. Figures 4.16a and 4.16b show only a sample of one of these studies where we separately chose the low and high energy fit windows for the super-sum spectral extraction of the 2011-2012, 2012-2013 datasets. We confirmed that the resulting fitting uncertainties as a function of the low and high energy cutoffs is smooth and ultimately resulted in a fit window chosen from  $195 - 645 \text{ keV}$  for both years (no appreciable difference when examining the two datasets with different fit windows).

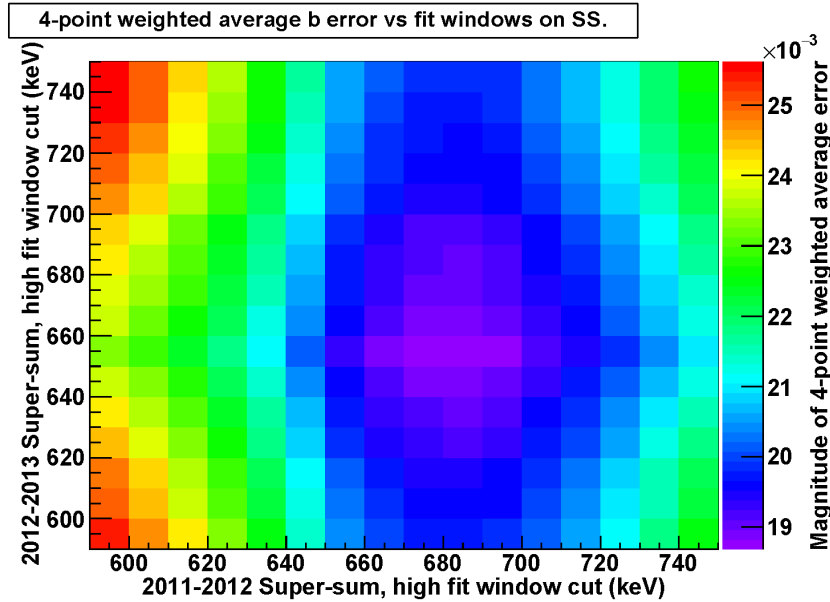
In addition, we also examine how the  $\chi^2$  distribution varies with the energy region cuts. This becomes particularly significant in the context of statistical error driven (asymmetry) vs systematic error driven (spectrum). We wanted to see what cuts were needed on energy region to ensure consistency with a standard  $\chi^2$  distribution so that our fitted error could be approximated as statistical. Figure 4.17 gives a sample of one of the  $\chi^2$  probability plots generated in this study. When we ultimately decided to only use the asymmetry data, we wanted to use this study as a guide to ensure consistency with a standard  $\chi^2$  distribution so that our fitting error could be dominated by statistical fluctuations and not begin to fold in systematics considerations.

After the systematic studies on energy fit region were concluded, we decided to use energy fit regions of  $195 - 645 \text{ keV}$  for the spectral fits and  $190 - 740 \text{ keV}$  for the asymmetry fits, for both the 2011-2012 and 2012-2013 datasets. In addition, we examined the effects of choosing different energy fit regions. We fit the asymmetry data with  $E_{low} - 30 \text{ keV}$ ,  $E_{low}$ , and  $E_{low} + 30 \text{ keV}$ , and with  $E_{high} - 60 \text{ keV}$ ,  $E_{high}$ , and  $E_{high} + 60 \text{ keV}$ . We take the average of these fit values on the low and high end and compare them to the central chosen value for the energy cutoff. At low energy, the shift induced was  $\Delta b \approx 0.003$ . At high energy, the shift induced was  $\Delta b \approx 0.009$ .

Due to the statistics-driven uncertainty of the asymmetry Fierz extraction, these numbers only show the stability of the fit with respect to different energy region choices. In the end there was no optimized method to choose a particular fit



(a) Combined uncertainty on  $b$  as a function of low energy fit window variation. The high energy cut off was originally fixed at  $\approx 735 \text{ keV}$ .



(b) Combined uncertainty on  $b$  as a function of high energy fit window variation. The low energy cut off was originally fixed at  $\approx 195 \text{ keV}$ .

Figure 4.16: A 2D histogram showing the resulting weighted error using a four-point weighted average, in the color bar, of  $b$  where the statistical error is the error used for the super-ratio extraction and the systematic error is the used for the super-sum extraction. The high energy cut off was originally fixed at  $\approx 740 \text{ keV}$ . In terms of minimizing the weighted average error on  $b$ , there is a large acceptable region for the low-energy cut off. The error is varied due to changing the low-energy cut offs for the 2011-2012 dataset against the 2012-2013 dataset.

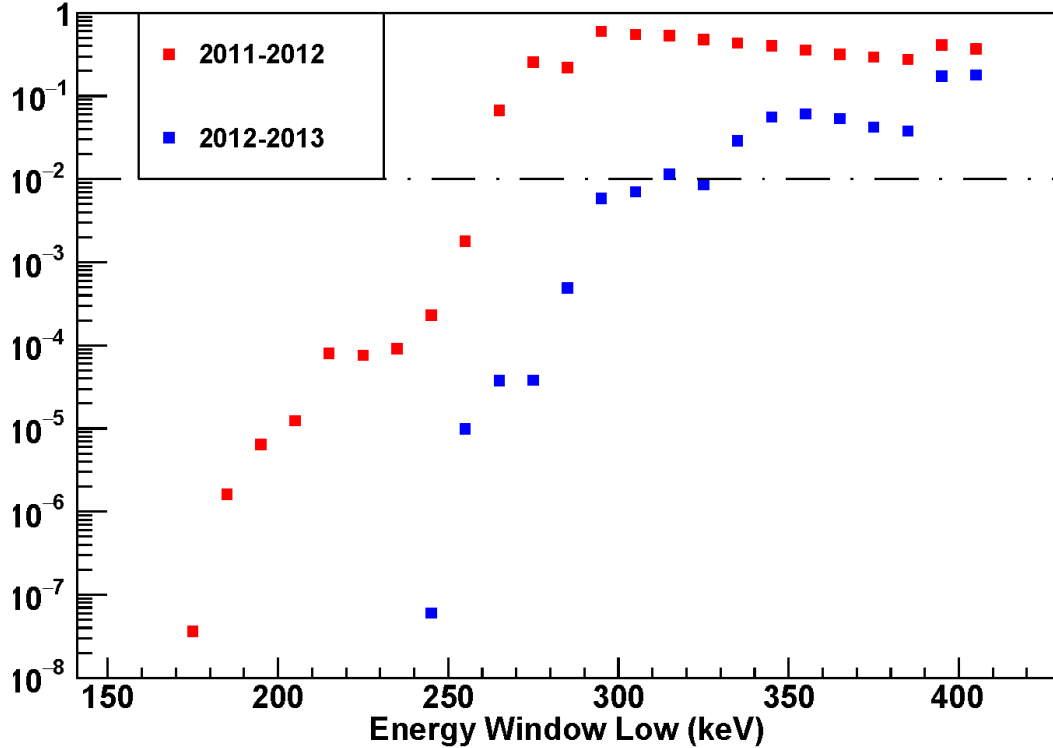


Figure 4.17: Different low energy fit window's  $p$  values. A high energy cut off at  $645 \text{ keV}$  is fixed. A dashed line is included at  $10^{-2}$  to represent the 1% probability that this fit was a statistical anomaly. We use  $10^{-2}$  as an approximate cut off before deciding a fit was dominated by uncertainties that were non-statistical (hence systematic). In general, we see the same behavior as discussed in section 4.2.2.4 with regards to the tin stitching: the 2012-2013 uncertainties are systematically shifted compared to the 2011-2012 uncertainties.

window over another once the decision to use only the asymmetry data in our final measurement was made. This was because trade-off between the systematic error on the spectral fit and the statistical error on the asymmetry fit is removed by omitting the spectral fit results.

#### 4.4.2 Position Fit Window Study

One additional study in the combination of extracted Fierz interference results was the position dependence on the face of the scintillator and how it contributed to the systematic error. The motivation was whether we could, by judicious choice of position cuts, reduce our systematic error in the spectral extraction to be competitive with the asymmetry extracted  $b$  results. This emerged as an interim study when we were considering a weighted average between all four Fierz interference measurements.

Since we had ample statistics for a spectral fit, even within each octet, we considered sacrificing a large fraction of events to focus on improving the systematic uncertainty, with a focus on the energy calibration uncertainty. For the general analysis preceding this section, the fiducial cut on the radius was  $0 < r < 49 \text{ mm}$ . In the following figures 4.18a, 4.18b, 4.18c we present three different position cuts with both the data and the data-like GEANT4 simulation. In these results, we see good agreement with data and Monte Carlo when fiducial radius  $0 < r < 49 \text{ mm}$ , excellent agreement when  $0 < r < 30 \text{ mm}$ , and poorer agreement when  $30 \text{ mm} < r < 49 \text{ mm}$ .

We can conclude on an octet-by-octet basis that the fitted  $b$  values are more accurate (when compared to GEANT4 Monte Carlo simulation with data processing similar to our real analysis) for events with a smaller radial position. In particular, the  $0 < r < 30 \text{ mm}$  fiducial cut seems to only keep highly accurate (compared to simulation) events. This is unsurprising because we know there is a position dependence of the energy response on the scintillator face because there are 12 light guides coupled to four PMTs mapping the four different quadrants of the scintillator. As the events deposit their energy at larger radial positions, the light guides receive a disproportionate fraction of light and the overall calibration loses fidelity in the spectral reconstruction and hence  $b$  extraction.

However, during the course of the position dependence studies, it was decided to primarily use the asymmetry extracted Fierz interference. Thus, it became less important to improve upon the energy response uncertainty and with complications from re-running the calibration and detector response model with a new fiducial cut, we ultimately decided not to implement these positions cuts in our final Fierz extraction. They remain an interesting study in the performance of the UCNA apparatus but do not change our final combined Fierz interference extraction procedure.

#### 4.4.3 Discussion on Unblinding Criteria

As discussed earlier, blinding was chosen for the later 2011-2012 and 2012-2013 dataset analyses to improve the integrity of the systematic error study. In particular, early in the analysis, we were focused on primarily using the spectral extraction of Fierz interference and had to safeguard against many energy dependent systematics.

Prior to the blinding, the unblinding criteria was not set. Once we reached the late stages of the Fierz interereference extraction, we settled on unblinding criteria as follows:

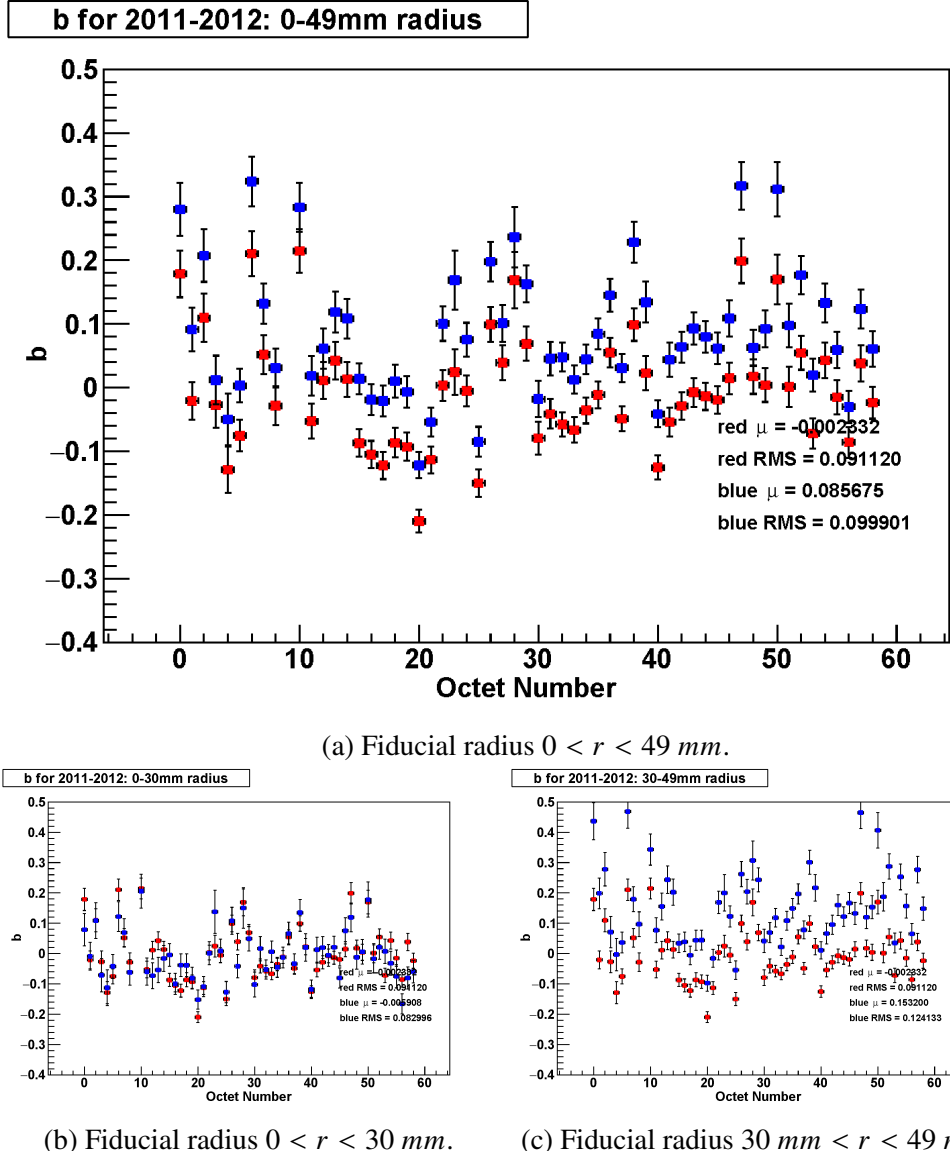


Figure 4.18:  $b$  extractions for different octets from GEANT4 simulations (red) and real data (blue). The simulation is created using initial kinematics generated from Monte Carlo, run through the GEANT4 simulation, and processed with our detector response model (unique to each octet) in order to generate “data-like” datasets from which the  $b$  value can be extracted. The data is created by using the same detector response model as the simulation uses.

1. All systematics, in particular the energy-dependent ones, were studied for both the spectral and asymmetry extraction methods. We determined a quantitative effect and studied the effects due to Monte Carlo  $b \neq 0$  inputs as well. Typically, Monte Carlo studies on non-zero  $b$  involved  $b = 0 \pm \approx (1 - 2)\sigma_b$ .
2. We locked in our event type cuts.
3. We locked in which data octets to use.
4. We decided on the energy fit regions (discussed below).
5. We decided on the fiducial volume cut (discussed below).
6. We chose a method for combining the spectral and asymmetry extractions in our final presented Fierz interference measurement (discussed below).

Upon settling on the unblinding criteria and locking in our analysis decisions, we unblinded the 2011-2012, 2012-2013 spectral and asymmetry datasets. We note a different blinding factor was applied to the two different years but within each year's dataset, the spectrum data and the asymmetry data had the same blinding factor applied. After the asymmetry analysis procedures were settled on, the same cuts were applied to the published asymmetry data (found in [Men+13]) to extract one additional measurement of  $b$  from super-ratio constructed asymmetry data. The decision to use the 2010 UCNA asymmetry dataset proceeded this way because the 2010 asymmetry data was already unblinded for use in the asymmetry analysis, a constraint we did not have in later datasets since Fierz was being extracted concurrently with the 2011-2012, 2012-2013  $A_0$  extraction.

#### 4.4.4 Weighted Averages

Throughout the course of the analysis, several considerations for averaging the four canonical measurements (2011-2012 spectrum, 2011-2012 asymmetry, 2012-2013 spectrum, 2012-2013 asymmetry) were discussed. These included taking regular weighted averages [HH10], weighted averages with asymmetric error bars (due to the asymmetric energy calibration uncertainty),  $\chi^2$  correcting the systematic error bars, and considerations with sample means [Hut14] since we were only going to average four measurements, amongst other considerations.

In particular, the blinded, weighted average final  $b$  extractions were combined for various energy region choices. The energy window studies gave us a quantified

limit on the variation due to choosing different energy limits, ultimately trading off between lower statistics (if we chose a high low-energy cut off in asymmetry data) and worse systematics (if we chose a low low-energy cut off in spectral data). This is discussed further in the next section.

After we reached all the unblinding criteria, prior to unblinding, the final decision was made to present only the asymmetry extracted  $b$  measurements in the final  $b$  average. This was largely due to the reduced quality of the energy reconstruction in 2012-2013 compared to 2011-2012 and the lack of year-to-year improvement in overall energy reconstruction precision compared to 2010. This was not surprising since the asymmetry analysis was not limited by energy calibration and hence there was no associated need to improve the calibration during the experimental upgrades.

## 4.5 Results and Discussion

This chapter concludes by presenting the results of the spectral extraction method and asymmetry extraction method for Fierz interference from the UCNA 2010, 2011-2012, and 2012-2013 datasets. These results are summarized in table 4.3. Furthermore, as discussed in section 4.3.2.1, the asymmetry  $A_0$  is re-extracted from these datasets in a simultaneous fit with  $b$ . The presence of a free parameter  $b$  leads to a correlated error and hence the error on the extracted  $A_0$ , under the paradigm of  $b \neq 0$ , is increased by  $\approx 10$ .

These extracted Fierz results represent the first direct measurement of  $b$  from neutron  $\beta$ -decay data [Hic+17]. The improved analysis procedure added to the direct spectral extraction measurements but also included the asymmetry extracted Fierz interference which was more robust against systematic effects that dominated the spectral extraction. These results were leading measurements of  $b$  extracted from neutron  $\beta$ -decay data [Sun+20], published around the same time as comparable measurements [Sau+20]. These measurements add to the PDG database on  $b$  measurements and further help constrain beyond Standard Model scalar and tensor interactions.

Recall from our introduction in section 1.3.2.2 that the Fierz interference term for the neutron can be decomposed in terms of  $b_{\text{Fermi}}$  and  $b_{\text{Gamow-Teller}}$ , the Fermi and Gamow-Teller components of the Fierz interference. It is given in equation 1.18 and again here

$$b_n = \frac{b_F + 3\lambda^2 b_{GT}}{1 + 3\lambda^2} \quad (4.25)$$

where, again,  $\lambda = \frac{g_A}{g_V}$  is the ratio of the axial-vector and vector coupling constants.

Fit Method	$b_n$ fit	$\sigma_{b,stat}$	$\sigma_{b,syst}$	range [keV]	$\chi^2_{\text{ndf}}$	$N [10^6]$
'10 spectrum	0.067	0.005	$+0.090$ $-0.061$	150-650	6.2	20
'11-'12 spect.	0.072	0.0042	$+0.101$ $-0.108$	195-645	2.2	22
'12-'13 spect.	0.044	0.0079	$+0.117$ $-0.174$	195-645	5.1	9.1
'11-'12 asymm.	<b>0.087</b>	<b>0.063</b>	$\pm 0.024$	190-740	0.71	23
'12-'13 asymm.	<b>0.046</b>	<b>0.083</b>	$\pm 0.024$	190-740	0.86	9.4
'10 asymm.	<b>0.052</b>	<b>0.071</b>	$\pm 0.024$	220-670	0.94	21
$\langle b_{\text{asymm}} \rangle = 0.066 \pm 0.041_{\text{stat}} \pm 0.024_{\text{syst}}$						

Table 4.3: Summary of  $1\sigma$  fit results for 5 independent measurements of  $b_n$ . The number of events is given after all cuts are applied. The spectral extractions use the energy calibration uncertainty combined in quadrature with other systematic uncertainties estimated with the techniques in [Hic+17]. Only the asymmetry results (bold values) are used in the weighted average. Table first published in [Sun+20]. We note the large  $\chi^2_{\text{ndf}}$  from the spectral extraction methods indicates the dominance of systematic uncertainty in the spectral analysis compared to the asymmetry-extracted analysis.

Recall again that the  $b_F$  component is a direct measure of beyond Standard Model scalar interactions (at the current measurement sensitivity) in neutron  $\beta$ -decay. The  $b_{GT}$  component is a probe of the tensor interactions. Current measurements of  $J^\pi = 0^+ \rightarrow 0^+$  are the strongest constraint on  $b_F$  and are stronger than the limits set on  $b_n$  in this work (see [HT15] for a review). However, at the time of publication constraints on  $b_{GT}$  were less stringent and generally came from consistency with Standard Model global fits (see [NG13] for a review prior to our published results, [GNS19] for a review that incorporates our results). Hence, these leading precision measurements on  $b$  for the neutron become leading constraints on  $b_{GT}$  from neutron decay data as an indirect probe of tensor couplings in beyond Standard Model interactions.

In this chapter, we provided additional details on the intermediate steps in the spectral extraction analysis and the asymmetry extraction analysis of the Fierz interference parameter. We included details of studies that did not significantly factor in to the final analysis choices but nevertheless represented data quality checks done along the way. We explicitly described the factors that compose the systematic uncertainty budget and provide more details compared to our publication [Sun+20] for estimating the subdominant systematic uncertainties.

## Chapter 5

### UCNA: DARK MATTER DECAY ANALYSIS

In this chapter, we discuss a separate analysis completed using the UCNA 2012-2013 dataset that directly addresses a proposed neutron to dark matter decay channel. In response to a theory first proposed in January 2018 by authors Fornal and Grinstein (what eventually became [FG18a]), the UCNA collaboration mobilized to provide a direct-data measurement of the proposed decay channel. Due to the attention received by this theory, this analysis was completed while the neutron physics community at large was investigating the experimental repercussions. The analysis described in this chapter illustrates the path we took to setting direct limits on a potential neutron to dark matter decay channel, originally proposed to address the neutron lifetime anomaly.

The majority of this chapter is adapted from publications [Sun+18] and [Sun+19]. [Sun+18] was our official Physical Review C publication detailing the analysis and our resulting limits, taken from the UCNA 2012-2013 dataset, on a potential neutron to dark matter plus electron-positron pair production. [Sun+19] was a summary publication in the conference proceedings journal after the International Workshop on Particle Physics at Neutron Sources 2018 (PPNS2018), held in Grenoble, France.

#### **5.1 The Neutron Lifetime Anomaly**

This section presents the experimental landscape that defines the neutron lifetime anomaly. We start by giving an overview of the neutron lifetime. We then present two classes of experiments that have differing central values of the neutron lifetime.

##### **5.1.1 The Neutron Lifetime**

The free neutron is not a stable particle and in absence of nuclear interactions will decay. This was given in equation 1.4 and presented again here:

$$n \rightarrow p + e^- + \bar{\nu}_e \quad (5.1)$$

where  $p$  is a proton,  $e^-$  is an electron, and  $\bar{\nu}_e$  is an electron anti-neutrino. The mean lifetime for this radioactive decay is approximately 15 minutes. The neutron decay is discussed in section 1.3.1 and the lifetime is discussed in section 1.3.2.3.

[GG16] provides a qualitative overview, [Wie18] provides a contemporary review of the current landscape of neutron lifetime measurements and their theoretical underpinnings. An older review can also be found in [WG11]. The overview in this section is described in more detail in those references.

The UCNA collaboration has close ties with a sister collaboration, UCN $\tau$ , which operates a neutron lifetime experiment (that we discuss later in this chapter) in an adjacent space to UCNA, in the LANL facilities. Indeed, throughout this dissertation work, some effort was spent at LANL helping UCN $\tau$  take data for the most recent neutron lifetime measurement (topic of [Fri22] and published in [Gon+21]), assist with general experiment running and operations improvement.

Historically, there have been two categories of experiments that aim to measure the neutron lifetime. They operate by detecting different components of equation 5.1. The first, bottle experiments, aim to measure the disappearance of neutrons over time and are covered in section 5.1.2. The second, beam experiments, aim to measure the appearance of protons from a neutron beam and are covered in section 5.1.3.

A third category of experiments is opening up with an experiment taking place which uses a Time-Projection Chamber (TPC) to detect the appearance of the decay electron from equation 5.1. Their preliminary work was shown at the PPNS2018 conference [Nag+19], with improved statistical precision and results on the horizon [Hir+20; Sum+21].

### **5.1.2 Experimental Methods: Bottle Experiments**

Bottle experiments that measure the neutron lifetime can be understood quite simply from a conceptual standpoint. Neutrons are trapped in a “bottle” from which they cannot escape. Within this bottle, a portion of the neutrons are periodically sent outwards to a neutron detector which measures the flux of neutrons and hence provides a measure of the remaining neutron population. Ignoring for now all the experimental factors such as losses in the bottle or adjusting for the neutron detection rate, this effectively gives the neutron population at regular time intervals and a neutron lifetime can be extracted when one applies standard radioactive decay formulas (extensively detailed in [Fri22]). Figure 5.1 gives a schematic representation of this procedure.

At a high-level, this is all one needs to understand neutron lifetime bottle experiments. Indeed, this is the focal point of the work of several collaborators in the

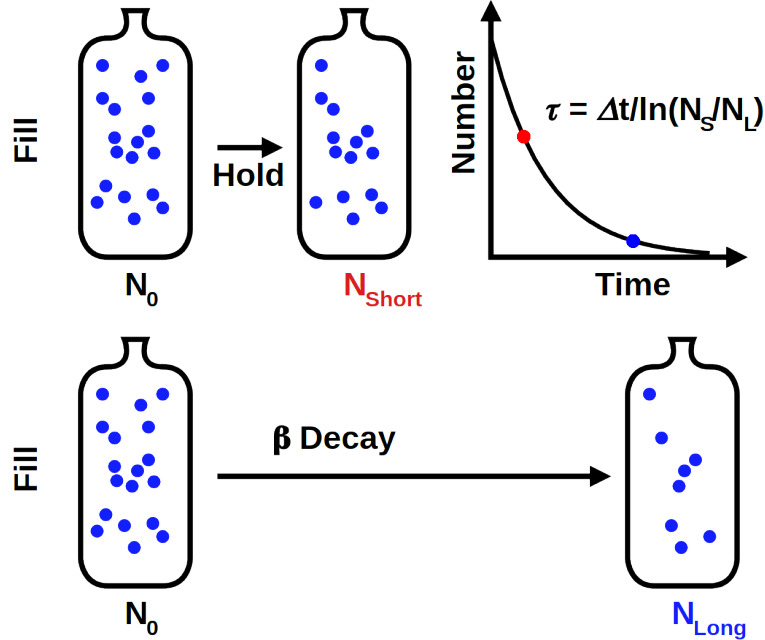


Figure 5.1: Simple schematic illustrating the concept of neutron lifetime bottle experiments [Fri22]. At minimum, two different holding times are used to measure remaining neutron populations and the differences in number and time can be used to deduce a neutron lifetime.

UCN $\tau$  collaboration [Mor+17; Pat+18; Fri22; Gon+21]. All the experimental details of UCN $\tau$  can also be found in those references. We take a moment here to highlight some of the main challenges associated with these types of experiments and the design innovations developed to address these challenges.

One of the largest challenges in bottle experiments is to effectively trap the neutrons and ensure that there are no loss mechanisms outside of equation 5.1 (or at least they are properly quantified and can be corrected with high precision). To that end, early bottle experiments used material bottles that had material properties such that they were largely reflective to UCNs. This is discussed in detail in section 1.2. Next-generation improvements were made to the material bottle and some experiments now use a fully magnetic bottle that reflects polarized neutrons of a particular spin state using a magnetic field generated from a specific configuration of magnets called a Halbach array (further detailed in [Sal+14]).

A second significant challenge and the final one we will discuss is related to measuring the number of stored neutrons at various time intervals. In order to get an accurate measurement of the lifetime, one needs to accurately measure how many

neutrons remain at any given time. One way this is done, for example in UCN $\tau$ , is by lowering a neutron detector that counts the remaining neutrons in the trap. From the experimentalists perspective, it is not necessarily a straight-forward procedure to relate the neutrons counted in the neutron counter to the total number of neutrons within the storage volume at different measurement times due to different detection efficiencies and overall difficulties with total number of neutrons loaded into the trap.

Both of these comprise some principle experiment challenges in the operation of neutron lifetime bottle measurements. Nonetheless, over the last several decades, many research collaborations have incrementally pushed the boundaries of statistical and systematic precision in neutron lifetime measurements using refined experiment design and techniques. Again, [Wie18] provides a contemporary discussion while [WG11] gives more historical context.

### 5.1.3 Experimental Methods: Beam Experiments

Beam experiments can also be understood quite simply from a conceptual standpoint. In beam experiments, the goal is to measure the decay proton from equation 5.1. This is done by taking a beam with a fixed flux of neutrons and surrounding it with spectrometers and detectors that allows decay protons to be trapped and later directed outwards. For example, in the Beam Lifetime (referenced below) experiments, a Penning trap captures the decay protons and when the neutron beam is turned off, the trap opens and the protons are released and detected with an efficiency applied for detector effects. If this efficiency can be precisely determined, then by knowing the number of outgoing proton detected and the number of incoming neutrons, we can extract a decay number over total number of neutrons and hence a neutron lifetime.

At a high level, one just considers a fixed length of and cross-sectional area of neutron beam, neutron density per time, and outgoing proton detection rate. This captures the essence of a neutron lifetime beam experiment. One such experiment being discussed for next-generation improvements is Beam Lifetime 3 (BL3), detailed in [Fom21] and [Wie18]. Figure 5.2 gives a schematic representation of how the beam lifetime experiment works. More details of neutron lifetime extraction from beam measurements can be found in the most recent result publication [Yue+13], and updates on the follow-up experiment can be found in [Hoo+19].

As with the bottle experiments section above (section 5.1.2), we pay special attention to some of the experimental considerations in the current development of beam

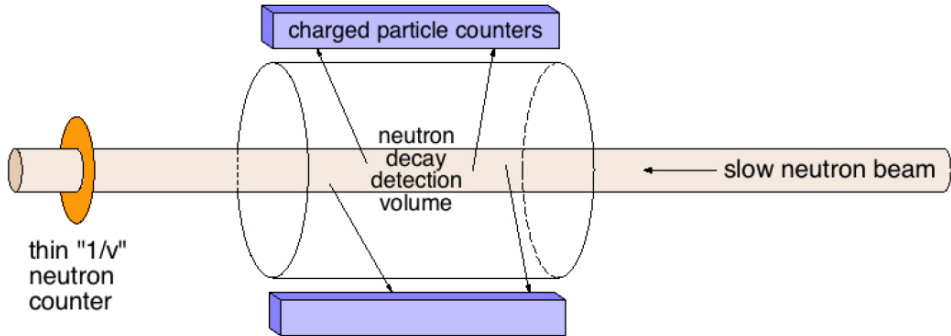


Figure 5.2: A schematic diagram of a typical neutron beam lifetime experiment. The slow neutron beam can be characterized before the decay volume as well as being counted after the decay volume. Figure taken from [Wie14].

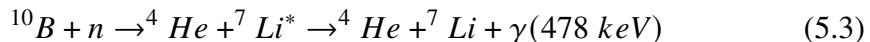
experiments. For a standard beam lifetime set-up described above, we have two main issues to consider: an absolute neutron flux characterization and the overall proton detection.

First, the absolute neutron flux in previous iterations of beamline lifetime (BL) experiments proved to be a dominant source of systematic error in [Nic+05]. These neutron flux measurements were done using a well-characterized  ${}^6Li$  deposit to interact and capture neutrons, producing the following reaction:



where  $t$  is a triton. Determinations of the neutron flux were done by using the detection rate of equation 5.2 decays, the  ${}^6Li$  density, and measured values of capture cross-sections that had to be continually updated. The total uncertainty in this determination was the dominant uncertainty in the original BL experiment.

Improvements in absolute flux determination lead to improved measurements when compared to the original BL experiment. This was due to an improved measurement of the neutron flux which used a  ${}^{10}B$  target (this target is called the “Alpha-Gamma” target due to the emission of an alpha particle and gamma ray and it is described in [Ada+19]) that had total absorption for the incoming neutron beam and produced the following reaction



where the \* indicates an excited energy state. The monoenergetic  $\gamma$  is a unique signature that is counted with two high-purity germanium (HPGe) detectors located

on either side of the target. This gives an absolute characterization of the neutron flux via absorption in a fully neutron absorbing target. This new technique for flux determination decreased the dominant systematic error in [Nic+05] by 5 (from 2.7 s to 0.5 s) and resulted in the improved measurement presented in [Yue+13].

Second, the overall proton detection efficiency (and uncertainty) proved to be a large contributor to experimental uncertainty. There are several improvements planned for BL2 to improve proton counting efficiency which are detailed in [Hoo+19]. Here, we provide a summary of a few key points. Improvements in detector understandings and simulation fidelity means that current-generation BL experiments can optimize the electric and magnetic fields applied as well as the trapping volume. This provides more stability and overall increased precision in the proton travel paths, and hence detection efficiency uncertainty for a standard proton. Furthermore, new pixelated silicon proton detectors are being developed for a next-generation BL3 experiment [Fom21]. This would allow for systematic studies and characterization of proton travel paths towards the proton counting detectors, and ultimately improve the systematic uncertainty associated with such a correction.

#### 5.1.4 The Anomaly

[GG16] provides an accessible introduction to this topic. In this section, we present the neutron lifetime anomaly which is, at the core, a  $4\sigma$  discrepancy between the measured values of the neutron lifetime from the two categories of experiments described above<sup>1</sup>.

Over the last  $\approx 2$  decades of neutron lifetime measurements, a clear discrepancy has emerged between the central values of the bottle experiments and those of the beam experiments. In particular, as each generation of experiments improve in precision, the discrepancy becomes larger. Today, in 2021, we currently have  $\approx 4\sigma$  discrepancy in the central values of these classes of measurements. Figure 5.3 shows this for different experiments over the decades. [Wie18] discusses the experiments that make up this plot and provides a more technical overview of each experiment. We wish to highlight that the beam lifetimes are  $\approx 8$  s, or equivalently  $\approx 1\%$ , longer than the bottle lifetimes. This will become relevant in the next section.

Why is this interesting? First and foremost, the neutron is a simple system in

---

<sup>1</sup>At the time of publication of this work and during the writing of this dissertation, this discrepancy was  $\approx 4\sigma$ . Recently, collaborators from UCN $\tau$  published a new bottle measurement of the neutron lifetime, improving the previous uncertainties and thus reducing the overall bottle experiment uncertainty. We note that the beam measurements uncertainty still dominates this  $\approx 4\sigma$  estimation.

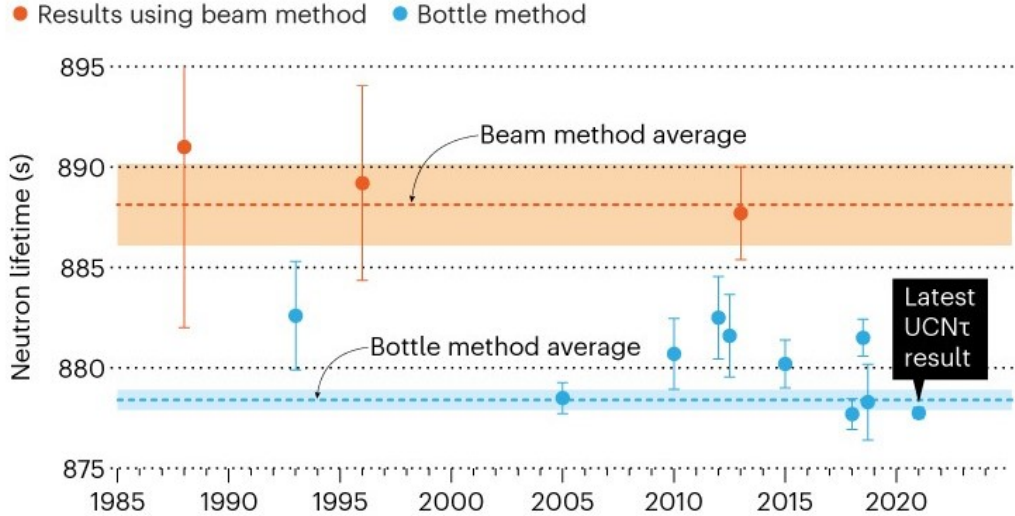


Figure 5.3: Historical trend of neutron lifetime experimental measurements. Orange points are beam experiments and blue points are bottle experiments. The shaded regions are weighted averages  $\pm 1$  standard deviation of uncertainty for beam vs bottle methods. Figure is taken and modified from [Cas21]. Details of each experiment are in [Wie18] and [Gon+21].

the context of contemporary nuclear physics and hence we would expect that we understand the weak interaction decay process it undergoes. The fact that there is such a large discrepancy in neutron lifetimes casts doubt on our fundamental understanding of the weak interaction and tantalizingly hints “is there something out there that we aren’t accounting for?” Alternatively, a precise neutron lifetime measurement which identifies unknown systematic effects in one or both techniques could resolve this anomaly and put to rest these questions. Secondly, the neutron lifetime plays a crucial role in Big Bang nucleosynthesis. In particular, after the initial “freeze out” period where free neutrons were no longer in abundance, the elemental composition in the universe was  $\approx 75\% p$ ,  $\approx 25\% {}^4He$ , and trace amounts of  ${}^2H$ ,  ${}^3He$ , and  $A > 4$  heavier nuclei. However, these abundances are dependent on the neutron lifetime because, for example, if the neutron lifetime is short there is less time to capture (two  $p$  and two  $n$  via various interactions) and create  ${}^4He$ . Thus, the relative rates of  ${}^4He$  formation and  $n$  decay are sensitive to a proper determination of the neutron lifetime. More precisely, this helium mass fraction is a parameter called  $Y_p$  and can be defined as

$$Y_p \propto \left( \frac{\omega_b}{\omega_{b,0}} \right)^{0.39} \left( \frac{\tau_n}{\tau_{n,0}} \right)^{0.72} \quad (5.4)$$

where  $\omega_b$  is the baryon density in the early universe,  $\tau_n$  is the neutron lifetime,

and  $\omega_{b,0}, \tau_{n,0}$  are fixed reference values. Other early universe elemental abundance calculations are based on the  ${}^4He$  abundance given in equation 5.4 and hence the neutron lifetime and associated uncertainty enter explicitly into these estimations (see [Ioc+09] for a review of these abundance calculations).

Typically, when one hears of this discrepancy, the first questions are whether there is an unknown systematic error in either of the measurement techniques that would yield a shift in the central value. From the perspective of the bottle experiments, several separate research collaborations have, over the decades, used multiple techniques to extract the neutron lifetime and have converged to a value with increasing statistical and systematic precision. However, from the beam perspective, there are just a handful of measurements that contribute to the central value. There is a legitimate argument that the beam lifetime measurements just need a next-generation experiment to definitively identify whether this was experimental error or not. That is what BL2 [Hoo+19] and BL3 [Fom21] aim to accomplish. Ideally, the next generation of bottle and, in particular, beam experiments should shed light on the validity of this anomaly and where potential sources of systematic error may lie<sup>2</sup>. However, in the interim, novel physics theories have been proposed that introduce exotic interactions that could lead to a real discrepancy between beam and bottle lifetime measurements. We examine one such theory in the next section.

## 5.2 A Dark Matter Decay Channel

In lieu of “smoking gun” evidence in any particular direction to resolve this neutron lifetime anomaly, we are left waiting for the next generation of higher-precision experiments to hopefully shed light on a root experimental cause. However, the research community does not rest there. In the Standard Model, equation 5.1 is the only valid decay channel for the neutron<sup>3</sup>. In this section, we consider certain beyond Standard Model theories that allow for additional loss mechanisms for the neutron and, in particular, exotic physics interactions. The topic of this chapter is to examine one such model: neutron decaying to a dark matter particle with additional visible constituents produced alongside.

The theory discussed in this chapter was first proposed by authors Fornal and Grinstein in [FG18a]. In it, the authors construct a decay mode that reduces the

---

<sup>2</sup>We note that to date the last two decades of experiments and analysis have not produced a systematic shift to eliminate this discrepancy.

<sup>3</sup>We note however that in a small fraction of these decays an associated photon is also emitted. This is called radiative decay. Measurements of this photon’s energy spectrum, branching ratio, and comparison with theory are given in [Bal+16].

standard model decay in equation 5.1 with a branching ratio of 100% to  $\approx 99\%$  and propose that the remaining  $\approx 1\%$  consists of

$$n \rightarrow invisible + visible \quad (5.5)$$

$$n \rightarrow invisible \quad (5.6)$$

where the “invisible” products would be the dark matter particles. The decay in equation 5.5 offers a chance for direct detection. For this to resolve the lifetime anomaly, the dark matter particles produced must be either stable or have an exceedingly long lifetime compared with the measurement times of neutron lifetime experiments so far. This forbids the decay  $\chi \rightarrow p + e^- + \bar{\nu}_e$  since the resulting decay  $p$  would be detected by beam experiments. This yields the constraint  $m_\chi < m_p + m_e = 938.783 \text{ MeV}$ , where  $\chi$  is the dark matter particle produced in this theory’s decay channel. Furthermore, a mass minimum constraint is imposed by examining the possibility of this channel in conventional nuclear decay. Namely, the decay channels in equations 5.5 and 5.6 could result in nuclear transitions. The most stringent limits on these nuclear transitions come from Beryllium-9 stability measurements [Wan+12] and yield a minimum  $m_\chi > 937.900 \text{ MeV}$ . Together, this gives

$$937.900 \text{ MeV} < m_\chi < 938.783 \text{ MeV} \quad (5.7)$$

The authors propose three decay channels:

$$n \rightarrow \chi + \gamma \quad (5.8)$$

$$n \rightarrow \chi + e^+ e^- \quad (5.9)$$

$$n \rightarrow \chi + \phi \quad (5.10)$$

where  $\chi$  is a dark matter particle,  $\gamma$  is a Standard Model visible photon,  $e^+ e^-$  is a positron-electron pair, and  $\phi$  is a second dark matter particle. The decays in equations 5.8 and 5.9 represent the decay channel given in equation 5.5. The decay in equation 5.10 represents the decay channel given in equation 5.6.

With the neutron mass as  $m_n = 939.565 \text{ MeV}$ , the electron and positron masses as  $m_{e^+}/m_{e^-} = 0.511 \text{ MeV}$ , and the mass constraints given in equation 5.7, the range of energies available for the decay in equation 5.8

$$0.782 \text{ MeV} < E_\gamma < 1.665 \text{ MeV} \quad (5.11)$$

and for the decay in equation 5.9 it is

$$1.022 \text{ MeV} < E_{e^+e^-} < 1.665 \text{ MeV} \quad (5.12)$$

where  $E_{e^+e^-}$  is the total energy available to the  $e^+e^-$  pair. Thus, the available kinetic energy range is  $E_{K,e^+e^-} \in [0, 0.644 \text{ MeV}]$  (see [FG18b] for explicit description).

If any of the decay channels in this theory or the sum of these decay channels are present at the 1% level, it would represent a resolution to the neutron lifetime anomaly. This is because decay rates observe the following relationship:

$$\Gamma_{total} = \Gamma_{\beta-decay} + \sum_i \Gamma_{loss,i} \quad (5.13)$$

where  $\Gamma$  is the decay rate. Thus, the lifetime is related by

$$\frac{1}{\tau_{total}} = \frac{1}{\tau_{\beta-decay}} + \sum_i \frac{1}{\tau_{loss,i}} \quad (5.14)$$

where  $\tau$  is the lifetime. Hence, a 1% change in the branching ratio would correspond to  $\approx 1\%$  change in the measured neutron lifetime which is about the right magnitude as noted in section 5.1.4.

In equation 5.13, we only measure the  $\Gamma_{\beta-decay}$  in beam experiments whereas in bottle experiments we would measure  $\Gamma_{total}$ . Thus, a dark matter decay channel that is present at the 1% level would resolve the  $\approx 1\%$  discrepancy in neutron lifetimes in the correct direction. Thus, throughout this analysis, we aim to place limits on the branching ratio of equation 5.9 with an overarching eye towards a 1% branching ratio.

### 5.3 UCNA Analysis of Dark Matter Decay

In the subsequent sections, we discuss UCNA's sensitivity to the theory presented in [FG18a] and illustrate the analysis we undertook to set limits on such proposed decay channels. Our analysis focused on the neutron to dark matter plus positron-electron pair (equation 5.9) decay channel. This analysis was completed in a timely fashion and the resulting confidence limits allowed for a data-driven discussion using UCNA data results at the May 2018 PPNS conference, a short five months after the initial theory was first proposed.

#### 5.3.1 Overview of UCNA Sensitivity to Decay

To set the stage for this analysis discussion, we first consider the sensitivity of UCNA to such a decay which results in a positron-electron pair produced. We recall from

chapter 2 that UCNA is an experiment designed to provide energy, position, and timing reconstruction on electron-like events that originate from neutron decay. As a result, we are in a unique position to directly test the decay channel in equation 5.9 since we would be sensitive to the visible decay products of such a decay<sup>4</sup>. However, we must be careful because UCNA was already an experiment designed for a specific purpose: an  $A_0$  measurement. Any UCNA dataset with the decay in equation 5.9 would potentially have its signal washed out by the large number of foreground events due to the conventional neutron  $\beta$ -decay given in equation 5.1. Luckily, UCNA’s unique set-up gave a solution to this potentially overwhelming problem.

UCNA is essentially a spectrometer with  $\approx 4\pi$  solid angle acceptance due to the imposed magnetic field directing the  $\beta$ -decay electrons outwards towards detectors on either side. A positron in the same environment would kinematically behave the same way (we discuss positron-electron differences in the apparatus in section 5.3.4.4). To get around the large foreground signal which would wash out dark matter decay particles (most optimistically present at the 1% level), we remind the reader that UCNA produces and detects several event types, discussed in section 2.4.4 and summarized in figure 2.7. Amongst those event types, we have Type 1 backscatter events which, in a single decay, trigger both the East and West scintillator detectors. Furthermore, we note that in a fraction of dark matter decay events from equation 5.9, the positron and electron pair will be produced with initial momentum vectors pointing towards opposite detectors. Thus, these  $e^+e^-$  pairs can deposit energy in both plastic scintillators (if the positrons and electrons themselves have no backscatter which  $\approx 95\%$  of conventional  $\beta$ -decay events do not). This type of analysis relying on event identification is summarized in figure 5.4.

The main thrust of the analysis is as follows: there is a minimum time needed for the  $\beta$ -decay Type 1 events to travel across the detector. The single  $\beta$ -decay Type 1 electron at the energies in UCNA requires  $> 15 \text{ ns}$  to traverse the  $4.4 \text{ m}$  scintillator-to-scintillator distance. The dark matter decay  $e^+e^-$  in equation 5.9 has no such constraint; the positron and electron can trigger the East and West scintillators with

---

<sup>4</sup>Collaborators from UCN $\tau$  at LANL were in a position to detect the decay channel in equation 5.8 and indeed published preliminary results around the same time we did [Tan+18]. They filled a volume with neutrons and placed a Germanium  $\gamma$  detector outside to get limits on a branching ratio of equation 5.8. Together, our limits on channels 5.9, 5.8 provided immense value for data-driven discussions on future resolutions to the neutron lifetime anomaly which was especially relevant with the PPNS2018 conference on the horizon at the time. Furthermore, we note that a second direct limit on the positron-electron decay channel was set in [Klo+19] at a later date.

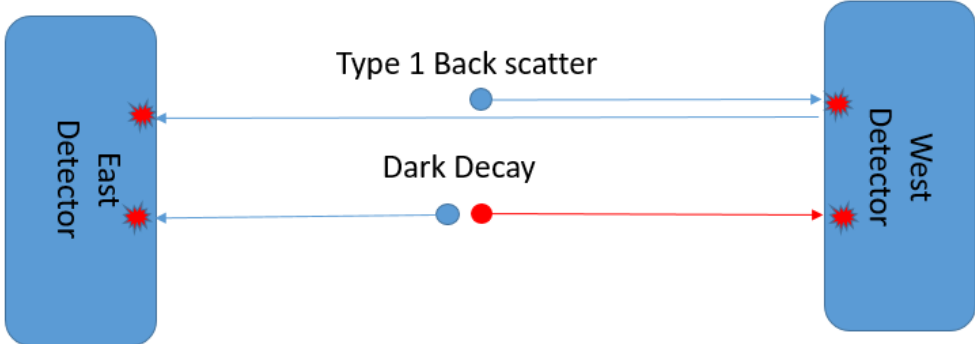


Figure 5.4: A diagram showing the travel paths of a proposed dark matter decay producing a  $e^+e^-$  pair, compared to a Type 1 backscatter event [Swa18]. Both would register the same electronic signature, but there exists a lower limit on the Type 1 backscatter travel time, which is set by the maximum velocity and the crossing distance between detectors (4.4 m). The  $e^+e^-$  pair has no such limitations. This timing signature is critical in the event separation that allows our analysis to proceed (see text).

any relative time differences based on their initial kinematics and decay position in the trap. Thus, by properly extracting a timing for coincidence triggers in both detectors for each event, we can nearly eliminate the foreground Type 1 signal by imposing a timing cut of nominally  $< 15\text{ ns}$  that removes all kinematically forbidden Type 1 decay events and leaves all candidate dark matter decay (equation 5.9) events with appropriate kinematics. Conceptually, this is the analysis that is illustrated in the remainder of this section, with final limits presented and discussed at the end of this chapter.

### 5.3.2 Event Classification

Early on, in January 2018, when the pre-print version of [FG18a] was posted on the Arxiv, we quickly switched our Fierz interference analysis to that discussed in the previous section with the goal of placing limits on the decay channel in equation 5.9.

Within our post-processor, different electronic signals and trigger logic are assigned to different particle IDs. In particular, we have a flag for events that are electron (or electron-like), one for gammas, and one for “other”, i.e., events which are unable to be identified. In the UCNA Fierz, asymmetry, and ultimately this dark matter decay analyses, we only use the particle IDs associated with “electron”. As a cursory look at the data, we extracted timing spectra from the 2012-2013 octet datasets, made a

cut at  $< 15 \text{ ns}$  and only electron events that trigger both scintillators, and plotted the histograms of counts we saw as a function of energy deposited (directly related to the mass range of the dark matter  $\chi$  particle). Every octet had 0 events that satisfied these criteria. We suspected that this was very unlikely. To double-check, we then went back to the initial data processor (a piece of code that hadn't been looked at for several years since these analyses were taking place in 2016-2020 and the data taking runs had concluded in 2013) and looked at the definition of particle ID. Within the post-processor, it turns out that all events with a coincidence signal and timing difference  $< 15 \text{ ns}$  were classified as "unphysical" and shunted to the "other" particle ID classification. Hence, our entire analysis to that point was based on events that were already removed from the category of events that we were interested in. Once we realized this, we re-ran the post processor to allow these "unphysical" events into the particle ID for electrons. This story serves as a note on the real-world complications of data analysis and a cautionary tale for those trying to rush their analysis.

### 5.3.3 Coincidence Time Calibration

#### 5.3.3.1 The TDC Data

As discussed in the analysis overview above (section 5.3), the timing of coincidence trigger events in the UCNA detector was crucial to the overall sensitivity of this measurement in order to differentiate between our candidate dark matter decay events and our original foreground events from conventional neutron  $\beta$ -decay. The UCNA experiment used CAEN V775AA 32-input, 12-bit, 1200-ns range time-to-digital converters (TDCs).

The TDCs used in the UCNA experiment used a "common-stop" signal. This meant that each individual subsystem start a "stopwatch" at each individual trigger and stop their measurement at a global trigger plus a fixed delay<sup>5,6</sup>. For the UCNA apparatus and a Type 1 event where both scintillators see only a single decay event each within the common stop time, this means the first triggered TDC has a large peak at the endpoint of the TDC, corresponding to the global trigger plus fixed delay time. This

---

<sup>5</sup>The fixed delay is composed of two components: a known electronic delay set in the instrumentation, and an unknown (detector-specific) cable length delay.

<sup>6</sup>The electronic trigger logic is presented in [Men14] and described in detail in [Bro18]. As a brief overview, for an event to register a global trigger in one detector, that detector must have a two-fold PMT trigger. That is, at least two of the four PMTs in that detector must have triggered above a pre-set threshold. In addition, a software MWPC threshold is applied to reject gammas, and a software muon veto coincidence is checked to reject cosmic muons.

is called the self-timing peak (STP). However, the opposite side TDC produces a standard Type 1 timing spectrum (relative to the STP) because its stopwatch started later relative to the global trigger plus fixed delay. So, for half the Type 1 events in each detector’s timing spectrum, we would see the timing structure of a neutron  $\beta$ -decay electron traversing the detector, and for the other half of Type 1 events we would see a STP.

For the 2010-2012 UCNA datasets, the TDC data was noisy. While clear coincidence signals were identified (which was needed for the  $A_0$  analysis), the spectra were not stable. The STPs of each TDC showed large electronic jitter and, in some octets, had up to three separate STPs of characteristic width  $2\text{ ns}$  (similar to the properly calibration TDC data), peaked at three locations separated by upwards of  $\approx 6\text{ ns}$ . Hence, the actual TDC data was not reliable to within  $> 6\text{ ns}$  unless there were separate calibrations for each type of TDC jitter. In addition, there were further complications with the quality of the remaining TDC data and concerns whether certain runs had the TDCs powered on. We ultimately chose not to use any of the 2011-2012 dataset in the dark matter decay analysis due to this unreliability in timing data.

During the beam shut down between the 2011-2012 and 2012-2013 data-taking runs, several components of UCNA were upgraded. We discussed some of the geometry changes in section 2.4. One additional upgrade was fixing the TDCs so that they operated reliably. In the 2012-2013 data-taking run, the TDCs were operating correctly and had standard TDC timing structures in their readouts. In particular, we could identify a clear STP and a signature timing spectrum for Type 1 backscatter events, both of which are shown in Figure 5.5 for East and West TDCs.

We note a few features. The large peaks at channel number 3100 (East) and 3250 (West) are the STPs. The peak structure at channel 2600 (both) is the  $\beta$ -decay electron timing spectrum from Type 1 events (we note this data is taken with a Type 1 event cut). A flat 150 channel shift was applied to the East TDC to get the Type 1 backscatter peak to align since this was our physically relevant check point. This shift in channels is likely due to different cable lengths for each TDC which are discussed below. We do note that the actual channel-to-time conversion is dependent on the center of the STP. This is because the conversion factor is set in the electronics so that the center of the STP can be converted to a physically relevant time. By shifting the East TDC spectrum up, we “compress” the resulting timing spectrum and conservatively ensure we capture as many events in a chosen analysis

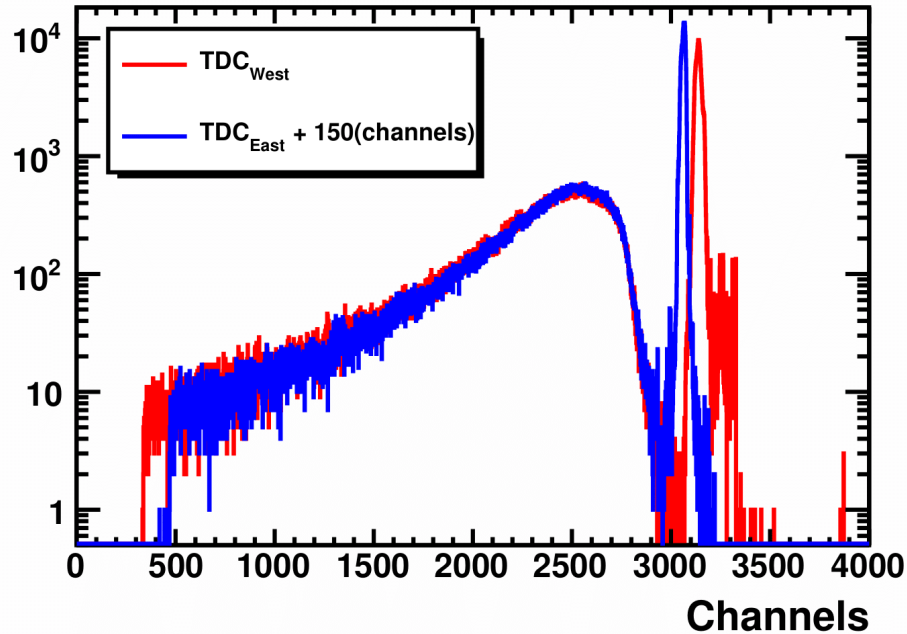


Figure 5.5: Timing spectra taken from East (red) and West (blue) TDCs in raw channel count, operated in a “common stop” mode, for Type 1 backscatter events. Self-timing peaks are seen centered around channel 3150 (red) and 3250 (blue). Significantly more electronic jitter is seen in the West TDC. A flat 150 channel offset has been applied in order to align the Type 1 backscatter peak at channel 2600. A conversion of  $44 \text{ ps}/\text{ch}$  was applied. Figure first published in [Sun+19].

time window as possible, within noise (see discussion on the timing window in section 5.3.4.2).

Throughout the course of the initial time analysis, we noticed that the backscatter and self-timing peaks did not align in the East and West TDCs. This hinted towards systematic offsets in the TDC data. Dr. Brad Filippone identified that this may be due to mis-matched wire lengths between the TDCs and the trigger logic that connected them. A simple diagram of the wire set-up is shown in figure 5.6 and it was used to guide the estimation of the wire length induced timing delay. In order

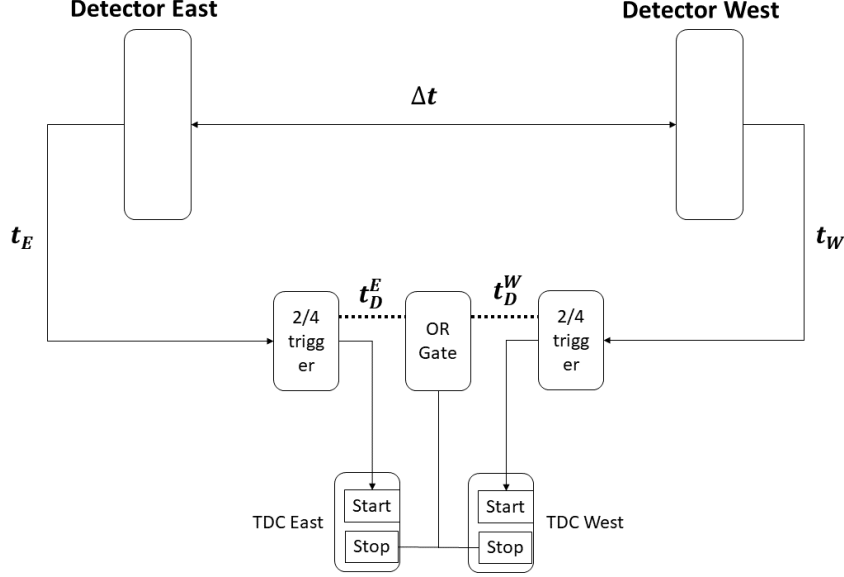


Figure 5.6: A simple diagram of wire connections between the TDCs and the UCNA detector [Fil18]. This was used as a guide to estimate the time delays due to potentially mismatched cable lengths (see text).

to perform this estimation, we identify that for the West TDC:

$$\begin{aligned} \text{start} &= t_W + \Delta t \\ \text{stop} &= t_E + t_D^W \\ \text{and } t_{\text{BSP}}^W &= \text{stop} - \text{start} = t_E + t_D^W - t_W - \Delta t. \end{aligned} \quad (5.15)$$

Similarly, for the East TDC we have  $t_{\text{BSP}}^E = t_W + t_D^E - t_E - \Delta t$

$$\begin{aligned} \text{with, additionally, } t_{\text{STP}}^W &= t_D^W \\ \text{and } t_{\text{STP}}^E &= t_D^E \end{aligned}$$

where BSP stands for backscatter peak, STP stands for self-timing peak as described earlier, E and W are East and West respectively, and D stands for delay. The “start” and “stop” represent the commands for the TDCs. From the TDC data, we have

$$t_{\text{STP}}^W = t_D^W = 3138 \text{ channels} \quad (5.16)$$

$$t_{\text{STP}}^E = t_D^E = 2917 \text{ channels} \quad (5.17)$$

$$t_{\text{BSP}}^W - t_{\text{BSP}}^E = 145 \text{ channels} \quad (5.18)$$

where the units are in TDC channels and we note that within the electronics there was a channels-to-time conversion setting of  $180 \text{ ns} = 4096 \text{ channels} \rightarrow 44 \text{ ps/ch}$ .

From equation 5.18, we get

$$2(t_E - t_W) + (t_D^W - t_D^E) = 145 \text{ channels} \quad (5.19)$$

$$2(t_E - t_W) + 221 \text{ channels} = 145 \text{ channels} \quad (5.20)$$

$$\implies \Delta t = t_W - t_E = 38 \text{ channels} \approx 1.7 \text{ ns} \quad (5.21)$$

Hence, the time delay in our wire length differences was  $\approx 1.7 \text{ ns}$ . This was adjusted for by applying a flat channel shift in downstream timing window analysis.

We take the characteristic TDC spectrum shown in Figure 5.5 for all the 2012-2013 data and convert to a physical time. We set the center of the STP at  $140 \text{ ns}$  which corresponded to  $44 \text{ ps/ch}$  as in the above wire length discussion. We show the negative difference of each point from the center of the STP<sup>7</sup> to turn our “common-stop” into a common zero and produce a conventionally understood timing spectrum. The resulting spectra for East and West TDCs are shown in Figure 5.7. Again, we note a few features here. The vertical dotted lines represent the nominal chosen timing window for the candidate dark matter decay events, discussed further below in section 5.3.4.2. The red overlaid timing spectrum is a simulated spectrum of Type 1 back scatter events with a  $2 \text{ ns}$  timing resolution applied. This is described in more detail in the following subsection below.

### 5.3.3.2 Simulations of the Timing Spectrum

For this analysis, we simulate two timing spectra: one corresponding to the Type 1 backscatter events and one corresponding to the relative time differences in coincidences between positron-electron pairs. The Type 1 backscatter event spectrum was generated using the full Monte Carlo simulation described in Chapter 3. The results can be seen as an overlay in figures 5.7, 5.8, as well as in figure 5.14 later in this section. The dark matter decay events timing spectrum is generated via simple kinematic 3-body phase space Monte Carlo decay involving the  $\chi, e^+, e^-$ . This simulated theoretical timing spectrum is described in more detail in section 5.3.4.1. We show the results of both of these simulations in figure 5.8, highlighting that the dark matter decay in equation 5.9 is described in more detail further below. For figure 5.8, we used the event type fractions in table 2.2 to adjust the number of events so that the dark matter decay appear as 1% of the total number of  $\beta$ -decays.

---

<sup>7</sup>We fit each STP with a Gaussian to determine the mean value. The structure of the STPs for the 2012-2013 was checked to be Gaussian. A similar analysis on the 2011-2012 TDC data showed that it could not be approximated in simple statistical forms and hence contributed to our decision to omit the 2011-2012 data.

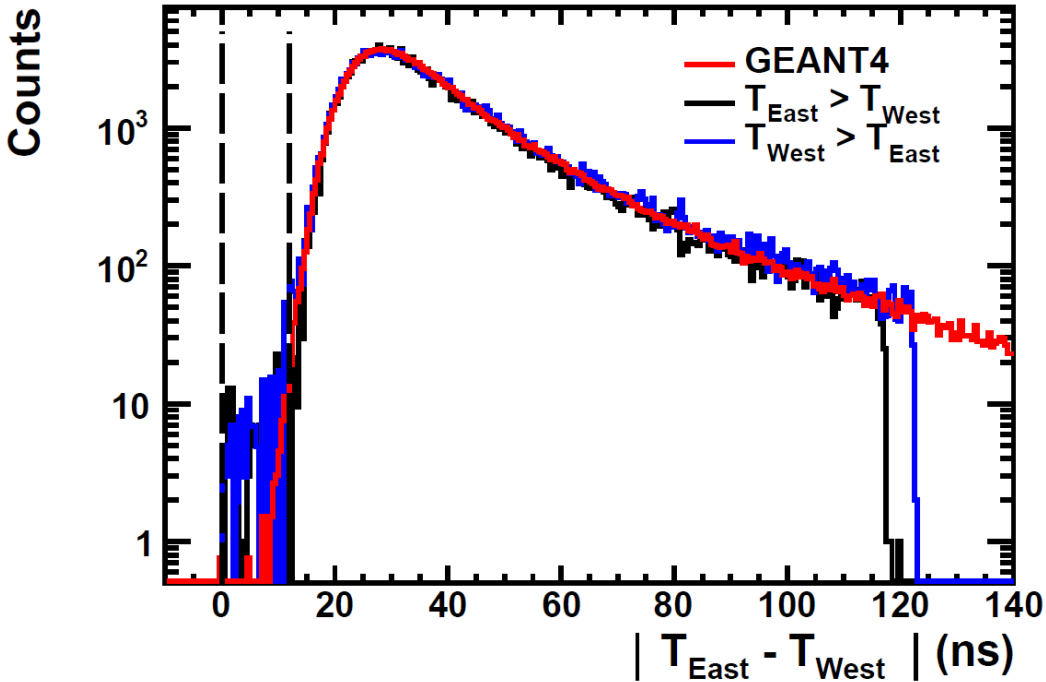


Figure 5.7: Shows the background-subtracted, relative time differences between events that first trigger the East detector (blue) and events that first trigger the West detector (black). An overlaid GEANT4 simulation (red) with a  $2 \text{ ns}$  timing resolution shows the expected timing spectrum for conventional  $\beta$ -decay Type 1 backscatter events. Dotted lines illustrate the chosen time window used in this analysis to identify candidate dark matter decays. Bin width of  $50 \text{ ps}$ . The channels are converted to time using the setting from the electronics. This figure was first published in [Sun+18; Sun+19].

For the Type 1 backscatter spectrum, in the ideal scenario there would be no events with transit times within the kinematically forbidden region. However, this is unrealistic because there is noise in the TDC timing resolution. Using our GEANT4 simulation, we were able to extract the relative time differences for Type 1 event coincidences. We performed a study with different timing resolutions by re-sampling the true transit time against a Gaussian centered on the travel time with characteristic widths of  $0 \text{ ns}, 1 \text{ ns}, 2 \text{ ns}, 3 \text{ ns}, 4 \text{ ns}$ . There was a clear match by eye with the Type 1 backscatter peak and the  $2 \text{ ns}$  timing resolution simulation, as shown in figure 5.9. Furthermore, this is consistent with the characteristic widths of the STPs determined earlier in initial timing data quality checks. Finally, we note that the GEANT4 simulation was only used as a qualitative comparison to illustrate the clear signal equation 5.9 would produce in the UCNA detector.

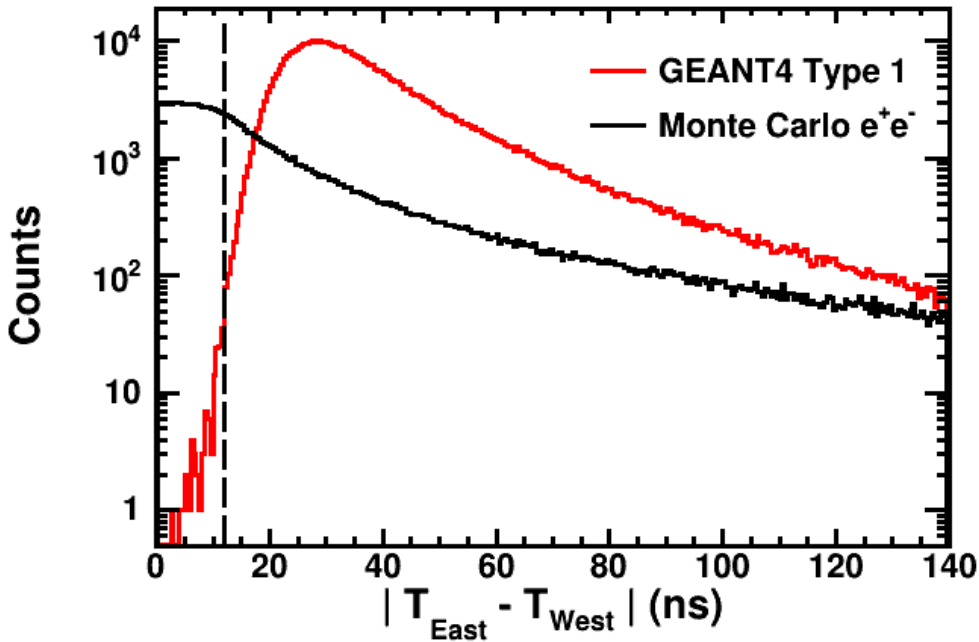


Figure 5.8: A simulated timing spectrum of a Type 1 decay event (red) vs a  $e^+e^-$  dark matter decay event (black), assuming a 1% branching ratio for the dark matter decay. The timing spectrum is generated by sampling a simple three-body phase space for the  $\chi, e^+, e^-$  and assuming the maximum available summed kinetic energy, 644 keV, for the  $e^+e^-$  pair. The dotted line represents the chosen timing window for this analysis. Bin width of 50 ps. Figure first published in [Sun+19].

### 5.3.3.3 Discussion on Background Subtraction

Here we discuss the background<sup>8</sup> subtraction in the final determination of foreground dark matter decay events. The events examined in this analysis are Type 1 backscatters. In order to properly identify these decay rates, the foreground runs must be adjusted for background. In the original UCNA experiment data-taking procedure, background runs were taken for only  $\frac{1}{5}^{th}$  of the time compared to foreground runs (the actual background to foreground ratio was 1:5.07). This was chosen to optimize the statistical precision of the UCNA  $A_0$  extraction. However, in the dark matter decay analysis, we have to scale the background run's live-time to that of the foreground runs, which effectively makes the background run's errors the dominant statistical error in the analysis. This is simply due to the data-taking

<sup>8</sup>The background runs are summarized in table 2.3. They involve the full experiment running but without UCNs loaded into the decay trap (they are stopped by the gate valve described in section 2.2.3). Typically, these events are background photons that interact with the plastic scintillators, producing a Compton scattered electron which travels in our apparatus and triggers both scintillators.

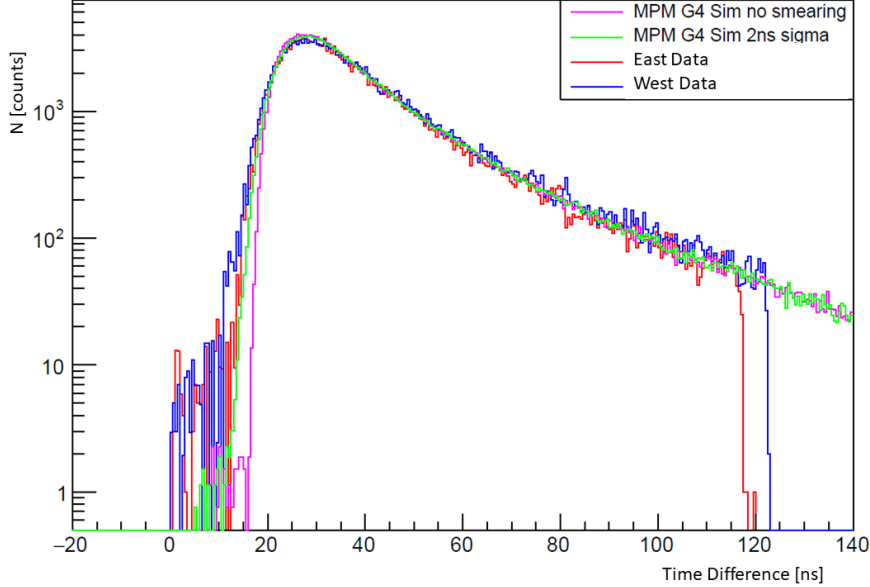


Figure 5.9: Simulated timing spectra for Type 1 backscatter events taken from GEANT4 simulation with different timing resolutions applied in post-processing (0 ns in purple, 2 ns in green). Background-subtracted data for East (red) and West (blue) TDCs also shown. From inspection, 2 ns makes the Type 1 backscatter timing peak match. Studies were performed with 1 ns time steps but not shown in order to simplify the overall presentation.

procedure prioritizing a structure that optimizes  $A_0$  sensitivity that has unfortunate consequences for the dark matter decay analysis. This ultimately does not prove to be a major limiting factor in impact of our extracted results.

### 5.3.4 Detection Efficiency Estimates

Once we have a total number of background-subtracted events in our kinematically forbidden region, we have an estimate of the number of candidate dark matter decays that UCNA detected. We then need to apply a conversion factor that relates the detected number of events to the true number of candidate dark matter decays produced. In this case, it would be the true number of  $e^+e^-$  pairs detectable by the UCNA apparatus. This is what we term the detection efficiency and it is composed of several factors which are all multiplicative and discussed below.

#### 5.3.4.1 Kinematic Acceptance

The kinematic efficiency can be described as the fractional number of dark matter decays where the UCNA detectors would have a coincidence trigger. Recall that this signature in our electronics is necessary otherwise the foreground neutron  $\beta$ -

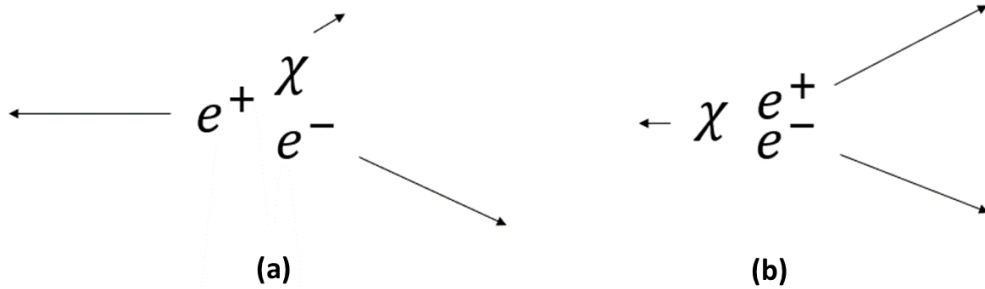


Figure 5.10: A simple diagram of the kinematic efficiency. The  $\chi$  particle is the dark matter particle and lost in the UCNA detector. The positron-electron pair must travel in opposite directions (a) to be detected or else their signal is washed out by the conventional Type 0 decays (b). In this diagram, the East and West detectors would be on the left and right respectively.

decay events would wash out any potential dark matter decay signals. Due to the  $\approx 4\pi$  angular acceptance of UCNA, this effectively reduces down to the fractional number of events where the decay electron and decay positron are generated with momenta in opposite hemispheres (as defined along the axis of the decay trap). The imposed 1 T magnetic field would direct those types of events outwards and create a coincidence trigger (assuming they had sufficient energy to trigger the detector). Figure 5.10 shows a schematic of the types of events that would be counted in this kinematic efficiency.

The kinematic efficiency is calculated over several values of  $m_\chi$ , the allowable mass range of the  $\chi$  particle. In practice, this means simulating different kinetic energies of the resulting  $e^+e^-$ . We pay special attention to the low energy cut-off of 144 keV when the trigger function begins to dominate (discussed in section 5.3.4.3). The widths were chosen to be comparable to the energy bin widths used in the final confidence limits. When we consider the full range of  $m_\chi$  and make our simplistic Monte Carlo simulation of the kinematic efficiency, the acceptance is  $\approx 40\%$ . Thus, this fraction of candidate dark matter decay events are detectable using our coincidence trigger criteria in this analysis.

### 5.3.4.2 Timing Window Acceptance

The second acceptance that gets included in the detection efficiency is the timing window acceptance. This represents the amount of candidate dark matter decays in equation 5.9 that we could detect in a given time window. When we simulate the

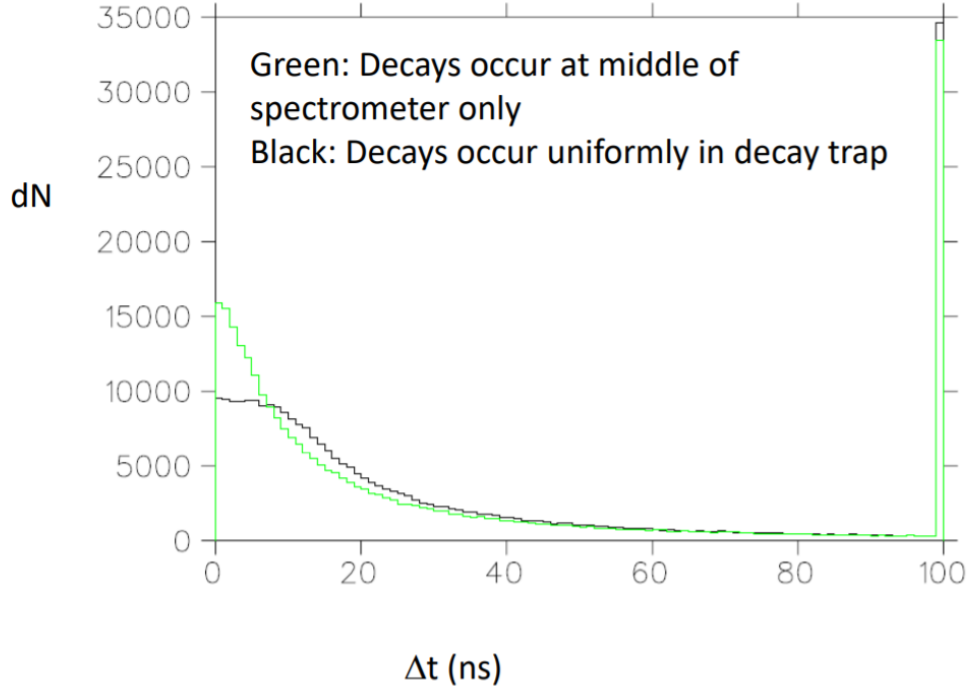


Figure 5.11: Monte Carlo simulation of arrival times in the detectors for a three-body decay where  $m_\chi$  is a minimum and hence there is maximum available kinetic energy to the  $e^+e^-$  of 644 keV. Timing spectra are overlaid for events generated in the center of the UCNA decay trap (green) and uniformly populated throughout the decay trap (black). The large bin at 100 ns represents an “over-fill” bin — a bin where all the events beyond are contained as well. In reality, there would be an arbitrarily long tail to the spectrum that extends  $> 100$  ns.

kinematic decay of equation 5.9 within the decay trap volume of UCNA, we obtain a spectrum of arrival times (shown in figure 5.11 for one value of  $m_\chi$ ). Due to the helical nature of the electron (or positron) trajectory, there are potentially long time delays between coincidence triggers. We simulate this by populating decays via equation 5.9 within the UCNA trap and performing a phase space three-body kinematic decay where we vary the mass of the  $\chi$  particle and hence the available kinetic energy for the  $e^+e^-$  pair.

We reproduced these simulations for different values of potential  $m_\chi$ , consistent with the energy resolutions of our final energy bin widths. Over the range of masses for candidate  $\chi$  particles, the acceptance probability ranges from  $\approx 20 - 40\%$  when using a  $\Delta t = 12$  ns timing window cut. The choice of timing window was studied and is discussed below.

At this stage, we remind the reader of a few points discussed throughout the course

of this section. First, the minimum transit time for a  $\beta$ -decay electron across the 4.4 m scintillator-to-scintillator distance is  $\approx 15\text{ ns}$ . Second, we have  $\sigma_t \approx 2\text{ ns}$ , as ascertained by the width of the STPs and corroborated by a GEANT4 timing spectrum simulation. Third, there is  $\approx 1.7\text{ ns}$  deadtime in the beginning of the West TDC associated with longer cable lengths when compared with the East TDC and hence the initial 1.7 ns is cut from the physically relevant timing region.

With these considerations in mind, we analyzed several choices of timing windows to see what background-subtracted events survived our cuts. In particular, we want to minimize any events from the true Type 1 backscatter signal. Some sample timing windows can be seen in figure 5.12. From this, we clearly see how, as the time window is opened up, there is a clear structure of Type 1 backscatter neutron  $\beta$ -decay events entering in the spectrum. It is interesting to note that even in the background only runs (see figure 5.12a) this peak still begins to enter in the spectrum shape. These could have originated from electrons produced from Compton scattering by background photons interacting with the plastic scintillator. These electrons could pass through the apparatus and trigger the opposite side detector.

We studied which timing window would be best to balance cutting out noise while optimizing our acceptance window and general robustness of results. For instance, a short time acceptance window would leave us with very few events and a stronger limit. However, we also wanted to be robust against systematic shifts in TDC channels from run-to-run or octet-to-octet and hence would like a larger time acceptance window. Furthermore, we wanted to avoid choosing a narrow time range and weaken the confidence in our studies on underlying systematic shifts in the timing data. Throughout the analysis, we kept in mind the overarching  $< 15\text{ ns}$  limit as the minimum transit time for a speed-of-light particle (noting that for typical Type 1  $\beta$ -decay electron energies, the fastest transit time would be  $\approx 16\text{ ns}$ ). We wanted to be  $(1 - 2)\sigma_{t,resolution}$  within the kinematically forbidden region and include as much of the timing window as possible. Ultimately, we settled on a timing window from 0 – 12 ns where the first  $\approx 2\text{ ns}$  of the West TDC values were cut out due to additional deadtime (this was adjusted for in our final acceptance). We varied this time window to study the effect of choosing different West TDC time cuts (and later East TDC) on the total number of events in the kinematically forbidden region. The results are shown in figure 5.13. We use the resulting count numbers in the figure to estimate our uncertainty in the timing window acceptance at  $\approx 15\%$ .

We note that this analysis was unblinded, in contrast to the Fierz interference

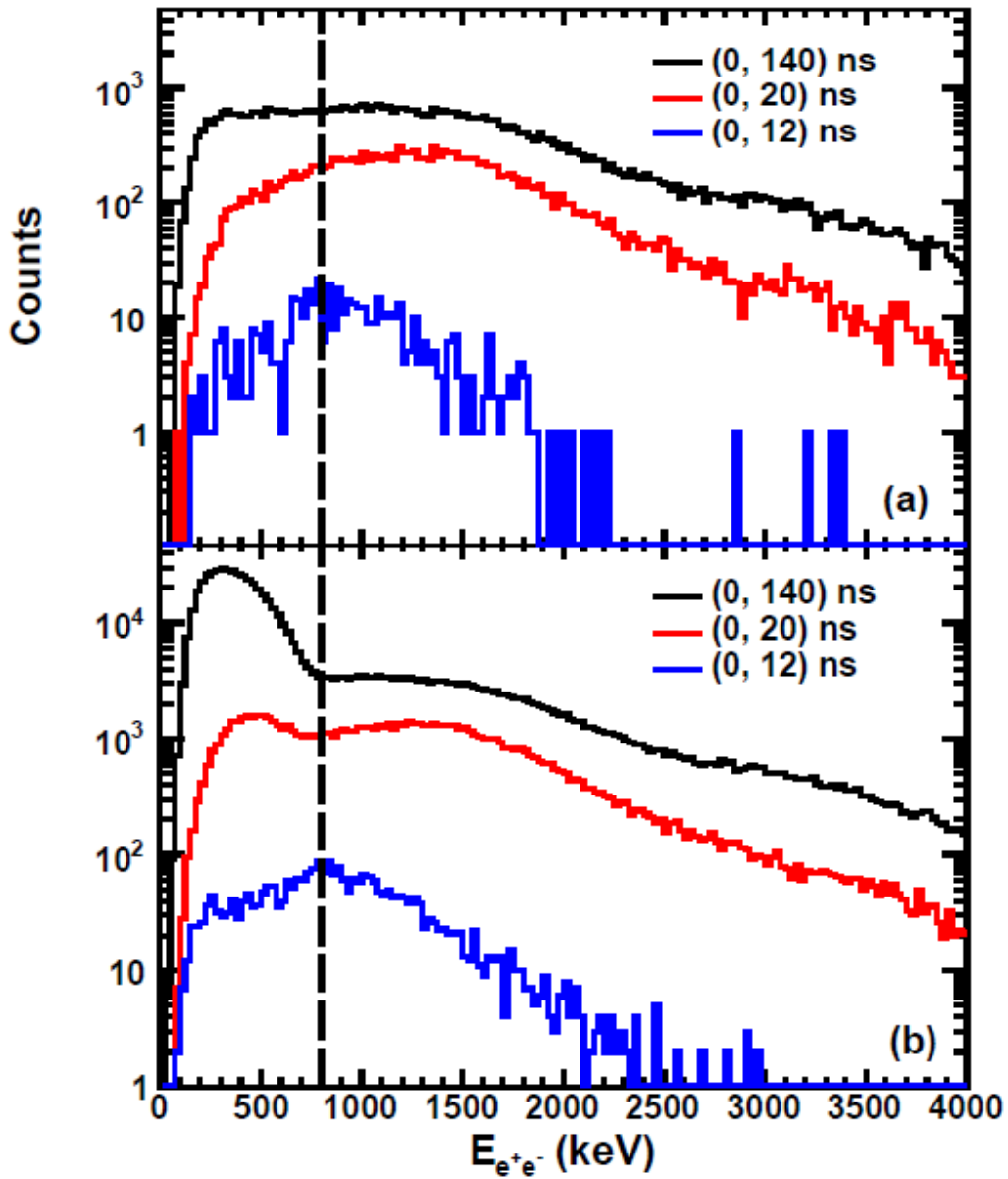


Figure 5.12: Energy spectrum of (a) background and (b) foreground runs, for three separate time-windows. We note that there is factor  $\approx 5$  difference between live times for the foreground and background runs, hence the differences in total count numbers. Clear structure of a neutron  $\beta$ -decay backscattering peak at 300 keV is visible for time-windows  $> 12$  ns in the foreground runs. Dashed lines at 0 keV, 800 keV indicate the energy region of interest used for the present analysis. Figure first published in [Sun+18].

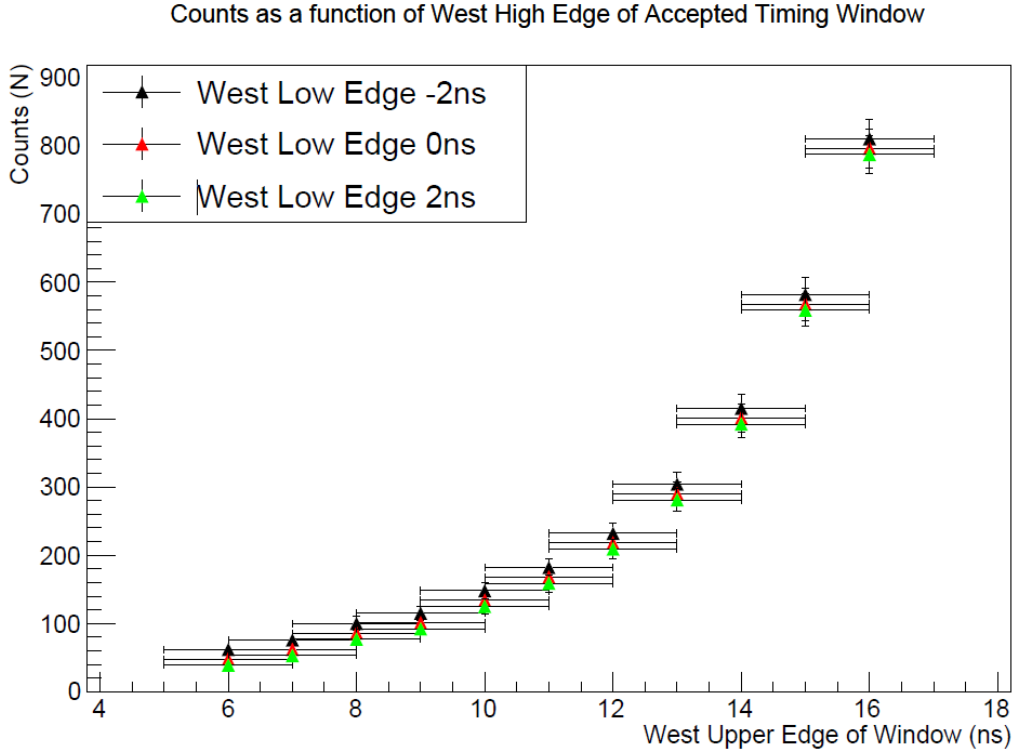


Figure 5.13: Number of background-subtracted events accepted within our chosen timing window as a function of the high time cut off. Three different low time cut offs are used:  $-2\text{ ns}$  (black),  $0\text{ ns}$  (red),  $2\text{ ns}$  (green). We note that the  $-2\text{ ns}$  is unphysical unless there was systematic electronic jitter in the TDCs. Vertical error bars are set by  $\sqrt{N}$  of the total number of counts and horizontal error bars are set to  $1\text{ ns}$  arbitrarily. The final chosen timing window for the West TDC was  $[2\text{ ns}, 12\text{ ns}]$  in order to cut out the additional dead-time from wire length differences (see text). For the East TDC, we used  $[0, 12\text{ ns}]$ . Efficiencies were adjusted for these East/West time window discrepancies.

extraction discussed in Chapter 4 using the same datasets. This was primarily due to the fact that the signal of a  $e^+e^-$  appearing at the 1% branching level would be so significant (see, for example, figure 5.8) it would be unrealistic to blind. Hence we were not concerned about making analysis cuts that would mildly bias our upper limits (we note that a 1% branch corresponds to  $100\times$  our upper limit).

After choosing our final timing window, we make an energy cut at  $644\text{ keV}$  which is the maximum allowable summed kinetic energy of the  $e^+e^-$  pair. This introduces another efficiency in the form of the energy resolution. Namely, decays with  $m_\chi$  resulting in  $E_{K,e^+e^-} = 644\text{ keV}$  would be smeared by the energy resolution and hence the peaks would be centered at  $644\text{ keV}$  with some characteristic width. An energy cut at  $644\text{ keV}$  would in principle miss half the events. We adjust for this

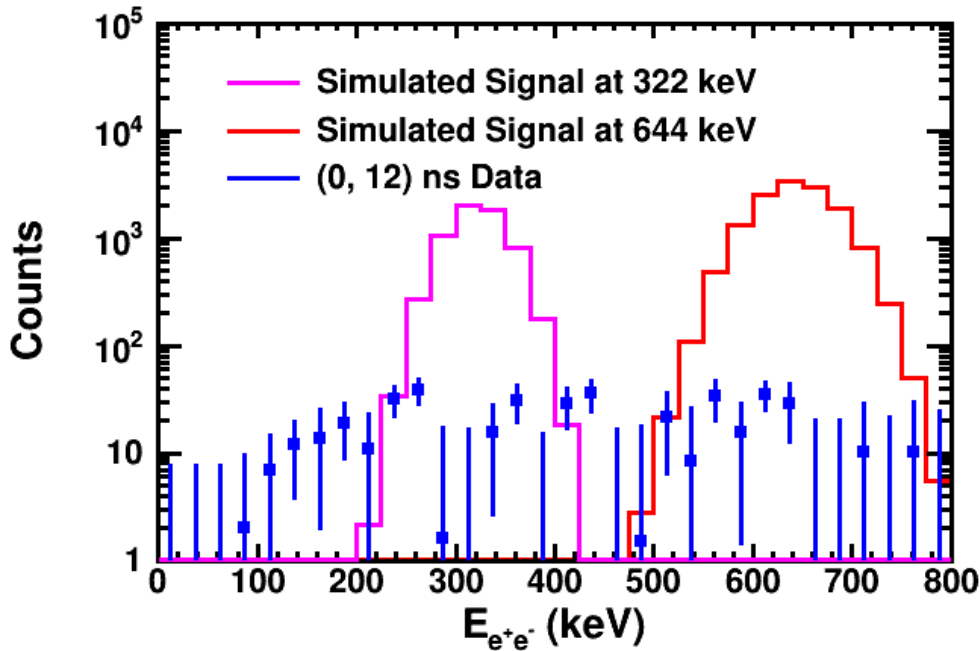


Figure 5.14: Background-subtracted  $e^+e^-$  pair kinetic energy spectra for events in the chosen analysis time-window. For comparison, simulated positive dark matter decay signals at summed  $e^+e^-$  kinetic energies of 322 keV, 644 keV are overlaid, assuming 1% branching ratio. Bin widths of 25 keV. Figure first published in [Sun+18; Sun+19].

efficiency as well in the final acceptance. In figure 5.14 we show the resulting events that pass our timing window cut from background-subtracted UCNA 2012-2013 data, restricted by our energy cut to  $E_{K,e^+e^-} \in [0, 644 \text{ keV}]$ . This data is overlaid with 1% branching ratio signals, simulated in GEANT4, as described in Chapter 3, at the endpoint energy and half the endpoint energy. As in figure 5.8, these overlaid signals are to give a qualitative impression of the relative signal strengths and are not propagated in quantitative limits discussed below.

At this stage, we have the final data with an acceptance time window of 0 – 12 ns and binned in 25 keV bins (comparable to energy resolution). We have determined the kinematic and timing window efficiencies. Next we determine the efficiency factors for the UCNA detector response.

### 5.3.4.3 Trigger Function Efficiency

There is an efficiency associated with the trigger function that is understood simply as an energy-dependent probability to detect a positron or electron in the UCNA

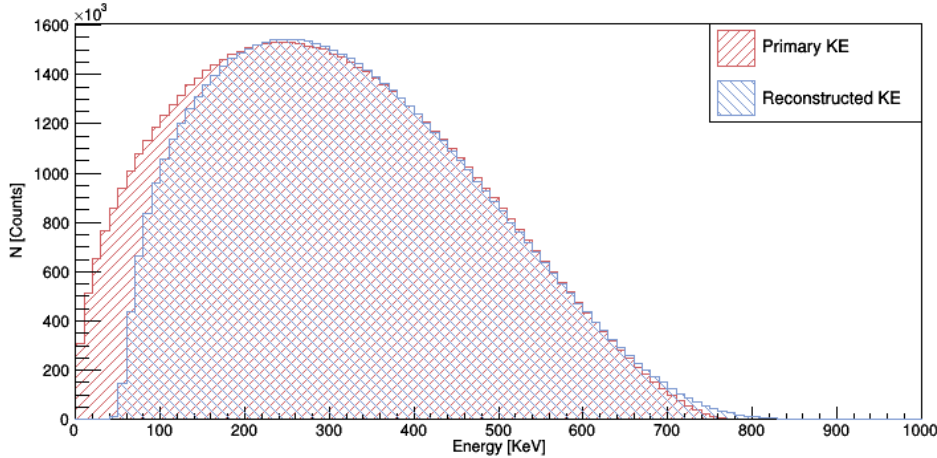


Figure 5.15: A diagram of the impact of the detector response model on simulated Monte Carlo spectra. The initial spectra is also presented for comparison. These simulated events have been processed with the 2012-2013 UCNA dataset calibration. The low energy effects ( $< 200 \text{ keV}$ ) are primarily due to the trigger function.

apparatus. We discussed the trigger function at length in section 3.4.4. In principle, the trigger function is actually unique to each PMT for each side detector. However, in the course of the asymmetry analysis, a global trigger function is deduced in units of reconstructed energy. We show the effect of this trigger function on a sample spectrum in figure 5.15. The trigger function can be extracted as the ratio of the data spectrum and the theory spectrum ( $\frac{P_{\text{data}}(E)}{P_{\text{theory}}(E)}$ ). The trigger function for the 2012-2013 detector response model is given in table 5.1.

Energy [keV]:	< 25	35	45	55	65	75	85	95	105
Trigger [%]:	0	0.05	1.6	15.9	43.1	61.4	73.6	80.9	85.6
Energy [keV]:	115	125	135	145	155	165	175	185	> 195
Trigger [%]:	88.9	91.3	92.9	94.6	95.9	96.9	97.9	98.8	> 99

Table 5.1: Value of trigger function for Type 0 events on 2012-2013 reconstructed energy spectrum for different energy bins spanning the low energy range ( $< 100 \text{ keV}$ ) of UCNA apparatus. The quoted energy value is the midpoint of the bin (for example, the  $35 \pm 5 \text{ keV}$  bin has trigger probability 0.05%).

We note that in this analysis, the trigger function actually needs to be applied twice because we are imposing the condition of a coincidence in both detectors. Each event uses the Type 0 trigger function. Hence, we use the square of the trigger function in our final efficiency.

We estimate the trigger function inefficiency at a conservative 20% at the high

energies (since the probability function is  $\approx 1$  at high energies, this results in us taking the maximum of the error associated with the trigger function), consistent with the procedure described in section 4.2.3. At the endpoint energies of the  $m_\chi$ , the summed kinetic energies of the  $e^+e^-$  would be 644 keV and result in a 2% reduction in the detection efficiency. At lower energies, the reduction is larger: at 244 keV the detection efficiency is reduced by 8%, and at 144 keV the reduction is 60%.

#### 5.3.4.4 Electron-Positron Detector Response

The final detector response efficiency to consider is the response of our UCNA apparatus when interacting with positrons instead of neutron  $\beta$ -decay electrons. In order to do this, we again make use of the GEANT4 simulation that we produced and discussed in Chapter 3. We run the simulation with  $10^5$  decay electrons and  $10^5$  decay positrons and examine the overall spectral response, prior to imposing any detector response model (note that we are folding in the detector response model in other parts of the detection efficiency so we do not use it here to avoid “double-counting”). We run these simulations at several energies: 644 keV (the endpoint kinetic energy of the summed  $e^+e^-$ ), 483 keV (the  $\frac{3}{4}$  point), 322 keV (the halfway point, shown in figure 5.16), and at 200 keV (near the edge of the trigger function “turning on”). The resulting energy spectra differences at the simulated initial kinetic energy for the positron and electrons define the detector response difference (within the detector resolution).

The detection probability of a positron in the UCNA apparatus at a specific energy is about 85% of the detection probability of an electron with the same initial kinetic energy. The remaining 15% of positrons produce energy deposition over a range of  $\approx 0 - 1$  MeV due to annihilation gammas and do not produce a candidate dark matter decay event ( $n \rightarrow \chi + e^+e^-$ ) signal. There is actually a range of detection probabilities for the positron that is dependent on and monotonically decreases as a function of the initial kinetic energy. At 200 keV, it is 0.86. At 644 keV, it is 0.84. To simplify the acceptance, we apply a fixed  $\frac{1}{0.85}$  acceptance factor for the differences in detector response to positrons vs electrons and note that there is an associated  $\pm 1\%$  uncertainty in this factor.

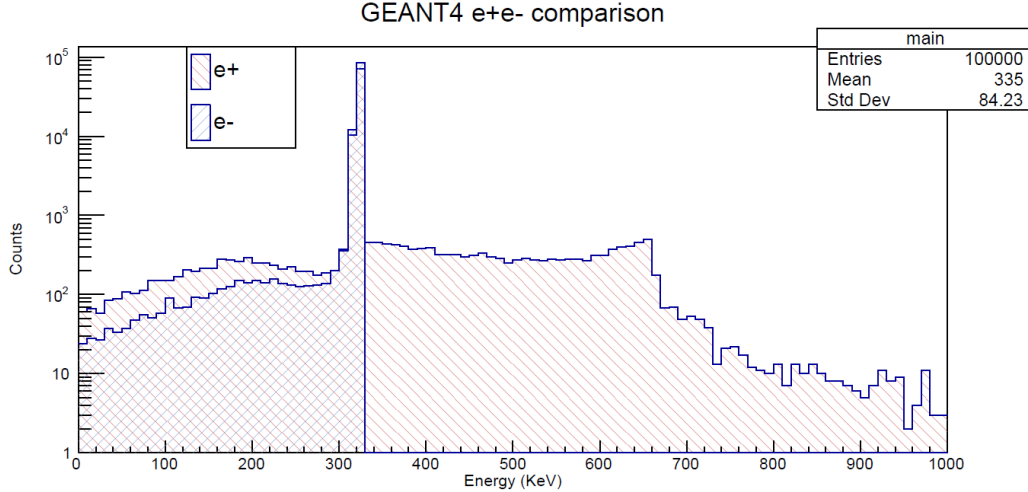


Figure 5.16: A comparison of the energy deposition spectra for electrons vs positrons in the UCNA GEANT4 simulation. Simulated by pointing  $10^5$  positron events with initial kinetic energy  $322\text{ keV}$  from the center of the decay trap towards the East detector. The number of positrons detected in the  $322\text{ keV}$  bin is 85% that of the electrons. All other events events are assumed to be “lost” from the efficiency calculation perspective. These positrons are converted into annihilation  $\gamma$ s that deposit energy in our detector over a range from  $0 - 1\text{ MeV}$  which is broad when compared to the peak width.

#### 5.3.4.5 Final Total Acceptance

The total detection efficiency, sometimes called the final acceptance, is the product as a function of summed kinetic energy of the aforementioned effects. This is shown in figure 5.17. Using the final acceptance, we can adjust our candidate dark matter detected events (with energy and timing cuts applied) to a “true” number of produced candidate dark matter events. To accomplish this, the data shown in figure 5.14 is divided by this detection efficiency. We note that the propagated statistical error bars (dominated by the background statistical errors) are also scaled by this detection efficiency.

### 5.4 UCNA Extracted Limits

Up until this point, we have discussed the initial concept of measuring a dark matter decay via equation 5.9 in UCNA, presented initial timing and energy cuts, and determined a final acceptance. In this section, we discuss some final adjustments and present our confidence limits on such a decay.

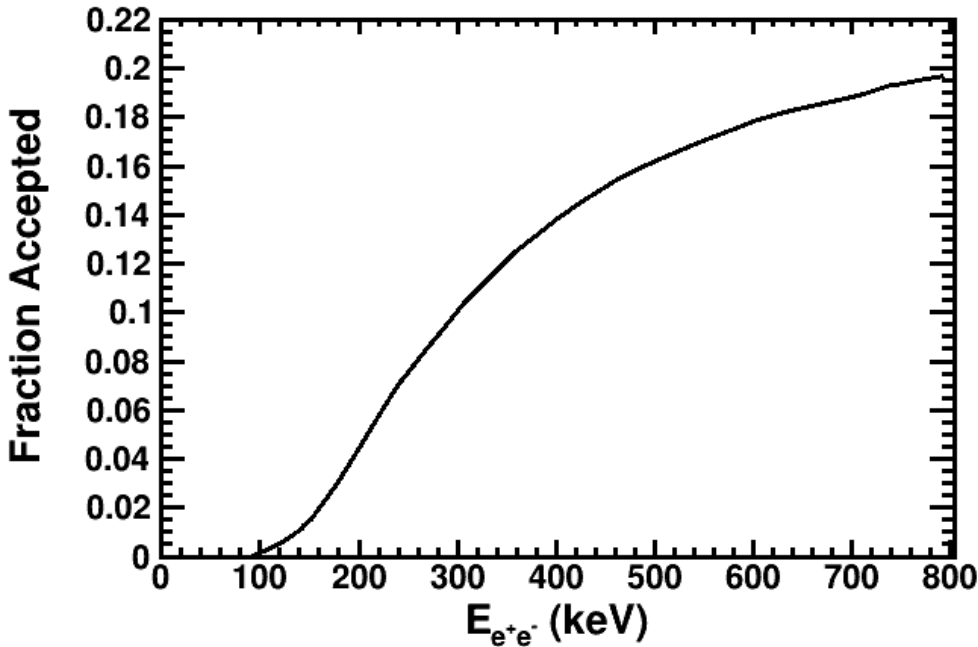


Figure 5.17: Total  $e^+e^-$  pair acceptance as a function of summed kinetic energy. We multiply three different efficiencies in this final acceptance: the kinematic efficiency, the timing window efficiency, and the trigger efficiency. Furthermore, we correct for the positron-electron differences in detector response via GEANT4 simulation calculated efficiencies. Figure first published in [Sun+18; Sun+19].

#### 5.4.1 Bin Aliasing Study

Upon examining the data points in figure 5.14, specifically the statistical error bars, we noticed there were some point-to-point variations that may have underlying structure. This may have been an artefact of “bin aliasing”, where the choice of binning gives artificial structure to the data. In order to study this effect, the analysis described in this chapter was repeated with all the energy bins shifted by half a bin width (12.5 keV). The final confidence limits (shown later) are presented with the data shown in figure 5.14 plus the data binned with a half-width shift.

#### 5.4.2 Look-Elsewhere Effect Correction

For the decay given by equation 5.9, there is a range of acceptable  $\chi$  masses which translates to an acceptable summed kinetic energy range for the  $e^+e^-$  pair of 0 – 644 keV. For a real dark matter decay channel of a fixed  $\chi$  mass,  $m_\chi$ , this amounts to searching for a peak structure over a range of energies. When one is performing such a peak search, the probability that fluctuations at other energies

could occur must be considered. This is usually termed the “look-elsewhere effect”: the probability that a statistically significant fluctuation will occur given enough samples [Lyo08]. The following discusses how we accounted for the look-elsewhere effect.

This look-elsewhere effect was accounted for numerically, drawing on the method used in [BCR18]. First, a statistical test was constructed,

$$\xi = \sum_i \frac{N_i - \mu_i}{\sigma_i} \text{ for } N_i > \mu_i \quad (5.22)$$

where  $N_i$  is a normally-distributed random variable for bin  $i$  with mean  $\mu_i$  and standard deviation  $\sigma_i$ , and both  $\mu_i$  and  $\sigma_i$  are given by the data.  $\xi$  is computed with a large number of Monte Carlo samples for each final energy bin, as well as the “single-bin” dataset, i.e. when all events are considered together. The ratio of the single-bin  $\xi$  distribution to the  $\xi_i$  distributions provides the look-elsewhere correction factor<sup>9</sup>. This correction is applied to the cumulative distribution function (CDF) of the single-bin confidence levels. The corresponding CDF for the individual energy bins is solved for numerically to obtain new confidence levels, giving us our final confidence limits.

### 5.4.3 Final Exclusion Limits

Our final confidence limits from the analysis discussed in this chapter are shown in figure 5.18. Our results give limits on a direct measurement of the neutron dark matter decay channel in equation 5.9. Assuming such a decay exists at the 1% level required to resolve the neutron lifetime anomaly, we exclude this possibility at  $\gg 5 \sigma$  for summed kinetic energies of the positron-electron pair of  $100 \text{ keV} < E_{e^+e^-} < 644 \text{ keV}$ . If equation 5.9 is not the only decay channel present, we set a branching ratio limit on it of  $\frac{\Gamma_{n \rightarrow \chi + e^+e^-}}{\Gamma_n \text{ total}} < 10^{-4}$  at the 90% confidence level, over the same energy range of  $100 \text{ keV} < E_{e^+e^-} < 644 \text{ keV}$ .

### 5.4.4 Discussion

In January 2018, authors Fornal and Grinstein proposed an exotic dark matter decay channel in [FG18a] for the neutron in order to resolve the neutron lifetime anomaly [GG16; Wie18; WG11]. One of the decay channels in the theory was neutron to dark matter  $\chi$  plus a positron-electron pair. The UCNA collaboration was in a unique position to analyze this particular decay channel because the UCNA

---

<sup>9</sup>Also known as the “trials factor” in other literature.

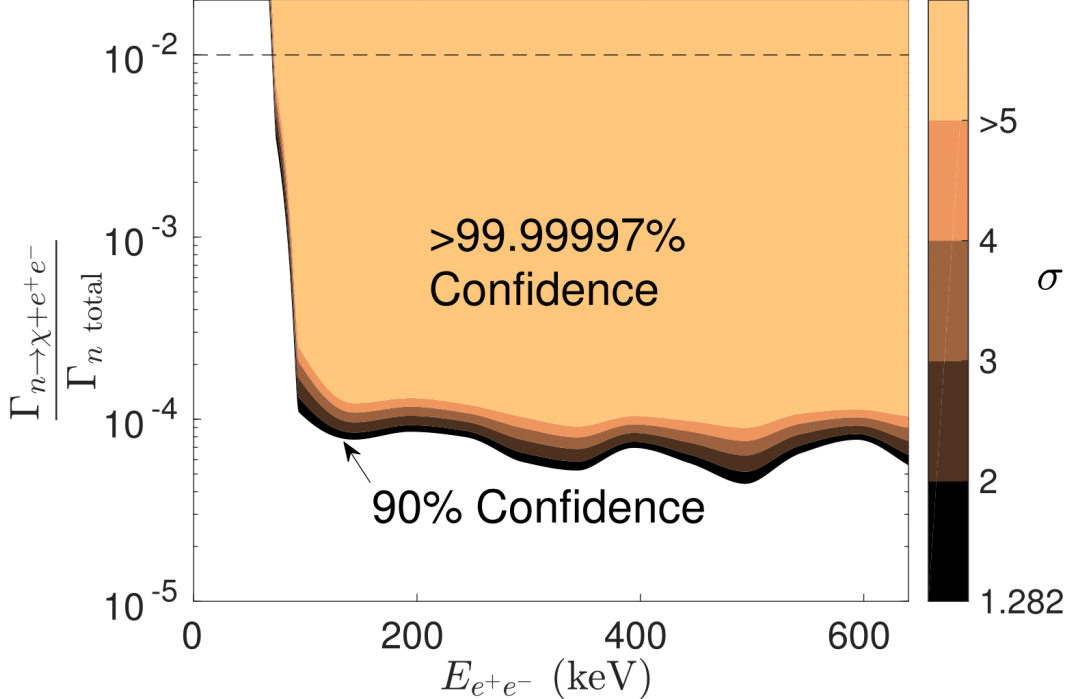


Figure 5.18: Confidence limits on the branching ratio of the neutron dark decay channel, as a function of the kinetic energy of the produced  $e^+e^-$  pair. This is directly related to the proposed  $\chi$  mass by  $m_\chi = m_n - 2m_e - E_{e^+e^-}$ , which has a range of  $937.900\text{ MeV} < m_\chi < 938.543\text{ MeV}$  in [FG18a]. A branching ratio of  $10^{-2}$ , which would be required to explain the neutron lifetime anomaly if  $n \rightarrow \chi + e^+e^-$  were the only allowed dark matter final state, is shown by the dashed line. Data taken from figure 5.14 is used to generate final confidence limits. We checked for bin aliasing and look-elsewhere effect (see text). Figure first published in [Sun+18; Sun+19].

experiment had completed data-taking and had originally measured the electron-like decay products of conventional neutron  $\beta$ -decay in order to extract the asymmetry parameter,  $A_0$ . The geometry of UCNA meant that by using judicious timing cuts on coincidence triggers between both East and West detectors, we could greatly suppress our conventional foreground signal and have unique sensitivity to these candidate dark matter decay events.

In our analysis, we used CAEN TDCs which were installed on UCNA. Due to poor functionality in the 2010-2012 TDC performance, we could only use the 2012-2013 TDC data. This was calibrated to a true timing spectrum for all electron-like events that resulted in a coincidence trigger. Event discrimination was used and a comparison timing spectrum for conventional  $\beta$ -decay Type 1 events was generated using our GEANT4 simulation. The total number of visible events that

passed all cuts were adjusted for the different efficiencies present in our detector and the resulting counts were translated to a branching ratio by dividing by the total number of  $\beta$ -decay events in the 2012-2013 dataset that satisfy our energy criteria ( $\approx 14.55 \times 10^6$ ).

We effectively rule out the positron-electron decay channel, equation 5.9, as the sole explanation for the neutron lifetime anomaly, for the summed kinetic energy of  $E_{e^+e^-} \in [100, 644] \text{ keV}$ . In conjunction with limits set on the photon decay channel, equation 5.8, in [Tan+18], direct-data measurements were used to set limits on [FG18a] as the sole explanation for the neutron lifetime anomaly. More results were published afterwards [Klo+19] but these direct-data measurements set the stage for a data-driven discussion at the PPNS conference. These results also corroborated the indirect limits set by the neutron star community; they analyzed the upper mass limits of neutron stars given this exotic decay channel and concluded that this additional decay channel would result in a mass limit smaller than some of the currently known neutron stars, and used this to extract a limit on the branching ratio of a dark matter decay channel [Bay+18; McK+18].

The neutron lifetime anomaly remains a mystery, with yet another promising explanation ruled out. However, this analysis in response to a novel theory reflected a period of movement in the field. In the next generation of high-precision experiments, the community as a whole hopes to find evidence that sheds light on this two-decade long discrepancy.

## Chapter 6

### NEDM@SNS: $B_0$ MAGNET

In this chapter, we discuss an experiment that is in development, nEDM@SNS. The nEDM@SNS aims to use UCNs to measure or place limits on the neutron electric dipole moment (nEDM) and will take place at the Spallation Neutron Source (SNS). The goal of this nEDM measurement, in brief, is to further constrain beyond Standard Model physics. However, since nEDM@SNS is still under development, the work discussed in this chapter will focus on the research and development efforts of one major component of the nEDM@SNS experimental apparatus: the  $B_0$  magnet coil. First, we provide an overview of the experiment, highlighting key features that will allow for an unprecedented high-precision measurement on the nEDM. At the end, we conclude with an outlook for the nEDM@SNS experiment.

#### **6.1 The Neutron Electric Dipole Moment**

Recall that in Chapter 1, we discussed electric dipole moments, with a focus on neutron electric dipole moments. They can be understood, classically, as an asymmetric charge distribution that arises within the neutron due the physical displacement of the valence quarks: two down quarks ( $q_d = -\frac{1}{3}e$ ) and one up quark ( $q_u = +\frac{2}{3}e$ ). This electric dipole moment of the neutron is what the nEDM@SNS experiment aims to measure.

##### **6.1.1 Overview of nEDM@SNS Experiment**

The nEDM@SNS experiment is described in detail in [Ahm+19]. In this section, we illustrate a few of the key concepts of the experiment. We provide a general overview of their technical components and physics implications. The details of the development and implementation of each key concept are left to the reference. There is one exception: the  $B_0$  magnet. We introduce and focus on the  $B_0$  magnet as a component of the nEDM@SNS apparatus and provide further details in later sections of this chapter.

###### **6.1.1.1 Introduction**

Most modern searches for neutron electric dipole moment, such as nEDM@SNS, make use of measurements of changes in the Larmor precession frequency of the

neutron under a reversing electric field and a constant, parallel magnetic field. The Larmor precession frequency of a neutron is given by

$$\omega_{\uparrow\uparrow} = -\frac{2ex}{\hbar}|\vec{E}| + \gamma|\vec{B}| \quad (6.1)$$

where  $e$  is the elementary charge,  $x$  is a characteristic displacement of the quarks,  $\vec{E}$  is the imposed electric field (that gets reversed),  $\vec{B}$  is the holding magnetic field, and  $\gamma$  is the gyromagnetic ratio of the neutron. The  $\uparrow\uparrow$  indicate that this formula holds when  $\vec{E}$  and  $\vec{B}$  are parallel<sup>1</sup>. In order to measure  $x$ , the characteristic displacement, and hence the dipole moment ( $\vec{d} := e\vec{x}$ ), we can measure the difference in angular frequency

$$\Delta\omega = \omega_{\downarrow\uparrow} - \omega_{\uparrow\uparrow} = \frac{4ex}{\hbar}|\vec{E}| = \frac{4d}{\hbar}|\vec{E}| \quad (6.3)$$

where  $d$  is the quantity of interest, the electric dipole moment.

The uncertainty on  $d$  can be shown to be

$$\sigma_d = \frac{\sqrt{2}\hbar}{4|\vec{E}|\tau\sqrt{N}} \quad (6.4)$$

where  $\tau$  is the observation time,  $N$  is the number of observations (polarized neutrons in our case), and we assumed  $\sigma_{\downarrow\uparrow} = \sigma_{\uparrow\uparrow}$  in this result, where  $\sigma_{\downarrow\uparrow}$  represents the uncertainty on  $\omega$  when the electric and magnetic fields are anti-aligned. The denominator gives a figure of merit to quantify and compare the sensitivities of different Larmor precession measurement experiments.

For comparison, current best limits on the nEDM are  $d_n = (0.0 \pm 1.1_{\text{stat}} \pm 0.2_{\text{sys}}) \times 10^{-26} e \cdot cm$  [Abe+20]. The goal sensitivity of nEDM@SNS is  $d_n \lesssim 2 - 3 \times 10^{-28} e \cdot cm$ .

### 6.1.1.2 Experimental Highlights

The details of the nEDM@SNS experiment is extensively detailed in [Ahm+19]. In this section, we provide a qualitative description of a few experimental highlights that allow nEDM@SNS to reach a sensitivity of  $\approx d_n < 10^{-28} e \cdot cm$ . In order

---

<sup>1</sup>Equation 6.1 for the angular frequency is derived from the Hamiltonian for a neutron interacting in an electric and magnetic field given by

$$H = -\frac{2ex}{\hbar}(\vec{s} \cdot \vec{E}) - \gamma(\vec{s} \cdot \vec{B}) \quad (6.2)$$

where  $\vec{s}$  is the spin operator which, for the neutron, has eigenvalue  $s = \hbar/2$ .

to improve the sensitivity of the nEDM measurement, nEDM@SNS uses a few dedicated efforts to increase the denominator in equation 6.4.

In order to maximize the number of neutrons produced and hence the number of observations,  $N$ , a volume of superfluid  $^4He$  is contained and cold neutrons are transported into the fluid. By interacting with the superfluid  $^4He$  and being moderated to the Ultracold Neutron (UCN) energy regime, the UCNs remain in the central cell volume in large populations. In particular, this *in situ* UCN production avoids any transport losses for UCNs into the central volume of the apparatus.

In order to maximize the observation time,  $\tau$ , UCNs are used in a highly-reflective neutron cell. Modern experiments use UCNs because they allow long observation times - their low kinetic energies make them ideal for trapping and several materials (as discussed in chapters 1 and 2) can act as excellent reflectors for UCNs. Current efforts are underway to produce highly reflective neutron cells used deuterated tetraphenyl butadiene (dTBP) via vapor deposition to coat the inner walls of the cells. This dTPB coating captures the scintillation light from equation 6.5 and emits it at a higher wavelength (easier to read out) while amplifying the signal. This re-emitted light is eventually captured by wavelength shifting fibers and transported to Silicon Photomultipliers (SiPMs).

Once the UCNs are produced *in situ*, parallel (or anti-parallel) electric and magnetic fields are turned on and act upon the volume of UCNs. The UCNs are contained in a bath of  $^4He$  within the holding cell. The  $^4He$  itself acts as a stronger insulator than vacuum and hence allows for larger electric field strengths, larger  $|\vec{E}|$  values, before reaching a break-down voltage. Thus, the choice of UCN production also provides the advantage of safely applying stronger electric fields than previous nEDM experiments. In nEDM@SNS, the electric field strength is  $\approx 7\times$  greater than fields used in previous generation nEDM measurements.

At this stage, we have discussed increasing the parameters that maximize sensitivity via the uncertainty on the nEDM measurement in equation 6.4. One remaining component of this measurement now is to discuss the magnetic field stability and its uniformity, as it appears in equation 6.1. The experiment itself needs to contain an extremely uniform magnetic field so that it maintains the polarization of the UCNs and uniformly manipulates them (see, for example, [Abe+19] for a detailed description). A uniformly polarized UCN population allows longer observation times, a larger number of observation (neutrons contributing to our measurement), and reduced systematic errors associated with polarization and drifts. The topic of

the uniform magnetic field applied parallel (or anti parallel) with the electric field, specifically the construction of such a magnet coil called the  $B_0$  magnet, is the topic of section 6.2.

### 6.1.1.3 Two Complementary Measurements

In order to reach the goal sensitivities described previously, the nEDM@SNS has made considerable efforts to reduce the projected systematic uncertainty below that of the statistical uncertainty. In order to accomplish this, the experiment has been designed to measure the nEDM via two measurement techniques: the free precession method and the critical spin dressing method. These two techniques can be applied on the same volume of UCNs in the same spatial region to extract an nEDM value. However, their separate operation implies that the systematic effects and hence uncertainties associated with each method are separate. In particular, this means that each method is associated with a different set of systematic uncertainties that can be cross-checked against each other for further downstream improvements in the overall systematic uncertainty study.

**6.1.1.3.1 Free Precession Method** The free precession method involves using a small population of  $^3He$  atoms as a co-magnetometer in the superfluid  $^4He$  in order to capture the UCNs as they precess with their Larmor frequency. In the experiment, a fraction of  $^3He$  atoms ( $\approx 10^{-10}$ ) will be injected into the superfluid  $^4He$ . We wish to minimize the effect on the UCN population since  $^3He$  is a strong UCN absorber. This chosen ratio of  $^3He$  to  $^4He$  will lead to a lifetime decrease of the UCNs in the volume comparable to the free neutron lifetime (discussed in Chapter 1 and in section 5.1.1) and hence a subdominant effect on the UCN loss. As an advantage, the strong neutron absorption produces a detectable signal via



where the 765 keV is released into the superfluid Helium volume, producing scintillation light which can then be carried and read out from the inner detection volume.

However, one critical feature is that the neutron capture on  $^3He$  described by equation 6.5 is highly spin-dependent and, in particular, maximized when the spin of the neutron and the  $^3He$  are anti-aligned. Thus, the reaction will proceed with an angular beat frequency of  $\omega' = B_0(\gamma_3 - \gamma_n)$  where  $\gamma_i$  is the gyromagnetic ratio of the  $i$  particle species. We note that a neutron and a  $^3He$  atom have similar values

for their gyromagnetic ratios:  $\gamma_3 \approx 1.1\gamma_n$ . With an applied electric and magnetic field, the scintillation frequency becomes

$$\omega = (\gamma_3 - \gamma_n) \frac{\omega_3}{\gamma_3} \mp \frac{2d}{\hbar} \quad (6.6)$$

where  $d$  is the electric dipole moment and the minus (plus) indicates the electric field is aligned (anti-aligned) with the magnetic field. We can extract  $d$  from equation 6.6 by measuring  $\omega_3$ , the precession of the  ${}^3He$  atoms, via a series of external superconducting quantum interference devices (SQUIDs) which provide a high sensitivity measurement of the time dependence of the  ${}^3He$  magnetization. This measurement technique is called the “free precession method” to extract the nEDM.

**6.1.1.3.2 Spin Dressing Method** There is a second method for measuring the nEDM using the experimental set-up described thus far: critical spin dressing. By applying an AC field perpendicular to the direction of  $B_0$  (this field strength is typically termed  $B_1$ ), we can “critically dress” the neutron and  ${}^3He$  so that they precess at the same relative frequency in the absence of an EDM. This critical dressing is achieved at

$$\gamma_n J_0(x_n) - \gamma_3 J_0\left(\frac{\gamma_3}{\gamma_n}x_n\right) = 0 \quad (6.7)$$

where  $x := \gamma_i \frac{B_1}{\omega_1}$ ,  $J_0$  is the zeroth order Bessel function of the first kind, and the index  $i$  runs over  $n, 3$  for the neutron and  ${}^3He$  respectively. When equation 6.7 is achieved,  $\dot{\theta}_{n,3} = 0$ . In other words, the rate of change of the angle between the neutron and the  ${}^3He$  is constant and hence the scintillation rate in equation 6.5 is constant. This can be compared with the previous section where there the scintillation rate exhibits a beat frequency.

In the presence of a non-zero nEDM,  $\dot{\theta}_{n,3} \neq 0$ , and in fact the relative angle between the neutron and  ${}^3He$  changes by

$$\theta_{n,3} = \phi_0 \pm (2d'E/\hbar)t \quad (6.8)$$

where  $d' = dJ_0(x_n)$ ,  $d$  is the electric dipole moment of interest and  $+(-)$  corresponds to aligned (anti-aligned) electric and magnetic fields. This method of extracting  $d$  from the changing scintillation rate of neutron and  ${}^3He$  capture at an applied AC frequency is called the critical spin dressing method.

## 6.2 The $B_0$ Magnet

The entire magnet package is designed to provide a precise, stable, and uniform magnetic field and gradient over the detection volume of the UCN cell in the final nEDM@SNS experiment. One of the major components of the magnet package is a magnet which produces DC holding field, typically termed the  $B_0$  field. This magnet is the focus of this component of the dissertation work. The  $B_0$  field must have a field strength of  $3 \mu T$  with uniformity requirements of a few parts per million over the distance scale of cm. We note that the measurement cell is of order several 10s of cm so this uniformity requirement effectively spans the sensitive region of the final apparatus.

However, the final figure of merit is that  $B_0$  must produce neutron and  $^3He$  coherence times from transverse relaxation ( $T_2$ ) greater than  $10^4$  s. Hence, throughout this chapter when discussing quality of magnet construction, we attempt to relate our simulated magnetic fields to an extracted  $T_2$  quantity whenever possible. Finally, we note a few other key specifications in order to satisfy these observation (or equivalently detection) times: uniform gradients along the  $B_0$  direction must be  $< 3 \text{ ppm/cm}$  and uniform gradients in the transverse directions must be  $< 1.5 \text{ ppm/cm}$ .

The uniformity requirements for the  $B_0$  magnetic field are stringent for a reason: magnetic field non-uniformities and, in particular, gradients would contribute to a false nEDM measurement on the level of the designed experimental sensitivity. The main systematic effect that arises due to magnetic field imperfections is the so-called the linear  $\vec{E} \times \vec{v}$ . It is described for the nEDM@SNS experiment in [Ahm+19] and a comprehensive treatment is given in [Pen+04]. This effect can be understood as the accumulation of a geometry phase (akin to Berry's phase) induced by the volume of UCNs traversing a region with a magnetic field gradient. In more detail, recall that a non-relativistic particle in motion in an electric field experiences a force given by the magnetic field

$$\vec{B}_v = \frac{\vec{v}}{c^2} \times \vec{E} \quad (6.9)$$

where  $v$  indicates the velocity of the particle and the direction will be in the plane perpendicular to the nominal applied  $\vec{E}$  and  $\vec{B}$  directions.

This effect where a time-varying field in the plane will induce a shift in the Larmor

precession frequency is called the Bloch-Siegert shift [BS40] and given by

$$\delta\omega = \frac{\gamma^2 B_1^2}{2(\omega_0 - \omega_r)} \quad (6.10)$$

where  $B_1$  is the magnitude of a perturbing field rotating with frequency  $\omega_r$  in the plane perpendicular to the nominal applied  $\vec{E}$  and  $\vec{B}$  fields (in our coordinate system, this the  $x-z$  plane). The presence of a magnetic field gradient gives a non-zero field in the perpendicular plane that is proportional to the gradient. Assuming cylindrical symmetry (for simplicity to illustrate and also representative of the Sussex-ILL experiment), we can derive a representation for  $B_1$  as

$$B_1^2 = |\vec{B}_v + \vec{B}_r|^2 \approx -\left(\frac{\partial B_y}{\partial y}\right) \frac{E}{c^2} \omega_r R \quad (6.11)$$

where  $\vec{B}_r = -\frac{1}{2}\left(\frac{\partial B_y}{\partial y}\right)\vec{r}$  is given by cylindrical symmetry, we assumed a circular orbit at radius  $R$ , and we took only the cross-term since it is linear in  $E$ . Then, equation 6.10 becomes

$$\begin{aligned} \delta\omega &= -\frac{\gamma^2 \left(\frac{\partial B_y}{\partial y}\right) \frac{E}{c^2} \omega_r R}{2(\omega_0 - \omega_r)} \\ \implies \overline{\delta\omega} &= \delta\omega_+ - \delta\omega_- = -\frac{\gamma^2 \left(\frac{\partial B_y}{\partial y}\right) E R^2 \omega_r^2}{c^2 (\omega_0^2 - \omega_r^2)} \end{aligned} \quad (6.12)$$

after averaging due to the isotropic UCN velocity distribution. Here, we note that the gradient contribution to the Bloch-Siegert shift in Larmor precession remains and thus must be accounted for in the design of the nEDM@SNS experiment (for example, see [LG05]).

These field uniformity and gradient uniformity requirements are technically challenging. In addition to these criteria, this magnet will be placed in a cryogenic vacuum chamber so it must be able to reach this performance after thermal cycling from room temperature to  $\approx 6$  K (thermal contractions are a concern) and mechanically support a few additional experiment components (stress and deflections are of a concern).

### 6.2.1 Constructing the $B_0$ Magnet

When I started working on the  $B_0$  magnet project, general design and testing of the components of the magnet had been completed or was being worked on concurrently with the construction of the magnet structure. The design and drawing of the magnet can be seen in figure 6.1. In it, we highlight the various structural components that

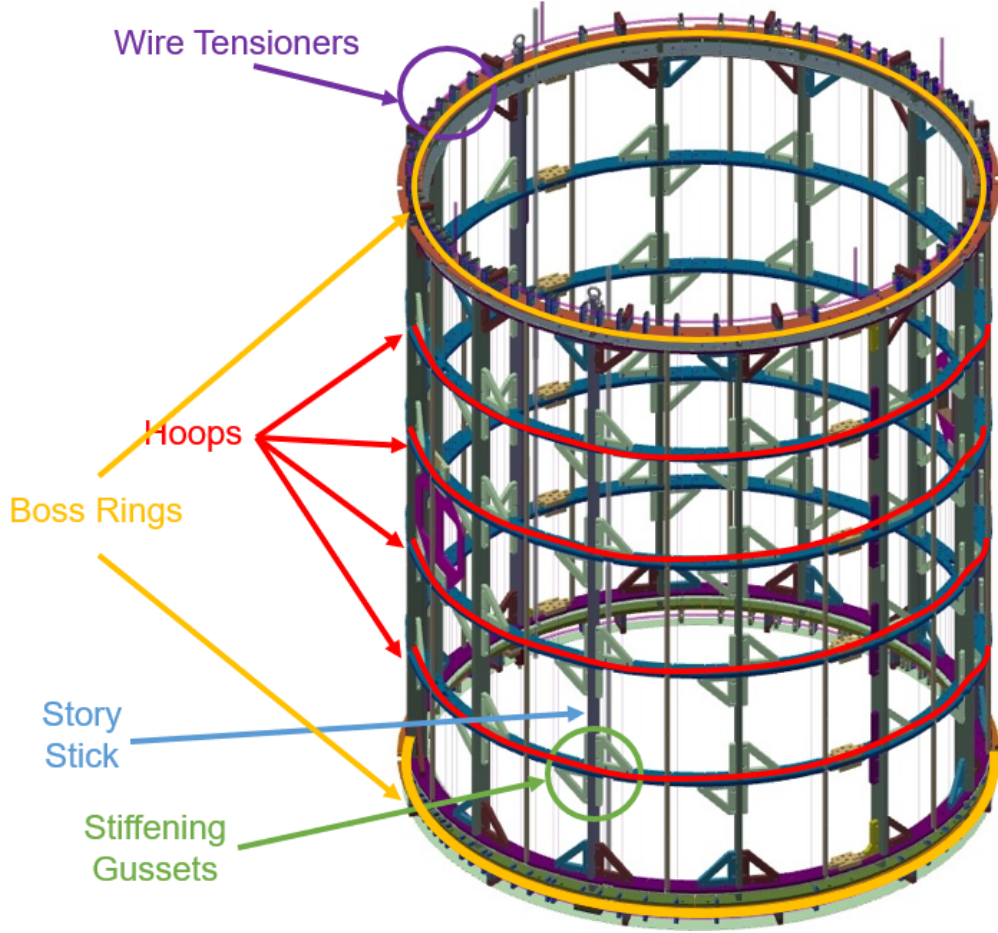


Figure 6.1: Engineer’s diagram showing the  $B_0$  magnet structure, constructed from G10 material [Ale21]. The wire windings are also shown. Several components in the structure are highlighted: the wire tensioners (purple), boss rings (yellow), inner hoops (red), story sticks (blue), and stiffening gussets (green). All components are described in the text.

needed to be procured or constructed. In particular, we take a moment here to highlight the four inner “hoops” and two “boss rings” in the diagram; these were logistically challenging and their assembly is described in greater detail compared to other components.

The chosen material for the construction of the  $B_0$  magnet frame was laminate G10. G10 is a fiberglass composite material that is soaked in epoxy resin and stacked to create thick sheets that can be cut into various shapes.

G10 was chosen for a few reasons. First, G10 is sturdy so that it can be relied upon to provide mechanical support to other components of the frame. In particular, the copper and lead shields are going to be thin substrates of copper and lead

that are glued to thin sheets of G10 that provide the structural backing. Second, G10 has a low thermal contraction coefficient. Thus, as the magnet cycles from room temperature to  $\approx 6\text{ K}$  working temperature, the overall thermal contraction of the frame will be fairly small compared to metals of the same size. Finally, the experiment itself needs to happen in a magnetically pure environment. Residual magnetization in standard metallic construction materials were too large for the magnetic environment specifications of the nEDM@SNS experiment. Furthermore, other potential materials such as Aluminum were not appropriate since they would have eddy currents induced by the interior spin-dressing coil. Thus, G10 was chosen as a non-magnetic material alternative to provide the structure of the magnet and support the other elements of the apparatus (such as shields and spin-dressing).

### 6.2.1.1 UVT: A Vacuum Lamination Table

In order to assemble the hoops and boss rings that are discussed later, the chosen assembly procedure was to obtain the different components in segments and “glue” them together. The “glue” that was chosen was DP190 epoxy. The other glue considered was StyCast due to internal experience. Several tests of mechanical strength and thermal cycling resilience of DP190 concluded that it suited our purposes. Due to the specifications on the magnet performance ( $T_2 > 10^4\text{ s}$  translates to positional tolerances on the order of  $\pm 0.010$  inches), we had to ensure that the segments were being glued to within sufficient precision.

In order to satisfy this requirement, we used our aluminum vacuum table to ensure that we were pressing our glued segments under an even, atmospheric pressure throughout the duration of the DP190 curing time period ( $\approx 1 - 2$  weeks). The vacuum table, internally termed the UVT for Unicorn Vacuum Table<sup>2</sup>, can be seen in figure 6.2.

In figure 6.2, we can see the overall aluminum vacuum table with two sets of “gauge plates” (four segments of circular aluminum plates, one set inside the other) that are used to set the outer radius of the glued segments. The outer circular set is used for the  $B_0$  magnet and thus was used for the work in this dissertation. The inner

---

<sup>2</sup>The story behind the naming of the UVT is an humorous one. One day, one of the engineers working on the nEDM@SNS apparatus as a whole was visiting a contractor in New Mexico for an unrelated project. They saw an aluminum vacuum table that was perfectly sized for this gluing and pressing operation in the junk yard outside. The table was purchased, sent to a machine shop to have various features machined into the surface, and eventually shipped to Caltech to allow us to do in-house gluing operations of high quality and quality assurance. This serendipitous find made the vacuum table “like a unicorn” and hence a name was created.

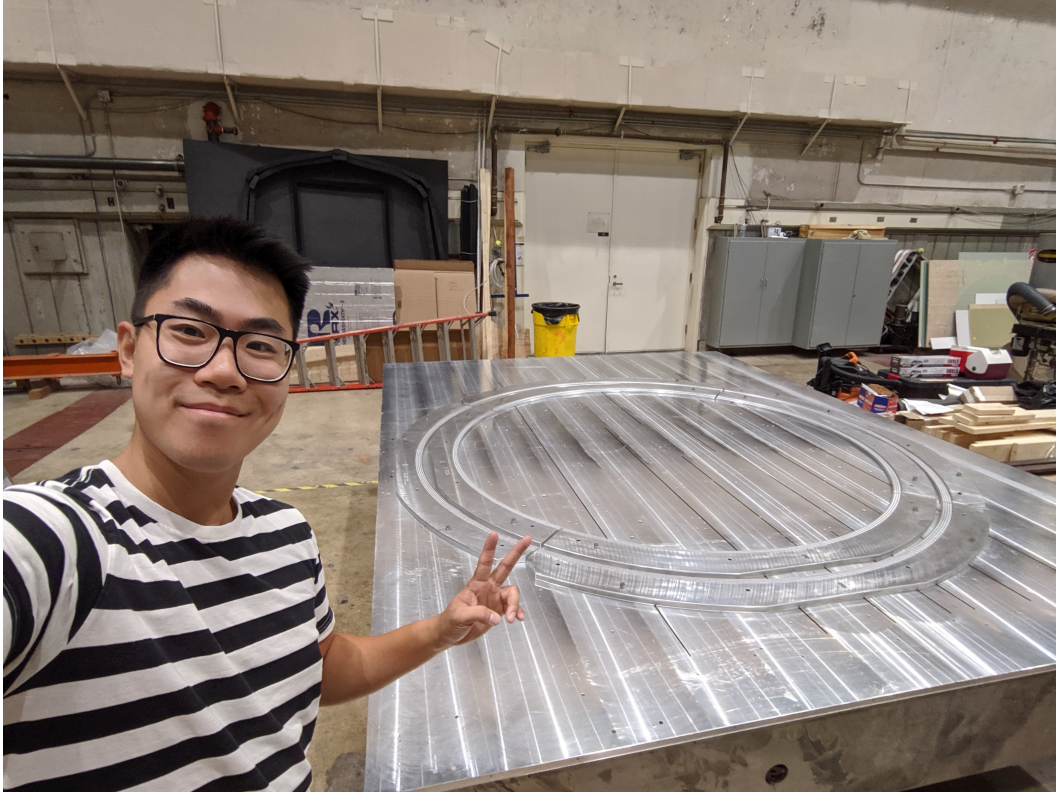


Figure 6.2: Photograph of author with the UVT in the synchrotron lab area at Caltech. Photo taken after UVT was delivered and surfaces were cleaned. Both sets of gauge plates were cleaned and laid out on the table for initial quality checks.

circular set is intended to be used for the spin-dressing magnet which is used in the critical spin dressing measurement method discussed in section 6.1.1.3. That work is intended to be completed at a later date in the overall project management cycle. Hence, the construction and assembly procedures developed here for  $B_0$  can be reused in the context of constructing a spin-dressing magnet which resembles the  $B_0$  magnet in design and assembly except with a smaller radius.

### 6.2.1.2 Inner Core Hoops

The inner core hoops are the four hoops that are contained (top and bottom) by the boss rings in the space frame (see figure 6.1). These hoops had 0.020 inches tolerances in the wire slot positions which are defined as the cut outs in the hoop that allow the wire winding of the magnet to pass through. The construction of the four inner hoops allowed us to develop an assembly procedure that we could trust to ensure high-quality assembly in advance of the boss rings which have the most stringent tolerances in the entire magnet construction.

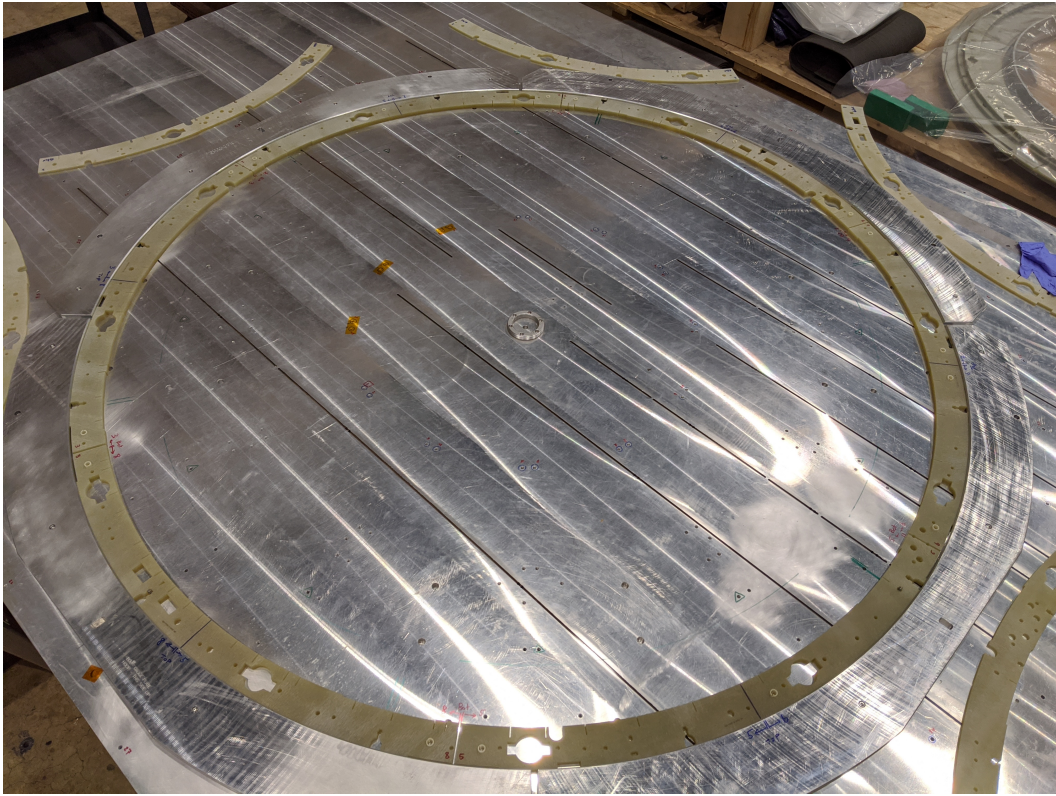


Figure 6.3: Photograph of completed dry fit assembly of an inner hoop. In this picture, the dry fit was completed and then disassembled to prepare for the gluing operation. The top layer segments are laid in position and then flipped over so that the glue side is upright. At this point in time, Saran wrap had not been prepared on the UVT — we added that into the procedure soon afterwards.

The hoop assembly procedure involved several stages. Prior to the gluing operation, we performed a “dry fit” of the components to ensure that everything would assemble and all the relevant features matched with the engineer drawings. See figure 6.3 for a picture of a dry-fitted hoop. In addition, the dry-fit gave the gluing operation leader a mental picture of the order of operations required when assembling the full hoop. This was important because the chosen epoxy DP190 had a working time of  $\approx 90$  mins before beginning to harden significantly. We wanted to ensure the full hoop was glued and pressed under vacuum before this working time was over so that any inconsistencies in gluing could “spread out” under atmospheric pressure and not set in the final configuration. This would improve our chances to maintain our positional tolerances.

Upon completing our pre-gluing work, typically 7-10 members of the lab research group would assemble the following day for the full gluing operation. This gluing

operation developed over the 1+ year of assembly so that the final boss rings glued had several procedural check points for different quality control assurances. The full procedure was also developed during 2020 which required Covid-19 protocol compliance. This significantly affected the logistics of the operation. The full gluing procedure for the “tight tolerance” components (the inner hoops and the boss rings) are discussed in section 6.2.2. For now, an overview of the process is given. The DP190 is spread over the top and bottom segment surfaces, aligning the features with G10 spring pins, and pressing them together. The glued hoop is wrapped in Saran wrap (does not stick to DP190 and protects the UVT from getting hardened glue which may impact future tolerances), custom-made wooden feather blocks are tightened to press the hoop segments against the gauge plates, and a plastic sheet is taped over the table so that a vacuum pump may produce a vacuum that ensures an even pressing on our glued hoop. After the vacuum is achieved, the hoop is left so that the DP190 epoxy may cure for  $\approx 7 - 10$  days. Once completed, the vacuum pump is turned off, the plastic sheet is removed, and the final glued hoop is ready. This is shown in figure 6.4.

After the gluing is completed, we need to check whether we were within our tolerances. Notable issues would be glue leaking into the feature cutouts and any misalignment between the segments leading to systematic misalignment in the wire-slot cutouts. These wire slot cutouts ensure the path of the magnet winding wire and directly reflect on our figure of merit:  $T_2$ . Section 6.2.3 discusses how we check the quality of our gluing operation for the inner hoop and several other components.

### 6.2.1.3 Lead End Caps (LECs)

A schematic of the different layers of the magnetic system is given in figure 6.5. In the following sections, we focus on the elements that comprise the lead end caps (LECs) and the  $B_0$  coil. The schematic places these elements in positional context within the magnet package.

Similar to the inner hoops, there is a gluing operation required for the LECs. The LECs are comprised of two layers of 6 segments of G10 for the top and bottom layers of the end cap (effectively, another hoop). After those segments are glued together, the outer face of the lead end cap is glued to an annulus of lead. This is shown in figure 6.6a. After curing, this lead is then cut so that it conforms to the shape of the underlying G10 hoop and all the feature cutouts in the G10 are preserved. A sample of the LEC with these features cut out is shown in figure 6.6b.

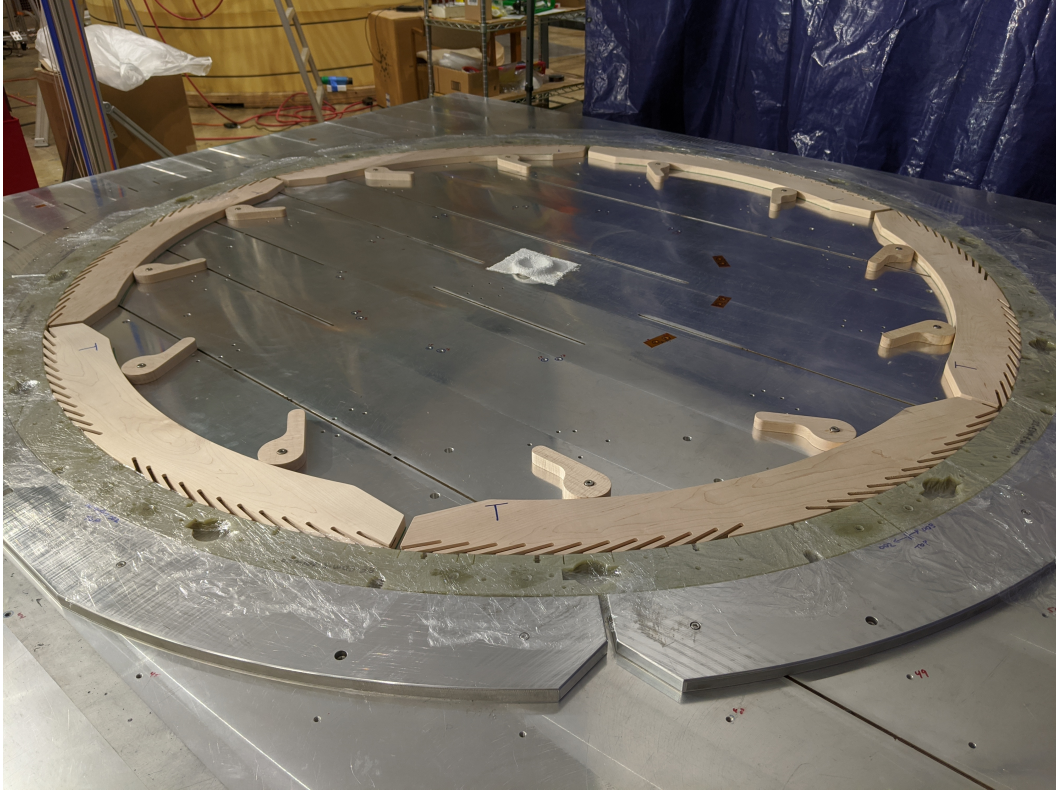


Figure 6.4: Photograph of completed inner hoop gluing and curing. Vacuum was removed and plastic sheet removed. In this picture, we can see the wooden feather blocks, Saran wrap around the hoop, and tell-tale discolorations that indicate where glue has been spread on the outer surfaces of the hoop.

In particular, we are interested in maintaining the integrity of the wire slot cutouts again, as well as the remaining structural features cut in to the lead end cap G10. The wire slots are checked via the same methods that are described in following sections. The other structural features are checked by using the components that interact with these features directly (for example, checking that a stiffening gusset can fit in the cut outs on the LEC).

#### 6.2.1.4 Superior Lead End Caps (SLECs)

The superior lead end caps (SLECs) were one of the first components to be glued and vacuum pressed together. This was because the positional tolerances on the SLECs are more forgiving than the other components of the magnet. In particular, within the magnet design, the SLECs are outside of the boss rings and hence there are no wire slot cut outs in the SLECs. Thus, the most stringent feature is absent from the SLEC and hence we started with the SLEC to develop our gluing procedure,

### Cross Section View of the Inner Magnet Volume (IMV)

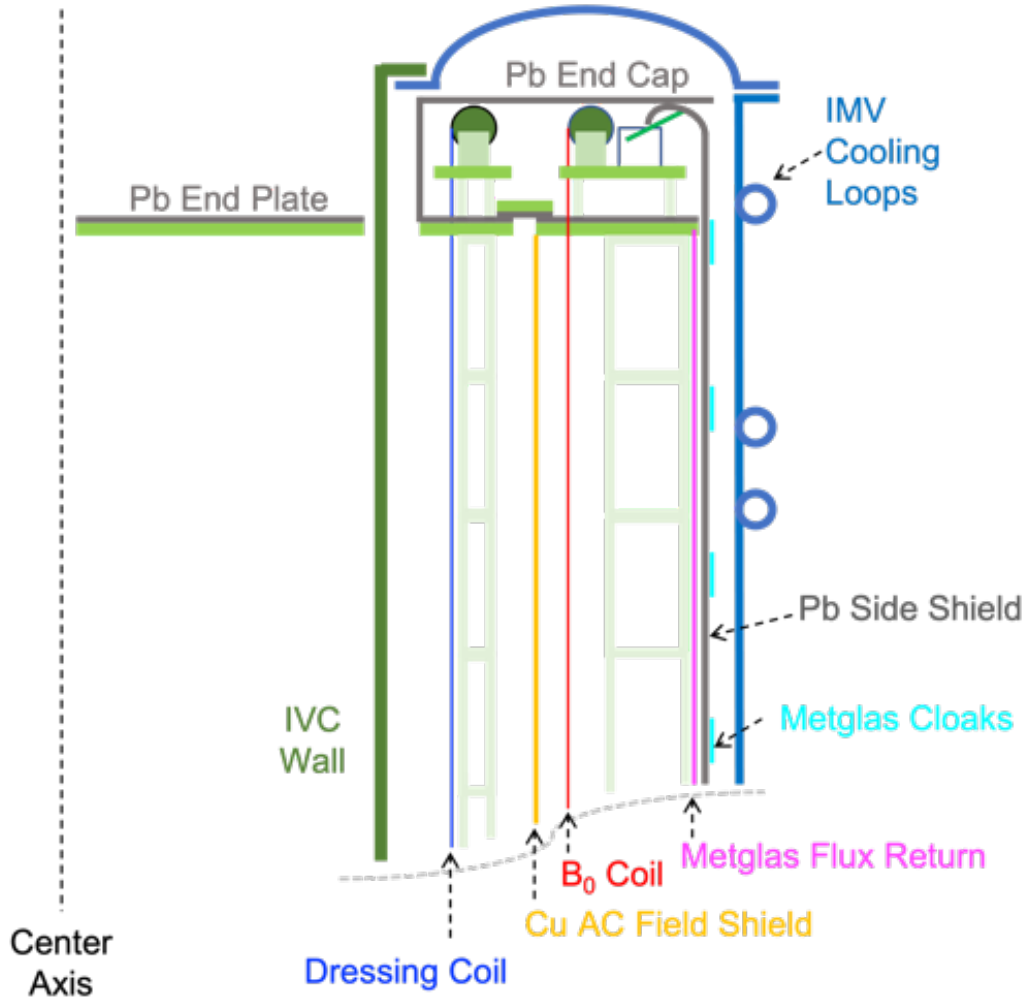


Figure 6.5: A schematic of the different elements within the magnet package. The center axis of the cryostat is given on the left-hand side and the different elements are placed according to their radial position in the experiment apparatus. The work in this section describes the Pb End Cap and the  $B_0$  Coil. In section 6.2.4.1 we briefly discuss the Metglas Flux Return and Pb Side Shield.



(a)



(b)

Figure 6.6: Photographs showing (a) completed LEC glued to a sheet of lead and (b) the same LEC zoomed in on several features cut out. The lead will give additional magnetic shielding once the magnet is in a cryogenic environment (the lead goes superconducting). The cutting is done with piano wire and filing tools.

teamwork skills, and quality benchmarks.

The SLEC in the middle of the gluing operation can be seen in figure 6.7a. The completed SLEC while being pressed under vacuum can be seen in figure 6.7b.

### 6.2.1.5 Boss Rings

The final major gluing operation involved the top and bottom boss rings. These were done last because we wanted to perfect our teamwork and quality assurance in the gluing operation before working on the magnet components with the tightest tolerances. The boss rings final wire slot positional tolerances were  $\pm 0.010$  inches and could not have any significant radial deviations or glue leakage in cut outs that house the wire tensioners (discussed below). Any deviations in quality of assembly for the boss ring propagate into our final magnet wire winding and hence directly into the  $T_2$  value of the magnet.

The boss rings were glued together during the Spring term of 2021. At this time, the full gluing operation can be found in the section below illustrating the Covid-19 constraints. Figure 6.8 shows a completed boss ring. We highlight the added challenges compared to the earlier inner hoops, namely the number of cut-outs included to house the 72 wire tensioners on each boss ring provided the majority of the challenge. They can be seen to be maximally dense on the left and right sides of figure 6.8. They are most dense on the beam-line axis, consistent with a  $\cos\theta$  coil, which was the design of the  $B_0$  magnet<sup>3</sup>.

### 6.2.1.6 Story Sticks

The story sticks are comprised of 12 vertical G10 sticks with various cutouts that allow the different hoops (see sections 6.2.1.5, 6.2.1.2, 6.2.1.3) and stiffening gussets (see section 6.2.1.7) to slot in. The action of connecting the horizontal hoop components with the vertical story stick components creates the overall structure of the magnet frame shown in figure 6.1.

From the in-house development perspective, there was little to do with the story sticks. A smaller scale space frame had been developed, tested, and assembled for a magnetic probe array by collaborators working with the same design engineers

---

<sup>3</sup>A  $\cos\theta$  coil refers to a distribution of wires that produce a magnetic field perpendicular to the magnet's cylindrical axis. The specific coil design of the  $B_0$  magnet is further optimized for the nEDM@SNS experiment specifications. See [Ahm+19] and references therein for a description of the magnet wire positioning design.



(a)



(b)

Figure 6.7: Photograph of first gluing operation. (a) Gluers applied glue directly to the surface of the SLEC and spread by hand. Some components were moved off the UVT on to separate work stations to have more working space. At this stage, there was little order to the operation and the total working time was 2-3 hours. (b) After gluing and assembly was completed, vacuum was applied and the whole assembly cured on the UVT. The SLEC had significantly looser tolerances so a set of small G10 gauge plates were used instead of the typical robust Aluminum gauge plates. Towels were laid over the sharper edges in order to protect the plastic sheet. A seam in the plastic was bunched up and channeled down to the green-taped lead brick — this techniques yields a better vacuum and less overall leakage.

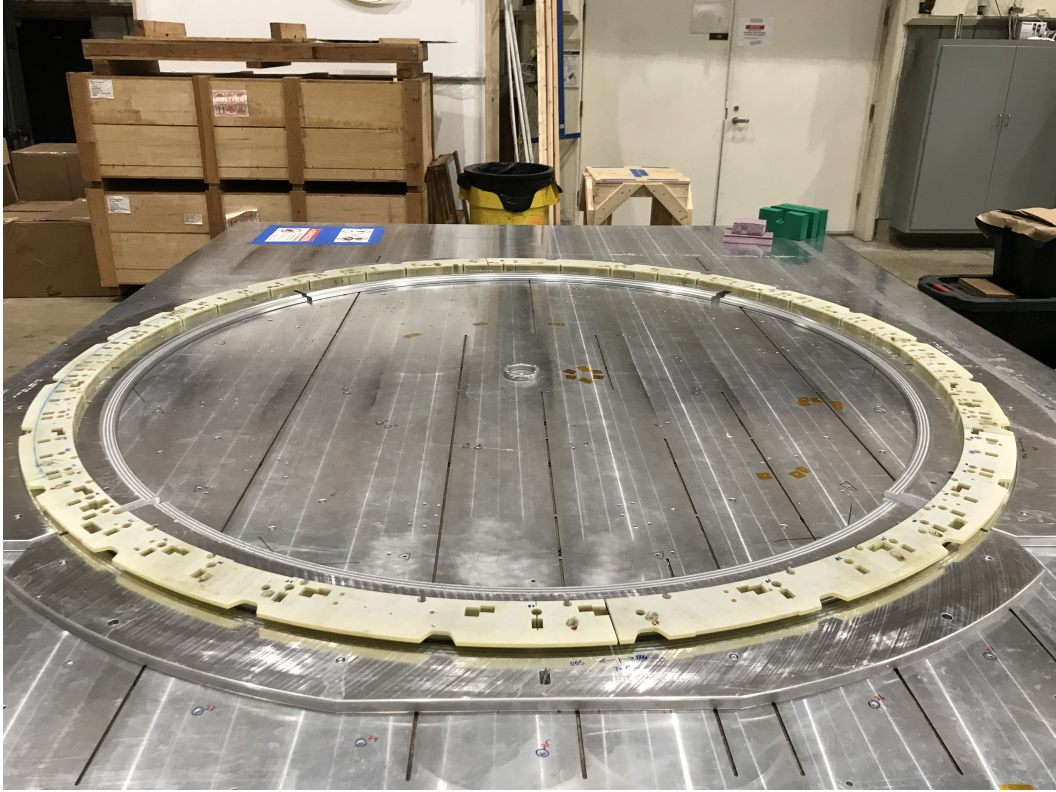


Figure 6.8: Photograph of first completed boss ring, removed from rest in the gauge plates, prior to position measurements with the ROMER arm. We highlight the challenge with this gluing operation by noting the large number of feature cut outs compared to previous magnet components (figures 6.6a and 6.4).

[Ale19]. Those prototype results confirm the use of story sticks to assemble our magnet structure on larger scales. The full set of story sticks were ordered from external vendors and can be seen in figure 6.9.

#### 6.2.1.7 Stiffening Gussets

In the final magnet design, 144 stiffening gussets were used (12 per story stick, 12 total story sticks) in order to provide mechanical support to the magnet frame. This provides general strengthening the frame during intermediate assembly procedures. The full set of stiffening gussets were ordered from external vendors and can be seen in figure 6.9.

#### 6.2.1.8 Wire Tensioners

The wire tensioners refer to 72 G10 and Torlon assemblies that are glued with DP190 epoxy to each boss ring. These assemblies house a pulley that precisely



Figure 6.9: Photograph of inventory of gussets and story sticks after procurement, stored in the synchrotron lab at Caltech.

aligns with the wire slot cut outs in the boss rings and inner hoops (described in more detail in sections 6.2.1.2, 6.2.1.5). The goal of these wire tensioners is to apply a spring force that tensions the winding magnet wire. It is important that we maintain a rigid wire in order to meet our stringent field uniformity and gradient uniformity requirements, as any of the wires slipping or losing tension would affect our final field quality. Furthermore, during temperature cycling of the magnet, there is differential thermal contraction between the G10 magnet frame and the superconducting NbTi (Niobium-Titanium) wire that forms the magnet. The wire tensioners are in place in order to account for this differential contraction.

The wire tensioner components were all purchased from external vendors and in

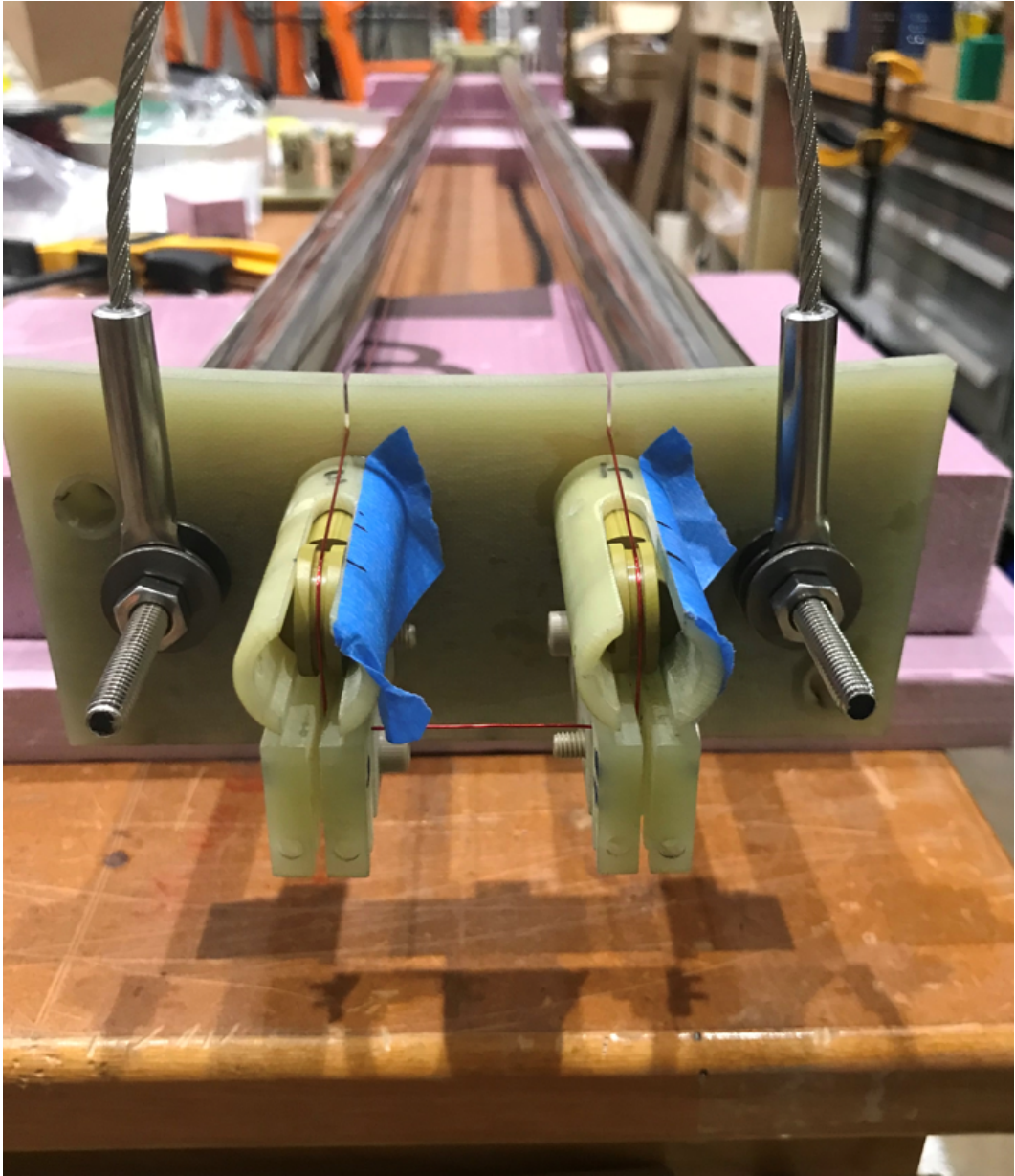


Figure 6.10: Photograph of a test set-up for the wire tensioners. Two tensioners are attached to a test segment of the boss ring (foreground) with a similar set-up in the background at the end of the two poles. Copper wire of 24-gauge is wound to mimic the final magnet winding. In the completed magnet, 72 of these wire tensioners are on each boss ring.

several simple segments. The segments are designed the way they are in order to simplify the manufacturing process and make it easier to bulk purchase the wire tensioner assembly. A test set-up in the late design phase (showing the final chosen design of the wire tensioner assembly) can be seen in figure 6.10.

### 6.2.1.9 Final Assembly of $B_0$ Magnet

Upon completing the assembly, gluing, and curing of the individual components such as the hoops and LECs, and upon procurement of the remaining components, we were ready to assemble. The assembly procedure involved sliding the story sticks through the four hoops and then rotating the story sticks once they were in position. Specialized wooden structures for holding the hoops in place vertically were used to assist with this locking mechanism. The stiffening gussets were installed, then the LECs, then finally the boss rings on the top and bottom. The boss rings had the wire tensioner assemblies installed before being installed on the magnet structure story sticks.

After completing the assembly, we wound the wire that would be used to turn the structure into a proper magnet. We used 0.5 mm diameter,  $\approx 200$  m of copper wire as an initial practice wind. This is due to the cheap price of copper wire compared to the costs and fragility associated with the NbTi wire. Furthermore, for the upcoming next test with the  $B_0$  magnet, the currents carried by the copper wire would be sufficient. The completed  $B_0$  magnet can be seen in figures 6.11a, 6.11b. In figure 6.11b, we highlight the arrangement of the wire tensioners and note that this is characteristic of a  $\cos\theta$  magnet coil. This winding arrangement ensures the direction of the imposed magnetic field is perpendicular to the axis of the magnet and the direction of the beam line.

### 6.2.2 Covid-19 Considerations

As with most work done during 2020-2021, there must be a discussion on Covid-19 considerations. In particular, for the work completed in this chapter, Covid-19 protocols required us to drastically change our gluing operations after settling in on a procedure. For us, this meant reducing the number of people in a gluing operation and utilizing additional work stations so that gluers could work with 400 sq. ft. of space for extended periods of time. In order to proceed with magnet construction, a proposal for a modified two-hour gluing operation was submitted and approved. The floor plan can be seen in a simple schematic in figure 6.12.

Towards the end of the hoop construction process, we had an optimized gluing procedure. Originally, when we started, we were using 10-12 people for 2-3 hours to glue the SLEC or the first inner hoop. Even under Covid-19 compliance restraints, we were able to glue inner hoops, LECs, and boss rings with 7 people in about 1 hour, with higher quality gluing (for example, less glue leakage and better alignment



(a) Side view.



(b) Top view.

Figure 6.11: Photograph of completed  $B_0$  magnet structure with partial winding. The winding pattern is such that we wound half the coil at a time. In this picture, we can identify the elements of figure 6.1. Wire tensioners are “loaded” using toothpicks, pictured in each wire tensioner. In the final magnet deployment, toothpicks will be removed to give spring tension to the wire winding.

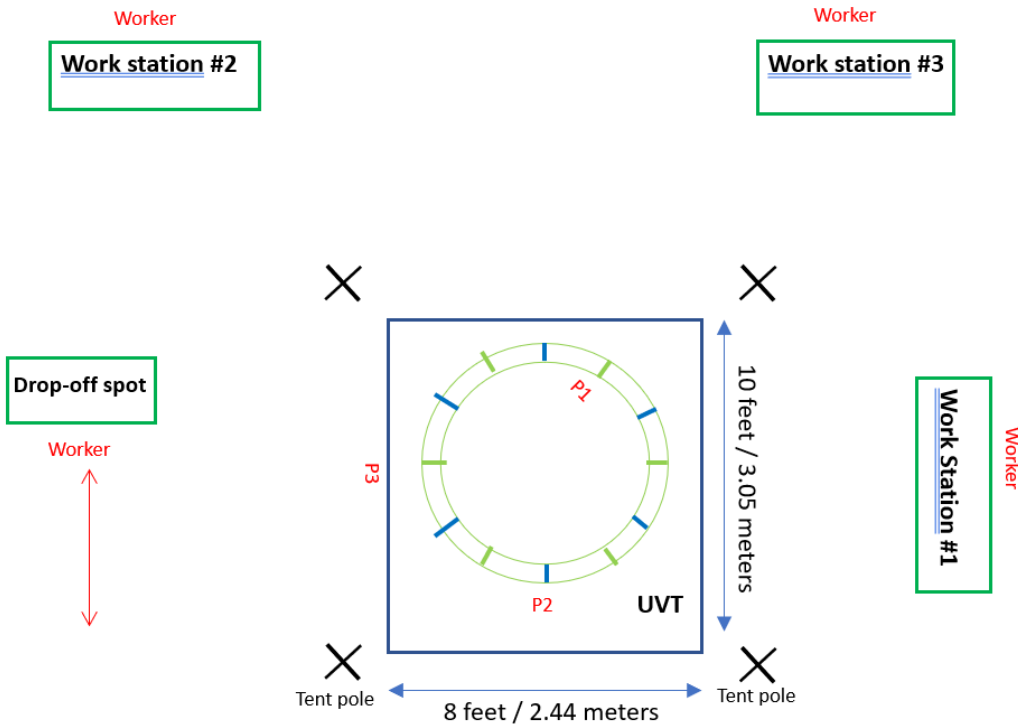


Figure 6.12: Simplistic floor plan diagram of gluing operation. The layout and worker placement was designed in order to comply with Covid-19 safety protocols (see text). Upon receiving approval, we were able to continue gluing  $B_0$  magnet components throughout the lockdown.

between pass-through features in the hoops).

This quality improvement was achieved through several process improvements. First, there was the pre-gluing preparations. The pre-gluing preparations typically included performing a full cleaning of the UVT and G10 hoop components. We would complete a dry fit of the components to test feature compatibility and generally get oriented for the gluing operation. We would mark up the segments on the glue side (equivalently called the interior side) between the top and bottom segments, as a guide for gluing and assembling so we would be clear in our order of operations during a timed operation. Saran wrap was taped to the UVT table and set up so that when the hoop was completed gluing, we could remove the tape and fold the Saran wrap over the hoop prior to laying down the plastic sheet and pressing. We set up the three work stations with gluing materials and a drop-off table with labelled drop-off points for glued segments so when under time pressure we could follow a system for operational order. Lastly, everyone was equipped with proper personal

protective equipment (PPE), namely gloves, face masks, and a face shield.

During the actual operation, the procedure went as follows:

1. 6 gluers were set up. 3 glue applicators worked on the UVT, gluing the bottom layer of the hoop. 3 glue applicators worked on 3 separate work stations to apply glue to top layer segments.
2. 1 additional person was operating the glue gun - they would fill small plastic trays with DP190 epoxy and place them at the drop-off location so that gluers could be working with fresh epoxy. This gave the added advantage of having more liquid epoxy to work with before it started setting (recall that the working time of DP190 epoxy is about 90 minutes).
3. On occasion, we had one additional person or the glue gun operator also apply DP190 epoxy to sets of spring pins that connected the top layer of G10 segments to the bottom layer of G10 segments. The epoxy applied on the spring pins was done using fresh epoxy to again ensure liquid flow so that inserting the spring pins was easier and we had more time before the epoxy set in.
4. Glue was applied to the 6 top segments and the 6 bottom segments. As each segment was ready to be connected, the top segments were placed over the bottom segments with the glue sides touching and spring pins were inserted. This was repeated across the hoop with a customary star pattern to minimize systematic offsets in assembly.
5. After laying down all 6 top segments on the glued bottom 6 segments, we folded the prepared Saran wrap over the hoop to protect the UVT and gauge plates from glue leakage.
6. We then installed wooden feather blocks and “pusher” knobs. These wooden feathers flexed against the inner radius of the hoop and the pusher knobs turned in order to push the hoop flush against the gauge plate.
7. We then covered the entire hoop and gauge plate assembly with towels to protect the plastic sheet from punctures on the sharp corners.
8. Finally, a prepared plastic sheet was laid over the UVT and taped to the top surface using simple packing tape. A vacuum pump connected to channels

machined into the UVT was turned on and a vacuum between the plastic sheet and the UVT was created, ensuring even atmospheric pressure on the hoop as the DP190 epoxy cured.

I would like to extend my appreciation to those who helped with the gluing operations throughout the course of the assembly: Alina Aleksandrova, Wanchun Wei, Brad Filippone, Chris Swank, Raymond Tat, Joe Benson, Robert Carr, and Umit Coskun.

### **6.2.3 Testing the Assembly Components**

#### **6.2.3.1 The ROMER Arm**

Throughout the course of this chapter, we have been discussing the assembly and construction procedures for making a large-scale  $B_0$  magnet. In reality, this magnet took nearly 2 years to complete. Of course, we could not continue this assembly procedure without some accurate way to check whether we were meeting our assembly tolerances along the way.

Recall that our tolerances in the assembly of the magnet was on the order of  $\pm 0.010$  inches in absolute position. Precision of this magnitude was non-trivial to measure. We accomplished this by borrowing a measurement device with computer read-out, called the ROMER arm manufactured by Measurement Solutions, from the LIGO (Laser Interferometer Gravitational-Wave Observatory) collaboration. We obtained this ROMER arm on a provisional basis for measurements of physical features on our magnet components. We had access to this arm from March 2020 onwards, using it to perform quality assurance measurements on the hoops, LECs, boss rings, and several intermediate structures used in the  $B_0$  magnet assembly. In the future, we hope to use this same ROMER arm for quality assurances on the spin-dressing coil which utilizes many of the same parts and assembly procedures.

A sample description of the general operation of a ROMER arm is described in [AB]. A summary of the pertinent details is presented below.

The software package used to operate the ROMER arm and take measurements was PowerInspect 2014 [Inca]. This came pre-packaged with the ROMER arm and instrumentation that LIGO was using. In particular, a Dell workstation laptop was used to connect to the arm and used a Windows operating system with PowerInspect already installed. We chose to use the existing infrastructure they were working with in order to make minimal changes on equipment we were borrowing.

In the subsequent sections, we will describe the different measurements and quality assurances that were taken throughout the duration of the magnet assembly. In this chapter, these aforementioned measurements are described separately and appear to be modular. In reality, these measurements had to be taken several times at different points in the magnet assembly since different components had to be uninstalled and reinstalled (and subsequently remeasured) from the UVT over the two-year assembly timeline.

### **6.2.3.2 Calibrating the ROMER Arm**

During the initial operation of the ROMER arm, there were concerns about offsets in the direct measurements and extracting physically relevant quantities with the arm. We elected to use the data points in a Point Cloud Spread (PCS) and apply our own correction factors in offline analysis. To this effect, we wanted to ensure we had a robust measurement of radius from the base of the arm. We used two concentric circles of precision tapped holes in the UVT - 24 on the interior of the gauge plate radius and 34 on the exterior. We used these tapped holes to provide a distribution of radius measurements at two radii. Furthermore, we applied fixed offsets in the X and Y directions (on the plane of the UVT, defined by the direction of the ROMER arm base) and minimized the RMS of the radius measurements in the tapped holes to identify when we were at the center of the UVT.

### **6.2.3.3 UVT Surface Measurements**

Once we had the ROMER arm, we wanted to check the flatness of the UVT and whether any large structures pressed over the entire surface would be flat within our design specifications. There was a small ring holder mounted to the center of the UVT that would allow the ROMER to connect to the UVT. From there, the degrees of motion would allow the ROMER to tap every location towards the outer edges of the UVT. We did this and recorded the data in PowerInspect as a point cloud, i.e., several points that must be interpreted offline together. The mounting operation required calibrating the six degrees of freedom available to the ROMER arm by taking them through their range of motions. This had to be done every time the arm was powered on or reconnected to the laptop. Figure 6.13 shows the ROMER arm mounted to the UVT with the associated electronics (power and readout) as well as the work station computer that had PowerInspect.

The ROMER arm's operation is relatively simple once the mounting, calibration,



Figure 6.13: Photograph of the ROMER arm mounted to the UVT. Power and connection wires extend from the ROMER to the Dell workstation used to operate the ROMER arm.

and PowerInspect software are set up. We typically used a Point-Cloud Spread for all our measurements. This was to ensure robust and easy to interpret data that was exported to Microsoft Excel. We then applied fixed offsets for the size of the ROMER arm tip (there was a 6mm diameter ruby ball attached to the tip of the ROMER arm to ensure that it would always touch a surface perpendicularly). We measured the UVT surface with  $\approx 1000$  touch points. There was overall structure in the shape, typically called “potato-chipping”, but the total deflections at the locations of the gauge plates (notably, where the hoop segments would rest and press) were within our tolerances. The scatter for a smaller, initial test of  $\approx 100$  touch points is shown in figure 6.14. From these measurements, we concluded that pressing our

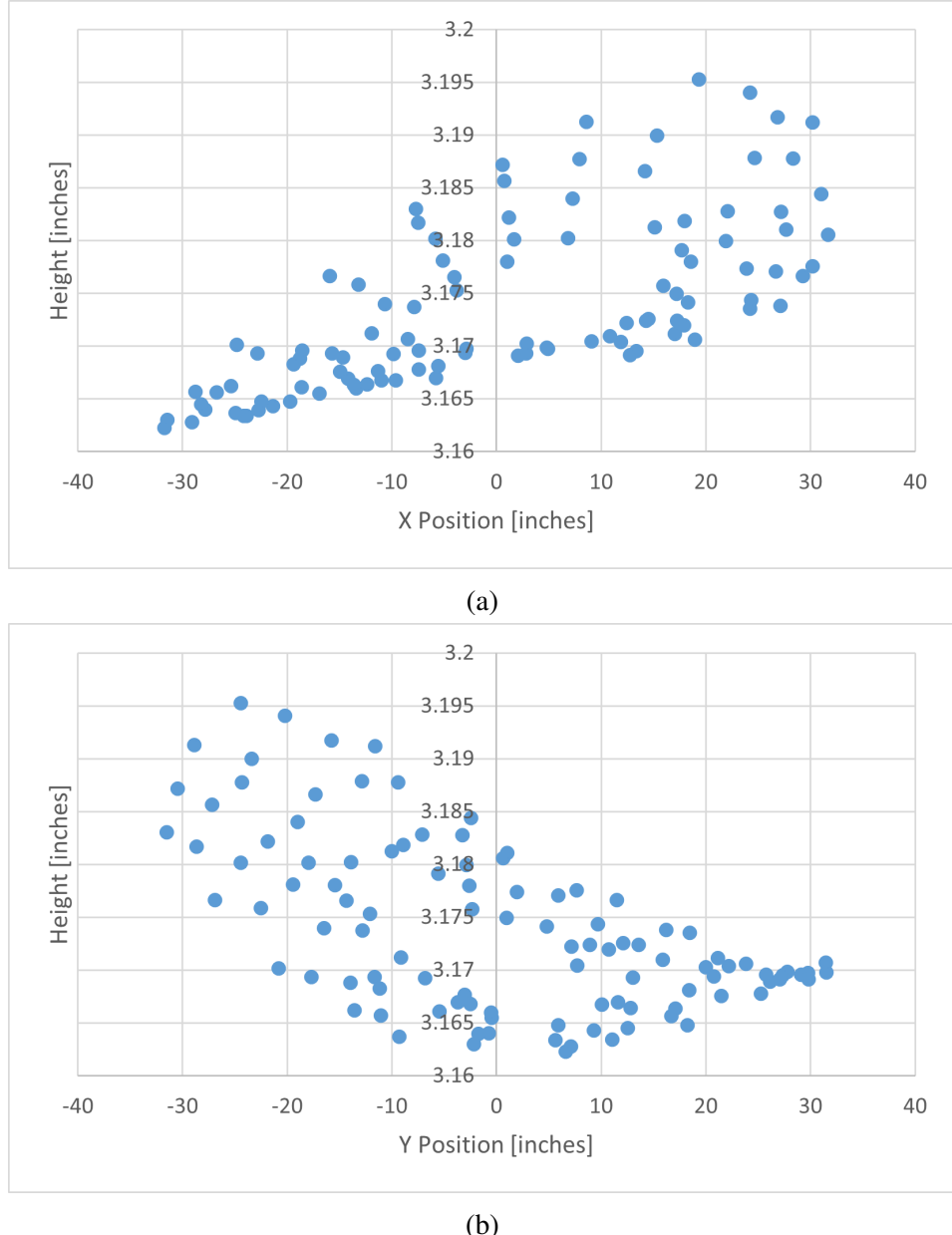


Figure 6.14: Measurements of the height of the ROMER arm against two orthogonal axes X (a) and Y (b). The coordinate axes are defined relative to the position of the ROMER arm base which is mounted to the UVT. The height includes a fixed offset for the height of the base.

hoops on the UVT would not deflect beyond our specifications out of the plane.

#### 6.2.3.4 Gauge Plates Inner Circumference Measurements

Prior to gluing the hoops, we needed to ensure that we had a robust measure of their outer diameter. This is because the outer diameter of the hoops is important for

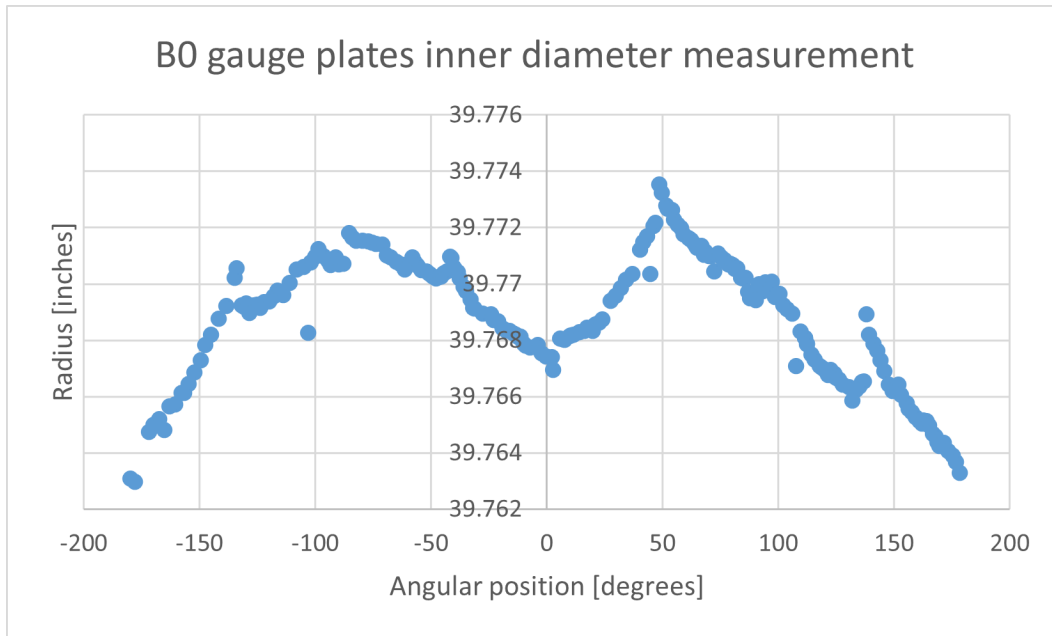


Figure 6.15: Distribution of ROMER arm captured points along the interior radius of the Aluminum gauge plates, taken when mounted on the UVT. An offset in X-Y has been applied to center the data taken from the ROMER arm by using the calibration holes on the UVT (see text). Falls within our positional tolerances of  $\pm 0.010$  inches.

the wire positioning, among other structural reasons further downstream in the final magnet installation. To do this, we have a set of four Aluminum gauge plates that were used to set the outer diameter of the hoops. These gauge plates are installed in the UVT using Aluminum dowel pins and screws. After installation, the ROMER arm was mounted to the UVT, calibrated, and used to measure the inner radius of the gauge plates. The results are shown in figure 6.15. While there is some structure in the radius measurements of the gauge plates, they are overall within our  $\pm 0.010$  inch tolerances on the wire slot positioning.

#### 6.2.3.5 Wire Slot Position Measurements

After our initial measurements and quality checks on the UVT and gauge plates, we were ready to measure the completed  $B_0$  magnet components. In particular, our most stringent tolerances were on the wire slot positions. There would be eight total hoops that had wire slots cut into them: four inner hoops, two LECs, and two boss rings. We wanted to measure the location of the back of each wire slot in each hoop. There are a total of 72 wire slots cut into each hoop.

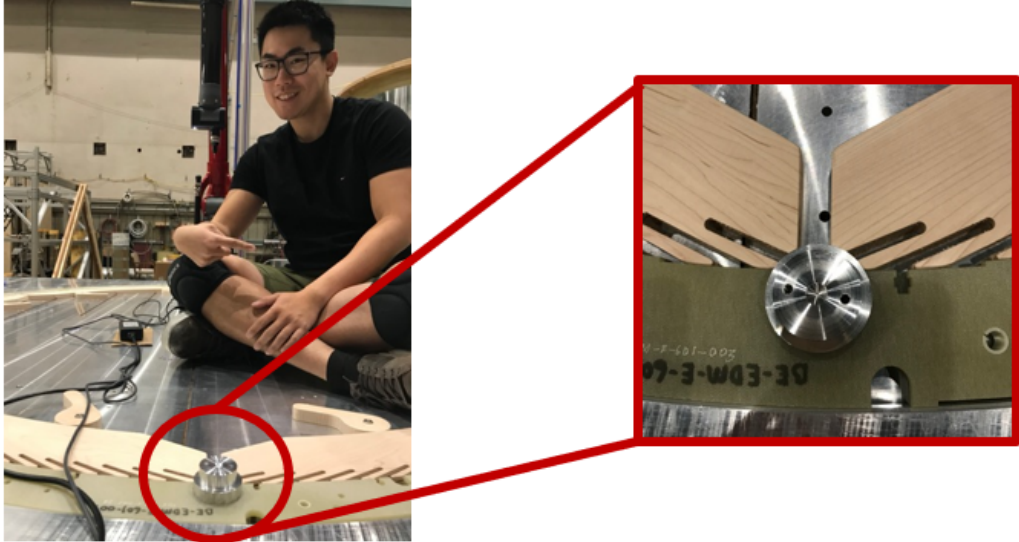


Figure 6.16: Photograph of author on the UVT ready to take wire slot measurements with the ROMER arm. On the right is a zoom in photograph of the custom-made wire slot measurement tool, designed to reliably position the ROMER arm to capture the wire slot.

In order to measure the wire slot positions, we needed a method to capture the position of the wire slot. We could not trust that the ROMER arm could dock and capture the back of the wire slot each time reliably. With the aid of Joe Benson from the Caltech machine shop, a specialized tool was made for this job. It can be seen in figure 6.16 when it is resting in a wire slot. The conical center of the tool allows for the ruby ball tip of the ROMER arm to automatically find the center of the tool each time. The data taken with this tool is adjusted for X-Y offset and shown in figure 6.17.

The data from the previous section is repeated for most of the different hoops after they were completed gluing. Furthermore, we also took wire slot measurements after each hoop was cold-cycled (cooled to liquid nitrogen temperatures and then warmed to room temperature, discussed below in section 6.2.3.6). The positions of the wire slot centers, as measured using the tool shown in figure 6.16, is given in figure 6.17 and used in a COMSOL simulation of the  $B_0$  magnet. The simulated magnet is adjusted to be in a magnetically clean environment with the associated shielding that surrounds and is encompassed in the magnet package (see [Ahm+19] for more details). The data in figure 6.17 produces a  $T_2 \approx 8.1 \times 10^4$  s or equivalently about 8 $\times$  our desired  $T_2$ . This ensures that a singular hoop gives us plenty of overhead on

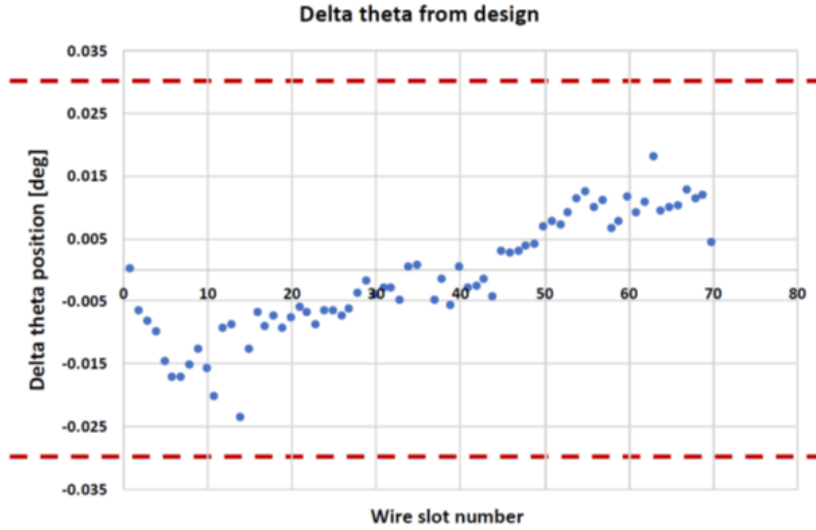


Figure 6.17: An example of the typically distribution of wire slot position measurements for a completed hoop. Dashed red lines are at  $\pm 0.030^\circ$  indicate our tolerances of  $\pm 0.5 \text{ cm}$  at cryogenic temperatures. This distribution is typical of our better hoops. For the first hoop glued, we were around  $\pm 0.030^\circ$  and we steadily improved the RMS with each subsequent gluing. Cold cycling with liquid nitrogen also improved the RMS of the wire slot distributions.

our figure of merit and that minor assembly issues can eat into the precision of the wire slots without dropping our main  $T_2$  value below the specifications needed in the final experiment

#### 6.2.3.6 Liquid Nitrogen Cold Tests

One major design benchmark was ensuring that the DP190 epoxy would mechanically survive multiple cold cycles to cryogenic temperatures since the final experiment would involve the epoxy-binded magnet and several temperature cycles. In the experiment, we would be going to temperatures of  $\approx 6 \text{ K}$ . The main concern with this temperature cycling would be the thermal contraction for the different materials in the experiment (in the  $B_0$  magnet, we are specifically referring to G10 and lead). The coefficient of thermal expansion for most materials used in the experiment decrease at lower temperatures and show relatively small change  $< 100 \text{ K}$  (see [Com] for data sheets on these materials). Thus, for the purposes of mechanical strength testing, we decided that liquid Nitrogen temperatures were sufficient.

To get a clearer picture of the mechanical strength of the DP190 epoxy, we decided to make a large bath of liquid Nitrogen and use vapor cooling of the magnet segments to

$\approx 77\text{ K}$  (liquid Nitrogen temperatures). The cold-test was done using a  $10\text{ ft} \times 10\text{ ft}$  wooden frame with Styrofoam that was epoxied together to form a base. A plastic sheet covers the entire frame and allows the liquid Nitrogen to pool at the bottom. Styrofoam material is placed on the bottom of the bath to lift the magnet segments above the liquid Nitrogen and allow Nitrogen vapor to do the majority of the cooling. This ensures a smoother transition to lower temperatures and better models the actual cooling process of the final experiment where cooling will take place over the time scale of 1-2 weeks (our  $LN_2$  tests took about 1-2 days).

After we completed the full set of inner hoops, LECs, and boss rings, we checked the alignment of the wire slots across all the structural components that form the  $B_0$  magnet. Namely, we aligned the hoops and boss rings on top of each other and inserted flat plastic trowels into the slots. We were able to fit trowels in every wire slot in the hoops, ensuring rough alignment between the wire slot positions and openings.

Upon completing the two boss rings, we had our physical components that we were most interested in for quality assurance. We performed another study where the boss rings were aligned with each other. 0.250 inch gauge pins were inserted at three locations arranged in equidistant segments along the boss rings. These are the same features to be used in the final assembly for checking alignment and clocking. We inserted gauge pins here to mock align the boss rings to each other as they would be in the final assembly. We note that the top boss ring had been cold-cycled twice to  $LN_2$  temperatures<sup>4</sup>. The bottom boss ring had not been cold tested yet. Previous cold tests indicated that the segment positions “relax” under thermal cycling so that the alignment between top and bottom segments on a single hoop becomes better aka more in agreement with the theoretical model magnet. After aligning the set-up, we inserted pin gauges at the back of each wire slot position to measure the “pass-through” clearance of the wire slots across both boss rings. The nominal width of a wire slot in the boss ring is 0.040 inches. Figure 6.18 shows the changes in the boss ring wire slot alignment after cold cycling one of the boss rings. This was checked for all the wire slot positions and we saw pin gauge measurements of 0.037 – 0.040 inches. From these measurements, we conclude that deviations in the boss ring wire slot width are order  $\approx 0.003$  inches when the boss rings are properly

---

<sup>4</sup>In reality, our temperature sensors indicated that our hoop segments reached about  $\approx 100\text{ K}$ , not the  $77\text{ K}$  of liquid nitrogen. This is likely due to the positioning of the temperature sensors and the thermal lag of the large G10 components. We deemed  $100\text{ K}$  sufficient for our tests and usually stopped the cold testing here.

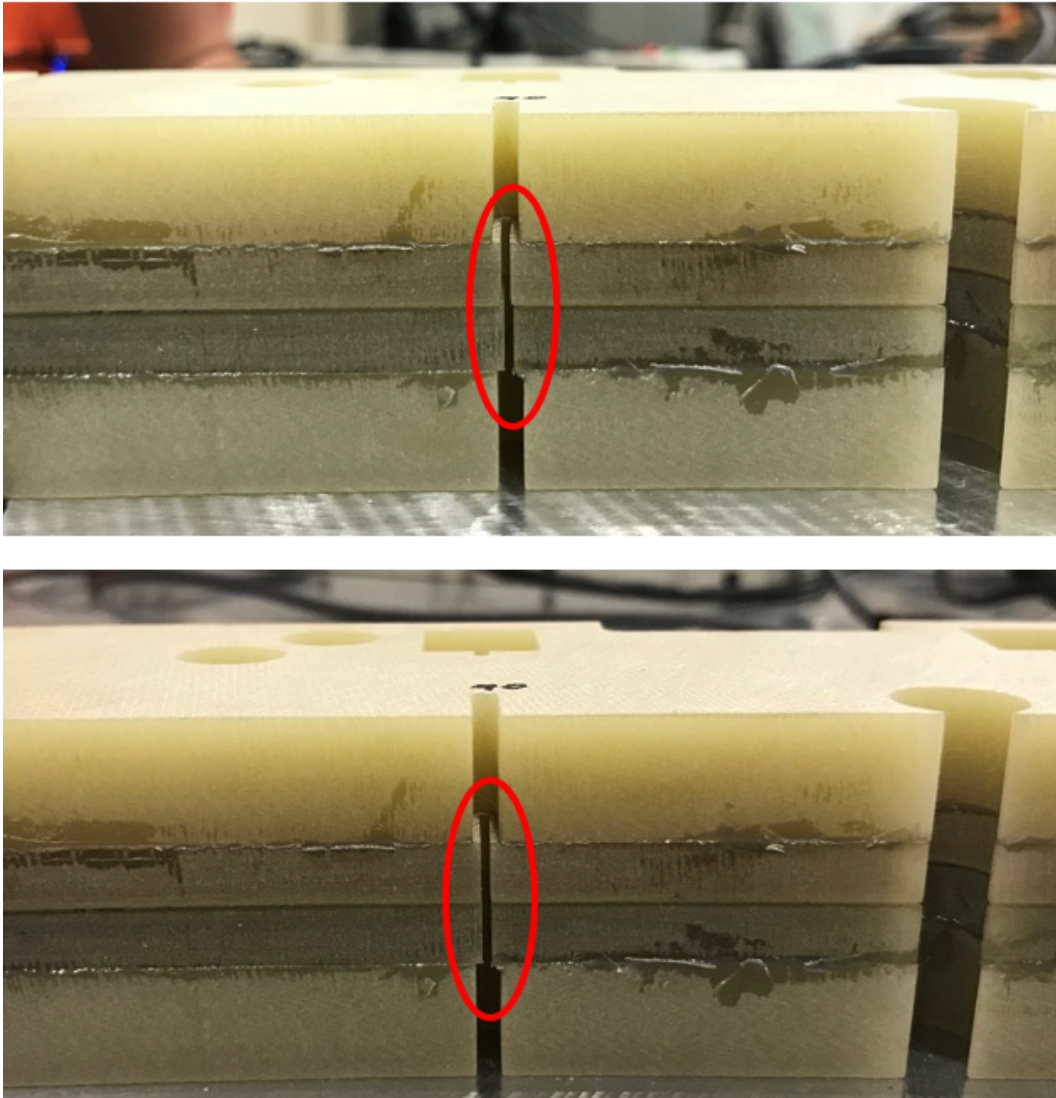


Figure 6.18: Photograph comparison of boss rings before and after cold cycling. In each of these pictures, the top segment is the bottom boss ring and the bottom segment is the top boss ring. They have been flipped from their standard order so we could test the narrow edges of the wire slots together. In the upper figure, the bottom boss ring had not been cold cycled. In the lower figure, the bottom boss ring had been cold cycled once. There is clear visual evidence of relaxation and improved wire slot positioning after cold cycling. This is corroborated with gauge pin measurements, described in more detail in the text.

aligned and thus there would be no issues with magnet wire being distorted by the edge of the wire slots since the wire is 0.020 inches in diameter.

### 6.2.4 Testing the $B_0$ Magnet Performance

In August, 2021, the magnet structure assembly and subsequent winding was completed. The finished assembly is shown in figures 6.11a, 6.11b and discussed earlier in this chapter. As a next step to check, we wanted to see if we could obtain a magnetic field measurement and compare with our in-house Comsol simulation. With a completed magnet, this meant that the only remaining tasks was to connect the magnet wire winding with a power supply and install a magnetic field mapping system. For the power supply, we used an Agilent E3645A single output DC power supply. For the field mapping system, we installed a Bartington Mag-03MCTPL70 3-axis magnetic field probe in the central volume of the magnet. This same field probe has been used internally in the collaboration for several years. In the following sections, we detail the measurement set-up and present results that benchmark our current  $B_0$  performance.

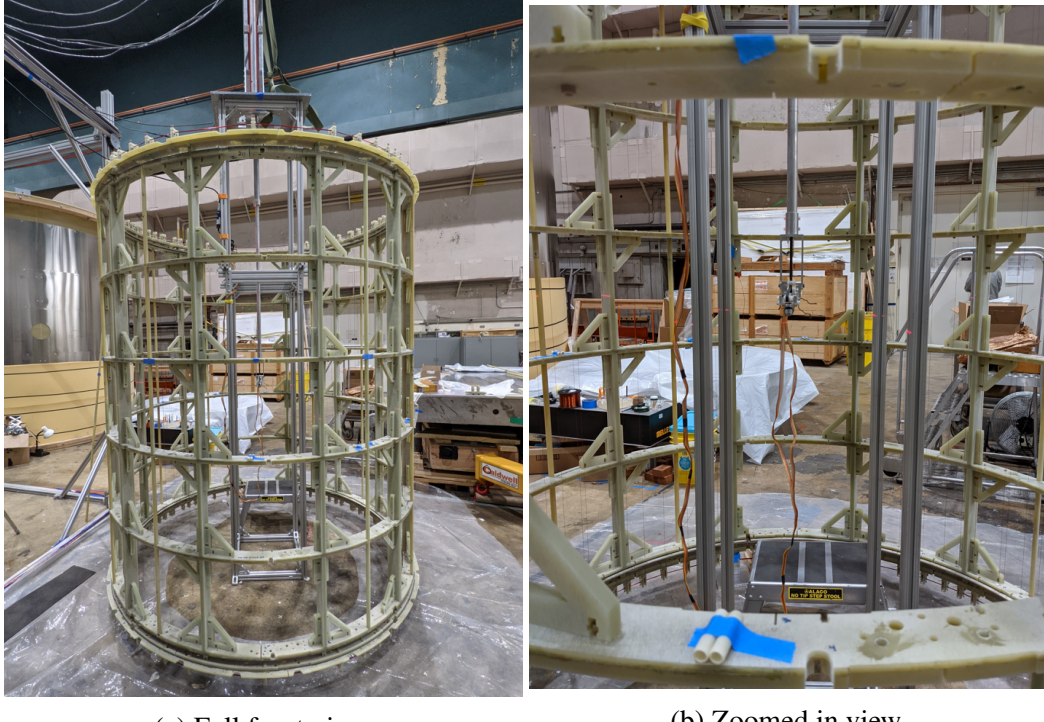
#### 6.2.4.1 Room Temperature Field Measurements

This set of measurements on the magnet is termed the “room temperature” field measurements. This measurement is intended to benchmark the performance after completing the winding of the magnet, prior to installing it in any other experimental apparatus. Furthermore, these measurements take place without being able to shield the magnet or use the active compensation coils because of space and logistical considerations. Finally, without the full experimental infrastructure, there would be no way to operate this magnet at a cooler temperature than room temperature.

The measurements are taken using the 3-axis field probe. This probe is mounted on an Aluminum table with several encoder motors used to translate, rotate, and raise/lower the probe arm. The region of interest for field mapping is the center of the magnet,  $\approx 10 - 20\text{ cm}$  (approximate scale of the UCN cells) in all directions. The mapper is originally mounted on a table that attaches to the top of the nEDM@SNS cryostat (this procedure is described in [Slu+17]). The vertical travel of the probe arm was insufficient for mapping the region of interest in the magnet. As a temporary fix, we constructed a rectangular prism frame made of 80-20 material<sup>5</sup> that was  $\approx 6\text{ ft}$ . tall and used 80-20 connector pieces to mount the mapper table to the frame. This gave us enough height that the vertical travel of the probe arm placed it in the center of the  $B_0$  magnet. As an added advantage, the additional height pushed the encoder motors out of the volume of the magnet, reducing the magnetic field distortions due

---

<sup>5</sup>A series of construction pieces made of aluminum designed to connect together to construct larger scale assemblies. Detailed description in [Incb].



(a) Full front view.

(b) Zoomed in view.

Figure 6.19: Photograph of completed mapper arm set-up, installed in the central volume of the  $B_0$  magnet. The original mapper arm structure (table, vertical shape, mapper arm) is lengthened by placing a 6 ft. tall 80-20 structure underneath. The entire structure is bolted to the floor to ensure stability and alignment of the mapper arm to the  $B_0$  magnet is done via laser level. This view is along the X direction of the  $B_0$  magnet and one of the cardinal directions in the magnet coordinate axes.

to operating these motors. The final mapping set up can be seen in figures 6.19a, 6.19b.

The entire mapping operation was operated automatically, beyond some initial test measurements done manually. We used a LabVIEW program<sup>6</sup> to operate the mapper arm. Furthermore, we connected the Agilent DC power supply to the computer running the LabView program so we could control the power supply in the program as well. We ran the program with a set number of mapping points, with the power supply set to 1 A constant current mode. To account for time-varying magnetic fields such as those due to sources in the lab or cars driving by on nearby roads, we did two things: first, we took data with the power supply on and off in consecutive runs to perform a background subtraction, and second, we ran the mapping program overnight (from 11pm to 6am). The LabView program for the mapping is shown in

---

<sup>6</sup>LabVIEW is a software program that allows integration of several hardware components for instrumentation control and data acquisition. Detailed description in [Cor].

figure 6.20.

#### 6.2.4.2 Results and Comparison to Free Space Model

We performed the magnetic field mapping over  $\pm 23\text{ cm}$  in height,  $\pm 22.7\text{ cm}$  along the trolley, and along the two cardinal directions (along beamline and along the nominal  $B_0$  direction). This is shown in figures 6.21a, 6.21b. We also simulate the final  $B_0$  magnet in free space, accounting for design changes in the position of the wire tensioners on the boss rings, and extract a prediction for the magnetic field. We show the simulation results along the two cardinal directions as well as our data in figures 6.22a, 6.22b.

The room temperature measurement only has the “bare”  $B_0$  magnet. In particular, this means the typical magnetic shielding that would be outside the  $B_0$  coil is not present and hence we expect significantly larger gradients in the field measurement (as corroborated by simulations). These shields, one made of superconducting lead and one made of Metglas, are in place to reduce magnetic field gradients and improve magnetic field uniformity prior to entering the  $B_0$  magnet. Outside the  $B_0$  coil is a cylindrical layer of several layers of Metglas 2826M material. This is designed to be a flux return to improve field uniformity, smooth out any distortions due to magnet wire misplacement, and reducing the effects of the cylindrical superconducting shield further outside the Metglas. Surrounding the Metglas flux return is a cylindrical superconducting lead (0.8 mm thick) shield. At the operation temperature of the experiment, the lead shield would become superconducting. In that state, the magnet is shielded against external time-varying fields and external distortions. These two shields, operated cryogenically, would offer substantial reduction in linear field gradients measured at the center of the  $B_0$  magnet. Without them, we expect our room temperature measurements to show large gradients. However, these measurements still serve value as tests of the magnetic field profile simulation of the completed  $B_0$  magnet.

The  $B_0$  magnet model has a flat 2.5 mG offset in field strength applied. With this minimal offset, the magnet field profile and strength is an excellent match to the model. Furthermore, the gradients seem to track the model. In the final  $B_0$  magnet coil, a series of shim coils will be wrapped around the magnet structure so that we can separately induce magnetic field in order to make minor adjustments to our overall field shape. With these preliminary results, we expect that our magnet will perform very well but some shimming may be required for production-level data.

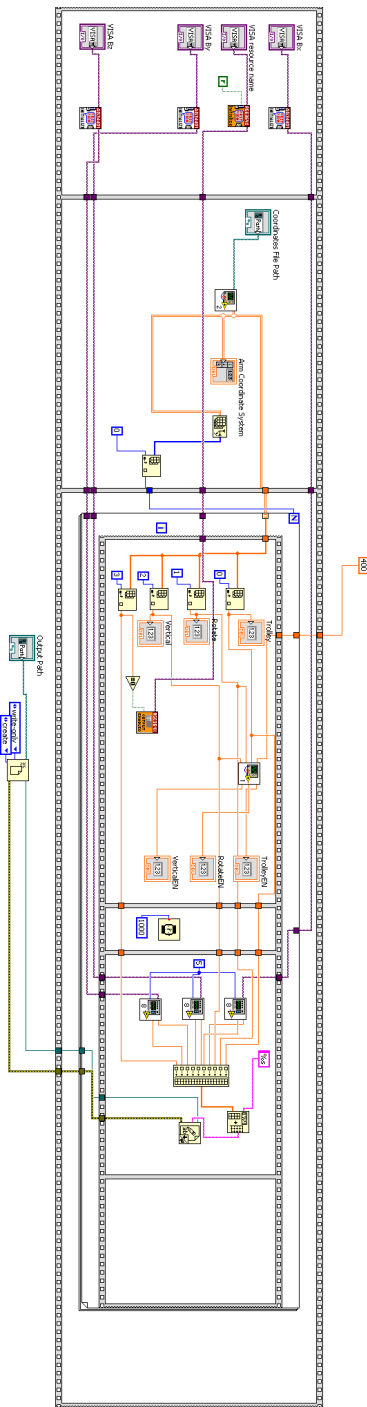


Figure 6.20: Diagram of LabVIEW program used to automate mapping procedure. Individual modules correspond to instruments used by the Caltech research group. Adapted from DAQ program used by graduate student Umit Coskun working on the cryo-probe array.

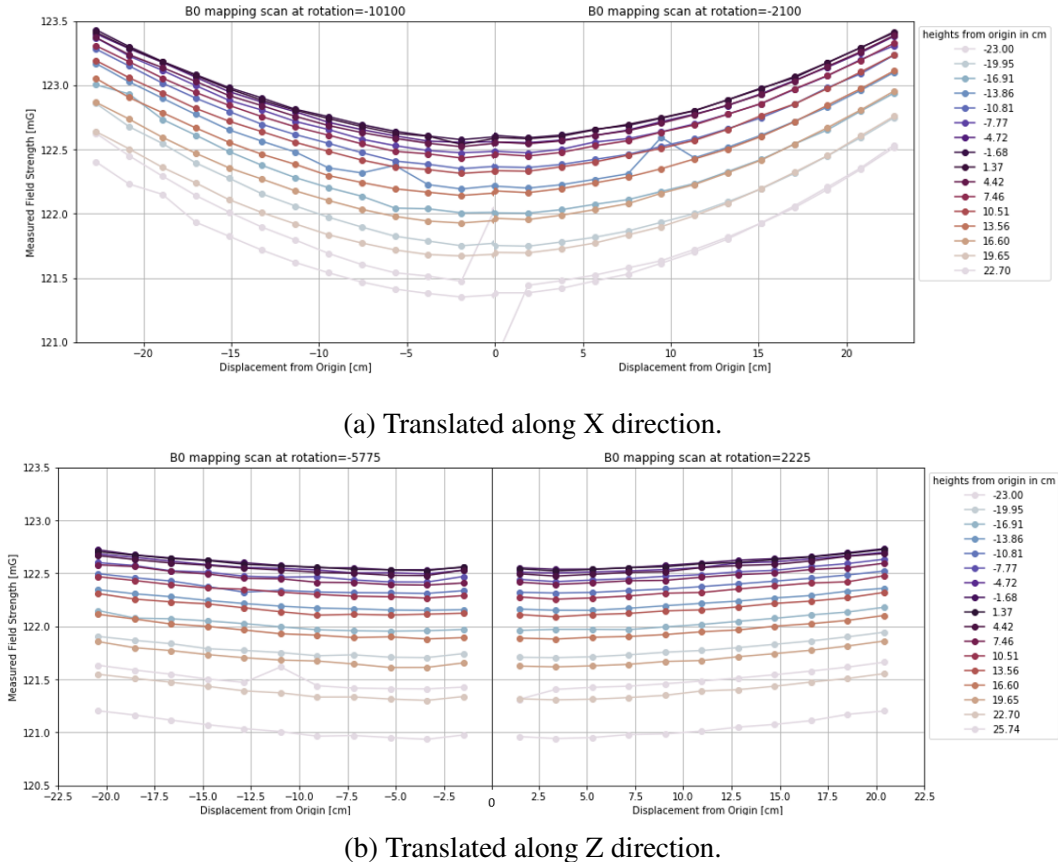


Figure 6.21: Magnetic field mapping data. The mapper arm was translated to several different heights relative to the center of the magnet. The values are background subtracted. Discontinuities or jumps in the field values likely correspond to disturbances in the field (for example, a car driving by outside the lab). The magnetic field  $B_0$  direction is along the X axis in the chosen coordinate system. The  $B_0$  values when translated along the z axis (b) have a 1.5 cm offset applied due to the position of the axes probes in the probe arm.

### 6.3 nEDM@SNS Experiment Outlook

This chapter concludes with a completed  $B_0$  magnet that has been measured at room temperature. There was significant effort and involvement from many parties at Caltech to complete this project. The magnet meets structural and cryogenic requirements for the final experimental apparatus and preliminary data taken in section 6.2.4 shows that the performance is within  $\approx 2\%$  of the predicted Comsol simulation with minimal linear gradients. The next steps of the  $B_0$  magnet will be shipping to Oak Ridge National Laboratory (ORNL) and producing a  $B_0$  field in cryogenic environments with the final NbTi superconducting wire. This is a project for a later date.

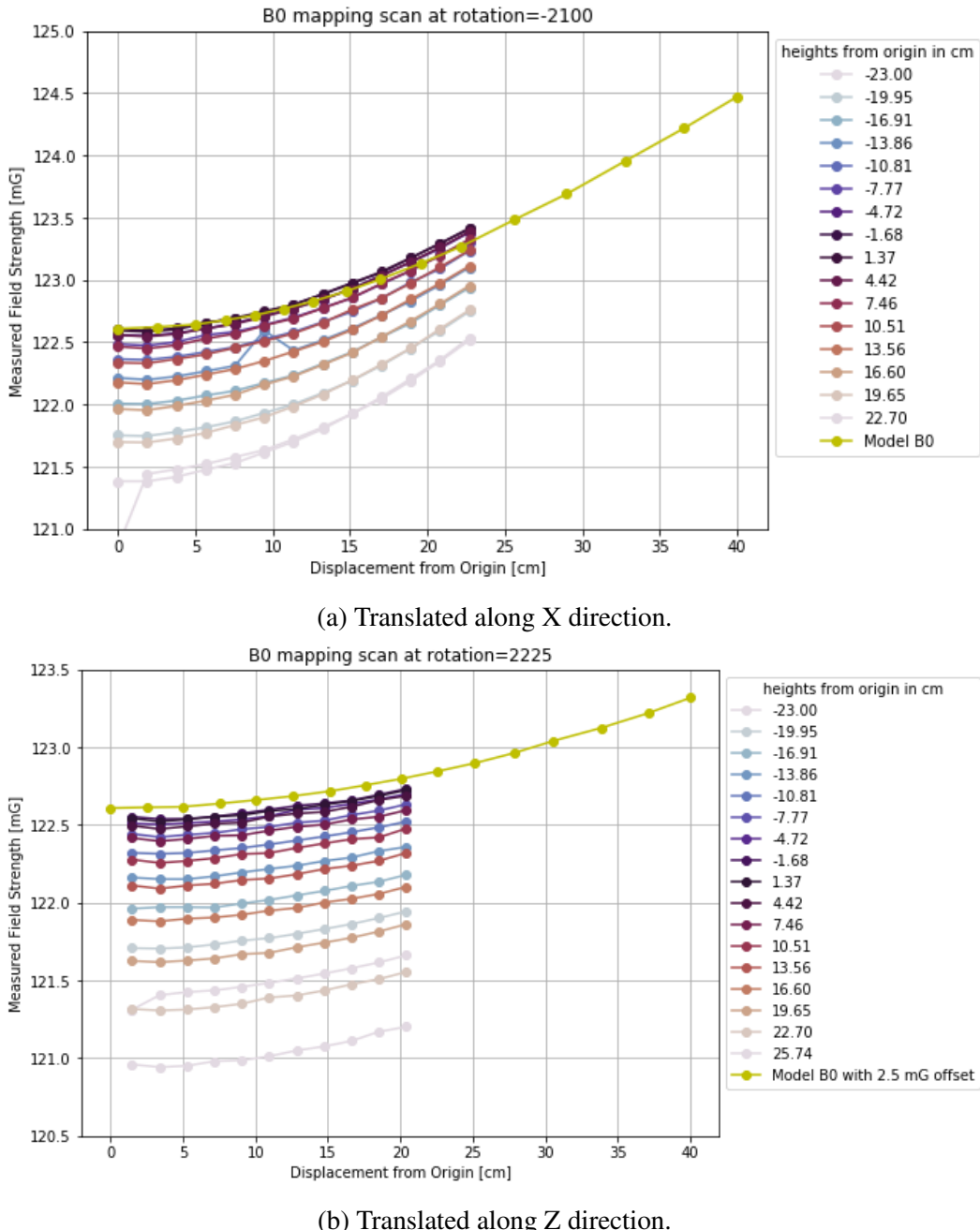


Figure 6.22: Same data as figure 6.21 except overlaid with prediction from Comsol model of the  $B_0$  magnet. A flat 2.5 mG offset is applied which aligns the field strengths at the center of the magnet. The same offset in the z translation as described in figure 6.21 is applied.

### 6.3.1 The Polarization Transmission Measurement

The next goal in the development of the nEDM@SNS experiment, specifically in the context of the magnet package, is the polarization and transmission (PT) test. This is intended to take place at ORNL in 2022.

The goal of this test is to use the active compensation coils, existing ORNL neutron guide infrastructure, magnetic shielding, and magnetic coils to test the polarization fraction of UCNs and transmission rates of UCNs to the UCN cell area for the final experiment. This will operate without the internal components of the apparatus and serves as a benchmark test to ensure that neutrons can be delivered at sufficient polarizations and pass through the different experiment layers at sufficient transmission rates. The UCNs on the beamline will pass through the entire experiment vessel, effectively travelling through 2× the layers as the final experiment, and be detected on the other side using a  $^3He$  neutron counter. This test measurement is expected to take several months when all the equipment is set-up.

### 6.3.2 The nEDM Measurement

After the PT test, the magnet package and specifically the  $B_0$  magnet will be at ORNL. There will be further work at ORNL on developing the remaining components of the experiment, shipping, assembly, and testing. Furthermore, the UVT and associated equipment must be transferred because the same procedures will be used to build the spin-dressing magnet structure at a later date. All of this will be housed in a separate building being constructed specifically for the nEDM@SNS experiment. The separate building, called EB-2, will be the final location of the experiment when it is operating. The current goal is to begin taking production data with UCNs in 2027. Further logistical discussions can be found in [Ahm+19] and associated references.

## Chapter 7

# CONCLUSION

In this dissertation, we opened by providing an introduction to Ultracold Neutrons (UCNs), the physics of weak decay in neutrons, neutron  $\beta$ -decay correlation coefficients, and neutron electric dipole moments (nEDMs). In Chapters 2 and 3 we gave a detailed overview of the UCNA experiment and our efforts to reproduce a simulation of the experiment in GEANT4. The main work in this dissertation made up the remaining chapters: we presented two main data analysis projects and one R&D instrumentation project. Specifically, in Chapter 4, we presented our analysis in extracting a measurement of the Fierz interference coefficient in the decay rate for the free neutron decay via the weak interaction. In Chapter 5, we presented a standalone analysis using the UCNA datasets to set a limit on a proposed neutron to dark matter decay (plus positron-electron pair) channel. Finally, in Chapter 6, we presented the assembly, testing, and measurement process for one of the major magnetic components in the nEDM@SNS experiment: the  $B_0$  magnet.

### 7.1 Where Are We Now?

At the conclusion of this dissertation work, we summarize the main result from each project worked on and present a brief overview of the main takeaways from each result. We note that a detailed summary is also presented at the conclusion of each of the chapters.

#### 7.1.1 Fierz Interference Measurements

In the analysis described in Chapter 4, we presented two main results: measurements of Fierz interference using UCNs from (1) direct spectral measurements and (2) energy distortions in the asymmetry term  $A_0$ . The measured results and final values with uncertainties can be found in Chapter 4.

The first component of this analysis project was the direct spectral extraction of the Fierz interference value from the 2010 UCNA dataset. The principle details of this analysis was published in [Hic+17] and the methodology described in this dissertation complements the systematic uncertainty analysis presented in that publication. In particular, the neutron  $\beta$ -decay data taken by UCNA during the 2010 data-taking run was converted into a super-sum spectrum. This combination of decay rates

removes any asymmetry effects in the final constructed spectrum. This spectrum is fit with a combination of a  $b = 0$  Standard Model spectrum and a  $b \rightarrow \infty$  spectrum which is summarized in equation 3.2 and shown in figure 3.4. The dominant systematic uncertainty is the energy calibration reconstruction uncertainty. This is studied by sampling a distribution of energy calibration variations according to our energy calibration uncertainty and the associated  $b$  values extracted from this distribution of variation calibrations produces our systematic uncertainty in extracted  $b$ . Other systematic effects are also characterized. A final value is presented in table 4.3 and the published value is  $b_{2010} = 0.067 \pm 0.005_{\text{stat}}^{+0.090}_{-0.061\text{sys}}$ . This value in [Hic+17] was the first published direct extraction of Fierz interference from the neutron  $\beta$ -decay electron spectrum and, at the time, produced leading limits on  $b_{GT}$  (the Gamow-Teller component of the Fierz interference coefficient) from neutron decay data. We note that  $b_F$ , the Fermi component of the Fierz interference coefficient, is more tightly constrained by super-allowed  $J^\pi = 0^+ \rightarrow 0^+$   $\beta$ -decay  $ft$  values and hence these measurements are not a stronger constraint on  $b_F$  than the current published literature [HT15].

The second component of this analysis project was to produce a follow-up Fierz interference extraction for the UCNA 2011-2012, 2012-2013 datasets using the procedures developed in the first publication. This meant we aimed to make direct spectral extractions on Fierz interference using two additional year's worth of UCN  $\beta$ -decay data. We estimated the energy calibration uncertainty using the same methods as before and performed additional studies such as position dependence and end point correction in an effort to improve systematic uncertainty precision. The final extracted values were  $b_{2011-2012} = 0.072 \pm 0.004_{\text{stat}}^{+0.108}_{-0.101\text{sys}}$ , and  $b_{2012-2013} = 0.044 \pm 0.008_{\text{stat}}^{+0.174}_{-0.117\text{sys}}$ . Ultimately, since we were not able to significantly improve the energy calibration uncertainty, we turned toward an asymmetry-extracted Fierz interference value. The Fierz interference can be extracted from the asymmetry by fitting for an energy dependence of the form in equation 4.23. We note that this fitting procedure is limited by statistical precision. We perform studies on the various systematic effects and conclude they are subdominant. The extracted Fierz interference values are given in table 4.3. The asymmetry-extracted Fierz interference is presented as a simple weighted average of the three dataset's values and is  $\langle b_{\text{asymm}} \rangle = 0.066 \pm 0.041_{\text{stat}} \pm 0.024_{\text{syst}}$ . This is an improvement over the 2010 UCNA dataset spectral extraction on Fierz interference by a factor of  $\approx 2 - 3$ , leading to a similar improvement in  $b_{GT}$  values as discussed above. This will be compared and contrasted with a publication by PERKEO II utilizing the same

analysis methodology which presented  $b = 0.017 \pm 0.021$  which is an improvement of factor  $\approx 2$  over our result [Sau+20].

When we fit the asymmetry to an energy dependence of the form in equation 4.23, we extract both a value of  $b$  and also of  $A_0$  (not to be confused with the traditional Standard Model  $A_0$  which assumes  $b = 0$ ). Under the paradigm of  $b \neq 0$ ,  $A_0$  is modified and the resulting fit has correlated uncertainties. The new extracted values of  $A_0$  for the 2010, 2011-2012, and 2012-2013 UCNA datasets are  $A_{0,2010} = -0.1231 \pm 0.0048$ ,  $A_{0,2011-2012} = -0.1258 \pm 0.0044$ , and  $A_{0,2012-2013} = -0.1236 \pm 0.0059$ . The currently published values of  $A_0$  (see [Men+13; Bro+18] as well as results from the PERKEO collaboration [Mär+19]) have uncertainties  $\approx 10\times$  smaller. This is because in the Standard Model interpretation, there is no  $b$  term and hence no correlated uncertainty. We note that with this  $\approx 10\times$  larger uncertainty, the new  $A_0$  values from the asymmetry extracted Fierz interference fit are consistent with the Standard Model ( $b = 0$ )  $A_0$  values.

### 7.1.2 Dark Matter Decay Limits

We have completed an analysis on the UCNA dataset in order to extract a novel proposed decay channel

$$n \rightarrow \chi + e^+ e^- \quad (7.1)$$

This exotic decay channel was originally proposed in [FG18a] as a possible resolution to the neutron lifetime anomaly. The anomaly itself refers to the  $\approx 4\sigma$  discrepancy in central value measurements of the neutron lifetime when the neutron lifetime is measured by bottle methods (neutron disappearance) vs beam methods ( $p$  counting from decay in equation 1.4).

We use the UCNA dataset to measure this decay channel by direct detection of coincident positron-electron pairs. We take all events that registered as a coincidence between the East and West detectors with relative timing interval  $< 12\text{ ns}$  to suppress all Type 1 backscatter events. We chose a lower time interval than the physically forbidden crossing time in the UCNA apparatus of  $\approx 15\text{ ns}$  in order to reduce Type 1  $\beta$ -decay events leakage due to timing resolution effects. We take the total number of events that satisfy these cuts subtracted for background rates, adjusted for acceptance and detection efficiency, and convert to confidence limits. These limits are presented in figure 5.18.

With our final confidence limits, we exclude the proposed dark matter decay channel described above at  $\gg 5\sigma$  over the energy range  $KE_{e^+e^-} \in [100, 644]\text{ keV}$ , which

corresponds to  $\approx 84\%$  of the mass range of the dark matter  $\chi$  particle. This effectively rules out the decay in equation 5.9 as the sole explanation for the neutron lifetime anomaly for a large fraction of the available phase space. In conjunction with collaborators at LANL who measured the decay rate for equation 5.8 [Tan+18], we effectively rule out the visible decay channels (see decay in equation 5.5) proposed to resolve the neutron lifetime anomaly.

If the positron-electron decay channel is not the sole dark matter decay channel, we set branching ratio limits of  $\frac{\Gamma_{n \rightarrow \chi + e^+ e^-}}{\Gamma_n \text{ total}} < 10^{-4}$  at the 90% confidence level, over the same energy range of  $100 \text{ keV} < KE_{e^+ e^-} < 644 \text{ keV}$ . These limits are far more stringent than the  $10^{-2}$  branching ratios required to resolve the neutron lifetime anomaly.

Despite the limits set in this work, we note that there is still available energy phase space available for such a dark matter  $\chi$  particle. In particular, due to the UCNA trigger function, our limits do not probe significantly summed kinetic energy  $< 100 \text{ keV}$ . In principle, this is still a region where an exotic dark matter  $\chi$  particle could exist. However, a follow-up publication by the PERKEO II collaboration further improved our limits and excluded the positron-electron decay channel from summed kinetic energy  $37.5 \text{ keV} < KE_{e^+ e^-} < 644 \text{ keV}$  [Klo+19]. As a result of these publications ([Tan+18; Sun+18; Klo+19]), the available phase space for this decay channel is significantly reduced as an explanation for the neutron lifetime anomaly. Modifications to the original model can be utilized to avoid these current limits by pushing the theory to more exotic interactions.

### 7.1.3 $B_0$ Benchmark Measurements

In the work described in this dissertation, we have completed the construction of a  $B_0$  magnet for the nEDM@SNS experiment. This consists of the  $B_0$  frame, the necessary structural components, and the winding of the entire magnet with copper wire that will be used for the next  $B_0$  benchmark test. This magnet is the culmination of  $\approx 2$  years of design, procurement, construction, and assembly. The final testing (for now) was the room temperature measurements to see if we could obtain a sensible magnetic field consistent with our  $B_0$  field simulations at room temperature without the associated shielding infrastructure.

The initial measurements of the magnetic field produced by our  $B_0$  magnet at room temperature are shown in figure 6.22. Included in the figures are COMSOL simulations of our  $B_0$  field using an accurate positioning representation of our final

constructed magnet structure. The agreement between the model and the measured field is within  $\approx 2\%$ , where we note we applied a flat  $2.5 \text{ mG}$  offset to the model in order to better match the measured field. Furthermore, the gradients in the field as a function of translated position in X-Z also seem to track the model well. These factors indicate that our magnet was constructed true to design without any critical failures.

We highlight that the final  $B_0$  magnet will have additional shim coils wound along a separate frame (the spin-dressing coil will house the shim coils). These shim coils are designed to allow separate currents to be run and induce magnetic fields that can cancel gradients along the different coordinate axes of the magnet. Thus, we expect that given our current field measurements we have a magnet that will perform at our design specification. We will also have fine control over the magnetic field once the shim coils are in place. From these initial room temperature measurements and additional improvements to be implemented later, we believe we will be able to achieve our design specification magnetic field uniformity and gradients in our final  $B_0$  magnet.

## 7.2 What's Next?

We now discuss briefly what extensions to these results will come in the near future. For the work on Fierz interference, we note that we do not present a comprehensive study of current experiments which aim to measure  $b$  because this is a growing list with differing sensitivity goals, frequently mixed up in other decay correlation coefficient experiments. This dissertation referenced the Nab collaboration as one example  $b$  experiment (see [Fry+19] for a description). Instead of giving a review, we present an introduction to a single experiment, UCNA+, which aims to be an improvement on the UCNA experiment that formed the majority of the analysis work in this dissertation. For the nEDM@SNS experiment, we present a rough timeline for measurements involving the  $B_0$  magnet.

### 7.2.1 UCNA+

The UCNA experiment was designed to make a high-precision measurement of the asymmetry parameter,  $A$ , and hence a high-precision measurement of  $\lambda = \frac{g_A}{g_V}$ , the ratio of axial-vector - vector couplings in the weak interaction. Over the course of several measurement campaigns, detailed in [Pla+08; Pla+12; Pla+19], the UCNA collaboration published high precision measurements of  $A$ . In the end, the final measurements yielded a 0.55% uncertainty on  $A$ . In addition, the UCNA datasets

provided extractions of several beyond Standard Model interactions such as limits on tensor couplings via the Fierz interaction and potential dark matter decay channels that produce positron-electron pairs. With these in mind, the UCNA experimental run provided data that derived many different results in fundamental neutron  $\beta$ -decay processes.

However, the original design goal of UCNA was a 0.2% precision measurement of  $A$  which was ultimately not achieved due to limitations from electron backscattering systematics. In a new proposal, an upgraded UCNA detector called UCNA+ is intended to operate and reach the original design sensitivity of a 0.2% measurement of  $A$ , with improved precision in follow-up data-taking runs.

The UCNA+ detector aims to improve upon UCNA by utilizing several upgrades. First, the UCN source at Los Alamos National Lab (LANL) was upgraded and now provides a  $\approx 6\times$  increase in UCN statistics. Recall from Chapter 4 that the asymmetry-extracted analysis was statistics limited (this was also true for the asymmetry measurement).

Second, the backscattering effect, the dominant systematic uncertainty in the asymmetry measurement, will be significantly reduced by removing the multi-wire proportional chamber (MWPC) and the plastic scintillator and light guide-to-PMT system. In their place, a 16-sided plastic scintillator with 128 edge-coupled Silicon Photomultipliers (SiPMs) will be used. We note that without the MWPC a new gamma ray veto system will have to be used. The lack of material interfaces (for example, the windows in the MWPC) will reduce backscatter rates and hence backscatter systematic effects. Furthermore, replacement of the light guide system with a direct light readout will improve light collection and hence energy reconstruction.

Third, the calibration sources used in the original UCNA were moved within the detector on a horizontal paddle, giving a calibration restricted to a single position axis. A new calibration system will use a remote-controlled scanner that allows the calibration source to be translated across the entire X-Y plane within the detector. This is intended to lead to improved position maps and higher quality energy calibrations. Ideally, the improved energy calibrations would contribute significantly to reducing the dominant uncertainty on a direct spectral Fierz interference extraction.

UCNA+ has completed a series of simulations in GEANT4 and PENELOPE that have verified that these changes will lead to a  $< 0.2\%$  measurement of  $A$  and

ultimately a < 0.1% when the full data-taking run is complete. They are currently in the prototype and design stage of the upgrades. Specifically, they are testing the systems that translate the calibration sources, a SiPM detector prototype, and a SiPM data acquisition system. After different components are tested and finalized, they must be installed on the UCNA apparatus at LANL before commissioning and production data-taking can occur.

### 7.2.2 nEDM@SNS

The next steps for the  $B_0$  magnet include testing in circumstances that mimic the final experiment to refine the development of the magnetic system for the UCNs in nEDM@SNS. The work in this dissertation discussed a series of room temperature measurements made with a remote controllable probe arm in the central volume of the magnet located on the lab floor. This was a rudimentary measurement to check the initial quality of the magnet winding.

In further tests, the  $B_0$  magnet must be moved into a magnetically shielded environment. This means being placed within the vacuum vessel that can mechanically support the  $B_0$  magnet, with three layers of shields installed on the  $B_0$  magnet. These shields are copper, superconducting lead, and Metglas, all of which are designed to make the field more uniform to reach our specifications. Furthermore, this vessel will be located at the center of a series of active compensation coils, i.e., a rectangular prism of wires wound along the Cartesian xyz coordinates that can induce field offsets and gradients. These additional coils are designed to cancel the Earth's magnetic field and remove gradients prior to reaching the shielding. The Caltech group will install the  $B_0$  magnet in the vessel and cool the entire system to the cryogenic design temperatures before turning on the  $B_0$  wire current. The magnetic field will then be measured using the same probe system.

Afterwards, the entire vessel and magnetics system will be disassembled and transported to Oak Ridge National Laboratory (ORNL) where the final experiment will be located. The  $B_0$  magnet will largely be intact during the transportation so there will be minimal assembly of the magnet once at ORNL. The next major test will be the Polarization-Transmission (PT) test. Most of the outer vacuum vessel and magnetic shielding will be installed and the  $B_0$  coil placed within. A beam of cold neutrons (8.9 Å) will pass through the entirety of the cylindrical experimental volume (effectively passing through each experiment material layer twice) and detected on the opposite side. The polarization fractions and transmission fractions will be deduced

from these measurements to check whether additional systems need to be installed to maintain high PT rates. These PT rates directly impact the final polarized UCN density in the experiment central volume and hence sensitivity to an nEDM. The  $B_0$  magnet system and associated shields play a crucial role in the characterization of the PT rates.

At some point during the lifetime of the experimental R&D at ORNL, the spin-dressing magnet must be constructed. It is nearly identical to the construction procedure described in this dissertation. It will be constructed with G10 hoops that have to be epoxied together on the Unicorn Vacuum Table (UVT) and assembled into a frame using G10 story sticks and G10 gussets. Wire tensioners made of Torlon and G10 will be installed at the top and bottom boss rings and wire will be wound around the spin-dressing magnet frame. The principle difference is that the spin-dressing magnet will have a smaller diameter for the hoops and therefore projects to be an easier construction process, although unforeseen difficulties are sure to arise.

After the PT measurement is completed, the next major task for the  $B_0$  magnet is producing a magnetic field for the final experiment configuration. In order to do this, the copper wire that forms the magnet must be unwound and replaced with a Niobium-Titanium (NbTi) wire. This is because the final magnet must be run in Persistent Current mode in order to provide a highly stable magnetic field. After the re-wind of the magnet, the experiment will be assembled in stages, tested, and configured for production level data. Current installation is expected to be complete in 2025 with production data coming in 2027 [Ahm+19].

## BIBLIOGRAPHY

- [AB] Hexagon AB. *ROMER is now part of Hexagon Manufacturing Intelligence*. URL: <https://www.hexagonmi.com/about-us/about-hexagon-manufacturing-intelligence/our-history/romer>.
- [Abe+19] C. Abel et al. “Magnetic-field uniformity in neutron electric-dipole-moment experiments”. In: *Phys. Rev. A* 99 (4 Apr. 2019), p. 042112. doi: [10.1103/PhysRevA.99.042112](https://doi.org/10.1103/PhysRevA.99.042112). URL: <https://link.aps.org/doi/10.1103/PhysRevA.99.042112>.
- [Abe+20] C. Abel et al. “Measurement of the Permanent Electric Dipole Moment of the Neutron”. In: *Phys. Rev. Lett.* 124 (8 Feb. 2020), p. 081803. doi: [10.1103/PhysRevLett.124.081803](https://doi.org/10.1103/PhysRevLett.124.081803). URL: <https://link.aps.org/doi/10.1103/PhysRevLett.124.081803>.
- [Ada+19] Adamek, Evan R. et al. “Precision neutron flux measurement using the Alpha-Gamma device”. In: *EPJ Web Conf.* 219 (2019), p. 10004. doi: [10.1051/epjconf/201921910004](https://doi.org/10.1051/epjconf/201921910004). URL: <https://doi.org/10.1051/epjconf/201921910004>.
- [Age19] Nuclear Energy Agency. *PENELOPE 2018: A code system for Monte Carlo simulation of electron and photon transport*. 2019, p. 420. doi: <https://doi.org/https://doi.org/10.1787/32da5043-en>. URL: <https://www.oecd-ilibrary.org/content/publication/32da5043-en>.
- [Ago+03] S. Agostinelli et al. “GEANT4: A Simulation toolkit”. In: *Nucl. Instrum. Meth.* A506 (2003), pp. 250–303. doi: [10.1016/S0168-9002\(03\)01368-8](https://doi.org/10.1016/S0168-9002(03)01368-8).
- [Ahm+19] M.W. Ahmed et al. “A new cryogenic apparatus to search for the neutron electric dipole moment”. In: *Journal of Instrumentation* 14.11 (Nov. 2019), P11017–P11017. doi: [10.1088/1748-0221/14/11/p11017](https://doi.org/10.1088/1748-0221/14/11/p11017). URL: <https://doi.org/10.1088/1748-0221/14/11/p11017>.
- [Ale19] Alina Aleksandrova. “Magnetic Field Monitoring in the SNS Neutron EDM Experiment”. PhD thesis. University of Kentucky, 2019.
- [Ale21] Alina Aleksandrova. “B0: Magnet Assembly”. nEDM@SNS Collaboration Meeting. 2021.
- [Atc+07] F. Atchison et al. “Measurement of the Fermi potential of diamond-like carbon and other materials”. In: *Nuclear Instruments and Methods in Physics Research Section B: Beam Interactions with Materials and Atoms* 260.2 (2007), pp. 647–656. ISSN: 0168-583X. doi: <https://doi.org/10.1016/j.nimb.2007.04.253>. URL:

- <https://www.sciencedirect.com/science/article/pii/S0168583X0700969X>.
- [Bal+16] M. J. Bales et al. “Precision Measurement of the Radiative  $\beta$  Decay of the Free Neutron”. In: *Phys. Rev. Lett.* 116 (24 June 2016), p. 242501. doi: 10.1103/PhysRevLett.116.242501. URL: <https://link.aps.org/doi/10.1103/PhysRevLett.116.242501>.
- [Bay+18] Gordon Baym et al. “Testing Dark Decays of Baryons in Neutron Stars”. In: *Phys. Rev. Lett.* 121 (6 Aug. 2018), p. 061801. doi: 10.1103/PhysRevLett.121.061801. URL: <https://link.aps.org/doi/10.1103/PhysRevLett.121.061801>.
- [BCR18] Frederik Beaujean, Allen Caldwell, and Olaf Reimann. “Is the bump significant? An axion-search example”. In: *Eur. Phys. J. C* 78.9 (2018), p. 793. doi: 10.1140/epjc/s10052-018-6217-y. arXiv: 1710.06642 [hep-ex].
- [Ber07] Carlos A. Bertulani. *Nuclear Physics in a Nutshell*. Princeton University Press, 2007. ISBN: 9780691125053.
- [Bil+59] S M Bilenkii et al. “ON THE THEORY OF  $\beta$ -DECAY OF NEUTRON”. In: (Jan. 1959). URL: <https://www.osti.gov/biblio/4205080>.
- [BPY05] W. Buchmuller, R.D. Peccei, and T. Yanagida. “LEPTOGENESIS AS THE ORIGIN OF MATTER”. In: *Annual Review of Nuclear and Particle Science* 55.1 (2005), pp. 311–355. doi: 10.1146/annurev.nucl.55.090704.151558. eprint: <https://doi.org/10.1146/annurev.nucl.55.090704.151558>. URL: <https://doi.org/10.1146/annurev.nucl.55.090704.151558>.
- [Bro+18] M. A.-P. Brown et al. “New result for the neutron  $\beta$ -asymmetry parameter  $A_0$  from UCNA”. In: *Phys. Rev. C* 97 (3 Mar. 2018), p. 035505. doi: 10.1103/PhysRevC.97.035505. URL: <https://link.aps.org/doi/10.1103/PhysRevC.97.035505>.
- [Bro18] Michael A.-P. Brown. “Determination of the Neutron Beta-Decay Asymmetry Parameter A Using Polarized Ultracold Neutrons.” PhD thesis. University of Kentucky, 2018.
- [BS40] F. Bloch and A. Siegert. “Magnetic Resonance for Nonrotating Fields”. In: *Phys. Rev.* 57 (6 Mar. 1940), pp. 522–527. doi: 10.1103/PhysRev.57.522. URL: <https://link.aps.org/doi/10.1103/PhysRev.57.522>.
- [Cas21] Davide Castelvecchi. *Physicists make most precise measurement ever of neutron’s lifetime*. Oct. 2021. URL: <https://www.nature.com/articles/d41586-021-02812-z>.

- [CDS12] Laurent Canetti, Marco Drewes, and Mikhail Shaposhnikov. “Matter and antimatter in the universe”. In: *New Journal of Physics* 14.9 (Sept. 2012), p. 095012. doi: [10.1088/1367-2630/14/9/095012](https://doi.org/10.1088/1367-2630/14/9/095012). URL: <https://doi.org/10.1088/1367-2630/14/9/095012>.
- [Chu+19] T. E. Chupp et al. “Electric dipole moments of atoms, molecules, nuclei, and particles”. In: *Rev. Mod. Phys.* 91 (1 Jan. 2019), p. 015001. doi: [10.1103/RevModPhys.91.015001](https://doi.org/10.1103/RevModPhys.91.015001). URL: <https://link.aps.org/doi/10.1103/RevModPhys.91.015001>.
- [Com] US Department of Commerce. *Properties of solid materials from cryogenic- to room-temperatures*. URL: <https://trc.nist.gov/cryogenics/materials/materialproperties.htm>.
- [Cor] National Instrument Corporation. *What Is LabVIEW?* URL: <https://www.ni.com/en-us/shop/labview.html>.
- [Dee19] Eric Dees. “On the Use of Ultracold Neutrons for Exploration of Electroweak Interactions and 5th Force Contributions to Gravitation..” PhD thesis. North Carolina State University, 2019.
- [Dom+21] Valerie Domcke et al. “MeV-scale seesaw and leptogenesis”. In: *Journal of High Energy Physics* 2021.1 (Jan. 2021), p. 200. ISSN: 1029-8479. doi: [10.1007/JHEP01\(2021\)200](https://doi.org/10.1007/JHEP01(2021)200). URL: [https://doi.org/10.1007/JHEP01\(2021\)200](https://doi.org/10.1007/JHEP01(2021)200).
- [FG18a] Bartosz Fornal and Benjamin Grinstein. “Dark Matter Interpretation of the Neutron Decay Anomaly”. In: *Phys. Rev. Lett.* 120 (19 May 2018), p. 191801. doi: [10.1103/PhysRevLett.120.191801](https://doi.org/10.1103/PhysRevLett.120.191801). URL: <https://link.aps.org/doi/10.1103/PhysRevLett.120.191801>.
- [FG18b] Bartosz Fornal and Benjamin Grinstein. “Dark Matter Interpretation of the Neutron Decay Anomaly”. In: *Phys. Rev. Lett.* 120.19 (2018). [Erratum: *Phys.Rev.Lett.* 124, 219901 (2020)], p. 191801. doi: [10.1103/PhysRevLett.120.191801](https://doi.org/10.1103/PhysRevLett.120.191801). arXiv: [1801.01124](https://arxiv.org/abs/1801.01124) [hep-ph].
- [Fie37] Markus Fierz. “Zur Fermischen Theorie des  $\bar{p}$ -Zerfalls”. In: *Zeitschrift für Physik* 104.7 (July 1937), pp. 553–565. ISSN: 0044-3328. doi: [10.1007/BF01330070](https://doi.org/10.1007/BF01330070). URL: <https://doi.org/10.1007/BF01330070>.
- [Fil18] Brad Filippone. “Timing details”. UCNA Electronic Logbook. Feb. 2018.
- [Fil21] Brad Filippone. Presentation for NSF Review. 2021.
- [Fom21] Nadia Fomin. “BL3: Next generation beam experiment to measure the neutron lifetime”. April American Physics Society Conference. 2021. URL: <http://meetings.aps.org/Meeting/APR19/Session/D14.2>.

- [Fri22] Eric Michael Fries. “Precision Measurement of the Neutron Lifetime.” PhD thesis. California Institute of Technology, 2022. doi: 10.7907/qr2k-7b09. URL: <https://resolver.caltech.edu/CaltechTHESIS:08292021-214153213>.
- [Fry+19] Fry, J. et al. “The Nab experiment: A precision measurement of unpolarized neutron beta decay”. In: *EPJ Web Conf.* 219 (2019), p. 04002. doi: 10.1051/epjconf/201921904002. URL: <https://doi.org/10.1051/epjconf/201921904002>.
- [FY86] M. Fukugita and T. Yanagida. “Barygenesis without grand unification”. In: *Physics Letters B* 174.1 (1986), pp. 45–47. issn: 0370-2693. doi: [https://doi.org/10.1016/0370-2693\(86\)91126-3](https://doi.org/10.1016/0370-2693(86)91126-3). URL: <https://www.sciencedirect.com/science/article/pii/0370269386911263>.
- [GG16] G. L. Greene and P. Geltenbort. “The Neutron Enigma”. In: *Sci. Am.* 314 (2016), pp. 37–41. doi: 10.1038/scientificamerican0416-36.
- [GNS19] Martin Gonzalez-Alonso, Oscar Naviliat-Cuncic, and Nathal Severijns. “New physics searches in nuclear and neutron  $\beta$  decay”. In: *Prog. Part. Nucl. Phys.* 104 (2019), pp. 165–223. doi: 10.1016/j.ppnp.2018.08.002. arXiv: 1803.08732 [hep-ph].
- [Gon+21] F. M. Gonzalez et al. “Improved Neutron Lifetime Measurement with UCN $\tau$ ”. In: *Phys. Rev. Lett.* 127 (16 Oct. 2021), p. 162501. doi: 10.1103/PhysRevLett.127.162501. URL: <https://link.aps.org/doi/10.1103/PhysRevLett.127.162501>.
- [GP77] R. Golub and J.M. Pendlebury. “The interaction of Ultra-Cold Neutrons (UCN) with liquid helium and a superthermal UCN source”. In: *Physics Letters A* 62.5 (1977), pp. 337–339. issn: 0375-9601. doi: [https://doi.org/10.1016/0375-9601\(77\)90434-0](https://doi.org/10.1016/0375-9601(77)90434-0). URL: <https://www.sciencedirect.com/science/article/pii/0375960177904340>.
- [Gri08] David Griffiths. *Introduction to elementary particles*. 2008. isbn: 978-3-527-40601-2.
- [GRL91] R. Golub, D. Richardson, and S.K. Lamoreaux. *Ultra-Cold Neutrons*. Taylor & Francis, 1991. isbn: 9780750301152. URL: <https://books.google.com/books?id=QPUjlCWNg78C>.
- [HH10] G. Ifan Hughes and Thomas P.A. Hase. *Measurements and their Uncertainties. A Practical Guide to Modern Error Analysis*. Oxford University Press, 2010.

- [Hic+17] K. P. Hickerson et al. “First direct constraints on Fierz interference in free neutron  $\beta$  decay”. In: *Phys. Rev.* C96.4 (2017). [Addendum: *Phys. Rev.* C96,no.5,059901(2017)], p. 042501. doi: [10.1103/PhysRevC.96.042501](https://doi.org/10.1103/PhysRevC.96.042501), [10.1103/PhysRevC.96.059901](https://doi.org/10.1103/PhysRevC.96.059901). arXiv: [1707.00776](https://arxiv.org/abs/1707.00776) [nucl-ex].
- [Hic13] Kevin Hickerson. “The Physics of Ultracold Neutrons and Fierz Interference in Beta Decay.” PhD thesis. California Institute of Technology, 2013.
- [Hir+20] K Hirota et al. “Neutron lifetime measurement with pulsed cold neutrons”. In: *Progress of Theoretical and Experimental Physics* 2020.12 (Dec. 2020). 123C02. ISSN: 2050-3911. doi: [10.1093/ptep/ptaa169](https://doi.org/10.1093/ptep/ptaa169). eprint: <https://academic.oup.com/ptep/article-pdf/2020/12/123C02/35931162/ptaa169.pdf>. URL: <https://doi.org/10.1093/ptep/ptaa169>.
- [Hoe03] Seth A. Hoedl. “Novel Proton Detectors, Ultra-Cold Neutron Decay and Electron Backscatter”. PhD thesis. Princeton University, 2003.
- [Hol+12] A. T. Holley et al. “A high-field adiabatic fast passage ultracold neutron spin flipper for the UCNA experiment”. In: *Review of Scientific Instruments* 83.7 (2012), p. 073505. doi: [10.1063/1.4732822](https://doi.org/10.1063/1.4732822). eprint: <https://doi.org/10.1063/1.4732822>. URL: <https://doi.org/10.1063/1.4732822>.
- [Hol12] Adam T. Holley. “Ultracold Neutron Polarimetry in a Measurement of the  $\beta$  Asymmetry.” PhD thesis. North Carolina State University, 2012.
- [Hoo+19] Shannon F. Hoogerheide et al. “Progress on the BL2 beam measurement of the neutron lifetime”. In: *EPJ Web Conf.* 219 (2019). Ed. by T. Jenke et al., p. 03002. doi: [10.1051/epjconf/201921903002](https://doi.org/10.1051/epjconf/201921903002).
- [Hoo21] Anson Hook. *TASI Lectures on the Strong CP Problem and Axions*. 2021. arXiv: [1812.02669](https://arxiv.org/abs/1812.02669) [hep-ph].
- [HT15] J. C. Hardy and I. S. Towner. “Superallowed  $0^+ \rightarrow 0^+$  nuclear  $\beta$  decays: 2014 critical survey, with precise results for  $V_{ud}$  and CKM unitarity”. In: *Phys. Rev. C* 91 (2 Feb. 2015), p. 025501. doi: [10.1103/PhysRevC.91.025501](https://doi.org/10.1103/PhysRevC.91.025501). URL: <https://link.aps.org/doi/10.1103/PhysRevC.91.025501>.
- [Hut14] Nicholas Hutzler. “A New Limit on the Electron Electric Dipole Moment: Beam Production, Data Interpretation, and Systematics”. PhD thesis. Harvard University, 2014.
- [Inca] Autodesk Inc. *3D measurement software for a wide range of hardware*. URL: <https://www.autodesk.com/products/powerinspect/overview>.
- [IncB] 80/20 Inc. *What is 80-20?* URL: <https://8020.net/what-is-8020>.

- [Ioc+09] Fabio Iocco et al. “Primordial nucleosynthesis: From precision cosmology to fundamental physics”. In: *Physics Reports* 472.1 (2009), pp. 1–76. ISSN: 0370-1573. doi: <https://doi.org/10.1016/j.physrep.2009.02.002>. URL: <https://www.sciencedirect.com/science/article/pii/S0370157309000374>.
- [Ito+07] T.M. Ito et al. “A multiwire proportional chamber for precision studies of neutron  $\bar{p}$  decay angular correlations”. In: *Nuclear Instruments and Methods in Physics Research Section A: Accelerators, Spectrometers, Detectors and Associated Equipment* 571.3 (2007), pp. 676–686. ISSN: 0168-9002. doi: <https://doi.org/10.1016/j.nima.2006.11.026>. URL: <https://www.sciencedirect.com/science/article/pii/S016890020602273X>.
- [Ito+18] T. M. Ito et al. “Performance of the upgraded ultracold neutron source at Los Alamos National Laboratory and its implication for a possible neutron electric dipole moment experiment”. In: *Phys. Rev. C* 97 (1 Jan. 2018), p. 012501. doi: [10.1103/PhysRevC.97.012501](https://doi.org/10.1103/PhysRevC.97.012501). URL: <https://link.aps.org/doi/10.1103/PhysRevC.97.012501>.
- [Jam] Fred James. *TMinuit Class Reference*. URL: <https://root.cern.ch/doc/master/classTMinuit.html>.
- [JTW57a] J. D. Jackson, S. B. Treiman, and H. W. Wyld. “Possible Tests of Time Reversal Invariance in Beta Decay”. In: *Phys. Rev.* 106 (3 May 1957), pp. 517–521. doi: [10.1103/PhysRev.106.517](https://doi.org/10.1103/PhysRev.106.517). URL: <https://link.aps.org/doi/10.1103/PhysRev.106.517>.
- [JTW57b] J.D. Jackson, S.B. Treiman, and H.W. Wyld. “Coulomb corrections in allowed beta transitions”. In: *Nuclear Physics* 4 (1957), pp. 206–212. ISSN: 0029-5582. doi: [https://doi.org/10.1016/0029-5582\(87\)90019-8](https://doi.org/10.1016/0029-5582(87)90019-8). URL: <https://www.sciencedirect.com/science/article/pii/0029558287900198>.
- [Klo+19] M. Klopf et al. “Constraints on the Dark Matter Interpretation  $n \rightarrow \chi + e^+e^-$  of the Neutron Decay Anomaly with the PERKEO II Experiment”. In: *Phys. Rev. Lett.* 122 (22 June 2019), p. 222503. doi: [10.1103/PhysRevLett.122.222503](https://doi.org/10.1103/PhysRevLett.122.222503). URL: <https://link.aps.org/doi/10.1103/PhysRevLett.122.222503>.
- [KR05] Joshua R Klein and Aaron Roodman. “BLIND ANALYSIS IN NUCLEAR AND PARTICLE PHYSICS”. In: *Annual Review of Nuclear and Particle Science* 55.1 (2005), pp. 141–163. doi: [10.1146/annurev.nucl.55.090704.151521](https://doi.org/10.1146/annurev.nucl.55.090704.151521). eprint: <https://doi.org/10.1146/annurev.nucl.55.090704.151521>. URL: <https://doi.org/10.1146/annurev.nucl.55.090704.151521>.

- [KRS85] V.A. Kuzmin, V.A. Rubakov, and M.E. Shaposhnikov. “On anomalous electroweak baryon-number non-conservation in the early universe”. In: *Physics Letters B* 155.1 (1985), pp. 36–42. ISSN: 0370-2693. doi: [https://doi.org/10.1016/0370-2693\(85\)91028-7](https://doi.org/10.1016/0370-2693(85)91028-7). URL: <https://www.sciencedirect.com/science/article/pii/0370269385910287>.
- [LG05] S. K. Lamoreaux and R. Golub. “Detailed discussion of a linear electric field frequency shift induced in confined gases by a magnetic field gradient: Implications for neutron electric-dipole-moment experiments”. In: *Phys. Rev. A* 71 (3 Mar. 2005), p. 032104. doi: [10.1103/PhysRevA.71.032104](https://doi.org/10.1103/PhysRevA.71.032104). URL: <https://link.aps.org/doi/10.1103/PhysRevA.71.032104>.
- [Liu02] Chen-Yu Liu. “A Superthermal Ultra-Cold Neutron Source”. PhD thesis. Princeton University, 2002.
- [Liu09] Chen-Yu Liu. “Cold Neutron and Ultracold Neutron Sources”. 2<sup>nd</sup> Fundamental Neutron Physics Summer School. June 2009. URL: [https://www.ncnr.nist.gov/summerschool/ss09/pdf/Liu\\_FP09.pdf](https://www.ncnr.nist.gov/summerschool/ss09/pdf/Liu_FP09.pdf).
- [LY56] T. D. Lee and C. N. Yang. “Question of Parity Conservation in Weak Interactions”. In: *Phys. Rev.* 104 (1 Oct. 1956), pp. 254–258. doi: [10.1103/PhysRev.104.254](https://doi.org/10.1103/PhysRev.104.254). URL: <https://link.aps.org/doi/10.1103/PhysRev.104.254>.
- [Lyo08] Louis Lyons. “Open statistical issues in Particle Physics”. In: *Ann. Appl. Stat.* 2.3 (Sept. 2008), pp. 887–915. doi: [10.1214/08-AOAS163](https://doi.org/10.1214/08-AOAS163). URL: <https://doi.org/10.1214/08-AOAS163>.
- [Mak05] Mark F. Makela. “Polarized Ultracold Neutrons: their transport in diamond guides and potential to search for physics beyond the standard model.” PhD thesis. Virginia Polytechnic Institute and State University, 2005.
- [Mam10] Russell R. Mammei. “Thin Films for the Transport of Polarized Ultracold Neutrons for Fundamental Symmetry Study.” PhD thesis. Virginia Polytechnic Institute and State University, 2010.
- [Mär+19] B. Märkisch et al. “Measurement of the Weak Axial-Vector Coupling Constant in the Decay of Free Neutrons Using a Pulsed Cold Neutron Beam”. In: *Phys. Rev. Lett.* 122 (24 June 2019), p. 242501. doi: [10.1103/PhysRevLett.122.242501](https://doi.org/10.1103/PhysRevLett.122.242501). URL: <https://link.aps.org/doi/10.1103/PhysRevLett.122.242501>.
- [McK+18] David McKeen et al. “Neutron Stars Exclude Light Dark Baryons”. In: *Phys. Rev. Lett.* 121 (6 Aug. 2018), p. 061802. doi: [10.1103/PhysRevLett.121.061802](https://doi.org/10.1103/PhysRevLett.121.061802). URL: <https://link.aps.org/doi/10.1103/PhysRevLett.121.061802>.

- [Men+13] M. P. Mendenhall et al. “Precision measurement of the neutron  $\beta$ -decay asymmetry”. In: *Phys. Rev. C* 87 (3 Mar. 2013), p. 032501. doi: 10.1103/PhysRevC.87.032501. URL: <https://link.aps.org/doi/10.1103/PhysRevC.87.032501>.
- [Men14] Michael Praetorius Mendenhall. “Measurement of the neutron beta decay asymmetry using ultracold neutrons.” PhD thesis. California Institute of Technology, 2014.
- [Mor+09] C.L. Morris et al. “Multi-wire proportional chamber for ultra-cold neutron detection”. In: *Nuclear Instruments and Methods in Physics Research Section A: Accelerators, Spectrometers, Detectors and Associated Equipment* 599.2 (2009), pp. 248–250. ISSN: 0168-9002. doi: <https://doi.org/10.1016/j.nima.2008.11.099>. URL: <https://www.sciencedirect.com/science/article/pii/S0168900208017543>.
- [Mor+17] C. L. Morris et al. “A new method for measuring the neutron lifetime using an in situ neutron detector”. In: *Review of Scientific Instruments* 88.5 (2017), p. 053508. doi: 10.1063/1.4983578. eprint: <https://doi.org/10.1063/1.4983578>. URL: <https://doi.org/10.1063/1.4983578>.
- [MR12] David E Morrissey and Michael J Ramsey-Musolf. “Electroweak baryogenesis”. In: *New Journal of Physics* 14.12 (Dec. 2012), p. 125003. ISSN: 1367-2630. doi: 10.1088/1367-2630/14/12/125003. URL: <http://dx.doi.org/10.1088/1367-2630/14/12/125003>.
- [Nag+19] Nagakura, Naoki et al. “New project for precise neutron lifetime measurement at J-PARC”. In: *EPJ Web Conf.* 219 (2019), p. 03003. doi: 10.1051/epjconf/201921903003. URL: <https://doi.org/10.1051/epjconf/201921903003>.
- [NG13] Oscar Naviliat-Cuncic and MartÃn GonzÃlez-Alonso. “Prospects for precision measurements in nuclear decay in the LHC era”. In: *Annalen der Physik* 525.8-9 (2013), pp. 600–619. doi: <https://doi.org/10.1002/andp.201300072>. eprint: <https://onlinelibrary.wiley.com/doi/pdf/10.1002/andp.201300072>. URL: <https://onlinelibrary.wiley.com/doi/abs/10.1002/andp.201300072>.
- [Nic+05] J. S. Nico et al. “Measurement of the neutron lifetime by counting trapped protons in a cold neutron beam”. In: *Phys. Rev. C* 71 (5 May 2005), p. 055502. doi: 10.1103/PhysRevC.71.055502. URL: <https://link.aps.org/doi/10.1103/PhysRevC.71.055502>.
- [Pat+18] R. W. Pattie et al. “Measurement of the neutron lifetime using a magneto-gravitational trap and in situ detection”. In: *Science* 360.6389 (2018), pp. 627–632. ISSN: 0036-8075. doi: 10.1126/science

- aan8895. eprint: <http://science.sciencemag.org/content/360/6389/627.full.pdf>. URL: <http://science.sciencemag.org/content/360/6389/627>.
- [Pen+04] J. M. Pendlebury et al. “Geometric-phase-induced false electric dipole moment signals for particles in traps”. In: *Phys. Rev. A* 70 (3 Sept. 2004), p. 032102. doi: 10.1103/PhysRevA.70.032102. URL: <https://link.aps.org/doi/10.1103/PhysRevA.70.032102>.
- [Pen12] Mike Pendelbury. “The future of neutron EDM experiments”. Presentation for Oak Ridge National Laboratory. 2012. URL: [https://www.phy.ornl.gov/groups/neutrons/nEDM\\_Workshop\\_2012/Presentations/The%20future%20of%20n%5C%20EDM%20expts%20Pendle.ppt](https://www.phy.ornl.gov/groups/neutrons/nEDM_Workshop_2012/Presentations/The%20future%20of%20n%5C%20EDM%20expts%20Pendle.ppt).
- [Pla+08] B. Plaster et al. “A solenoidal electron spectrometer for a precision measurement of the neutron  $\hat{I}^2$ -asymmetry with ultracold neutrons”. In: *Nuclear Instruments and Methods in Physics Research Section A: Accelerators, Spectrometers, Detectors and Associated Equipment* 595.3 (2008), pp. 587–598. ISSN: 0168-9002. doi: <https://doi.org/10.1016/j.nima.2008.07.143>. URL: <https://www.sciencedirect.com/science/article/pii/S0168900208011339>.
- [Pla+12] B. Plaster et al. “Measurement of the neutron  $\beta$ -asymmetry parameter  $A_0$  with ultracold neutrons”. In: *Phys. Rev. C* 86 (5 Nov. 2012), p. 055501. doi: 10.1103/PhysRevC.86.055501. URL: <https://link.aps.org/doi/10.1103/PhysRevC.86.055501>.
- [Pla+19] B. Plaster et al. “Final results for the neutron  $\beta$ -asymmetry parameter  $A_0$  from the UCNA experiment”. In: *EPJ Web Conf.* 219 (2019), p. 04004. doi: 10.1051/epjconf.201921904004. URL: <https://doi.org/10.1051/epjconf/201921904004>.
- [Rio+11] R. Rios et al. “Sealed drift tube cosmic ray veto counters”. In: *Nuclear Instruments and Methods in Physics Research Section A: Accelerators, Spectrometers, Detectors and Associated Equipment* 637.1 (2011), pp. 105–108. ISSN: 0168-9002. doi: 10.1016/j.nima.2010.12.098. URL: <http://www.sciencedirect.com/science/article/pii/S0168900210028780>.
- [Sak67] A. D. Sakharov. “Violation of CP Invariance, C asymmetry, and baryon asymmetry of the universe”. In: *Pisma Zh. Eksp. Teor. Fiz.* 5 (1967). doi: 10.1070/PU1991v034n05ABEH002497.
- [Sal+14] D. J. Salvat et al. “Storage of ultracold neutrons in the magneto-gravitational trap of the UCN $\tau$  experiment”. In: *Phys. Rev. C* 89 (5 May 2014), p. 052501. doi: 10.1103/PhysRevC.89.052501. URL: <https://link.aps.org/doi/10.1103/PhysRevC.89.052501>.

- [Sau+04] A Saunders et al. “Demonstration of a solid deuterium source of ultra-cold neutrons”. In: *Physics Letters B* 593.1 (2004), pp. 55–60. ISSN: 0370-2693. doi: <https://doi.org/10.1016/j.physletb.2004.04.048>. URL: <https://www.sciencedirect.com/science/article/pii/S0370269304006781>.
- [Sau+13] A. Saunders et al. “Performance of the Los Alamos National Laboratory spallation-driven solid-deuterium ultra-cold neutron source”. In: *Review of Scientific Instruments* 84.1 (2013), p. 013304. doi: [10.1063/1.4770063](https://doi.org/10.1063/1.4770063). eprint: <https://doi.org/10.1063/1.4770063>. URL: <https://doi.org/10.1063/1.4770063>.
- [Sau+20] H. Saul et al. “Limit on the Fierz Interference Term  $b$  from a Measurement of the Beta Asymmetry in Neutron Decay”. In: *Phys. Rev. Lett.* 125 (11 Sept. 2020), p. 112501. doi: [10.1103/PhysRevLett.125.112501](https://doi.org/10.1103/PhysRevLett.125.112501). URL: <https://link.aps.org/doi/10.1103/PhysRevLett.125.112501>.
- [Sau18] Alexander Saunders. “Los Alamos Beta Decay Experimental Program”. Talk at the Amherst Beta Workshop. Nov. 2018. URL: [https://www.physics.umass.edu/acfi/sites/acfi/files/slides/2018\\_lanl\\_beta\\_decay\\_amherst\\_1.pdf](https://www.physics.umass.edu/acfi/sites/acfi/files/slides/2018_lanl_beta_decay_amherst_1.pdf).
- [Slu+17] S. Slutsky et al. “Cryogenic magnetic coil and superconducting magnetic shield for neutron electric dipole moment searches”. In: *Nuclear Instruments and Methods in Physics Research Section A: Accelerators, Spectrometers, Detectors and Associated Equipment* 862 (2017), pp. 36–48. ISSN: 0168-9002. doi: <https://doi.org/10.1016/j.nima.2017.05.005>. URL: <https://www.sciencedirect.com/science/article/pii/S016890021730534X>.
- [Sum+21] N. Sumi et al. “Precise Neutron Lifetime Measurement Using Pulsed Neutron Beams at J-PARC”. In: *JPS Conf. Proc.* 33 (2021). Ed. by Naohito Saito, p. 011056. doi: [10.7566/JPSCP.33.011056](https://doi.org/10.7566/JPSCP.33.011056). arXiv: [2102.09758 \[hep-ex\]](https://arxiv.org/abs/2102.09758).
- [Sun+18] X. Sun et al. “Search for dark matter decay of the free neutron from the UCNA experiment:  $n \rightarrow \chi + e^+e^-$ ”. In: *Phys. Rev. C* 97 (5 May 2018), p. 052501. doi: [10.1103/PhysRevC.97.052501](https://doi.org/10.1103/PhysRevC.97.052501). URL: <https://link.aps.org/doi/10.1103/PhysRevC.97.052501>.
- [Sun+19] X. Sun et al. “Search for neutron dark decay:  $n \rightarrow \chi + e^+e^-$ ”. In: *EPJ Web Conf.* 219 (2019). Ed. by T. Jenke et al., p. 05008. doi: [10.1051/epjconf/201921905008](https://doi.org/10.1051/epjconf/201921905008).
- [Sun+20] X. Sun et al. “Improved limits on Fierz interference using asymmetry measurements from the Ultracold Neutron Asymmetry (UCNA) experiment”. In: *Phys. Rev. C* 101 (3 Mar. 2020), p. 035503. doi:

- [10.1103/PhysRevC.101.035503](https://doi.org/10.1103/PhysRevC.101.035503). URL: <https://link.aps.org/doi/10.1103/PhysRevC.101.035503>.
- [Swa18] Christopher Swank. “Search for a Dark Matter Decay of the Free Neutron from the UCNA Experiment”. Talk at the Conference on the Intersections of Particle and Nuclear Physics. <http://cipanp18.berkeley.edu/>. 2018.
- [Tan+18] Zhaowen Tang et al. “Search for the Neutron Decay  $n \rightarrow X + \gamma$ , Where X is a Dark Matter Particle”. In: *Physical Review Letters* 121.2 (July 2018). doi: [10.1103/PhysRevLett.121.022505](https://doi.org/10.1103/PhysRevLett.121.022505).
- [Teaa] ROOT Team. *Analyzing petabytes of data, scientifically*. URL: <https://root.cern/>.
- [Teab] ROOT Team. *TFractionFitter Class Reference*. URL: <https://root.cern/doc/master/classTFractionFitter.html>.
- [Wan+12] M. Wang et al. “The AME2012 atomic mass evaluation (II). Tables, graphs and references”. In: *Chin.Phys.C* 36 (2012), p. 1603.
- [WG11] Fred E. Wietfeldt and Geoffrey L. Greene. “Colloquium: The neutron lifetime”. In: *Rev. Mod. Phys.* 83 (4 Nov. 2011), pp. 1173–1192. doi: [10.1103/RevModPhys.83.1173](https://doi.org/10.1103/RevModPhys.83.1173). URL: <https://link.aps.org/doi/10.1103/RevModPhys.83.1173>.
- [Wie14] Fred Wietfeldt. “BL3: Next generation beam experiment to measure the neutron lifetime”. The 8<sup>th</sup> International Workshop on the CKM Unitarity Triangle. 2014. URL: <https://indico.cern.ch/event/253826/contributions/567387/>.
- [Wie18] F. E. Wietfeldt. “Measurements of the Neutron Lifetime”. In: *Atoms* 6.4 (2018), p. 70. doi: [10.3390/atoms6040070](https://doi.org/10.3390/atoms6040070).
- [Wil82] D.H. Wilkinson. “Analysis of neutron  $\beta$ -decay”. In: *Nuclear Physics A* 377.2 (1982), pp. 474–504. ISSN: 0375-9474. doi: [https://doi.org/10.1016/0375-9474\(82\)90051-3](https://doi.org/10.1016/0375-9474(82)90051-3). URL: <https://www.sciencedirect.com/science/article/pii/0375947482900513>.
- [Wil89] D. H. Wilkinson. “Evaluation of beta-decay Pt 1”. In: *Nuclear Instruments and Methods in Physics Research, Section A* 275.2 (Feb. 1989), pp. 378–386. ISSN: 0168-9002. URL: [http://inis.iaea.org/search/search.aspx?orig\\_q=RN:20028415](http://inis.iaea.org/search/search.aspx?orig_q=RN:20028415).
- [Wil90] D.H. Wilkinson. “Evaluation of beta-decay: II. Finite mass and size effects”. In: *Nuclear Instruments and Methods in Physics Research Section A: Accelerators, Spectrometers, Detectors and Associated Equipment* 290.2 (1990), pp. 509–515. ISSN: 0168-9002. doi: [https://doi.org/10.1016/0168-9002\(90\)90570-V](https://doi.org/10.1016/0168-9002(90)90570-V). URL: <https://www.sciencedirect.com/science/article/pii/016890029090570V>.

- [Wil93] D.H. Wilkinson. “Evaluation of beta-decay Part III. The complex gamma function”. In: *Nuclear Instruments and Methods in Physics Research Section A: Accelerators, Spectrometers, Detectors and Associated Equipment* 335.1 (1993), pp. 305–309. ISSN: 0168-9002. doi: [https://doi.org/10.1016/0168-9002\(93\)90285-P](https://doi.org/10.1016/0168-9002(93)90285-P). URL: <https://www.sciencedirect.com/science/article/pii/016890029390285P>.
- [Wil95] Denys H. Wilkinson. “Evaluation of beta decay. 5. The Z independent outer radiative corrections for allowed decay”. In: *Nucl. Instrum. Meth. A* 365 (1995), pp. 497–507. doi: [10.1016/0168-9002\(95\)00495-5](https://doi.org/10.1016/0168-9002(95)00495-5).
- [Yue+13] A. T. Yue et al. “Improved Determination of the Neutron Lifetime”. In: *Phys. Rev. Lett.* 111.22 (2013), p. 222501. doi: [10.1103/PhysRevLett.111.222501](https://doi.org/10.1103/PhysRevLett.111.222501). arXiv: [1309.2623 \[nucl-ex\]](https://arxiv.org/abs/1309.2623).
- [Zel59] Ya. B. Zel'dovitch. In: *Sov. Phys. JETP* 9.1389 (1959).